Computational Study of Radiation-Induced Defects in Topaz

Elisabeth Adela Ruzena Krizek
Department of Chemistry
University College London (UCL)

Thesis submitted for the degree of
Doctor of Engineering (EngD)
12^{th} September 2014

I dedicate this thesis to my parents, Hana and George, my bother and sister, Jan and Olga, and my boyfriend, David, who have been a constant pillar of support these past four years.

I, Elisabeth Adela Ruzena Krizek confirm that the work presented in this thesis is my own. Where information has been derived from other sources, I confirm that this has been indicated in the thesis.

Acknowledgements

First and foremost, I am indebted and would like to thank above all my supervisor, Dr. Furio Corà, for his continued guidance and support throughout this project and all my time at UCL. I am grateful to Dr. Florian Schiffmann for his assistance with CP2K and your advice to me in your time at UCL.

There are a great number of people to thank, both within the chemistry department and the university as a whole, that have made UCL an enjoyable place to do research. I would like to therefore thank in particular, Isaac, Will, Giota, Jay, Nic, Nuru, Alan, Jamie, Ralph and Clyde.

I must also thank my industrial sponsors, Atomic Weapons Establishment (AWE), for their continued interest and for their funding, in particular Dr David Plant's guidance and advice during with my project. I am also grateful to the Engineering and Physical Research Council (EPSRC), for their funding of this project, and to the Engineering Doctorate (EngD) centre at UCL for their programme.

For the services I used, I must also acknowledge the UK national supercomputing service, HECToR, for its outstanding facility and service, without which the most challenging part in this thesis could not have been achieved. Also the High Performing Computing service at UCL, Legion, and the computer cluster in the chemistry department, faraday. I am hugely grateful to Jörg Saßmannshausen, for managing faraday and for all the technical assistance you were able to provide.

Outside academia, I would also thank for their support, David, my family, Philippa, Kathy, the choir of Trinity College Cambridge and all those around the Cambridge area, my friends from back home and my friends from school, for Jarad who advised me to pursue this course, and to Anthea, without her guidance and tutoring at a young age, I could not have hoped to come this far.

Abstract

This purely theoretical investigation considered the irradiation induced and other intrinsic defects that may form colour centres in topaz. Topaz is an aluminium flouro/hydroxy-silicate and undergoes a colourless to blue optical transformation during irradiative treatment. The depth of hue and quality of the colour is dependent on the type of radiation used, whether thermal annealing was involved, and the origin of the samples. Since the colour centres for any of these processes are not well understood for topaz, a detailed investigation into all likely defects cited in the literature was performed. Ground state electronic structure calculations, using full electron basis sets and hybrid functionals, were performed using the CRYSTAL and CP2K codes, to gain the relative stabilities and structural properties of optimised open shell defect models; as well as the density of states, localised spin densities, and certain EPR parameters. The molecule dynamics time-dependent density functional theory (MD TD-DFT) scheme within the CP2K code was used to generate calculated UV-Vis spectra to compare with experimental data supplied by literature.

Contents

List of Figures

List of Tables

Chapter 1

Introduction

The subject of radiation induced defects in the creation or enhancement of colour in gemstones has become a source of interest among gemologists [1], spectroscopists [2, 3], regulators [4] and the general public, ever since radiation was first used to treat gemstones in the early 20^{th} century shortly following its own discovery [5]. The commercial treatment of topaz by radiation actually began in the 1940's, and today topaz is the most commonly irradiated gemstone: with approximately tens of millions of carats of blue topaz being irradiated each year, where other gemstone varieties manage fewer quantities. One of the main reasons for this wide spread treatment of topaz, is that topaz displays the best example of any gemstone for colour enhancement by the application of irradiation.

Generally topaz is colourless, but high energy particles, such as electrons or neutrons, and electromagnetic ionising radiation sources, like gamma rays, can tranform the stone into a gemstone by creating colour centres in the crystal. Following neutron irradiation, colourless topaz typically changes immediately to a saturated blue colour (medium to dark hues) [4, 6–9], with some sources reporting an intermediate reddish pink colour [10], which can be removed by heating to reveal blue. Gamma or electron irradiation treatment leads to grayish or brownish colours in topaz, which can be bleached out, again by use of thermal annealing treatments, typically either removing all colour from the crystal or leaving a pale blue hue [4, 7, 11–13].

A colour centre involves the creation and stabilisation of defect species inside the crystal, which in turn facilitates the transfer and trapping of an electron from its normal low energy occupied position, into a stable energy level inside the band gap. Electrons can only absorb certain wavelengths (colours) of light, and since their energy level within the band leads to a decrease of the band gap, the absorption edge is reduced from thr UltraViolet (UV) to the visible range, including the optical colour change observed in the material. The type and variety of defects possible within the

topaz crystal are substantial, and are known to depend on the type of irradiation. Presently the discussion in the literature as to which type of defects are responsible for producing the colours seen in topaz is inconclusive. The majority of studies to date have been experimental: the main techniques used for analysing defects in insulators are optical absorption and Electron paramagnetic resonance (EPR). Their success is compromised when angular information is lost, and when studying intrinsic defects, which are not paramagnetic, one can only rely on absorption bands and no direct argument for describing and identifying defect centres [14].

Here we present a computational investigation, with the aim of applying modern electronic structure computational methods, in order to study the structural and defect chemistry of topaz. By calculating the electronic structure of known open shell defects and simulating comparable data to that of experiment, such as band gaps and UltraViolet-Visible (UV-Vis) absorption spectra, this approach can complement and offer additional information about the electronic and chemical composition of likely colour centres that can form in topaz, and ultimately help answer the question, *"what makes topaz blue?"*.

A computational investigation has the advantage over experiment that a number of parameters, such as the chemical composition, oxidation state of open shell defects, defect concentration and their location (including substitution site and the placing of multiple defect with respect to their separation), can all be predetermined. The electronic structure of an optimised system including open shell defects, can also be interrogated, using computational techniques, to identify the location of unpaired electrons (spin centres), with regards to chemical species and band structure. In addition, with ever increasing computer capability,[1] [2] together with the evolution in modern computational chemistry codes to include more advanced quantum chemical techniques, such as Time Dependent Density Functional Theory (TD-DFT), the ability to model optical and excited state properties of solid state materials is being made possible.

Although computational methods provide *ideal* solutions about materials, which are by their nature more complicated than we can model, the atomic level information available, both on the local and long range scale, and regarding structure, oxidation state and relative stability, is nevertheless detailed and informative. The challenge for this investigation, given the high computational cost of electronic struc-

[1]This work made use of the facilities of HECToR, the UK's national high-performance computing service, which is provided by UoE HPCx Ltd at the University of Edinburgh, Cray Inc and NAG Ltd, and funded by the Office of Science and Technology through EPSRC's High End Computing Programme.

[2]The authors acknowledge the use of the UCL Legion High Performance Computing Facility (Legion@UCL), and associated support services, in the completion of this work.

ture calculations, will be choosing which of the likely defects will be of highest interest of characterise in full detail, and ascertaining whether the models and techniques employed will be accurate enough to predict the optical properties observed by experiment.

It should be noted for this investigation that, though we can calculate the defect energy or relative stability of topaz systems with defects that are the result of high energy radiation bombardment through computational means, it is extremely challenging to follow directly their formation upon irradiation, since the energy released by these treatments can be as high as several MeV - or the energy equivalent of several million chemical bonds. We shall therefore focus only on the defects left in the material after the irradiation treatment, whose formation energy is largely irrelevant. However, with regards to the discussion of chemical annealing and the mechanisms involved, computational chemistry techniques can provide analysis as to likely paths and rearrangements of migrating ions.

In order to provide a structured discussion of our computational investigation into irradiation induced defects in topaz, this thesis have been divided into the four main sections: background material, computational method, results and discussion, and conclusion and future work. The first section, background material, is split into two chapters: chapter 2 is a literature review of what is currently known about topaz, including discussions about likely defects that form in the crystal following irradiation, and their optical spectra; chapter 3 presents the theory behind the quantum chemical and computational techniques employed in our calculations. The second section is outlined in chapter 4, and provides the details involved in the computational methods employed, i.e. codes used, settings, basis set choices, functionals, and calculation type. The third section, results and discussion, is divided into five chapters, where each chapter focuses on a single type of defect or a related family of defects in topaz, and comes out of the discussion in chapter 2 as to the (likely) defect chemistry of topaz. To begin with, chapter 5 focuses on pure topaz and the intrinsic chemical composition variety of topaz crystals; chapter 6 relates to pink topaz and the defects that result from chromium(III) ion substitution; chapter 7 presents the phosphorus family defects; chapter 8 relates to silicon based defects; and chapter 9 introduces defects based on the hydroxy group. Finally, the concluding statements and remarks about the future direction for this investigation are presented in chapter 10.

Chapter 2

Literature Review of Topaz

The aim of this section is to present what is currently known about topaz, with emphasis on defect chemistry and models suggested in the literature to explain irradiation-induced colouration. The application of topaz as a dosimeter is also introduced.

2.1 Composition

Topaz is an aluminium fluro/hydroxy-silicate that forms naturally at low pressures as an accessory mineral in aluminum and fluorine-rich rocks [15]. Topaz has a fairly consistent chemical composition of $Al_2SiO_4(F,OH)_2$, where OH^- may substitute on F^- sites, and rarely exceeds 30 mol % concentration in natural topaz [6, 16–18]. The highest hydroxyl content of natural topaz was discovered in the ultrahigh-pressure rocks of Eastern China. Here the concentration was as high as 55 mol % [19]. Wunder *et al.* [20] were the first to synthesize the fully hydrated analogue of topaz, $Al_2SiO_4(OH)_2$, for which high pressures were used (above 7.0 GPa) in multi-anvil experiments.

In this investigation, the $Al_2SiO_4(OH)_2$ composition is often referred to as topaz-OH and $Al_2SiO_4F_2$ as topaz-F. The majority of the mixed F:OH composition in this investigation is usually equally split. Therefore, topaz-FOH refers to the $Al_2SiO_4(F,OH)_2$ with a 50 : 50 ratio of F^- and OH^- ions, unless otherwise specified.

2.2 Structure

Topaz crystallises in the orthorhombic space group *Pbnm* (D_{2h}^{16}), with four formula units per unit cell. The lattice parameters are $a = 4.6399$ Å, $b = 8.7968$ Å and $c = 8.3909$ Å [6]. These can alter slightly depending on the OH/F ratio and other

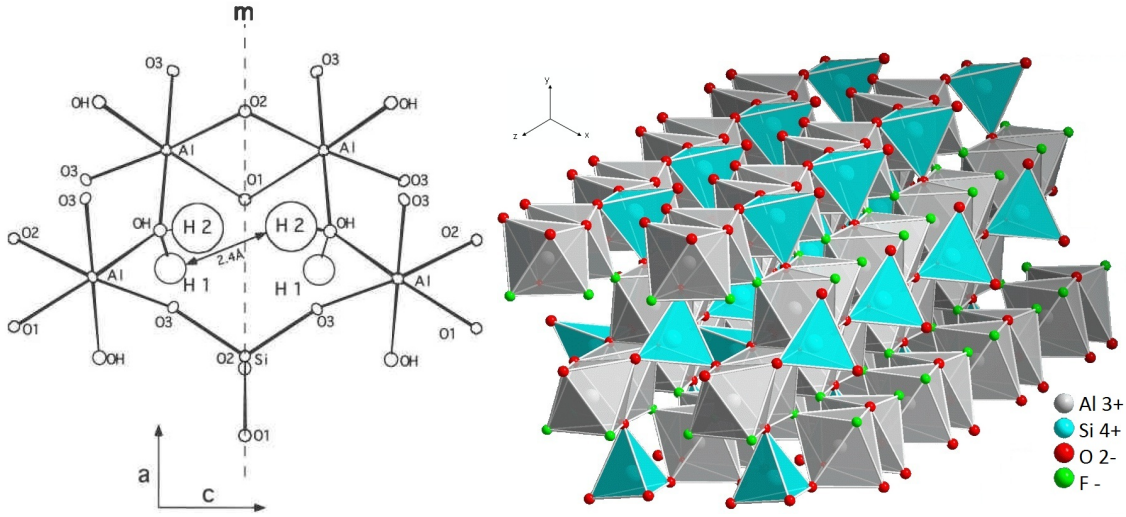

(a) H1 H2 positions

(b) Crankshaft Chains

Figure 2.1: Ilustrating the structure of topaz; (a) the two lattice sites of H, and (b) the crankshaft chains of topaz, AlO_4(F,OH) octahedra linked with SiO_4 tetrahedra linked in a zig-zag like fashoin, parallel to the *c*-axis. Illustrations reproduced from references [18] and [23] respectively.

defects or mineral impurities [1, 17]. Northrup *et al.* [18] were the first to characterise $Al_2SiO_4(OH)_2$, using single-crystal X-Ray Diffraction (XRD), with a reduced space group symmetry of $Pbn2_1$. The symmetry mirror plane of the *Pbnm* space group is broken by the disorder caused due to the fact that the H of the hydroxyl groups can adopt one of two possible orientations (Figure 2.1(a)). In this investigation, these two H sites are labeled H1 and H2, following the Northrup *et al.* [18] notation (Figure 2.1(a)).

The topaz structure is made up of distorted $AlO_4(F,OH)_2$ octahedra, with four oxygen ions (two in 4*c* and two in 8*d* Wyckoff positions) and two fluoride or hydroxyl ions (8*d*). The Al^{3+} ions occupy 8*d*, whereas Si^{4+} ions are in 4*c* Wyckoff positions [21]. The octahedra are linked together by nearly undistorted $[SiO_4]^{4+}$ tetrahedra, in a zig-zag fashion parallel to the *c*-axis (Figure 2.1(b)): geologically, topaz qualifies as a *nesosilicate*, since it contains isolated SiO_4 structural units. The aluminium octahedra are also linked to other octahedra: the four structural O^{2-} ions are edge shared with two other octahedra, whilst the two OH^-/F^- ions both form corner sharing units with two other octahedra. An alternative way to view the structure of topaz is to consider it as double hexagonal close packed (dhcp), where anion layers of O^{2-} and F/OH ions alternate in an *ABAC* sequence, with Al and Si cations located interstitially between the anion layers [17]. Layers B and C consist of four fluorines and two symmetry related oxygens, are identical except for inversion, and are stacked parallel to the *b*-axis [22].

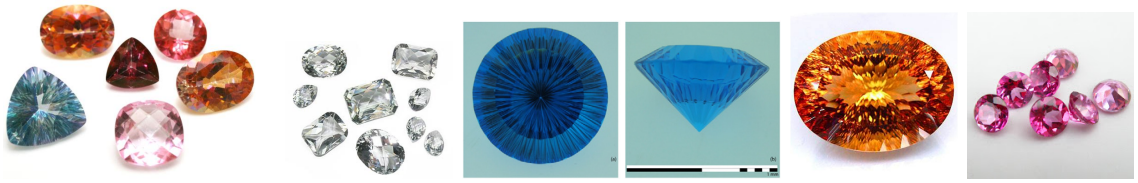

(a) Topaz gemstones (b) White (c) Blue (d) Imperial (e) Pink

Figure 2.2: Various examples of coloured of topaz gemstones: (a) a selection of coloured topazes (form left to right: grey-blue, orange, wine, pink, reddish-pink and sherry-gold), (b) white topaz, (c) blue topaz, (d) Imperial topaz and (e) pink topaz. Reproduced from references [26, 28–31].

2.3 Appearance

The most common forms of topaz found naturally are colourless (or transparent) crystals (Figure 2.2(b)). This is the *pure* form of topaz (or *white topaz*) and has a bandgap greater than 6.2 eV [14]. Since white topaz is the most common form of natural topaz, it has little commercial value and is therefore usually treated. It has been found that white topaz has a higher susceptibility and sensitivity to radiation (γ-rays and UV light) than coloured forms of the crystal [24, 25].

Besides rarity, the value of a gemstone depends on the size, purity, shape, cut, and colour. The colours of gemstones are sometimes due to small inclusions in the matrix, or impurities, or ionising radiation damage, which cause colour centres in the crystal [26]. Topaz can be found to include a wide variety of trace elements [8], most commonly V, Ti, Mn, Cr and Fe [1]. Topaz can adopt a range of colours: pale-blue, yellow, green, brown, reddish-orange, pink (naturally very rare) and wine (Figure 2.2).

Blue topaz does occur naturally, but is exceptionally rare, especially the darker hues (Figure 7.1). The majority of blue topaz commercially available has therefore undergone treatment of some kind. Typically colourless, blue, gray or pale yellow crystals of topaz are transformed into darker hues of blue, by a combination of ionising irradiation and/or heat application. The defect centre(s) responsible for the blue colouration in topaz is still subject to discussion in the literature. A low hydroxyl content is usually found in colourless or natural blue topaz [27].

Imperial topaz refers to stones with sherry-red, deep pink and reddish-orange colours. Generally this excludes less intense peach-orange and medium golden hues. The highest natural concentrations of OH are found in Imperial topaz, together with elevated Cr^{3+} and Fe^{3+} impurity concentrations.

2.4 Optical Phenomena of Irradiated Topaz

The optical phenomena observed in irradiation damaged topaz are demonstrated in Figure 7.1: all blue hues of topaz pictured here can be manufactured from colourless topaz through irradiative treatment, plus sometimes thermal treatment also. A summary of colour changes observed in topaz following specific radiation treatment types follows.

Figure 2.3: The entire range of topaz's blue hues and their classification.

Gamma ray irradiation of colourless topaz induces brown or gray colouration with sometimes patchy coverage. Thermal annealing ($\sim 150 - 220$℃) removes the intermediate colour to reveal a colourless crystal or one with light to medium blue hues [7]. **High-energy electrons** ($10 - 20\,\mathrm{MeV}$) produce similar effects, causing a brown or greenish-brown intermediate colour [32], stable to ~ 220℃ and resulting in a medium blue hue. Radioactivity in some topaz samples can be induced with high energy electrons. These phenomena are summarised in the following equation:

$$\text{topaz(colourless)} \xrightarrow{\gamma,\ e^-} \text{topaz(brown)} \xrightarrow{\Delta} \text{topaz(light blue/colourless)} \quad (2.1)$$

Neutron-irradiated topaz reveals an immediate and intense saturated blue colour know as London blue (Figure 7.1): no additional treatment with heat is required [12, 33]. An investigation into whether neutron-induced colour centres were due to thermal ($E < 0.5\,\mathrm{eV}$) or fast neutrons, found that fast neutrons were responsible for the blue colour:

$$\text{topaz(colourless)} \xrightarrow{fast\ neutrons} \text{topaz(London blue)} \quad (2.2)$$

Thermal neutrons were found to lead to some radioactivity, thought to be due in part to some unknown impurities already present in the sample [8].

The depth of colour depends on the dose but also on the type of irradiation: the blue colour centres of gamma and electron irradiated topaz differ in some way from those of natural blue topaz and neutron irradiated topaz [6]. The following

sections (2.4.1 and 2.4.2) document literature spectroscopic data, which present optical evidence of differences between the induced colour centres of gamma and neutron irradiation in topaz respectively.

2.4.1 Gamma Irradiation

The first study into the colouration phenomena of topaz, caused by defects induced by gamma ray irradiation, is as early as 1923 [34]. Here, colourless samples of topaz adopted brownish amber colours, and smoky topaz samples had their own shades intensified, by irradiation from 200 mg rad of gamma-rays (see Section 2.9 for units of radiation). In 1975, Nassau and Prescott [12] conducted an extensive study into gamma irradiated topaz, using 123 samples that probably originated from Brazil. Of the samples, 86 were colourless, and following gamma-ray irradiation and moderate heating, only 21 exhibited any blue coloration (Table 2.1).

Initial Colour	Irradiated Colour	No. of Specimens
Colourless	No change to pale-yellow	28
	Med. yellow to light brown	26
	Brown to dark brown	32*
Pale Yellow	No change to darker yellow	14
	Medium to dark sherry	17
Sherry	Slightly darker	1
Blue to Green	Pale brown (with an olive or greenish tint)	2
	Medium to dark brown	3

*Heating of these produced a blue colour in 21 specimens some of which had an olive or greenish tint; in all the other 102 specimens heating merely restored the original colour.

Table 2.1: Colour changes of gamma irradiated (10 Mrad) topaz specimens. Table reproduced from reference [12].

The blue colour in transmitted light is attributable to the optical band near 620 nm in the absorption spectra (see Figure 2.5(c)) [35]. Colourless topaz samples also showed unevenness in gamma irradiation-induced colouration: patches of brown (or colour zoning) and striation (ridges) formed upon gamma irradiation (Figure 2.4(a)). Table 2.2 and Figure 2.4 summarise the absorption characteristics and sample history, together with the reference spectra of literature optical absorption data from gamma irradiated topaz respectively.

In the following discussion, we review literature findings and suggested defect models of gamma induced-damage in topaz.

Absorption	Sample History	Spectra	Ref.
	High-Energy Electron Radiation		
625 nm (16 000 cm^{-1}) X-spectrum 602 nm (16 600 cm^{-1}) Y-spectrum			[32]
	Gamma-ray Radiation		
625 nm (16 000 cm^{-1}) X-spectrum			[32]
420 nm 460 nm	• 1.5×10^5 Gy h^{-1} dose rate • 5 to 1000 kGy h^{-1} total accumulated dose	2.5(a)	[7]
620 nm	• 8.0×10^4 Gy h^{-1} dose rate • 10^7 Gy h^{-1} dose at room temperature • 373−473 K thermal treatment for 24 h	2.5(b)	[36]
470 nm - Transmittance Band 620 nm - Absorption Band	• Gamma Irradiated • 200 °C heating for 24 h	2.5(c)	[35]
620 nm (0.62 μm)	• 0.058 Mrad of gamma rays from ^{60}Co cell (15 min) • 12.6 Mrad half dose (18 h) • 200 °C thermal treatment for a few hours	2.5(d)	[12]

Table 2.2: Spectroscopic data of literature gamma-ray irradiated topaz.

Standard gemological tests would suggest that the blue colour in irradiated topaz (by any radiation type) is visually indistinguishable from that of naturally-occurring blue topaz: the unpolarised optical absorption spectra in Figure 2.5(d) show natural and irradiated blue topaz curves both have a broad absorption around 620 nm (0.62 μm) [12]. Polarised optical spectra can, however, detect dichroic[1] dependences and therefore can distinguish between different defects centres.

Many references given in Table 2.2 indicate an optical absorption at around 620 nm in the UV-Vis absorption spectra of gamma irradiated blue topaz. The relative absorption of polarised light at the 620 nm band of the optical absorption spectra in natural and irradiated (neutron, gamma and electron) blue topaz (Figure 2.4(b)), demonstrates not only the dichroic nature of topaz, but also the different polarisation dependence of the colour centres within each of these topaz sample types [14]. Topaz crystals that turned blue following gamma rays or electron irradiation, display very different polarisation dependencies to the naturally blue topaz crystals

[1]Dichroism (or pleochroism) can be a property of orthorhombic minerals and is evident by a change in colour when the material is rotated upon its axis under plane-polarised light.

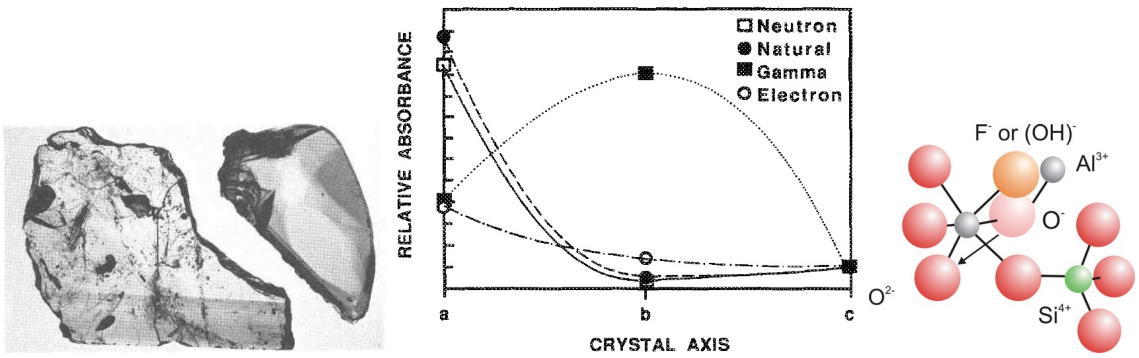

(a) (b) (c)

Figure 2.4: (a) The colouration zoning in a sample of gamma irradiated topaz. (b) The relative absorbance of natural and treated topaz at the 620 nm absorption peak of the optical spectra, demonstrating the dichroism of topaz. (c) An O^- bound small polaron defect, modeled in the topaz structure, as being located on the OH^- site prior to irradiation. The four structural equivalent oxygen ions in the vicinity of the O^- is thought to be possible hole polaron transfer sites, indicated by the arrow and induced by radiation. Reproduced from references [14], [37] and [12] respectively.

or those which underwent neutron irradiation.

Krambrock *et al.* [7] showed that the absorption band near 620 nm (2.0 eV),[2] in both gamma and neutron irradiated topaz, is caused by a paramagnetic O^- hole centre, the same small bound polaron defect da Silva *et al.* [6, 38] found in their neutron study of topaz. Observations found that topaz turns gray at low doses of gamma-ray irradiation, and brown at higher doses. The optical absorption spectra for gray and brown topaz (Figure 2.5(a)), indicate a broad absorption band at 420 nm and an intense absorption band at 460 nm respectively. Both types of spectra show a strong absorption increase in the UV range, and both colours, gray and brown, fade to pale or medium hues of blue, following thermal treatments between 150 and 200 °C. The O^- hole centre was attributed responsibility for causing the blue colour and is thought likely to form at the hydroxyl OH^- lattice site following the removal of a neutral hydrogen atom. The O^- hole centre was linked to the absorption band at around 620 nm, and subsequently the blue colouration, since they were shown to have the same thermal stability [6, 8, 38].

The model of O^- hole centres, was developed further for oxide materials by Schirmer [37]. A (positive) hole h^+ is formed in topaz by irradiation of the hydroxyl (OH^-) group and stabilised by lattice distortions. It can be classed as an acceptor defect[3] and is essentially an O^- polaron, which can be thought of as a hole trapped

[2]Also see Section A.1 for additional unit conversions of energy and wavelength specific to visible light portion of the electromagnetic spectrum.

[3]Electrically active point defects and impurities that are acceptors, donors, or as isoelectronic impurities, are described in the following way: donor defects contribute electrons to the host material; acceptor defects accept electrons from the host or donate holes to the host; and isoelectronic impurities are substitutional species that share the same oxidation state as the substituted species

at an O^{2-} site. The acceptor defect is trapped by a few nearby equivalent structural oxygen ions, which form a cluster and create other possible hole transfer sites (Figure 2.4(c)) [37]. Subsequent literature discussions of topaz including the O^{-} bound small polaron defect, refer to the defect accordingly.

Krambrock *et al.* [7] also found two paramagnetic centres in topaz following gamma irradiation by EPR measurements: a doublet related to the phosphorus radical, i.e. the $[PO_4]^{4-}$ centre where one electron is trapped on the P_{Si} site (following the model outlined by Petrov [39]), and a broad isotropic line of an unknown defect, thought to be related to the brown colouration since both have the same thermal stability ($150 - 200$ °C) [7]. Gamma radiation was also found to be responsible for forming the paramagnetic O^{-} hole centres in topaz, but only at low concentrations, hence the pale hues of blue. This is thought to be due to the lack of preexisting intrinsic defects, natural damage or electron trapping sites within topaz to stabilise the creation of O^{-} defects. Gamma treated samples of topaz with higher O^{-} concentrations were found to also have a higher concentrations of Fe^{3+} [6, 7]. The blue colour centres were found to reach maximum concentrations after high doses of gamma-ray or electron radiation was applied (100 Mrad, or 1 MGy) respectively) [8, 37]. The O^{-} hole centres are thought to only be produced in topaz with precursor or intrinsic defects that can stabilise the hole polaron, and therefore strongly depends on the origin of the sample. Other possible precursor centres could include: Al^{3+} ions on Si^{4+} sites, as in the colour centre in irradiated quartz that produces it's signature 'smoky' colour [8, 37], or Fe^{3+} ions on Si^{4+} sites, as in the interstitial in irradiated amethyst.

Many silicates, including topaz, dehydrate at temperatures ~ 500 °C [14]. Heating naturally colourless topaz *prior* to gamma irradiation effects the intensity of the radiation induced absorption band at 620 nm. Albuquerque *et al.* [40] found this to occur at temperatures above 573 K, whereas a later study by Isotani *et al.* [36] gave the temperature range of thermal decay at $373 - 553$ K.

Isotani *et al.* [36] also document a well-defined absorption band occurring at around 620 nm that is strongly influenced by an absorption in the UV region of the optical absorption spectra of gamma induced blue topaz (Figure 2.5(b)). The strong absorption below 400 nm is at about 314 nm and is attributed (tentatively) to a silanone (=Si=O) defect, previously defined by Bonventi *et al.* [35]. The broad shoulder to the 620 nm band at $800 - 1100$ nm, is loosely attributed to Fe^{3+} on octahedral sites, as this is the same optical region at which the absorption of this defect occurs in other materials containing Fe^{3+} defect centres [41–44]. Sharp bands

in the host.

and small bands at 1290 nm (8271 cm^{-1}) and 1226 nm (8157 cm^{-1}) respectively, are assigned to a combination of the first overtone of the stretching mode of OH^- (3644 cm^{-1}) and the bending mode of Al−OH (1160 cm^{-1}) respectively, and that of the first overtone of the stretching mode of OH^- and a very weak band observed at 1079 cm^{-1} in some samples of topaz [36, 45].

Bonventi *et al.* [35] assigned spectral lines 41630 and 38 510 cm^{-1} (240 and 260 nm respectively) to the dangling silicon bond defect (=$Si_{\cdot}$), and the line at 60 900 cm^{-1} (164 nm) to an oxygen vacancy (≡Si−Si≡). Thermal decomposition at 200 °C, of the line at about 16 000 cm^{-1} (625 nm), was attributed to lattice distortions that stabilise an O^- hole defect close to an acceptor defect, e.g. Al^{3+} or Si^{4+}. Two further lines, around 313 and 238 nm (32000 and 42 000 cm^{-1} respectively), were assigned as the silanone (=Si=O) defect.

2.4.2 Neutron Irradiation

Table 2.3 summarises literature data on the optical absorption characteristics and sample history of neutron irradiated topaz, and Figure 2.6 comprises the accompanying reference spectra. In neutron irradiated topaz, the optical absorption spectral features generally observed are a strong absorption band at $620 - 625$ nm, a weak absorption band at $410 - 420$ nm, an absorption valley at 475 nm, and a UV absorption shoulder at around 354 nm [7, 8, 14, 37]. The absorption valley at about 475 nm indicates that the sample of topaz is blue [7]. Since the absorption band at 620 nm in both the neutron irradiated and natural blue topaz absorption spectra show the same polarised light dependences [14], as seen in Figure 2.4(b), the optical absorption properties for natural blue topaz were also included in Table 2.3 for comparison.

Neutron damaged topaz crystals all displayed a uniform blue colouration, i.e. without colour zoning [14]. In addition, all samples displayed the same colour upon irradiation, independently on the source of the sample (cf. gamma ray irradiated topaz sample colours were dependent on source of the gemstone [8]). Induced colour also appears not to reach a saturation limit in the concentration of irradiation induced colour centres, since the absorption band intensities linked with irradiation damage continue to increase even up to the highest dose applied (70 h) [7, 8]. The predominant absorption band at 620 nm is stronger in the neutron than gamma ray irradiated blue topaz [6]. It has therefore been considered that the colour centres responsible are produced by a nuclear reaction, generating P_{Si} centres [32, 39], as will be discussed further in section 2.6.2.2.

Applying a defect model to irradiation damaged topaz, Priest [14, 22] found

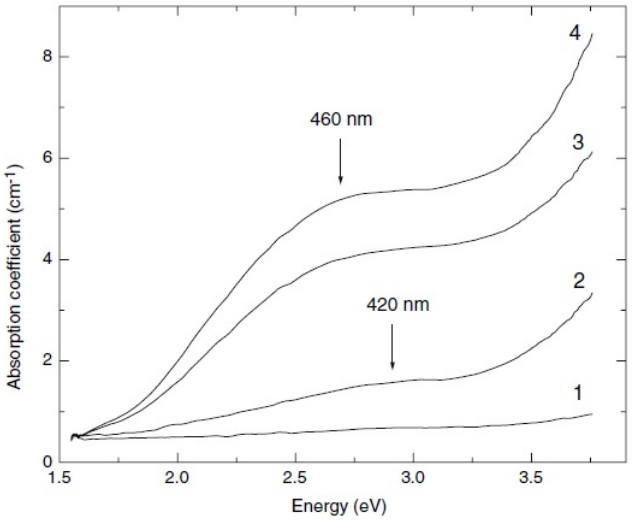

(a) Optical absorption spectra of gamma-irradiated topaz at room temperatures and with light propagating along the *c*-axis. The numbers indicate the dose of radiation applied: *1.* indicates the reference sample of clear topaz, *2.* indicates 5 kGy, *3.* indicates 250 kGy, and *4.* indicates 1000 kGy. Spectrum reproduced from reference [7].

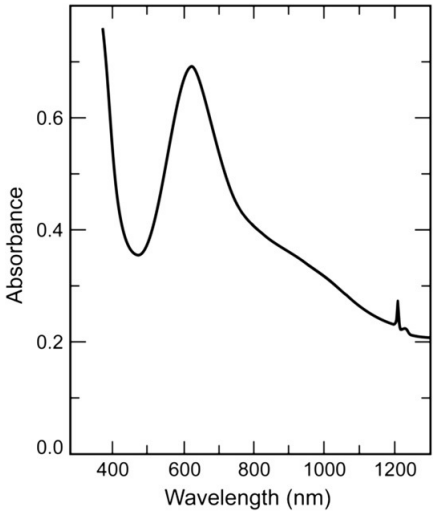

(b) Typical absorption spectra of blue topaz. Spectrum reproduced from reference [36].

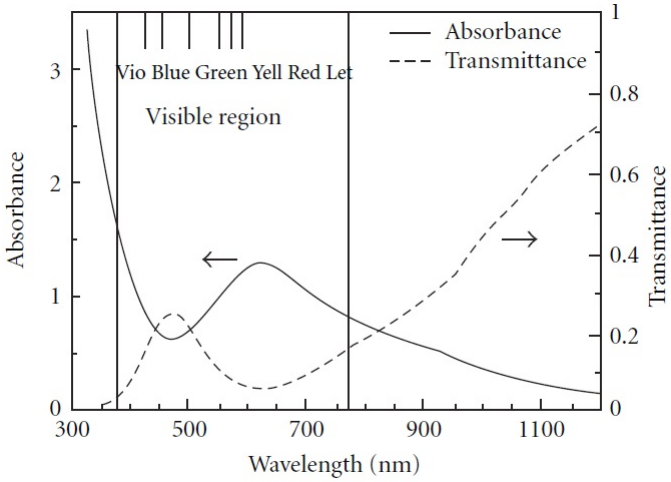

(c) Optical absorption spectra of blue topaz. Spectrum reproduced from reference [35].

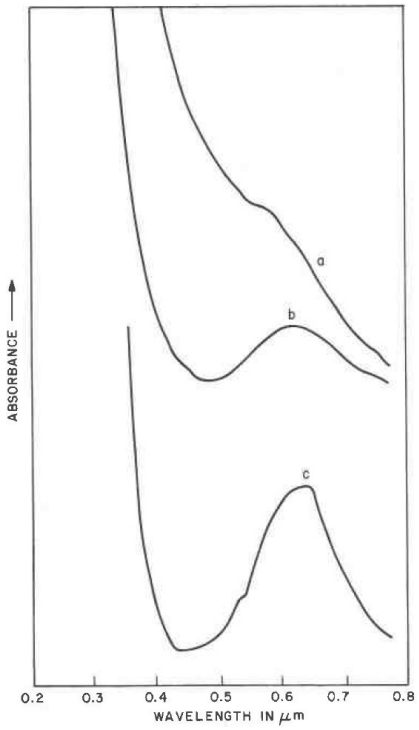

(d) Unpolarised optical absorption spectra of *a.* colourless topaz turned brown following 20 hr of gamma irradiation; *b.* same as *a.* but blue topaz after thermal treatment; *c.* natural blue topaz. Spectrum reproduced from reference [12].

Figure 2.5: Optical absorption spectra of literature gamma irradiated topaz.

Absorption	Sample History	Spectra	Ref.
	Natural Blue Topaz		
410 nm (3.0 eV) Weak 620 nm (2.0 eV) Strong			[6, 38]
	Neutron Radiation		
625 nm ($16\,000\,\mathrm{cm}^{-1}$) 690 nm ($14\,500\,\mathrm{cm}^{-1}$)			[32]
420 nm Less Intense Band 475 nm Absorption Valley 620 nm Strong Band	• $4.3 \times 10^{12}\,\mathrm{cm\,s}^{-1}$ Thermal Neutrons • $4.1 \times 10^{12}\,\mathrm{cm\,s}^{-1}$ Fast Neutrons • $10^{18}\,\mathrm{cm}$ Total Integrated Neutron Flux	2.6(a)	[7]
620 nm Strong	• $6 \times 10^{11}\,\mathrm{cm}^{-2}\,\mathrm{s}^{-1}$ Fast Neutrons • $10^{18}\,\mathrm{cm}$ Total Neutrons		[6, 7]
620 nm	• Total time: 3.5, 7, 14, 35 and 70 h	2.6(b) 2.6(c)	[8]
410 nm 620 nm		2.6(d)	[37, 38]
620 nm (2 eV) Absorption Band 354 nm (3.5 eV) UV Absorption Band	• Fast Neutrons • A Few Times $10^{18}\,\mathrm{cm}$ Total Neutrons	2.6(e)	[14]

Table 2.3: Spectroscopic data of literature neutron irradiated topaz.

that both natural and neutron irradiated blue topaz crystals contain EPR active superoxide (or peroxy) $\equiv\mathrm{Si}-(\mathrm{O}_2^-)$ radicals: an oxygen molecule bonded to a silicon, a defect well known in silica glass [46]. The 620 nm absorption band was attributed to the previously mentioned doubly occupied dangling silicon bond, i.e. a lone pair of electrons on the Si, which forms from a neutral oxygen vacancy in an isolated structural SiO_4 tetrahedron. Since the formation of a superoxide mass balences the creation of an interstitial, then it follows that the number of oxygen vacancies by neutron irradiation must also increase. EPR measurements also indicate the presence of a superperoxy radical O_2^- [7, 14, 22] and an unknown defect (the same as in gamma-irradiation). The concentration of O_2^- and O^- defects were shown to increase without reaching saturation upon increased neutron irradiation (maximum rate $1 \times 10^{18}\,\mathrm{cm}^{-1}$).

Thermal studies show that the radiation-induced centre responsible for the absorption band at 620 nm is stable up to 500 °C [38], and it is thought by da Silva *et al.* [38] that the defect responsible is the hole centre O^-. Their EPR measurements

also indicate that the O^- hole centre is located on an OH^- site, as the resolution of hyperfine interactions indicate that the defect has two equivalent nearest neighbour Al nuclei [37] (see Figure 2.4(c)). Neutron irradiation is thought to cause some lasting and irreversible defect in topaz, that becomes intrinsic and stabilises the O^- hole centre. The O^- hole centre is thought to be the cause of the intense blue colouration in irradiated topaz [6, 7, 38]. The bound small polaron model introduced by da Silva *et al.* [6] could be used to interpret this.

As it has been shown already in this short subsection, there is a variety of valid defect models amongst literature sources that have been argued as the ones responsible for the absorption band at 620 nm in blue topaz (this case neutron irradiated). Our aim in modeling the colour centres of topaz is to explore as many of these likely cases as possible.

2.5 Why do we see colours in minerals?

Colour is the consequence of how photons of light or other electromagnetic energy interact with an object, and in particular, which of wavelengths of the electromagnetic spectrum are absorbed or emitted. The colour seen is due to electronic transitions between discrete occupied and empty electronic levels. If colour is observed, these electronic states must have an energy difference that falls within the visible range of the electromagnetic spectrum (380 to 750 nm, see Appendix A.1 for colour break down). The intensity of an electronic transition is governed by selection rules. The fundamental features that control colour in minerals are summarised in the following sections.

2.5.1 Band Theory

Similar electronic structure arguments that are used to describe the conductivity of a material can be also used to describe optical properties. By simply extending the molecular orbital (MO) theory and noting that due to Fermi Dirac statistics no two electrons can occupy the same energy level, **bands** of discrete energy levels form in solids from the overlap of multiple atomic orbitals (AO)s, and this characterises the delocalisation of valence electrons throughout the entire structure (Figure 2.7). The energy separation between the valence and conduction bands is a region of forbidden electronic energy and termed the **band gap**. A strong absorption of energy that results in transitions across the band gap, i.e. a *fundamental absorption*, is also known by the absorption edge or band edge.

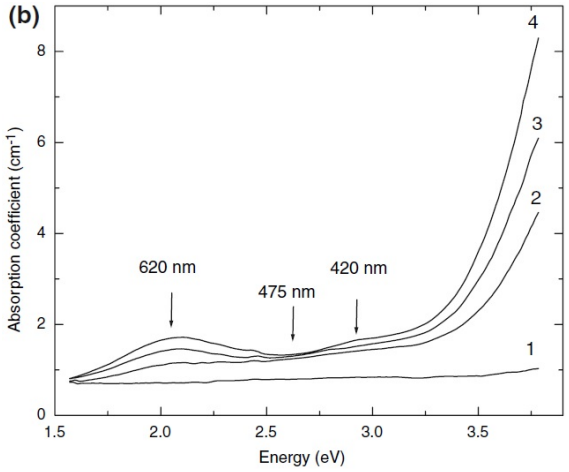

(a) Varying Neutron Dose

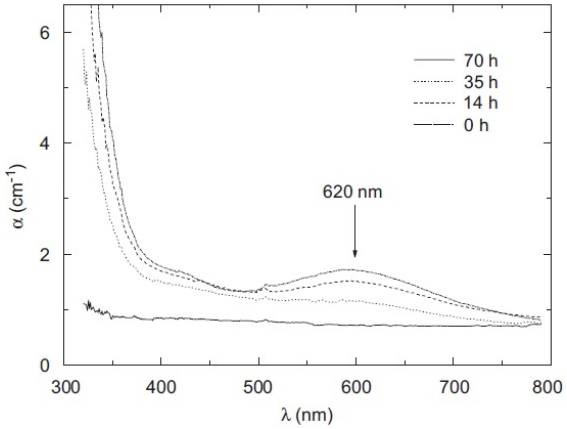

(b) Varying Neutron Exposure Time

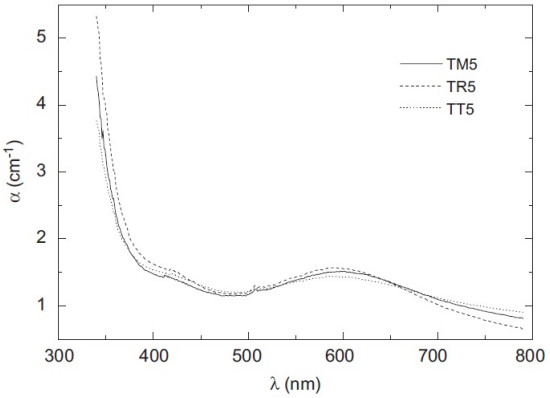

(c) Varying Topaz Samples

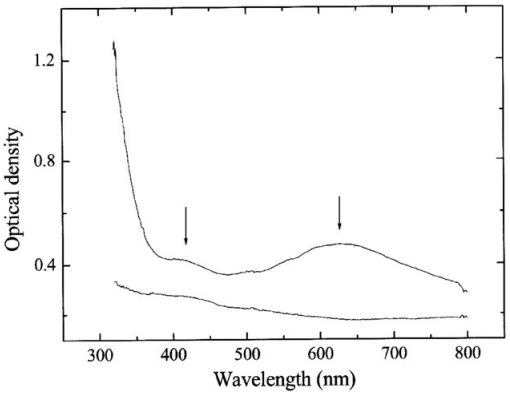

(d) Irradiated and Reference Sample

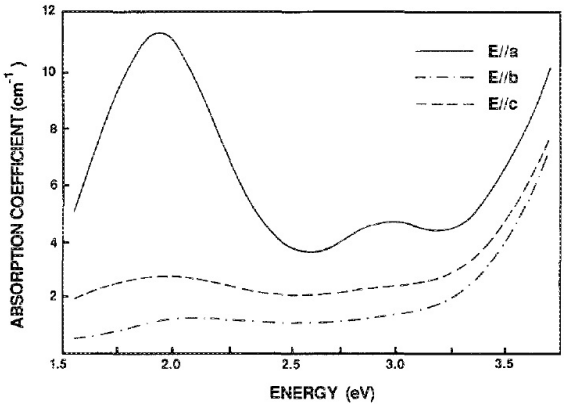

(e) Varying Topaz Samples

Figure 2.6: The optical absorption spectra of neutron-irradiated topaz using using light propagating along the c-axis. The graphs depict the evolution of pecks with increasing (a) dose and (b) exposure time. The numbers of the lines in (a) show the following integrated neutron flux doses: *1* indicates the reference sample of clear topaz, *2* indicates $1 \times 10^{17}\,\mathrm{cm}^{-2}$, *3* indicates $5 \times 10^{17}\,\mathrm{cm}^{-2}$, and *4* indicates $1 \times 10^{18}\,\mathrm{cm}^{-2}$. In figure (b) the time of the neutron exposure is indicated in hours. Figure (c) are the optical spectra of three different samples of topaz irradiated to the highest total neutron flux for 70 h. Figure (d) indicates the optical density of neurton irradiated topaz (upper trace) [38] with unirradiated reference for comparison (lower trace). Figure (e) is the optical absorption spectra of topaz irradiated with fast neutrons with linearly polarised light alond the axis indicated for each curve. Spectra (a), (b) and (c), (d), and (e) were reproduced from references [7], [8], [37] and [14] respectively.

The **Fermi level** is the highest occupied molecular orbital (HOMO) for the solid at $T = 0$. The location of the Fermi level within the bands and in particular with respect to the conduction band, is a crucial factor in determining the electronic properties of the solid. The probability of finding an electron occupying an energy state for a given temperature is given by the Fermi function. From the Fermi function the electron **density of states** can be derived, which shows how many electrons are likely to reach the conduction band.

The highest energy band containing electrons (at $T = 0$) is the **valence band**, and the next one higher (which is normally empty at $T = 0$), is termed the **conduction band**: these correspond to the HOMO and the lowest unoccupied molecular orbital (LUMO) in MO terms. The size of the gap between these two bands is dependent on the electron count, separation and strength of the AOs interactions, e.g. in metals there is no band gap due to the Fermi level falling within one of the allowed energy bands. The properties of metals, semiconductors and insulators can be successfully explained using the band structure model, and in a similar way, so too can the radiative electronic transitions of photon absorption in coloured materials also be understood.

Defects present within a crystal structure may cause a variety of electronic changes to the character of the band gap. For instance, lattice defects, which are normally present in all solids, take the form of structural or composition imperfections; intrinsic point defects manifest as either vacancies and/or interstitial particles displaced from lattice positions. Extrinsic point defects, on the other hand, are due to impurities (e.g. transition metal ions present in trace amounts): if introduced to the structure, they are referred to as dopants. The doping of solids with atoms with more or fewer electrons then those they substitute, leads to the formation of narrow donor or acceptor bands inside the band gap, which is responsible for n-type or p-type semiconductivity [47].

If electronic transitions between states associated with defect species corresponds to wavelengths of the visible spectrum, then colour is observed. The relationship between the energy of an electronic transition and the frequency of the absorbed light required for excitation is given by,

$$f = \frac{c}{\lambda} \text{ and } E = \frac{hc}{\lambda} \tag{2.3}$$

where f is frequency, E is energy (J) and λ is the wavelength (h is Plank's constant and c is the speed of light). A material with a large band gap appears transparent: such as pure diamond, topaz, and quartz. A material with a small band gap means the material appears opaque. Only in the latter case does a material have the optical

property of colour.

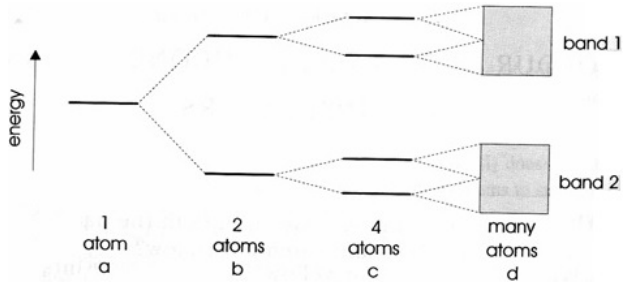

Figure 2.7: From an isolated atom to the band structure of a crystal. Figure reproduced from reference [48].

In the case of transition or rare earth metals, the typical type of electronic transitions concerns excitations from the usually degenerate the d- or f-orbital energy levels. The presence of a crystal field has the effect of partially removing the degeneracy and making $d \rightarrow d$ and $f \rightarrow f$ transitions feasible. Crystal Field Theory (CFT) can be used to link the structural properties of the transition metal complexes and the redistribution and splitting of degenerate states to the features of the optical absorption spectra.

2.5.2 Crystal Field Theory of Transition Metals

CFT in crystals describes how the energy levels associated with d- or f-orbitals of transition metal ions. These electronic levels are degenerate for the isolated transition metal ions, but are split by their interaction with the surrounding atoms. Therefore, CFT is useful when attempting to rationalise the optical, thermodynamic and magnetic properties of metal complexes and solids. Figure 2.8 demonstrates the splitting of the five degenerate $d-$orbitals as a result of different crystal filed symmetries. A more detailed examination of interpreting the absorption spectra resulting from a Cr^{3+} ion complex in an octahedral environment, as found in pink topaz, using CFT, is given in Section 6.2.

Taking the Cr^{3+} ion as an example metal ion, we know that the d states of the transition metal ion are located within the band gap, from which the electronic transitions $d - d$ and charge-transfer (CT) (see Section 2.5.3) can occur (see Figure 2.9(a), and again Section 6.2 for justification of these transitions). The electronic configuration for Cr^{3+} is $1s^2 2s^2 2p^6 3s^2 3p^6 3d^3$, so it has three electrons in the incomplete valence $3d$ shell. In an octahedral geometry, the five degenerate $d-$orbitals split into two sets of degenerate orbitals; the higher e_g two electronic levels (d_{z^2} and $d_{x^2-y^2}$) and the lower t_{2g} three electronic levels (d_{xz}, d_{yz} and d_{xy}) are separated by an energy quantity denoted as Δ, see Figure 2.9(b).

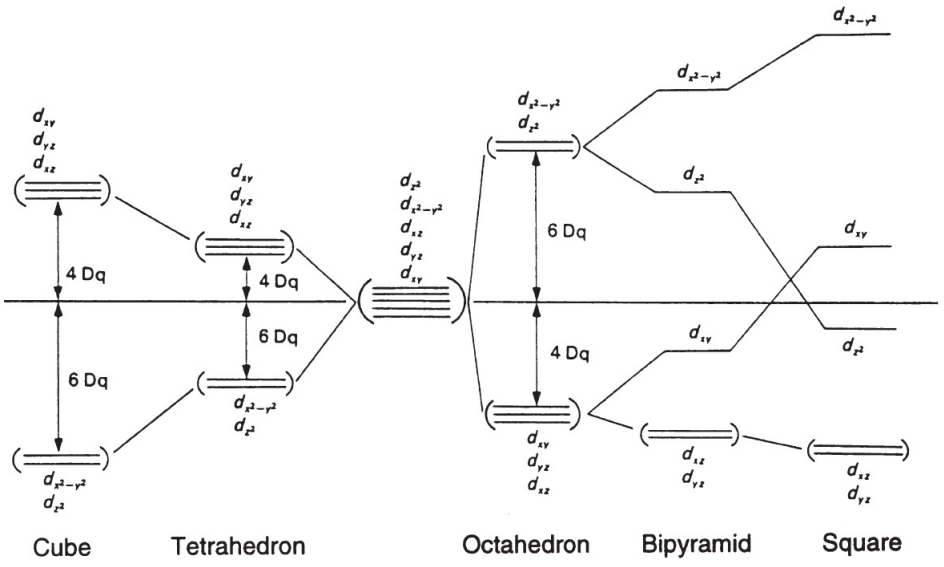

Figure 2.8: The crystal field splitting of d-orbitals under the influence of different ligand field symmetries. Figure reproduced from reference [47].

To calculate the energy levels of a metal ion under the influence of a crystal field, various factors have to be considered, including the valence state of the metal ion, its coordination environment, and the strength or nature of the bonding in the crystal field. To illustrate the effect of changing the crystal field strength on the energy of the electron levels, one can compare the optical absorption spectra of three Cr^{3+} ion containing minerals (ruby, alexandrite, and emerald) as given in Figure 2.9(c). By a relatively small change in the strength of the ligand field, a drastic change in colour is observed for Cr^{3+} containing minerals, going from the ruby (red) to the emerald (green). The alexandrite has an intermediate absorption scheme between that of the ruby and emerald, it can display colours from red to green depending on the nature of the ambient light.

Chromium exists in these gemstones as an impurity present in quantities of less then 1%. The resulting colour is therefore classified as *allochromatic*, i.e. a mineral with no colour itself, but bearing coloured impurities. An *idiochromatic colour* is described as resulting from elements that are an essential component of the material, such as minerals containing Cr^{3+} as the main component, like crocoite (orange) $PbCrO_4$; phoenicochroite (red) Pb_2OCrO_4; and uvarovite (green) $Ca_3Cr_2(SiO_4)_3$.

2.5.3 Colour Centres

Colour centres are point defects within a crystal lattice structure that absorb light in the visible part of the spectrum, in materials that would otherwise be transparent. Many radiation-induced defects fall in this category. A typical example are

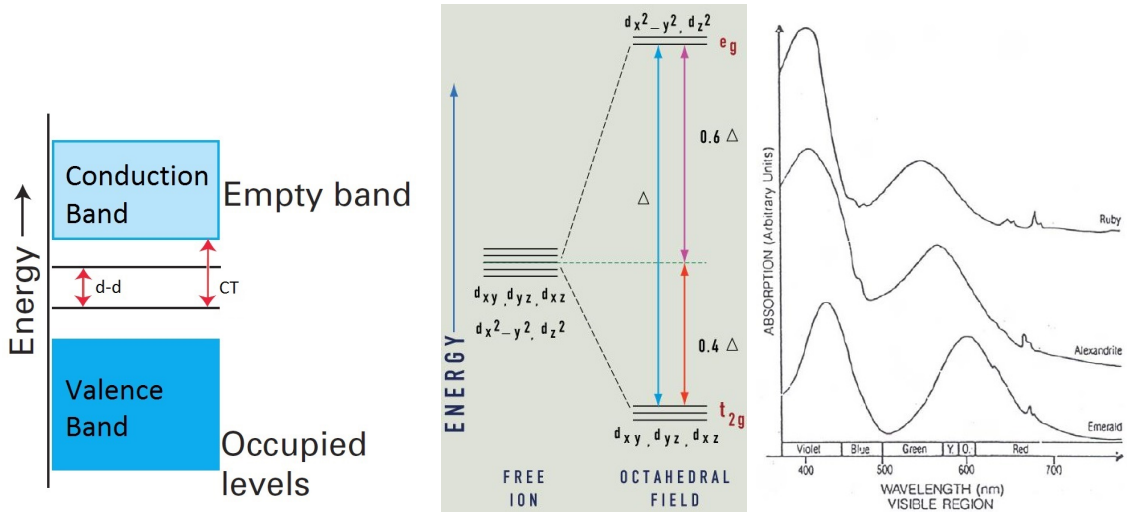

(a) (b) (c)

Figure 2.9: (a) the electronic structure diagram of a solid containing a transition metal ion dopant, characterized by bands of filled (valence) and empty (conduction) orbital energies and the dopant d-levels occurring within the band gap. The optical absorption $d-d$ and CT electronic absorptions are indicated, occurring from the Fermi energy (the highest occupied orbital at $T=0$). (b) the octahedral (O_h) crystal field splitting of d-orbitals, and (c) the optical absorption spectra of Cr^{3+} containing minerals: ruby (Al_2O_3), alexandrite ($BeAl_2O_4$), and emerald ($Be_3Al_2(Si_6O_{18})$). Figures (b) and (c) are reproduced from references [49] and [50, 51] respectively.

F-centres (German *Farbe* meaning "colour"), which are a type of colour centre, where an electron is trapped on a vacant anion site. F-centres produce a number of discrete energy levels between the valence and conduction band of the band gap. The excitation of the electron from and into these defect states causes the colour observed.

Another type of defect is a hole colour centre, and occurs when an electron is missing from its original atomic orbit. Such examples include 'smoky' quartz, where the colour centre consists of an Al^{3+} impurity substituting for a Si^{4+} ion, charge neutrality can be achieved either in interstitial positive cations, or in the removal of one electron (to generate an electron hole h^+) from one of the anions nearest neighbour to the Al^{3+}.

An electronic transition is further denoted as of CT type when the electron is excited between levels centred on adjacent ions, for instance from an occupied metal d- AO to an empty level on one of its neighbouring anions (see Figure 2.10).

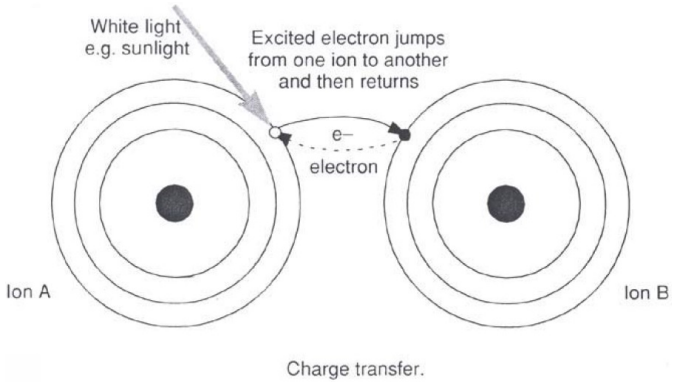

Figure 2.10: The charge transfer or an electron from one ion, being excited to the orbital of another another ion, through the absorption of electromagnetic radiation. Figure reproduced from reference [50].

2.6 Defects and Possible Colour Centres of Topaz

The topaz structure includes a number of intrinsic defects, the principle one being its composition, where a natural disorder and random arrangement of the F^- and $(OH)^-$ anions occurs, and both anions can substitute onto equivalent octahedrally bonded sites. The orientation of the $(OH)^-$ groups can also alter to minimise local electronic and steric effects. In terms of cation disorder, only one third of the octahedral sites are expected to be occupied by Al^{3+} cations, while one twelfth of tetrahedral site are filled with Si^{4+} [1]. None of these defects are thought to be responsible for causing colour, but their presence may contribute to altering optical properties of colour generating defects, by means of modifications of the local environment of the colour centre.

Despite the vast quantities of topaz irradiated annually, the irradiation-induced defect centres responsible for the blue or brown/grey colouration, or indeed any other colour change observed in topaz, are still not well understood. Much of the published work relating to the dosimetric properties of topaz uses models suggested in the PhD thesis by Petrov [39].

Through optical absorption and EPR spectroscopic investigations, Petrov [39] divided the various colours of topaz into three groups. The first group described the paramagnetic chromium defect centre responsible for the pink/violet colour. The second group comprises all those defect centres that are responsible for a variety of special colours seen in topaz: those being red, yellow, blue and green colours. The third group was classified as those defect centres that form combinations of chromophoric ions with different colour centres. These colours range from yellow, yellow-orange, orange, orange-violet through to violet, and therefore is referred to

here as the Imperial topaz group.

2.6.1 Pink Topaz (Group I)

Trivalent chromium, Cr^{3+}, is the most stable form of chromium and it is in this state that a wide range of minerals adopt deep colours and bright luminescence. As already mentioned, ruby, emerald, alexandrite, and mullite are all examples of natural or synthetic gemstones whose colour is caused by Cr^{3+} ion impurities present within the material.

The colour pink is unusual in that it does not correspond to a single specific wavelength of visible light, i.e. it does not form one of the constituent colours of white light that make up the rainbow (red, orange, yellow, green, blue indigo and violet).[4] However, since pink (or magenta, or fuchsia) does not feature as a constituent wavelength of white light, how is it that we can perceive it?

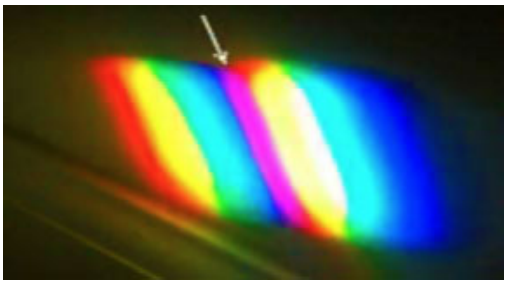

Figure 2.11: Sir Isaac Newton observed magenta when experimenting with prisms: when the red end of one spectrum was superimosed with the blue/violet end of another, the colour observed in the overlapping section was magenta.

The pink colour is classified as a non-spectral (or extra-spectral) colour and is made by combining the two extremes of the visible spectrum: a mixture of red and blue/violet light (see Figure 2.11). Normally, when our eyes encounter multiple wavelengths of light, our brain interprets them as the sum of the input. For example, if both red and green light enter the eye simultaneously, the resulting colour our brain perceives is yellow, since it corresponds to the wavelength of light halfway between red and green in the spectrum. So, when our eyes detect wavelengths from the two extremes of the spectrum (i.e. red and violet light), we should expect to see green, as this corresponds to the wavelength of light halfway between the wavelengths of red and violet, but instead our brain invents a new colour (pink), which is more representative of a red and violet mixture. The variation in pink hue is be due to

[4]The electromagnetic radiation is a continuous spectrum of frequencies and these devisions of colour definitions are only arbitrary: a single "colour" can be better described as a range of wavelengths of visible light.

the ratio of red and violet intensities and specific wavelengths. Alternatively, pink is the colour our brains perceive when green light is removed from white light, i.e. green is the complementary colour to pink (see Appendix A.2).

Pink topaz is caused by trace amounts of chromium ion impurities contained within the topaz crystal structure. Chromium acts as a point defect by isomorphically substituting onto the octahedrally coordinated aluminium site, i.e. Cr^{x}_{Al} (using the Kröger–Vink notation[5]):

$$[AlO_4(OH,F)_2]^{7-} + Cr^{3+} \longrightarrow [Cr^{\times}_{Al}O_4(OH,F)_2]^{7-} + Al^{3+} \tag{2.4}$$

resulting in three structurally non-equivalent Cr^{3+} centres, depending on the F^- and OH^- anion distribution in the first coordination sphere of chromium(III). The three chromium(III) complex centres that can form in topaz are therefore $[Cr^{\times}_{Al}O_4(OH)_2]^{7-}$, $[Cr^{\times}_{Al}O_4(OH)F]^{7-}$, and $[Cr^{\times}_{Al}O_4F_2]^{7-}$, and are an inherent part of the natural disorder in the composition of topaz, since both anions F^- and OH^- are randomly distributed onto the same crystallographic sites. The pink colour is caused by the spin-allowed $d-d$ electronic transitions of Cr^{3+}. The crystal field of the Cr octahedral environment is believed to be distorted, or at least influenced, by the local F/OH distribution [52] (see Chapter 6 where we discuss our results concerning the Cr^{3+} defect in topaz).

2.6.2 Blue Topaz (Group II)

Many defect centres have been suggested for the blue colour in topaz. Petrov [39] investigated a variety of paramagnetic centres, including such defects as $[PO_4]^{4-}$, $[PO_3]^{2-}$, $[SiO_4]^{3-}$, $[SiO_3]^{3-}$ and $[AlO_4]^{4-}$, all defects originating from the silicate tetrahedra ($[SiO_4]^{4-}$), and transition metals. As mentioned before, other sources have also suggested additional centres, such as the superoxide radical anion O_2^- [7] and small bound polaron O^- [7, 8, 37].

[5]Kröger–Vink notation is the defect notation used here to describe the lattice position and electrical charge of point defects within the crystal structure. In the notation M^C_S: M corresponds to the species that substitutes onto a specified lattice site. These can be atoms (e.g. Al, P, OH, or F), vacancies (V or v), interstitials (indicated by i), electrons (e), or electron holes (h). S indicates the lattice site of M, e.g. an Cr replacing an Al in topaz would be indicated by Cr_{Al}. C corresponds to the remaining electrical charge after the substitution has occured, i.e. the difference between the two species. A null charge is indicated with an $\times$, a single positive charge remaining is indicated with a $\bullet$, and a excess negative charge is given a $\prime$ symbol.

2.6.2.1 The 'Smoky Quartz' Colour Centre in Topaz

The $[AlO_4]^{4-}$ defect (formally $[Al'_{Si}O_3O^{\bullet}]^{4-}$), consisting of an aluminium substitutional defect onto a silicon tetrahedral site, coupled with an electron hole trapped on one of the tetrahedral oxygen nearest neighbours to the aluminium [39], is supposed to be the colour centre responsible for the smoky quartz appearance of topaz [53]. Since studies using XRD have identified quartz within topaz minerals [54], it seems likely that this defect could contribute to the colour-changing process in topaz. A possible reaction pathway to generate the $[AlO_4]^{4-}$ colour centre following irradiation, involves loss of one electron from a substitutional Al'_{Si} ion to an electron deficient site, such as the $[PO_4]^{3-}$ site (or $[P^{\bullet}_{Si}O_4]^{3-}$), as detailed below:

$$[SiO_4]^{4-} + [P^{\bullet}_{Si}O_4]^{3-} \xrightarrow[-Si^{4+}]{+Al^{3+}} [Al'_{Si}O_4]^{5-} + [P^{\bullet}_{Si}O_4]^{3-} \xrightarrow{\pm e-} [Al^{\times}_{Si}O_4]^{4-} + [P^{\times}_{Si}O_4]^{4-} \tag{2.5}$$

da Silva *et al.* [6] observed the $[AlO_4]^{4-}$ centre and found it to be isotropic in the *ab* plane. The $Al^{\times}_{Si}O_4$ (or $P^{\times}_{Si}$) is commonly discussed as the defect responsible for the radiation-induced reddish-brown colour with thermal stability to about 220 °C [6, 32].

2.6.2.2 Phosphorus-Containing Defects

Through EPR investigations of the gamma- and neutron-irradiated blue topaz, Petrov [39] assigned the induced colour centres to $[PO_4]^{4-}$ (i.e. $[P^{\times}_{Si}O_4]^{4-}$) and $[PO_3]^{2-}$ (i.e. $[P^{\times}_{Si}O_3]^{2-}$) radicals. The light-blue colour that remains in topaz following gamma-ray irradiation and subsequent heat treatment, was argued to be dependent on trace elements, such as phosphorus, and/or precursor centres already present in topaz. Defects, such as Fe^{3+} and Al^{3+} impurities on silicon sites (Fe'_{Si} and Al'_{Si}), are thought to act as precursors to stabilise phosphorus defect centres.

Since the blue hue resulting from neutron-irradiated topaz is found to be so much deeper in intensity then that resulting from gamma-ray irradiation, it is assumed that the defect colour centres responsible for the observed colour change are present in much higher concentrations. Phosphorus is thought to form on Si^{4+} sites in topaz *in situ* by nuclear reaction via β^- decay. Following the capture of a neutron by a ^{30}Si nucleus, one of the neutrons in the nucleus then decays into a proton emitting

an electron and an electron antineutrino ($^1_0n \rightarrow ^1_1 p + e^- + \bar{\upsilon}_e$):

$$^{30}_{14}\mathrm{Si} + ^{1}_{0}\mathrm{n} \longrightarrow ^{31}_{14}\mathrm{Si} \xrightarrow{\beta^-} ^{31}_{15}\mathrm{P} + \mathrm{e}^- + \bar{\upsilon}_\mathrm{e} \tag{2.6}$$

The isotope ^{30}Si makes up 0.03% of natural silicon. ^{31}Si decay has a half-life of 2.62 h, hence it is reasonable to expect P to form from neutron capture at Si within topaz. Given the high penetration depth of neutrons, this process will occur homogeneously throughout the topaz crystal. This interpretation is supported by the characteristics that are observed in neutron-irradiated topaz, i.e. no colour zoning or saturation in colour centre concentration upon increased doses. The nuclear reaction mechanism cited here is known commercially as a method of doping phosphorus in silicon semiconductors [32]. Phosphorus based defects within topaz could therefore act as dominant charge compensation centres in blue neutron-irradiated topaz, analogous to how phosphorus behaves in zeolites [55].

Further evidence comes from atomic emission studies of various samples of topaz. When irradiated with neutrons for 100 h , the topaz sample appeared blackish-blue and the phosphorus content was found to be as high as 140 ppm. Following gamma irradiation (^{60}Co) and subsequent heat treatment, the lightly coloured blue topaz was found to contain only 15 ppm phosphorus. Samples of topaz that did change colour following gamma-irradiation where found to have no traces of phosphorus. Finally, a naturally blue topaz of medium hue, which underwent no artificial thermal or radiative treatment, bore a phosphorus concentration of 110 ppm [32].

2.6.2.3 Polaron Hole Centre

An alternative microscopic model presented by da Silva *et al.* [6], on the basis of EPR and UV-Vis absorption results, is the O^- hole centre, which was identified in both natural and neutron irradiated forms of blue topaz. The O^- hole was found to be located at the F/OH (8d) Wyckoff positions, which was supported by a number of factors. Firstly, the spin Hamiltonian parameters and positive g-factors suggested a hole centre, and the superhyperfine (shf) interactions indicated two equivalent Al nuclei. In addition, when considering the bond distances involved in the topaz structure, together with the orientation of the g-tensor being perpendicular to the plane spanned by Al−OH/F−Al, confirms the position of O^- on an F/OH site.

The paramagnetic centre observed was shown to have the same thermal stability, up to 500 °C, as the absorption band at 620 nm in the UV-Vis absorption spectrum, which is responsible for the blue colour. The linear correlation between the optical

absorption band at 620 nm and the integrated EPR intensity of the O^- hole centre, demonstrates a link between the two and the dependence of the O^- hole centre concentration as a function of sample history and treatment (Figure 2.12). They suggest that through irradiation, the hydroxyl radical OH^- loses a neutral hydrogen atom, which then either combines with another to form diamagnetic H_2 molecules or is trapped by other impurities.

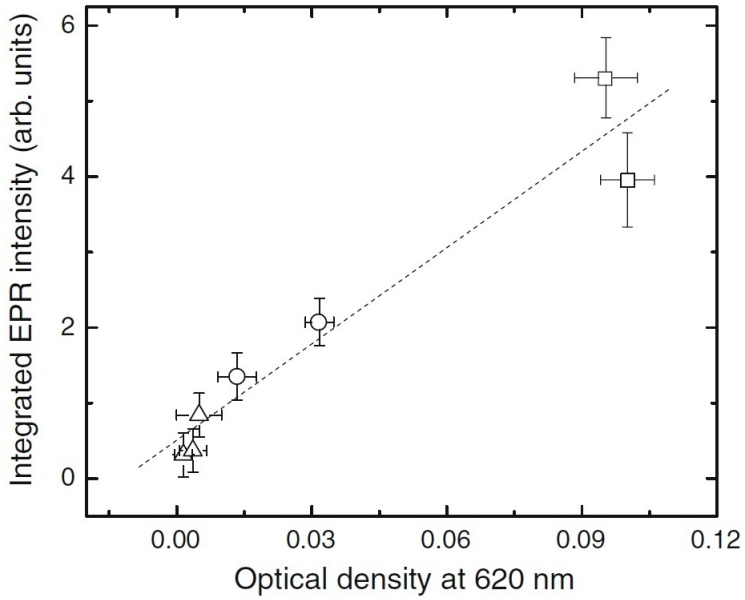

Figure 2.12: Literature correlation of the optical absorption band measured at 620 nm and the EPR signal intensity of the polaron hole centre. Samples studied include: natural colourless topaz (*triangle*), natural blue topaz (*circle*), and neutron irradiated topaz (*square*). Figure reproduced from reference [6].

Krambrock *et al.* [7] brought together the findings from Priest *et al.* [22] and da Silva *et al.* [6] and stated that the neutron irradiation of topaz leads to two dominant paramagnetic centres being formed: (1) the peroxy radicals O_2^- and (2) the O^- hole centres. These centres were found to not saturate, even up to the total integrated neutron flux applied (1×10^{18}neutrons cm), and were independent of the number and type of impurities present in the sample [7]. However, the total neutron flux was dominated by thermal neutrons and the fast neutron flux was at least one order of magnitude lower. Gamma irradiation also forms O^- hole centres but at much lower concentrations (about one order in magnitude), and does not produce peroxy radicals (O^{2-}).

2.6.3 Imperial Topaz (Group III)

The colours that Imperial topaz can obtain have been previously described in Section 2.6. Pink topaz can be included in the definition of an Imperial topaz, but, where the predominant colour centre in pink topaz is undisputedly the $Cr^{\times}_{Al}$ defect, in Imperial topaz there are other dominant colour centres that also influence the colour and complicate this simple defect model.

The orange-red colour observed in some Imperial topazes, is thought to be caused by Cr^{4+} centres originating from the depletion of Cr^{3+} centres. Two precursor Cr^{3+} ions in neighboring Al^{3+} sites are thought to form and stabilise the Cr^{4+} centre, through disproportionation:

$$2\,Cr^{3+} \longrightarrow Cr^{4+} + Cr^{2+} \tag{2.7}$$

Spectroscopic evidence for this scheme is presented in section 2.8. Unusually high quantities of Fe^{3+} have been found in yellow (and some samples of blue and colourless) topaz [1], which suggests Fe as a possible colour centre.

2.7 Optical Properties of Pink Topaz

Microprobe analysis of pink topaz indicates a vast array of transition metals and other impurities within the crystal [2]. However, the defect that causes the particular optical, pleochroism and luminescence properties seen in pink topaz is undoubtedly the Cr^{3+} ion impurity [2, 3, 52]. This can be shown in selective quantitative atomic emission spectra of Cr^{3+}, which indicate two broad bands in the visible region at around 410 and 580 nm (Figure 2.13(a)) that closely resemble optical absorption bands in the UV-Vis spectra of a pink/violet topaz (Figure 2.13(b)) [52]. These bands were assigned to the spin-allowed d-d transitions, $^4A_{2g} \rightarrow^4 T_{1g}$ and $^4A_{2g} \rightarrow^4 T_{2g}$: the characteristic d^3 transitions of a Cr^{3+} ion in a sixfold octahedral coordination environment (Figure 2.13(c)) [1, 2, 52, 56]. (A discussion of atomic terms, how they are derived, and selections rules for d^3 electronic transitions are given in Section 6.2 to support our electronic structure defect calculations of Cr^{3+} impurities in topaz).

The full-width at half-magnitude (FWHM) of the bands $^4A_2 \rightarrow^4 T_1$ and $^4A_2 \rightarrow^4 T_2$ were found to be particularly broad, when compared with other Cr^{3+} containing minerals. The FWHM of chromium-bearing topaz resembles more closely the FWHM of mullite containing Cr^{3+}, which can form one of two stoichiometries

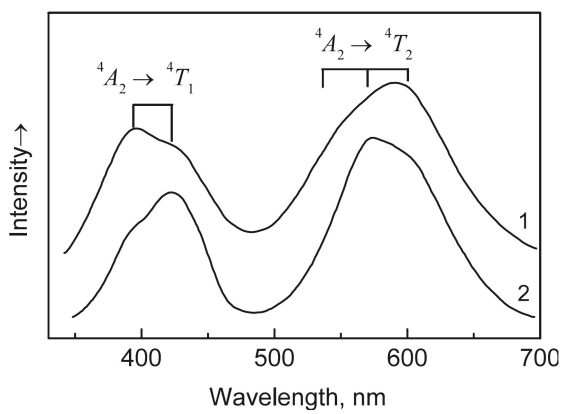

(a) Selective Cr^{3+} Excitation Spectra

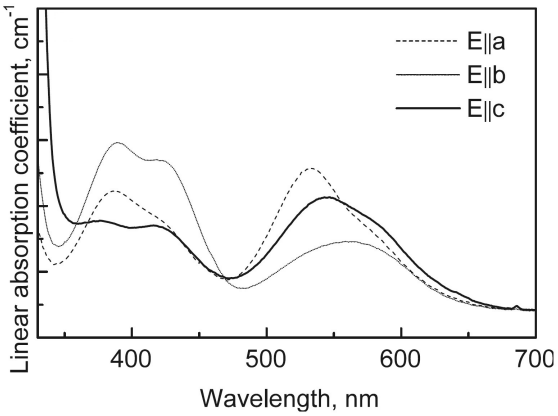

(b) Polarized Optical UV-Vis Absorption

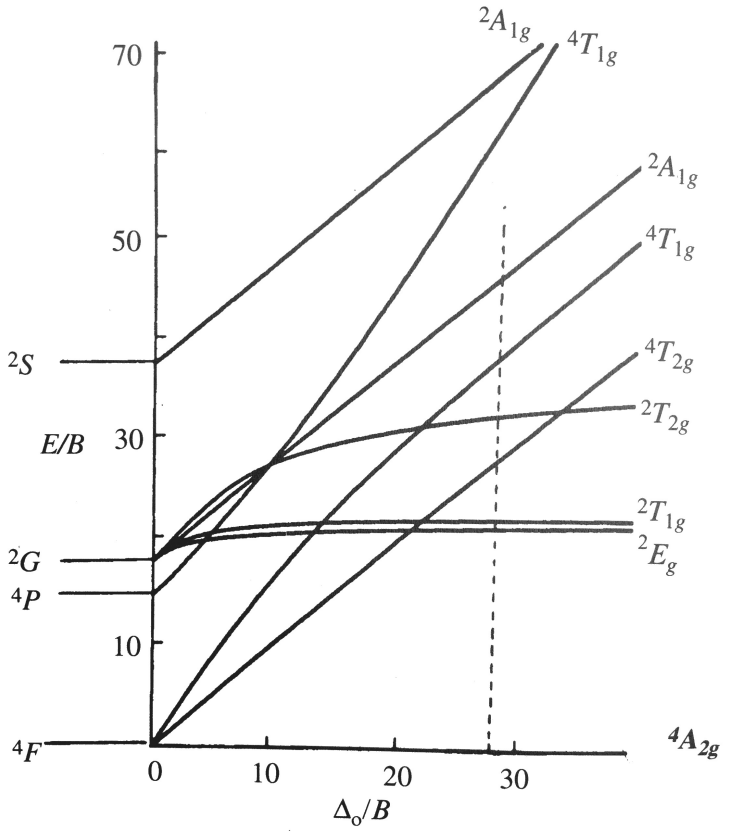

(c) Energy level diagram

Figure 2.13: Figure (a) shows the selective excitation spectra of Cr^{3+} in violet topaz, and Figure (b) the optical absorption spectra using polarised light on the same violet coloured topaz sample containing 0.03 wt% Cr^{3+}. Figure (c) shows the Tanabe-Sugano energy level diagram of a ligand-field free Cr^{3+} ion in an octahedrally coordinated environment. The dashed line at $28.5\Delta_o/B$ (where $\Delta_o = 18150\,\mathrm{cm}^{-1}$ and $B = 635.6\,\mathrm{cm}^{-1}$) here indicates the Cr^{3+} transitions for ruby (Al_2O_3) . For topaz, the $\Delta_o/B = 25.5$ (where $\Delta_o = 18150\,\mathrm{cm}^{-1}$ and $B = /711.4\,\mathrm{cm}^{-1} = 25.5$). Figures (a) and (b), and (c) were reproduction from references [52] and [56] respectively: the Δ_o/B values were calculated from data cited within reference [56].

$3\,Al_2O_3 \cdot 2\,SiO_2$ or $2\,Al_2O_3 \cdot SiO_2$, then ruby whose stoichiometry is α-Al_2O_3:Cr^3. Mullite ceramics are typical examples of multi-Cr^{3+} centres, while ruby is an example of a single-Cr^{3+} site. It has therefore been argued that topaz containing chromium also has sites of multiple Cr^{3+} ion clusters as colour centres [2, 52].

The three non-equivalent Cr^{3+} complexes formed in topaz by isomorphic substitution onto Al^{3+} octahedral sites, $[Cr^{\times}_{Al}O_4F_2]^{7-}$, $[Cr^{\times}_{Al}O_4OH,F]^{7-}$ and $[Cr^{\times}_{Al}O_4(OH)_2]^{7-}$, vary in thermal stability and are thought to account for the variation in photoluminescence[6] properties observed for differently coloured topazes. Photoluminescence up to 1150 °C of Cr-containing topaz, shows the two bands responsible for the $^2E_g \rightarrow^4 A_{2g}$ transition broadened and split into three sub-bands, indicating three different Cr^{3+} environments [2].

The fluorine content in Imperial topaz is generally found to be much lower, at about $12wt\%$, then white topaz: cf. the theoretical value of F which is $20.6wt\%$ in pure $Al_2SiO_4F_2$ [2]. Through annealing, the $[Cr^{\times}_{Al}O_4F_2]^{7-}$ complex was found to be the most stable of the three complexes, only disappearing at above ~ 1250 °C, when topaz transforms into mullite. The $[Cr^{\times}_{Al}O_4(OH)F]^{7-}$ and $[Cr^{\times}_{Al}O_4(OH)_2]^{7-}$ complex centres decay at the temperature range of $950 - 1100$ °C [52]. The pleochroism characteristic is attributed to the $(OH)^-$ group, as the dipole lies in the 010 plane at an angle of 29° to the $c-$axis, resulting in an increased $E \parallel Z(\parallel C)$ IR intensity and an ordering of intensities in polaised spectra that follows $Z \gg X \gg Y$.

2.8 Optical Properties of Imperial Topaz

Taran *et al.* [2] conducted an optical spectroscopy study of natural and X-ray irradiated Imperial topazes; the polarised absorption spectra of four different topaz samples, identified as $K1$, $K2$, $K3$, and $K4$, are reproduced in Figure 2.14. They identified three spectral features, which were labeled (1), (2), and (3), that were tracked through irradiation, annealing, and photoluminescence investigations. Set (1) refers to the pair of broad bands, with maxima at ~ 560 nm (~ 18000 cm^{-1}) and ~ 400 nm (~ 25000 cm^{-1}), denoting the spin-allowed $d-d$ transitions of Cr^{3+} ions, $^4A_{2g} \rightarrow^4 T_{2g}$ and $^4A_{2g} \rightarrow^4 T_{1g}$ respectively. The spectra of topazes $K1$ and $K2$ (Figure 2.14 a. and b. respectively) show these bands the best. The colour of the

[6]Photoluminescence is a type of luminescence. Luminescence is an emission process whereby a material radiates of light following some form of stimulation to promote electronic excitation, e.g. electrical energy, chemical reactions, subatomic motions, or stress on a crystal. It is a cold body radiation, i.e. it does not result in the emission of heat energy. Photoluminescence is the result of photon absorption. There are two forms of photoluminescence: fluorescence and phosphorescence. These processes are the result of a singlet-singlet or a triplet-singlet electronic relaxation respectively.

crystal depends on the relative intensity of these two bands. The minerals colour can vary from light rose to deep violet, and, due to the pleochroism of Cr^{3+}-containing topaz, can display characteristic colours, such as yellow $\mathbf{E} \parallel X$ ($\parallel$ **a** axis), violet $\mathbf{E} \parallel Y$($\parallel$ **b** axis), and pink $\mathbf{E} \parallel Z$($\parallel$ **c** axis), under polarised light.

Set (2) denotes to the intense UV absorption edge at 330 nm that is weakly polarised and made up of two parts: a thermally stable ligand-to-metal CT part of trace transition metals (Ti, Cr, Fe, V and Mn) present within the natural samples, and a thermally unstable part caused by unknown radiation induced defect(s).

Set (3) type are described as being the two broad bands with maxima around $\sim 540 - 530$ nm ($\sim 18500 - 19000$ cm^{-1}) ($X > Y \approx Z$) and ~ 420 nm (~ 24000 cm^{-1}) ($Y \approx Z \gg X$). Bands (3) are most pronounced for sample $K3$ (Figure 2.14 c.), and are attributed to the unique orange-red colour of Imperial topazes, with characteristic orange-red ($E \parallel X$) and rose-yellow ($E \parallel Y$, ($E \parallel Z$) pleochroism.

2.8.1 Irradiation Induced Colour Change

It was observed that the two yellowish rose coloured topazes ($K2$ and $K4$) turned an orange-red colour following X-ray irradiation, which was attributed to a quenching of the Cr^{3+} centres. The absorption edge was shown to have increased along with the (3) band. Often observations made by the source authors remain unexplained; for instance, the orange-red topaz ($K3$) turned dark orange-red following either $X-$ or gamma-irradiation, and a colourless topaz with a Cr_2O_3 content of $0.00wt\%$ turned deep yellow: no defect explanation was attempted for either. No colour or optical spectral change was observed of the light violet coloured topaz ($K1$), even after 10 h of X-ray irradiation.

2.8.2 Annealing

Annealing leads to a decrease in the high energy absorption intensity of set (3) at $\sim$400 nm (25 000 cm^{-1}) and the band partially obscured by the $^4A_{2g} \rightarrow^4 T_{1g}$ band of set (1). The latter is attributed to the yellow-hue in some samples and is consequently bleached (see (a) and (b) of Figure 2.15). This was observed for the topaz sample $K2$ from reference [2] after $\frac{1}{2}$ h and at 700 °C, and for $K4$ at $\sim$ 600 °C. Upon thermal decay of the yellow-hue, the samples acquired a rose colour and an absorption spectra that more closely resembled that of $K1$ (cf. Figure 2.14 a. and Figure 2.15(b) b.). Thermal annealing also results in a slight increase in the $^4A_{2g} \rightarrow^4 T_{2g}$ transition of Cr^{3+}, the band at $\sim$ 570 nm (17 600 cm^{-1}), and is attributed to an increase in Cr^{3+} ion concentration (Figure 2.15(b)). Since the

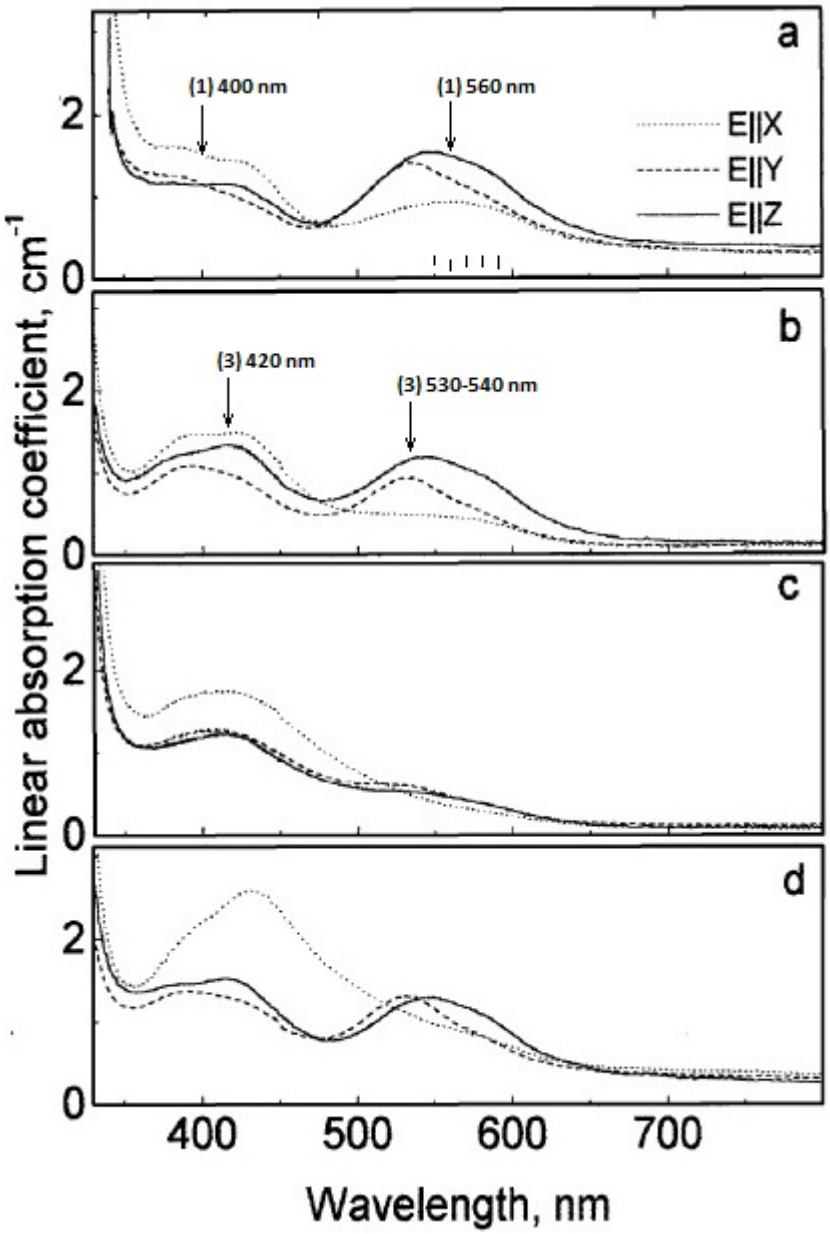

Figure 2.14: The optical absorption spectra of various coloured Imperial topazes containing chromium: **a.** refers to the light violet Imperial topaz labelled $K1$ and containing $0.02wt\%$ Cr_2O_3, **b.** to $K2$ yellowish rose in colour with $0.06wt\%$ Cr_2O_3, **c.** to $K3$ orange topaz with $0.04wt\%$ Cr_2O_3, and **d.** to $K4$ also yellowish rose in colour but with $0.01wt\%$ Cr_2O_3. Spectra reproduced from reference [2].

chemical content of a crystal can not change under these conditions, the chromium must be in a different form before annealing.

Other annealing observations show that the artificially (i.e. radiation) induced band sets (2) and (3) are unstable and disappear after a week of exposure to room temperature or daylight. The process of band decay increased at temperatures of ∼150 °C and annealing for a few minutes. Natural crystals with these optical bands already present do not demonstrate the same behaviour. Here the band set (3) decays at temperature ≥300 °C. The Cr^{4+} ions thought responsible for the orange-red colour, are more strongly stabilised in natural samples than artificially irradiation-induced samples [2]. Chromium clusters were again thought a likely explanation for this observation: $Cr^{4+}-Cr^{2+}$ pairings, assumed more likely to form during crystallisation than through ion migration, are more likely to occur and stabilise in naturally orange-red topaz from $Cr^{3+}-Cr^{3+}$ pairs, than in irradiated topaz [2]. The ligand shell, particularly the F/OH ordering was also felt significant towards the stabilisation of the Cr^{4+} centre, but no reasonably model could be presented.

2.8.3 Defect Centres

Following the suggestion made by Taran *et al.* [2] that the orange-red colour of some Imperial topazes is caused by the formation and stabilisation of Cr^{4+} centres, the scheme whereby Cr^{4+} ions are created from disproportionation of two precursor Cr^{3+} ions in neighboring Al^{3+} substitution sites was assumed most likely:

$$2\,Cr^{3+} \longrightarrow Cr^{4+} + Cr^{2+} \tag{2.8}$$

The reasons for this scheme are as follows. The topaz samples $K2$ and $K4$ were found to contain a lower Cr^{3+} content after turning orange-red following irradiation. The orange-red colour is attributed to the Cr^{4+} ions and not the Cr^{2+} ions, since according to references cited within [2], the spin-allowed transition of a d^4 complex ($^5T_{2g} \rightarrow^5 E_g$) occurs at much lower absorption energy then those seen in (orange-red) topaz. The absorption bands at ∼ 540 nm (∼ 18500 cm^{-1}) and ∼ 417 nm (∼ 24000 cm^{-1}) in topaz are therefore assumed to be those spin-allowed transitions of a d^2 complex ($^3T_{1g}(^3F) \rightarrow^3 T_{2g}(^3F)$ and $^3T_{1g}(^3F) \rightarrow^3 T_{1g}(^3P)$): see Section 6.2 for a discussion of atomic terms.

In Cr-containing topaz samples, where isolated Cr^{3+} ions exist rater than $Cr^{3+}-Cr^{3+}$ pairs, the formation of the orange-red colour following irradiation is

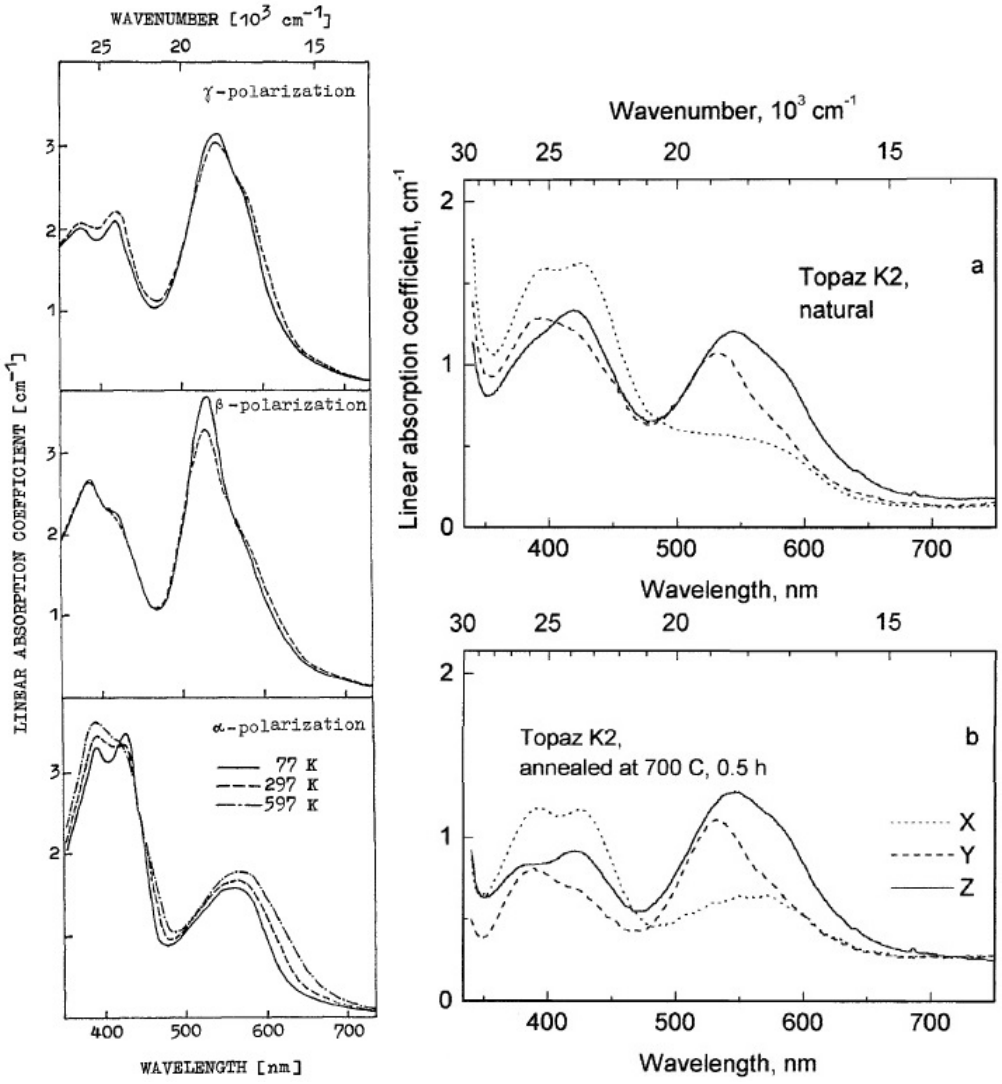

(a) (b)

Figure 2.15: (a) polarised spectra of Cr^{3+}-bearing topaz annealled in the temperature range 77 to 5997 K; and (b) the optical spectra of annealed $K2$ topaz **a.** before and **b.** after treatment at 700 for 30 min. Figure created from spectra reproduced from references [57] and [2] respectively.

not seen. This is the case for sample $K1$ even though the Cr content is not low. The naturally orange-red $K3$ topaz sample, assumed to have formed the Cr^{4+} colour centres during crystallisation, is stable up to ∼300 °C, where upon the colour is annealed out. The stablisation of this centre is assumed to be by other unknown impurity ions and/or other defect centres present within the crystal: for instance, a charge transfer from an O^- ion generated following radiation-induced loss of a H atom from a neighbouring hydroxyl group:

$$Cr^{3+} \cdot OH^- \longrightarrow Cr^{3+} \cdot O^- + H^{\cdot} \longrightarrow Cr^{4+} \cdot O^{2-} + H^{\cdot} \tag{2.9}$$

The irradiation induced orange-red centres were found to be unstable to thermal treatment (∼ 150 ℃) or following exposure to daylight for a week.

In addition to these experimental studies of topaz, some computational studies of the defect in topaz have also been carried out in the literature. In 2002, the first computational efforts to model the structure and lattice properties of topaz, distinguishing between topaz-OH and topaz-F analogues, and predict defect energies of some intrinsic defects, were presented by Jackson *et al.* [58]. They employed interatomic potentials and the Mott-Littleton approach [59] within the GULP package [60]. Later Jackson and Valerio [61, 62] presented an extensive list of defect formation energies for intrinsic point defects, Frenkel and Schottky defects, and substitutional and solution energies for transitional metal dopants, together with calculated Infrared (IR) and Raman frequencies for pure topaz, using the same derived potentials from the earlier investigation. Goto *et al.* [3] simulated the UV-Vis absorption spectra of yellow and pink topaz by using a cluster model and employing the configuration interaction (CI) method of single MO excitation within the GAUSSIAN98 code.

2.9 Dosimeter Application

Irradiation-induced defects in topaz were studied primarily to understand the process of colour enhancement in gemstones. The demonstration that the response of topaz to applied radiation can also be use in solid state dosimetry has generated renewed research interest [24, 25, 63–72]. The crystals of topaz are small and durable and they display comparatively favourable thermoluminescence (TL) emission characteristics compared to existing well-known commercial dosimeter materials, such as $CaSO_4$:Dy and LiF [73]. Topaz can be annealed and re-used without much loss in performance sensitivity, and fades at a rate of about 5%/year. It exhibits a linear

TL response up to 7×10^4 R and is sufficiently stable to environmental temperatures that, without further modification, may be used in commercial thermoluminescence dosimeter (TLD) readers [74]. Work has been done to test the TL sensitivity of topaz as a composite material, such as with Teflon [69] or glass [65], with promising applications in radiotherapy.

Thermoluminescence is a useful tool for measuring dose. The process of TL involves the formation of charge carriers that trap some of the energy absorbed by the material during irradiation. These irradiation induced defects generate defect states located within the band gap and can sometimes alter the appearance of the material, i.e. the colour. The defects created by irradiation can be thermally stable and only an application of heat treatment can remove them by annealing. The process is sometimes referred to as *bleaching* and involves the entrapment and recombination of charge carriers: typically this process gives rise to a characteristic TL emission by the material. Up to the saturation point of charge carriers within the material, the intensity of light emitted is proportional to the amount of radiation absorbed. The colour of luminescence and the temperature at which it occurs are properties related to the defect centres created. It is usual for thermal treatments to not "reset" the material entirely, in that some irradiation damage incurred by the material remains. This can reduce the TL sensitivity and lifespan of the material.

2.9.1 Human Dose Response

In toxicology, the relationship between the dose of radiation received and its effect on an organism is highly significant. The term *dose* simply means quantity, but in this context it refers to the amount of radiation absorbed by a body of mass (strictly speaking dosage refers to the rate of absorption). When a human body is exposed to radiation it absorbs only some of the energy. The amount of energy absorbed by a material depends on the type of ionising radiation, the energy or count rate of that radiation, and the nature of the absorbing material, i.e. a soft X-ray may deposit four times the dose in bone as it does in air. The quantities of radiation dose to humans are usually referred to as the absorbed, equivalent and effective dose.

An *absorbed dose* is a measure of the amount of energy imparted to a substance by ionising radiation per unit of mass. It is measured in units of gray (Gy) and is defined as the absorption of one joule of energy by one kilogram of matter.

The *equivalent absorbed radiation dose*, or simply the equivalent dose, is a measure used when assessing the potential health risk of radiation exposure to humans. It is the computed average measure of absorbed radiation by a fixed body of biological mass. It attempts to account for the different levels of susceptibility to radiation

damage different types of tissue have the potential to undergo, and in addition also taking into account the effect different types of radiation may have. For instance, 1 Gy of alpha radiation is more harmful than 1 Gy of beta radiation. The equivalent dose is calculated by summing the multiplication of the absorbed dose averaged over the mass of the tissue of interest, by the radiation weighting factor specific to the type of (and energy of) radiation, over all types of radiation, i.e.

$$H_T = \sum_R W_R \cdot D_{T,R} \tag{2.10}$$

where H_T is the equivalent dose (measured in sievert (Sv)) absorbed by tissue T, $D_{T,R}$ is the absorbed dose in tissue T by radiation type R, and W_R is the radiation weighting factor (see Table 2.4). Therefore the equivalent dose for 1 Gy of alpha particle radiation is 20 Sv.

Radiation	Energy	W_R
x-rays, gamma-rays, beta rays		1
Slow nuetrons	$<$ 10 keV	5
Resonance neutrons	10 keV - 100 keV	10
Intermediate neutrons	100 keV - 2 MeV	20
Fast neutrons	2 MeV - 20 MeV	10
Relativistic neutrons	$>$ 20 MeV	5
protons	$>$ 2 MeV	2
alpha particles		20

Table 2.4: The equivalent dose weighting factors for different types of radiation [75].

Since different types of matter have different susceptibilities to radiation, the measure of *effective dose* takes into account the radiation exposure risk associated with a particular organ or tissue to calculate the overall health, or the risk of cancer, to that organism. It is calculated by multiplying the equivalent dose with a factor associated with each type of tissue and is measured again in sievert.

2.9.1.1 Absorbed Dose

The dose response of topaz is claimed to be similar to the equivalent dose response of humans and for this reason, along with its relative natural abundance, has made topaz an interesting candidate as the active material in personal dosimetry. The unit of the specific energy of absorbance for any material is the Gray (Gy), while the equivalent dose for biological tissues is measurable in sievert (Sv). Both units describe the concentration of absorbed ionising radiation in terms of energy per

unit of mass, the difference being that the equivalent dose experienced by biological tissue is weighted according to the type of radiation (see Table 2.4).

2.9.2 Ideal Dosimeters

The desirable properties of a good solid-state TL dosimeter can be summarised as follows: (*i*) a good level of TL sensitivity in the dose range typically involved in personal dosimetry ($10^{-4} - 100\,\mathrm{Gy}$), (*ii*) the potential to translate its functionality into a manufactured hand-held device, (*iii*) the mechanical resistance to withstand the conditions of normal use (temperature, light and humidity), (*iv*) low cost production, (*v*) known response dependence to radiation type and dose/energy, (*vi*) the same TL response independent to orientation of device to radiation source, (*vii*) a time separation between the response of irradiation and reading [70, 76]. In addition to the TLD requirements outlined here, there is a need for the material to have a long life span, to be sensitive enough for detection but not so sensitive that radiation damage cannot be reversed in the bleaching process: i.e. a practical number of radiation-heat cycles before the material requires replacement. As far as we know, no solid-state dosimeter currently available can meet all of these requirements.

2.9.2.1 Topaz TL Functionality in Subsidiary Materials

de Magalhães *et al.* [64, 65] studied the Thermally Stimulated Exoelectron Emission (TSEE) and TL response of topaz-glass composites and topaz-Teflon pellets, as a function of applied radiation energy and as a function of absorbed dose. A linear TL and TSEE response was observed by topaz-glass composites to a dose range of $0.01 - 1\,\mathrm{Gy}$ and $5 - 40\,\mathrm{mGy}$ for X-ray and gamma irradiation respectively, and the TSEE peaks of topaz-glass composites were found to be higher than for topaz-Teflon pellets. However, within the field of dosimetry in medical radiotherapy treatment (see Table 2.5 for dose comparisons in some standard irradiative medical treatments), the dose response of topaz-glass and topaz-Teflon based dosimeters are comparable. Results confirm these two new dosimeters are relevant and useful in the detection and monitoring of the radiation source quality, especially in the investigation of dose distribution throughout a targeted planned area of irradiation.

2.9.2.2 Artificially Implanted Defects in Topaz

Colourless samples of topaz have also been artificially implanted with defect ions in order to study what changes occurred to the optical and TL properties. Ions inserted into colourless topaz included Cr, Al, W, Fe and Co [68, 77, 78]. Despite

Description	Energy Applied (J)	Energy Adsorbed (Gy)	Equivalent Dose (Sv)
Dental X-ray	0.0000025	0.000005	0.000005
Chest X-ray	0.001	0.0001	0.0001
Average CT Scan	0.05	0.01	0.01
EPA yearly radiation limit	0.07	0.001	0.001
Radiotherapy (total treatment dose)	30	60	60
Radiotherapy (single fraction treatment)	1	2	2

Table 2.5: Energy comparison of radiation doses in some examples of standard medical treatments using radiation therapy [75].

thermal treatment to encourage diffusion, in most cases an amorphous layer of inserted ions remained. Between $600 - 700$℃ of the annealing process, fluorine is lost from the damaged region. Colouration of colourless topaz samples following implantation were observed. High doses of Fe^{3+} and Cr^{3+} changed colourless topaz into dark brown, and subsequent annealing at 900 °C Fe-topaz turned yellow [78], while annealing at 800 °C turned Cr-topaz into pale green [77]. Co and W implantation were found to produce no colour changes within the samples. The TL sensitivity of natural colourless topaz was shown to be enhanced with Cr^{3+} and Al^{3+} ion insertion and to be suppressed with Fe^{3+} ions [68].

2.10 Summary

Many colour centres were highlighted as a result of this literature review. Our aim is to incorporate them into our computational investigation of the colour effecting defects of topaz, to ascertain whether these models are in fact stable, and evaluate their spectroscopic signatures to facilitate assignment of experimental observations.

Chapter 3

Theory

In this chapter we discuss the theory underpinning the computational chemistry techniques used to perform *ab initio* electron structure calculations in this thesis.

3.1 Atomic Theory

The challenge of finding an accurate way to describe the physical and chemical properties of matter has been a preoccupation of scientists down the ages. The ancient Greeks guessed that matter must be made up from a collection of indivisible particles and it is from them that we have the term *atom*. More then twenty centuries later and through the systematic work of Mendeleyev the periodic table of elements was established. Later in 1897 the discovery of the electron by Sir Joseph Thomson would pave the way towards the first recognisable description for the structure of the atom. Sir Ernest Rutherford's work in 1910 showed that the atom was made up of a small nucleus with positive charge (Ze), which is neutralised by a number (Z) of negatively charged ($-e$) electrons.

Astronomy analogies were made between planetary motion in the solar system and electrons "orbiting" a nucleus, but an increasing number of experiments and observations were beginning to make this picture of the atom incorrect. For instance, according to electromagnetic theory, the circular orbital motion of a charged electron should radiate energy with each change in direction in order to maintain radial acceleration. Under such a model, the electron would be caused to decelerate with the eventuality that it would collapse onto the nucleus, implying that all matter is essentially unstable. Since this is not our everyday experience, the planetary analogy falls apart. The laws of classical mechanics and electromagnetism can therefore not be applied to matter on such a small scale.

Quantum Mechanics or *quantum theory*, the terms used to group together the

physical phenomena that govern matter on microscopic scales, was established when Max Planck and Albert Einstein postulated that when light interacts with matter, the energy that is emitted or absorbed can only occur in discrete amounts, known as *quanta* (singular quantum). This became incorporated into the *Bohr model* of an atom, which states that an electron can only exist in a particular orbit around the nucleus, with fixed energy and angular momentum, and distance proportional to its energy. Promotion to and from this orbital can only occur instantaneously with the absorption or emission of a quanta of energy. An appealing aspect of this model is that an electron can not decay spirally into the nucleus as energy can not be lost in a continuous fashion. Later, Louis-Victor de Broglie postulated and proved, with his famous electron diffraction experiments, that *all* matter has both particle and wave-like duality and that the properties of a wave are not just confined to the parameters of electromagnetic radiation.

3.2 The Schrödinger Equation

These ebullient ideas cumulated in a new type of mathematical language that was being developed in order to describe the quantum state of a physical system. Erwin Schrödinger, who thought the momentum of an electron could be better described as a wave, developed the Schrödinger equation, the quantum mechanical equivalent to Newton's second law of motion, and postulated that if the wave function of an electron or an atom were known, a complete description of the physical state of a system could be determined.

A system of P nuclei with coordinates $\boldsymbol{R} = (\boldsymbol{R}_1 \dots \boldsymbol{R}_P)$ and N electron with coordinates $\boldsymbol{r} = (\boldsymbol{r}_1 \dots \boldsymbol{r}_N)$ is known to obey the time-dependent Schrödinger equation, which is a partial differential expression of how the system evolves with time:

$$i\hbar\frac{\partial}{\partial t}\Psi(\boldsymbol{R},\boldsymbol{r},t) = \hat{H}\Psi_{total}(\boldsymbol{R},\boldsymbol{r},t) \tag{3.1}$$

where i is the imaginary number, $\hbar$ is Planck's constant, Ψ is the total wave function of the system with n quantum states, and $\hat{H}$ is the Hamiltonian operator. The Hamiltonian is associated with the energy of a system and contains the operations that describe the kinetic and potential energies of the system. For a single point in

time, the Hamiltonian can be written in the form

$$\begin{aligned}\hat{H} = -\sum_{I=1}^{P}\frac{\hbar^2}{2M_I}\nabla_I^2 - \sum_{i=1}^{N}\frac{\hbar^2}{2m_i}\nabla_i^2 + \frac{e^2}{2}\sum_{I=1}^{P}\sum_{J\neq I}^{P}\frac{Z_I Z_J}{|\boldsymbol{R}_I - \boldsymbol{R}_J|} \\ + \frac{e^2}{2}\sum_{i=1}^{N}\sum_{j\neq i}^{N}\frac{1}{|\boldsymbol{r}_i - \boldsymbol{r}_j|} - e^2\sum_{I=1}^{P}\sum_{i=1}^{N}\frac{Z_I}{|\boldsymbol{R}_I - \boldsymbol{r}_i|}\end{aligned} \tag{3.2}$$

where Z_I and M_I are nuclear charges and masses respectively. Electrons are fermions (a particle with half-integer spin) and therefore obey the Fermi Dirac statistics. One consequence is that electrons obey the Pauli (exclusion) principle, which states that the overall wave function must be antisymmetric for the simultaneous interchange of the coordinates of two identical fermions. The total electronic wave function must then be antisymmetric, i.e. a change in sign should occur for every exchange of two electrons. All the ingredients for solving Schrödinger's equation for a moment in time and obtaining the eigenvalue energy are well known; however, the formidable task of treating the problem in a full quantum mechanical framework, the wave function antisymmetric with respect to exchange of electronic coordinates and symmetric or antisymmetric with respect to exchange of the nuclear variable, is in practice almost impossible to achieve. A number of approximations can be made to alleviate the problem and make the task manageable.

3.2.1 Adiabatic Approximation

The first assumption was made after observing the motion of nuclei and electrons and the relative time scale on which these actions occur. Given that the mass ratio between a proton and an electron is high (1836 : 1), it could be argued, using classical mechanics, that the velocity of an electron is much greater then that of the heavy particle (the proton), and therefore the electronic motion adapts instantaneously to any change in the nuclear coordinates.

In 1927, the Born-Oppenheimer (BO) approximation was proposed and has remained an indispensable part of quantum chemistry. The scheme states that the constituent motions of the total system, the electronic motion and the nuclear vibrations and rotations, can be treated separately, and therefore the total wave function can also be separated into its individual component wave functions for the electrons and nuclei:

$$\Psi_{total}(\boldsymbol{R}, \boldsymbol{r}, t) = \Theta_n(\boldsymbol{R}, t)\Phi_n(\boldsymbol{R}, \boldsymbol{r}) \tag{3.3}$$

where $\Theta_n(\boldsymbol{R}, t)$ is the wave function of the nuclear subsystem evolving with time, within one of the corresponding *adiabatic* electronic eigenstates $\Phi_n(\boldsymbol{R}, \boldsymbol{r})$. The adiabatic approximation in quantum mechanics states that the instantaneous electronic eigenstate that satisfies the time-independent Schrödinger equation (of the electronic state)

$$\hat{h}_e \Phi_n(\boldsymbol{R}, \boldsymbol{r}) = E_n(\boldsymbol{R}) \Phi_n(\boldsymbol{R}, \boldsymbol{r}) \tag{3.4}$$

remains the same for a nuclear perturbation, if the nuclear motion occurs within a small enough time frame ($\Delta t \to 0$). The Hamiltonian for the eigenstate electronic system ($\hat{h_e}$),

$$\hat{h}_e = \hat{T}_e + \hat{U}_{ee} + \hat{U}_{en} = \hat{H} - \hat{T}_n - \hat{U}_{nn}. \tag{3.5}$$

is found by removing the nuclear interactions from the total Hamiltonian ($\hat{H}$) in Equation 3.2. Here $\hat{T}_e$ is the electronic kinetic operator, $\hat{U_{ee}}$ is the potential energy operator arising from electron-electron Coulombic repulsion, $\hat{U_{en}}$ is the potential energy operator for the electrons-nucleus Coulombic attraction, $\hat{T}_n$ is the nuclear kinetic operator, and $\hat{U_{nn}}$ is the potential energy operator for the nuclei-nuclei Coulombic repulsion. This approximation can only be made by neglecting any off-diagonal matrix elements of the coupled partial differential (Equation 3.1) in electronic and nuclear coordinates.

3.2.2 The Time-Independent Schrödinger Equation

The time-dependent form of the Schrödinger equation (3.3) predicts the formation of standing waves by the wave function. This occurs when the Hamiltonian acting on a wave function generates a result that is proportional to that same wave function. In this instance the Hamiltonian is no longer an explicit function dependent on time, i.e. time-independent. Consequently, the wave function can then be split into its subsidiary spatial and temporal parts, $\Psi(x, t) = \psi(x)\tau(t)$, and a proportionality constant can replace the energy operator $\hat{E} = i\hbar\partial/\partial t$ as the energy eigenvalue.

The time-independent from of the Schrödinger equation is therefore a member of a class of equations known as eigenvalue equations and takes the form

$$E\Psi = \hat{H}\Psi. \tag{3.6}$$

Here the Hamiltonian operator ($\hat{H}$) (a second order differential operator), acts on the wave function (Ψ) and one of its eigenfunctions correspond to an eigenvalue (E). The property of the eigenvalue is interpreted as is the definite energy for that particular state, as opposed to the probability distribution of different energies (in the time-dependent form). In chemistry these standing waves are referred to as AO or MO.

3.3 The Hartree-Fock Method

In electronic structure calculations, the primary objective is the solution of the time-independent many-body Schrödinger equation. Exact solutions are impossible, hence a different number of approximated theories have been proposed, the main ones being Hartree-Fock (HF) and Density Functional Theory (DFT) that we discuss here.

The HF method is an *ab initio* approach for the determination of the wave function and the energy of a quantum many-electron problem in a stationary state. The assumptions made are that the many-body wave function can be approximated by a single Slater determinant, and that the electrostatic field felt by a single electron is the sum of the potential interactions on the nuclei, together with that of the field created by all the other electrons in the system.

Representing the Schrödinger equation in the Bohn-Oppenheimer approximation is given as the sum of all the one- and two-electron operator terms:

$$\begin{aligned} \hat{h}_e &= \hat{T}_e + \hat{U}_{en} + \hat{U}_{ee} \\ &= \sum_{i=1}^{N} \hat{h}_1(i) + \hat{U}_{ee} \end{aligned} \tag{3.7}$$

The one-electron operator ($\hat{h}_1(i)$) describes the motion of individual electrons in the system in terms of their kinetic ($\hat{T}_e$) and potential ($\hat{U}_{en}$) energy. The kinetic energy of a particle can be related to its momentum ($T = \frac{1}{2}\frac{p^2}{2m}$) through Newton's laws of motion. The quantum kinetic operator of an electron with mass m can be defined in terms of the momentum operator $\hat{p} = -i\hbar\nabla$, which is itself the dot product of two vectors:

$$\hat{T} = \frac{\hat{\boldsymbol{p}} \cdot \hat{\boldsymbol{p}}}{2m} = \frac{\hat{p}^2}{2m} = -\frac{\hbar^2}{2m}\nabla^2. \tag{3.8}$$

where ∇^2 is the Laplacian.

The one-electron potential energy operator refers to the attraction between the

electron and all the nuclei in the system, and any other external field. The one-electron operator is given by

$$\hat{h}_1(i) = -\frac{\hbar^2}{2m}\nabla^2_{\boldsymbol{r}_i} - e^2 \sum_{I=1}^{P} \frac{Z_I}{|\boldsymbol{R}_I - \boldsymbol{r}_i|}. \tag{3.9}$$

The one-electron eigenvalue Schrödinger equation should now read:

$$\sum_{i=1}^{N} \left[-\frac{\hbar^2}{2m}\nabla^2_{\boldsymbol{r}_i} - e^2 \sum_{I=1}^{P} \frac{Z_I}{|\boldsymbol{R}_I - \boldsymbol{r}_i} + \frac{e^2}{2} \sum_{j \neq i}^{N} \frac{1}{|r_i - r_j} \right] \phi_i = \varepsilon_i \phi_i \tag{3.10}$$

where $\frac{e^2}{2} \sum_{i=1}^{N} \sum_{j \neq i}^{N}$ is the potential energy operator term accounting for the repulsion between electrons. Equation (3.10) would be correct if the orbital wave function could be expressed as a simple product and not a determinant. Taking into account for the determinantal form of the wave function introduces a second two electron term, called exchange.

The variation principle states that for a trial wave function ϕ_i that is a normalised and well-behaved function, whose coordinates match those of the system's particles and satisfy the boundary condition of the problem, the expectation value ε_{trial} for the ground state that are calculated using the time-independent Hamiltonian operator, are always greater than or equal to the exact ground state energy of the system E_0:

$$\varepsilon_{trial} \geq E_0. \tag{3.11}$$

Therefore the best wave functions are those which yield the lowest energy. In practice, the wavefunction is expressed as a linear combination of simple functions ϕ_i (for instance AO's or plane waves) called basis sets. Solution of the hf equation requires to find coefficients of the linear combination that minimises the energy under the constraint that ϕ_i are orthonormal, i.e.

$$\int \phi_j^* \phi_i d\tau = \delta_{ji}. \tag{3.12}$$

The Hartree-Fock equation may be written simply as

$$\hat{F}(1)\phi_i(1) = \varepsilon_i \phi_i(1) \tag{3.13}$$

where $\hat{F}$ is the Fock operator. The notation suggests that the electron labeled 1 is

in orbital ϕ_i. The Fock operator is given as

$$\hat{F}(1) = \hat{h}_1 + \sum_{j \neq i} \left(\hat{J}_j(1) - \hat{K}_j(1) \right). \tag{3.14}$$

Here the terms $\sum_{j \neq i} \left(\hat{J}_j(1) - \hat{K}_j(1) \right)$ are closely related to the electron-electron repulsion term, $\sum_{j \neq i}^{N} \frac{1}{|r_i - r_j}$, in the one-electron Schrödinger equation (3.10).

The term $\hat{J}_j(1)$ refers to the **Coulomb Operator** and corresponds to the energy terms resulting from the electrostatic repulsion between charge clouds:

$$\hat{J}_j(1)\phi_i(1) = \left[\int \phi_j^*(2) \left(\frac{1}{r_{12}} \right) \phi_j(2) d\tau \right] \phi_i(1) \tag{3.15}$$

The term $\hat{K}_j(1)$ refers to the **Exchange Operator** and comes from the fact that the wave function is a determinant and not the simple product of component orbitals. There is no classical interpretation of the exchange operator.

$$\hat{K}_j(1)\phi_i(1) = \left[\int \phi_j^*(2) \left(\frac{1}{r_{12}} \right) \phi_i(2) d\tau \right] \phi_j(1) \tag{3.16}$$

The result of operating with the exchange operator $\hat{K}_j$ on an electron in a molecular orbital ϕ_i involves knowing ϕ_i throughout all space, since the integral involves ϕ_i over all space $d\tau$. This makes the exchange operator *non-local*, which is difficult to evaluate. In contrast, the Coulomb operator $\hat{J}_j(1)$ operating on an electron in the molecular orbital ϕ_i, involves an integral containing only ϕ_j. Therefore, the evaluation of $\hat{J}_j(1)\phi_i$ at any given point in space only depends on knowing ϕ_j throughout all space, and therefore $\hat{J}_j(1)$ is a *local operator*.

The HF Schrödinger equation may look like another eigenvalue problem, but the evaluation of the Fock operator ($\hat{F}(1)$) is dependent on the atomic orbitals through the coulomb ($\hat{J}_j(1)$) and exchange ($\hat{K}_j(1)$) terms. Therefore, the HF Schrödinger equation is better classified as a **pseudo-eigenvalue equation**, since the atomic orbitals (ϕ_i) need to be known before evaluating any integrals.

3.3.1 The Secular Equations

The Schrödinger equation for the overall molecular wave function is

$$\hat{H}\psi_{molecule} = E\psi_{molecule}. \tag{3.17}$$

A similar equation can be written for the one electron equation, whose solutions are the MO's ϕ_i,

$$\hat{h}_1 \phi_i = \varepsilon_i \phi_i. \tag{3.18}$$

Here $\hat{h}_1$ is the one-electron Hamiltonian operator and ε_i is the energy of an electron in the MO ϕ_i. Once a basis set χ_k is chosen, the MO ϕ_i is obtained as a linear combination of the χ_k functions

$$\phi_i = \sum c_{ik} \chi_i. \tag{3.19}$$

The one electron equation (3.18) can be rewritten as

$$\Rightarrow \hat{h}_1 \sum_k c_{ik} \chi_k = \varepsilon_i \sum_k c_{ik} \chi_k. \tag{3.20}$$

Introducing a matrix notation, where H_{ij} is the Hamiltonian integrals, and S is the overlap matrix, i.e. $H_{ij} = \int \chi_i^* \hat{h}_1 \chi_k d\tau$ and $S_{lk} = \chi_i^* \chi_k d\tau$ respectively, the matrix representation of Equation 3.18 is given by the **Secular equations**:

$$\begin{aligned} &\Rightarrow \sum_k c_{ik} H_{lk} = \varepsilon_i \sum_k c_{ik} S_{lk} \\ &\Rightarrow \sum_k c_{ik} \left(H_{lk} - \varepsilon_i S_{lk} \right) = 0. \end{aligned} \tag{3.21}$$

All quantum mechanical codes will aim to solve these secular equations, with appropriate choices of basis sets χ_k. To evaluate the Secular equations, the problem needs an iterative solution and so the Self-Consistent Ffield (SCF) theory was developed (see Figure 3.1).

3.4 Antisymmetric Wave functions of Spin-Orbitals

The wave function for a multi-fermionic system must, as already stated, satisfy the anti-symmetric requirement of the Fermi-Dirac statistic. The initial approximation of the wave function could be to take the factorisation of orthogonal wave functions (appropriately chosen) that represent the particles of the system. For the simplest multi-fermionic system, a two particle system, e.g. a two electron atom like He in the

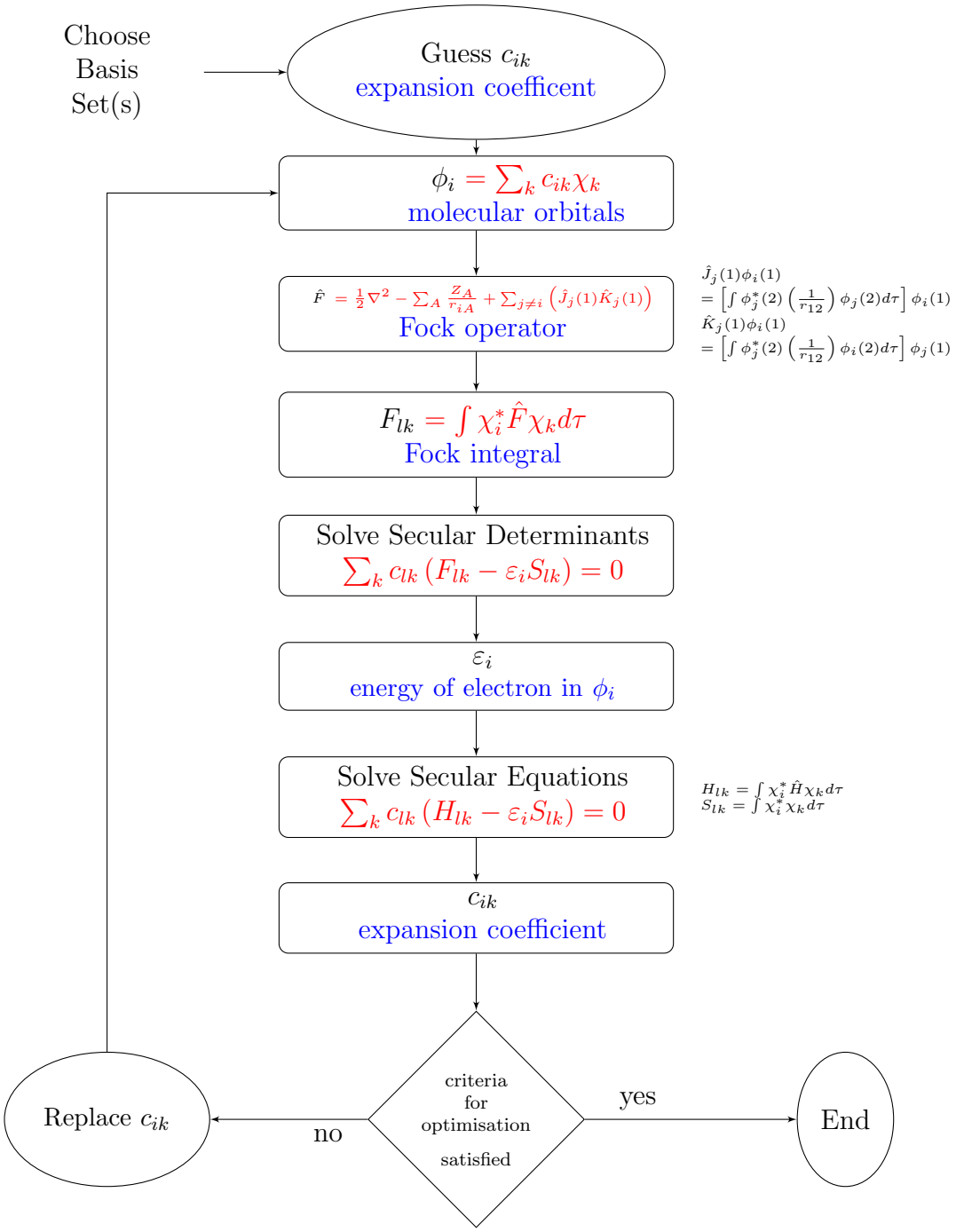

Figure 3.1: Hartree-Fock SCF Method

lowest energy configuration $1s^2$, the wave function can be written as the a product of n (in this case two) one electron wave functions, $1s^{\alpha}(1)$ and $1s^{\beta}(2)$.

Using an abbreviation, where $1s^{\alpha}(1)$ and $1s^{\beta}(2)$ can be rewritten as $1s(1)$ and $1\bar{s}(2)$ respectively, an initial guess of the $1s^2$ wave function could be represented by an expression such as

$$\psi_{\mathrm{He}} = 1s(1)1\bar{s}(2). \tag{3.22}$$

The problem with (3.22) as a wave function description of a two electron system, is that it does not satisfy the Pauli (exclusion) principle for fermions, because the wave function is not antisymmetric, i.e. $\Psi(x_1, x_2) = -\Psi(x_2, x_1)$:

$$\psi_{\mathrm{He}}^{interchange} = 1s(2)1\bar{s}(1) \neq -\psi_{\mathrm{He}}. \tag{3.23}$$

This problem can be overcome by taking the linear combination of the Hartree products formed from exchange:

$$\psi_{\mathrm{He}} = \frac{1}{\sqrt{2}}\left[1s(1)1\bar{s}(2) - 1s(2)1\bar{s}(1)\right]. \tag{3.24}$$

In Equation 3.24, if electron(1) were swapped with electron(2), the wave function (ψ_{He}) becomes negative ($-\psi_{\mathrm{He}}$), and therefore satisfies the Pauli principle whilst retaining the orbital approximation description in (3.22).

Extending this model further, the wave function description of the three electron atomic system lithium, the linear combination of the $1s^2 2s^1$ orbital can be approximated as

$$\begin{aligned}\psi_{\mathrm{Li}} = \frac{1}{\sqrt{6}}\Big[&1s(1)1\bar{s}(2)2s(3) - 1\bar{s}(1)1s(2)2s(3) + 1\bar{s}(1)2s(2)1s(3) \\ &- 1s(1)2s(2)1\bar{s}(3) + 2s(1)1s(2)1\bar{s}(3) - 2s(1)1\bar{s}(2)1s(3)\Big].\end{aligned} \tag{3.25}$$

A four electron atomic system, i.e. beryllium, would generate 24 terms between the brackets. The expressions (3.24) and (3.25) are simply an expanded form of matrix determinants. For example, the Li wave function (3.25) can be rewritten as

the determinant

$$\psi_{\mathrm{Li}} = \frac{1}{\sqrt{6}} \begin{bmatrix} 1s(1) & 1s(2) & 1s(3) \\ 1\bar{s}(1) & 1\bar{s}(2) & 1\bar{s}(3) \\ 2s(1) & 2s(2) & 2s(3) \end{bmatrix}. \tag{3.26}$$

Therefore, the general expression for a system with n fermions can be written as a determinant:

$$\begin{aligned} \Psi(x_1, x_2, \cdots, x_n) &= \frac{1}{\sqrt{n!}} \begin{bmatrix} \chi_1(x_1) & \chi_1(x_2) & \cdots & \chi_1(x_n) \\ \chi_2(x_1) & \chi_2(x_2) & \cdots & \chi_2(x_n) \\ \vdots & \vdots & \ddots & \vdots \\ \chi_n(x_1) & \chi_n(x_2) & \cdots & \chi_n(x_n) \end{bmatrix} \\ &\equiv |\chi_1\ \chi_2\ \cdots\ \chi_n|, \end{aligned} \tag{3.27}$$

where x_k are spatial coordinates of particle k and χ_n the occupied one electron MO's from 1 to n. The final expression in (3.27) is the compact notation of the leading diagonal of the determinant and defines the wave function of an n-electron system. Here the normalisation constant $\frac{1}{\sqrt{n!}}$ and fermion labels are understood and only exhibited in the expanded wave function form. The determinantal form of the wave function of the atomic systems He and Li are then

$$\begin{aligned} \psi_{\mathrm{He}} &= |1s(1)1\bar{s}(2)| \\ &= |1s1\bar{s}| \end{aligned} \tag{3.28}$$

and

$$\begin{aligned} \psi_{\mathrm{Li}} &= |1s(1)1\bar{s}(2)2s(3)| \\ &= |1s1\bar{s}2s| \end{aligned} \tag{3.29}$$

respectively. Determinantal wave functions were devised by Slater and as such are referred to as **Slater Determinants**, i.e. the electronic configurations of atoms (and molecules) are *not* simple products but are Slater determinants.

3.5 Density Functional Theory (DFT)

The problem with solving the wave function in terms of a Slater determinant of one-electron orbitals, is that while the function preserves some semblance of chemical interpretation, since each electron is still treated independently, the computational

costs of a wave function dependent on one spin and three spatial coordinates for every electron (i.e. fixed nuclear positions) is quite high. However, if one only requires the total energy of the system and possibly other properties stemming from the energy, then a physical *observable* needs to be found that permits *a priori* construction of the Hamiltonian operator. The Hamiltonian depends only on the number of atoms, the positions of the nuclei and the total number of electrons. The electronic density ρ, defined as the probability of finding an electron at a generic position in 3-dimensional space, could therefore serve as the useful physical observable for calculating the properties of a system, since when integrated over all space, gives the total number of electrons N, i.e.

$$N = \int \rho(\mathbf{r}) d\mathbf{r} \tag{3.30}$$

3.5.1 Thomas-Fermi Model

In 1927, Thomas-Fermi (TF) [79, 80] presented the first many-body electronic structure model in quantum mechanics to be formulated exclusively in terms of the electronic density and not wave function theory. The energy of interacting electrons is divided into kinetic and potential components. The kinetic energy T^{TF} is approximated using the quantum statistical (fictitious) *jellium* model, where the electron density $\rho(\mathbf{r})$ of constant density is a non-interacting, spin-unpolarised gas, subject to a uniformly distributed positive change:

$$T^{TF}\left[\rho(\mathbf{r})\right] = \frac{3}{10}\left(3\pi^2\right)^{\frac{2}{3}} \sum \rho^{\frac{5}{3}}(\mathbf{r}) d\mathbf{r} \tag{3.31}$$

The potential energy terms, the attraction between electronic density and nuclei,

$$V_{Ne}\left[\rho(\mathbf{r})\right] = \sum_{k}^{nuclei} \int \frac{Z_k}{|\mathbf{r} - \mathbf{r}_k|} \rho(\mathbf{r}) d\mathbf{r} \tag{3.32}$$

and the electron-electron self-repulsion term,

$$V_{ee}\left[\rho(\mathbf{r})\right] = \frac{1}{2} \int \int \frac{\rho(\mathbf{r}_1)\rho(\mathbf{r}_2)}{|\mathbf{r}_1 - \mathbf{r}_2|} d\mathbf{r}_1 d\mathbf{r}_2 \tag{3.33}$$

are treated using purely classical mechanics. Square bracket notation indicates a

function whose argument is also a function, i.e. a functional. The density is itself a function of three-dimensional spatial coordinates and, therefore, the terms T and V are referred to as 'density functionals'.

Even though the underlying assumptions render the TF equations, together with their implied variational principle, sufficiently inaccurate and, therefore, impractical for modern quantum chemical use (i.e. in TF theory, the stability of molecules relative to their constituent atoms is unfavorable and so dissociation is predicted [81]), the model is viewed for historical reasons as the precursor theory to modern-day DFT, because the energy is computed without reference to the wave function.

3.5.2 Hohenberg-Kohn Theorem

Nearly 40 years later, in 1964, the Hohenberg-Kohn (HK) formulation [82] of the N-particle Schrödinger equation finally expressed the ground state energy E of a fermionic many-particle system entirely in terms of the density $\rho(\mathbf{r})$. The derivation presented an alternative method to using wave functions and became one of the founding principles of DFT.

Given all the physical constraints of the density, i.e. $\rho(\mathbf{r}) \geq 0$ and $\int d\mathbf{r}\rho(\mathbf{r}) = N$, one should first consider the Hamiltonian $\hat{H}$ of a non-relativistic stationary many-body system,

$$\hat{H} = \hat{T} + \hat{V}_{Ne} + \hat{V}_{ee}, \tag{3.34}$$

where the operators $\hat{T}$, $\hat{V}_{Ne}$ and $\hat{V}_{ee}$ correspond to the kinetic energy, the external potential and the electron-electron two-particle interaction, respectively. It can be noted that the functions $\hat{T}$ and $\hat{V}_{ee}$ are identical for all electronic systems (i.e. atoms, molecules and solids), and only differ by the external potential $\nu(\mathbf{r})$ and the total number of electrons N of the system. Therefore, the many-electron ground state $|\Psi\rangle$ and the ground state energy $E[\nu]$ are both functionals of ν, and the time-independent Schrödinger equation can be written as

$$\hat{H}\,|\Psi\rangle = \left(\hat{T} + \hat{V}_{Ne} + \hat{V}_{ee}\right)|\Psi\rangle = E\,[\nu]\,|\Psi\rangle\,. \tag{3.35}$$

An essential part of the HK theorem is to show that the external potential $\nu(\mathbf{r})$ can be rewritten in terms of the electron density $\rho(\mathbf{r})$, since there is a $1:1$ correspondance between $\nu(\mathbf{r})$ and $\rho(\mathbf{r})$.

Every ground state expectation value of an operator $\hat{O}$ is, according to HK, a unique functional of the density according to

$$O[\rho] = \langle \Psi[\rho] | \, \hat{O} \, | \Psi[\rho] \rangle \, . \tag{3.36}$$

The Hohenberg-Kohn HK universal functional F_{HK} can be defined as

$$F_{\mathrm{HK}}[\rho] = \langle \Psi[\rho] | \, \hat{T} + \hat{V}_{ee} \, | \Psi[\rho] \rangle \, , \tag{3.37}$$

and is so called because it amalgamates the terms of the time-independent Schrödinger equation that do not include the system-dependent external potential $\nu(\mathbf{r})$ and considers the electron-electron two-particle interaction to be fixed. Therefore the energy functional becomes

$$E[\rho] = \int d\mathbf{r} \nu(\mathbf{r}) \rho(\mathbf{r}) + F_{\mathrm{HK}}[\rho]. \tag{3.38}$$

Were the HK universal functional able to be formally known, one could solve the Schrödinger equation *exactly* and for *any* system. Unfortunately, since $F_{\mathrm{HK}}[\rho]$ contains both the functionals for the kinetic energy and the electron-electron interaction, for which there is no classical description due to the instantaneous correlations of electrons (i.e. *Coulomb* and *exchange*), one would in practice require good approximations of these functionals in order to evaluate them. One such approximation method is the Kohn-Sham approach (in Section 3.5.3).

The HK theorem makes use of the **variational principle** in quantum mechanics, and states that only the true ground state charge density ρ_0 will deliver the ground state and also the lowest energy E_0 of the system from the HK functional $F_{\mathrm{HK}}[\rho_0]$:

$$E_0 \leq E[\rho] = T[\rho] + E_{Ne}[\rho] + E_{ee}[\rho]. \tag{3.39}$$

Therefore, the ground state energy of a system can be written by combing Equations 3.38 and 3.39

$$E_0 = \min_{\rho \to N} \left(\int d\mathbf{r} \nu(\mathbf{r}) \rho(\mathbf{r}) + F_{\mathrm{HK}}[\rho] \right) . \tag{3.40}$$

It should be noted that the variation principle is applicable, but also limited, to the

ground state, and so its strategy cannot be easily transfered to an excited states problem.

3.5.3 Kohn-Sham Self-Consistent Field Methodology

To surmise the discussion above, in DFT, if the density of a system is known, the external potential can also be determined and so too can the Hamiltonian. This in turn leads to the determination of the wave function, and if both the Hamiltonian and the wave function are know, then the (ground state) energy of the system can also be evaluated. In practice, however, the Schrödinger equation is still, in most cases, too difficult to solve, as the exact form of the Hamiltonian is unknown and the MO theory requires further simplification.

More specifically, the major challenge in DFT is the explicit form of the universal functional $F_{HK}[\rho]$, as defined by Hohenberg and Kohn, since the functional contains expressions for the kinetic energy $T[\rho]$ and the electron-electron self-interaction $V_{ee}[\rho]$ (Equation 3.37), both of which contain non-classical contributions that are unknown in their complete form. For instance, the kinetic energy cannot be explicitly treated by the $-\frac{1}{2}\sum_i^N \left(\nabla^2_{\boldsymbol{r}_i}\right)$ term in the Hamiltonian (Equation 3.9), as the positions and velocities of the electrons in a many-body system are unknown due to electron correlations.

Kohn and Sham noticed that the Coulomb repulsion (or kinetic energy) was much better dealt with under the Hartree-Fock (HF) scheme, and so gathering much inspiration from this approach, in 1965 they proposed a new method, still within the confines of DFT methodology, whereby the overall ground-state energy of a *real* system of *interacting* electrons would be the same as the ground-state energy of a *fictitious* system where the electrons were *non-interacting* [83].

Treating all the electrons as non-interacting particles of a reference system enables factorisation of the n-electron problem into the product of n one electron electronic orbitals, as in HF, the Kohn-Sham (KS) *effective* Hamiltonian $\hat{H}_{eff}$ was built that included a term for an *effective* one-electron potential $\hat{V}_{eff}(\mathbf{r})$,

$$\hat{H}_{eff} = \sum_i^N \left(-\frac{1}{2}\nabla^2 + \hat{V}_{eff}(\mathbf{r}) \right), \tag{3.41}$$

which contained the nuclear-electron field potential and the average electron-electron repulsion (the Coulomb term and the exchange-correlation potential) terms. The total Hamiltonian is the sum of N one-electron contributions to the Schrödinger

equation

$$\hat{H}_{eff} = \sum_{i}^{N} \hat{h}(\mathbf{r}). \tag{3.42}$$

Much like in HF, the "Kohn-Sham" wave function Φ^{KS} for this newly non-interacting N-electron reference system is defined as a Slater determinant, and is an exact eigenfunction of N non-interacting one-electron "Kohn-Sham" orbitals ϕ_i^{KS}, which are determined by solving the N one-electron Schrödinger equation

$$\hat{h}\phi_i^{KS} = \epsilon_i \phi_i^{KS}. \tag{3.43}$$

(Strickly speaking these KS orbitals have no physical significance, except for the highest occupied KS orbital, which (given an approximated Koopman's theorem) is the negative of the ionisation energy). The Kohn-Sham density for an N particle fictitious system $\rho^S(\mathbf{r})$ *exactly* equals the ground state density of the real system $\rho^0(\mathbf{r})$, and is given by

$$\rho^0(\mathbf{r}) \equiv \rho^S(\mathbf{r}) = \sum_{i}^{N} \left|\phi_i^{KS}\right|^2, \tag{3.44}$$

where N in the number of electrons.

The next stage involved dividing the energy functional into classical and non-classical contributions, in order that as much of the kinetic energy term could be salvaged and to facilitate ease of analysis. Since we already have an expression for the density from Equation 3.44, Equation 3.39 then becomes

$$E[\rho(\mathbf{r})] = T_{non-int.}[\rho(\mathbf{r})] + V_{Ne}[\rho(\mathbf{r})] + V_{ee,Coulomb}[\rho(\mathbf{r})] + \Delta T[\rho(\mathbf{r})] + \Delta V_{ee}[\rho(\mathbf{r})], \tag{3.45}$$

where terms $T_{non-int.}[\rho(\mathbf{r})]$, $V_{Ne}[\rho(\mathbf{r})]$ and $V_{ee,Coulomb}[\rho(\mathbf{r})]$ refer, respectively, to the non-interacting portion of the electronic kinetic energy (or Coulomb potential), the nuclear-electron interaction, and the classical portion of the electron-electron repulsion. Corrections in the kinetic energy and the electron-electron interaction terms are indicated in the terms $\Delta T[\rho(\mathbf{r})]$ and $\Delta V_{ee}[\rho(\mathbf{r})]$ respectively, and originate from the self-interaction nature of the electrons towards each other and the non-classical quantum mechanical part of their repulsion.

As in HF, the kinetic energy term is only dealt with in a classical way, and therefore the full Coulombic interaction, including the instantaneous repulsion known as the electron-electron **correlation** interaction, is not accounted for. However, the additional repulsive force felt by the electrons towards other electrons with anti-parallel spin that occupy the same region of space, is dealt with in HF, as the construction of the wave function stipulates that it must also satisfy the Pauli exclusion principle. This is known as the **exchange** interaction.

The way in which DFT has been derived means that it does not contain approximations and therefore is *exact*. However, while Hohenberg and Kohn proved that such a functional of the density must exist, no guidance was given as to its form, and so these 'difficult' terms are approximated by

$$\Delta T[\rho(\mathbf{r})] = T[\rho(\mathbf{r})] - T_{non-int.}[\rho(\mathbf{r})] \tag{3.46}$$

and

$$\Delta V_{ee}[\rho(\mathbf{r})] = V[\rho(\mathbf{r})] - V_{ee,Coulomb}[\rho(\mathbf{r})], \tag{3.47}$$

and grouped together into one term, commonly referred to as the exchange-correlation energy V_{xc}:

$$E[\rho(\mathbf{r})] = T_{non-int.}[\rho(\mathbf{r})] + V_{Ne}[\rho(\mathbf{r})] + V_{ee,Coulomb}[\rho(\mathbf{r})] + V_{xc}[\rho(\mathbf{r})]. \tag{3.48}$$

The total 3-dimensional electronic energy can be expressed as a functional of the ground state density ρ_0, exact for the kinetic energy term that still needs to be written in terms of orbitals, as under the HF scheme:

$$E[\rho(\mathbf{r})] = -\frac{1}{2}\sum_{i}^{N}\left\langle \phi_i^{KS}\right| \nabla^2 \left|\phi_i^{KS}\right\rangle + \frac{1}{2}\iint \frac{\rho(\mathbf{r}_1)\rho(\mathbf{r}_2)}{|\mathbf{r}_1 - \mathbf{r}_2|} - \int \frac{Z\rho(\mathbf{r})}{|\mathbf{r}|}d\mathbf{r} + E_{xc}[\rho]. \tag{3.49}$$

Furthermore, if Equations 3.43, 3.44 and 3.49 are combined, the Schrödinger equation for a set of single-particle equations can be written as

$$\left(-\frac{1}{2}\nabla_i^2 + \sum_{k}^{nuclei}\frac{Z_k}{|\mathbf{r}_i - \mathbf{r}_k|} + \int \frac{\rho(\mathbf{r}')}{|\mathbf{r}_i - \mathbf{r}'|}d\mathbf{r}' + \upsilon_{xc}\right)\phi_i(\mathbf{r}) = \epsilon_i\phi_i(\mathbf{r}). \tag{3.50}$$

The exchange-correlation potential υ_{xc} is a **functional derivative** of E_{xc} and is defined as

$$\upsilon_{xc}(\mathbf{r}) = \frac{\partial E_{xc}}{\partial \rho(\mathbf{r})}. \tag{3.51}$$

The υ_{xc} potential is best described as the one-electron operator for which the expectation value of the KS Slater determinant in E_{xc}.

Equations 3.49, 3.50 and 3.51 constitute the Kohn-Sham equations [83]. From this approach, all the energies originating from classical and non-interacting terms are known and can be explicitly described by the Kohn-Sham Hamiltonian. These refer to the non-interacting portion of the kinetic energy, the classical nuclear interaction, and the classical average Coulomb electron-electron repulsion. The remaining complicated correction terms of the real interacting system are gathered into the *exchange-correlation* term and need instead to reach the *exact* ground state, which can only be achieved through an iterative procedure: the KS effective potential V_{eff}, which itself depends on the electron density, is required also to build the KS orbitals in order to compute the electron density. Thus, in order to reach a minimum energy, it requires an iterative solution. A KS self-consistent field scheme is shown in Figure 3.2. One starts by guessing the initial orbitals, and then computing the density, determine the effective potential V_{eff}, build the effective Hamiltonian $\hat{H}_{eff}$ to solve the Schrödinger equation , and finally recalculate the orbitals to repeat the process until convergence is reached.

3.5.4 Exchange-Correlation Functionals

As emphasised above, the Exchange-Correlation (XC) energy E_{xc} is the accountable difference in the electron-electron repulsion between classical and quantum mechanical approaches, but also includes the difference in kinetic energy between the real interacting system and fictitious non-interacting system. In practice, functionals are not constructed to explicitly compute this portion of the energy. Instead, the term is either ignored, or approximations are made by constructing a 'hole' function to incorporate the interacting and non-interacting kinetic energy difference. Many different types of XC functionals have been developed for practical use over the years. Several topical reviews of how different functionals perform for different properties are available (see references [84–90]) and they will not be covered further here. In our calculations we have chosen the PBE0 hybrid electronic functional [91], as it gives a good description of band gaps, electronic localisation in open shell defects, and

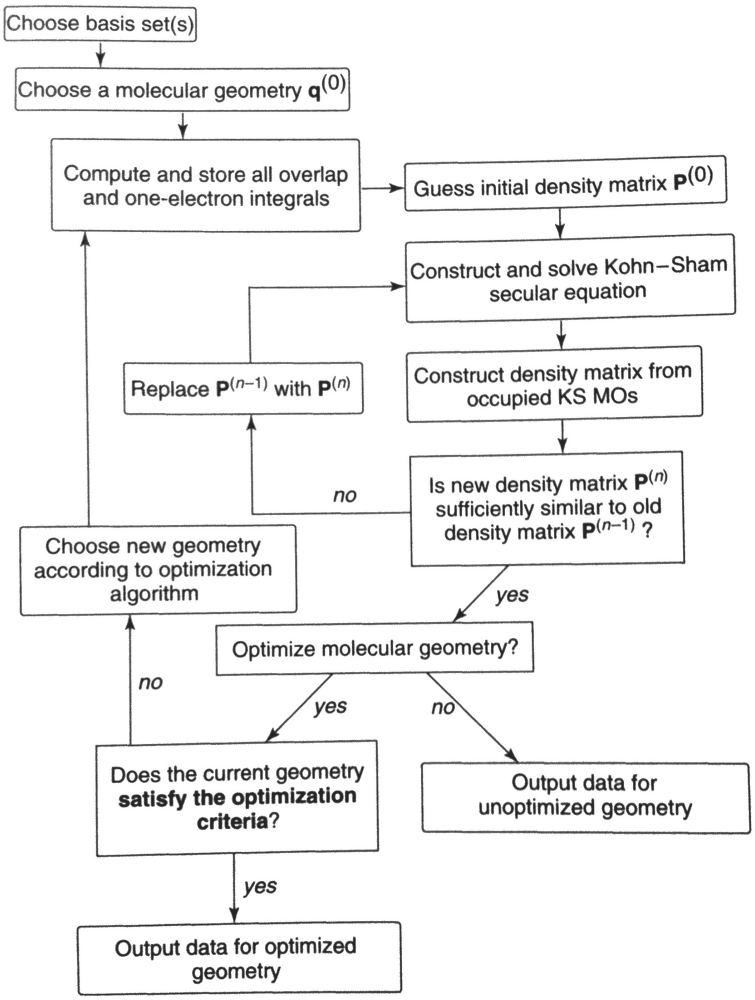

Figure 3.2: Kohn-Sham Self-Consistent Field Procedure. Reproduced from reference [81].

can even predict remarkably good excitation energies with time-dependent methods [92, 93].

3.6 Time-Dependent Density Functional Theory (TDDFT)

In the majority of condensed-matter systems, DFT can predict a range of ground state experimental properties, within a normal error range of $\sim 1-2\%$. These include the atomic structure and lattice parameters (i.e. XRD data), the total energy and phase stability, the electronic density (scanning tunneling microscopy (STM), scanning tunneling spectroscopy (STS)),the elastic constants, and phonon frequencies (IR, Neutron scattering, and Raman spectroscopies). DFT cannot, however, predict the electronic structure, band gap, or optical and dielectric properties, since these all involve knowing excited state electronic energy levels. DFT may be used to predict the electronic structure, but cannot be blamed if it does not succeed.

Theories based on *ab initio* principles are, however, required to calculate spectra in order to explain observed phenomena, to offer reference spectra to experimentalists, and to predict the properties of materials before synthesis or experiment. The interpretation of UV-Vis spectra of defects in topaz, which is one of the main goals of this thesis, is a typical example where not only the ground, but also the electronic excited states need to be simulated. Neither HF nor DFT theories are suitable for this purpose, as they do not describe the excited states. Extensions to these theories need to be considered. Of the possible *ab initio* excited state theories, TD-DFT in the random phase approximation (RPA) and Time Dependent Local-Density Approximation (TDLDA) are concerned with neutral excitations (i.e. optical absorption seen in optical and dielectric spectroscopy). With some approximations of Many-Body Perturbation Theory (MBPT), charged excitations such as inverse photoemission seen in photoemission spectroscopy can also be calculated. Here we focused primarily on TD-DFT.

TD-DFT can be viewed as an exact reformulation of time-dependent quantum mechanics, where the fundamental variable is no longer the many-body wavefunction as in the time-independent Schrödinger equation , but the one-body electron density $\rho(\mathbf{r}, t)$. Here, basic ideas involved in ground-state DFT are extended to the treatment of excitations or more generally the time-dependent phenomena with a time-dependent external potential.

The success of obtaining the electronic density for an interacting system lies in how well it can be approximated to a fictitious system of non-interacting electrons,

such as is outlined in the (time-dependent) KS auxiliary system [83]. The potential is therefore unknown and has to be approximated: the electrons feel the effective time-dependent KS potential.

The issue with constructing such a non-interacting electronic system is more complex in TD-DFT, in that time-dependent quantum mechanics suffers from the mathematical problem known as the *initial value problem*. Since the time-dependent Schrödinger equation is a first-order differential, the wave function (or the electronic density) together with the XC potential, is dependent on the initial state. In the Runge-Gross (RG) theorem, this implies a fixed initial state. In contrast, the static second order differential equation in space coordinates of the Schrödinger equation is a boundary value problem. Consequently the development of time-dependent approximations for implementation in TD-DFT is behind that of DFT, with applications routinely ignoring this memory requirement.

3.6.1 The Gross and Kohn theorem

The Runge-Gross (RG) theorem (1984) [94] is the time dependent extension of the HK theorem (1964) [82] and the formal foundation of TD-DFT. For the ground-state HK system, the external potential, $\nu_{ext}(\mathbf{r})$, and hence the total energy, gives a unique functional of the electron density, $\rho(\mathbf{r})$,

$$\nu_{ext}(\mathbf{r}) \Leftrightarrow \rho(\mathbf{r}). \tag{3.52}$$

The RG analogue demonstrates that, for a given initial wave function, there is a unique one-to-one mapping between the time-dependent external potential and the time-dependent density of a system: the two potentials, $\nu(\mathbf{r},t)$ and $\nu'(\mathbf{r},t)$, do not produce the same time-dependent electron density, $\rho(\mathbf{r},t)$ and therefore must differ by more than just the time-dependent function $c(t)$, i.e.

$$\nu(\mathbf{r},t) \neq \nu'(\mathbf{r},t) + c(t) \Leftrightarrow \rho(\mathbf{r},t) \neq \rho'(\mathbf{r},t). \tag{3.53}$$

The complexity of the mathematical problem is reduced from a many-body wave function (i.e. a function in $3N$-dimensional space, where N is the number of electrons in the system), to a simple one-body electron density function dependent on the 3-dimensional vector $\mathbf{r}$. These two descriptions of the system are equivalent by implication and all the properties of that system can thus be determined from

knowledge of the density alone.

Determining the ground-state of a static quantum mechanical system in DFT can be achieved through the minimisation of the total energy functional,

$$E[\Phi] = \langle \Phi | \hat{H} | \Phi \rangle \tag{3.54}$$

Since there can be no variational principle in time-dependent systems, on the grounds that the total energy is not a conserved quantity, the only analogous quantity is the quantum mechanical action,

$$A[\Phi] = \int_{t_0}^{t_1} \mathrm{d}t \langle \Phi \left| \mathrm{i}\frac{\partial}{\partial t} - \hat{H}(t) \right| \Phi(t) \rangle, \tag{3.55}$$

where $\Phi(t)$ is a N-body function defined in space. The action in quantum mechanics is a much less useful quantity then the static counterpart for the following reasons:

i. A "stationary principle" governs over a "minimum principle" as in the static case: meaning the function $\Psi(t)$ that makes equating the functional derivative $\Phi^*(t)$ to zero and thereby arriving at the time-dependent Schrödinger equation , will be the solution to the time-dependent many-body Schrödinger equation .

ii. The stationary point of an action functional is always zero, i.e. $A[\Psi] = 0$, and is defined in the Keldysh formalism [95].

Consequently, the proof of the RG theorem is more involved than the HK theorem: here we only provide a summary. The RG approach considers a single-component system moving in a scalar external field, for which the Hamiltonian takes the form,

$$\hat{H}(\mathbf{r}, t) = \hat{T}(\mathbf{r}) + \hat{W}(\mathbf{r}) + \hat{V}_{ext}(\mathbf{r}, t), \tag{3.56}$$

where $\hat{T}(\mathbf{r})$ accounts for the kinetic energy of the electrons,

$$\hat{T}(\mathbf{r}) = -\frac{1}{2} \sum_{i=1}^{N} \nabla_i^2, \tag{3.57}$$

and $\hat{W}(\mathbf{r})$ for the Coulomb repulsion between electrons,

$$\hat{W}(\mathbf{r}) = \frac{1}{2} \sum_{i,j=1,i\neq j}^{N} \frac{1}{|\mathbf{r}_i - \mathbf{r}_j|}. \tag{3.58}$$

The form of the final term, the generic time-dependent potential, $\hat{V}_{ext}(\mathbf{r}, t)$, is defined by the number of electrons and the time-dependent system. The many-body wave function evolves according to the time-dependent Schrödinger equation under a single initial condition,

$$i\frac{\partial}{\partial t}\Psi(\mathbf{r}, t) = \hat{H}(\mathbf{r}, t)\Psi(\mathbf{r}, t), \tag{3.59}$$

where $|\Psi(\mathbf{r}, 0)\rangle = \Psi(\mathbf{r})$. The electronic density is given through integration of the N-electron wave function: these depend upon the $3N$ spatial and N spin coordinates

$$\rho(\mathbf{r}, t) = N \sum_{s_1} \dots \sum_{s_N} \int d\mathbf{r}_2 \dots \int d\mathbf{r}_2 |\Psi(\mathbf{r}_1, s_1, \mathbf{r}_2, s_2, ..., \mathbf{r}_N, s_N.t)|^2. \tag{3.60}$$

From Equation 3.53, the spatially independent and time-dependent function $c(t)$, the difference of two external potentials, gives rise to wave functions differing by a phase factor $e^{-ic(t)}$, and therefore RG theorem provides a mapping that is invertible from an external potential to the electronic density

$$\nu(\mathbf{r}, t) + c(t) \rightarrow e^{-ic(t)}|\Psi(t)\rangle \rightarrow \rho(\mathbf{r}, t). \tag{3.61}$$

A functional of the external potential and initial wave function, the electronic density differs by more than the addition of $c(t)$:

$$\rho(\mathbf{r}, t) = \rho[\nu, \Psi_0](\mathbf{r}, t) \Leftrightarrow \nu(\mathbf{r}, t) = \nu[\rho, \Psi_0](\mathbf{r}, t). \tag{3.62}$$

3.6.2 Time-dependent Kohn-Sham Equations

Every observable, the Runge-Gross theorem claims, can be calculated from knowledge of the one-body density, but how to calculate this quantity was not stated. Still utilising the non-integrating electrons auxiliary system (Kohn-Sham) to solve

the interacting time-dependent Schrödinger equation , and subject to the same external local potential as in of the Runge-Gross theorem, $\nu_{KS}(\mathbf{r},t)$, the Kohn and Sham non-interacting Hamiltonian, $\hat{H}_s(\mathbf{r},t)$, still has the problem of determining the external or Kohn-Sham potential,

$$\hat{H}_s(\mathbf{r},t) = \hat{H}(\mathbf{r}) + \hat{V}_{KS}(\mathbf{r},t). \tag{3.63}$$

The Hamiltonian (see Equation 3.59) determines a determinantal wave function, which is constructed in terms of a set of N time-dependent Kohn-Sham orbitals to obey the time-dependent Schrödinger equation ,

$$i\frac{\partial}{\partial t}\varphi_i(\mathbf{r},t) = \left[-\frac{\nabla^2}{2} + \nu_{KS}(\mathbf{r},t)\right]\varphi_i(\mathbf{r},t), \tag{3.64}$$

and generate the time-dependent density of the interacting system,

$$\rho(\mathbf{r},t) = \sum_{i}^{occ} \left|\varphi_i(\mathbf{r},t)\right|^2. \tag{3.65}$$

Numerically Equation 3.64 can be easily solved, and if the exact Kohn-Sham potential, $\nu_{KS}(\mathbf{r},t)$, can be known or well-approximated, then the exact Kohn-Sham orbitals could be determined and consequently, the correct density of the system.

Analogously to DFT, the Kohn-Sham potential is decomposed in the following way

$$\nu_{KS}(\mathbf{r},t) = \nu_{ext}(\mathbf{r},t) + \nu_{Hartree}(\mathbf{r},t) + \nu_{xc}(\mathbf{r},t), \tag{3.66}$$

where $\nu_{ext}(\mathbf{r},t)$ is again the external potential, $\nu_{Hartree}(\mathbf{r},t)$ is the Hartree potential accounting for the classical electrostatic or Coulomb interaction between electrons,

$$\nu_{Hartree}(\mathbf{r},t) = \int d^3r' \frac{\rho(\mathbf{r},t)}{|(\mathbf{r}-\mathbf{r}')|}, \tag{3.67}$$

and $\nu_{xc}(\mathbf{r},t)$ the exchange-correlation potential consisting of all the non-trivial many-body effects of the time-dependent system. To extend to TD-DFT the same variational derivation of the Kohn-Sham equations approach, as used in DFT, to obtain

the exact expression of $\nu_{xc}(\mathbf{r}, t)$ as a functional derivative of the XC energy, is not straightforward to solve, since the problem related to causality [96, 97]. However in 1998, van Leeuwen solved the problem and defined a new action functional [95],

$$\nu_{xc}(\mathbf{r}, t) = \left[\frac{\partial \tilde{A}_{xc}}{\partial \rho(\mathbf{r}, \tau)} \right]_{n(\mathbf{r},t)} \tag{3.68}$$

by using the Keldish formalism: here τ is the Keldish pseudo-time.

Approximations of the exact expression of the functional of the density ν_{xc} in TD-DFT are still very much in their development, but importantly these are the only fundamental approximations TD-DFT makes [98]. These include the adiabatic local density approximation (ALDA), the time-dependent exact-exchange functional [99], and the attempt to construct an XC functional with memory by Dobson, Bünner and Gross [100], neither of which we go into detail here.

3.6.3 Linear Response TDDFT

Linear-response time dependent density functional theory (Linear-response (LR)-TD-DFT) may be used in cases where the external potential is small enough not to completely destroy the ground-state structure, and where it is not necessary to fully solve the time-dependent Schrödinger equation . The advantage of LR-TD-DFT is that perturbation theory to first order may prove sufficient in determining the linear change behaviour of the density, and allow e.g. the optical absorption spectrum to be calculated.

Assuming that the system is subject to a nuclear potential $\nu^{(0)}$ at $t < t_0$, and that at t_0 the system experiences a small well-behaved perturbing potential $\nu^{(1)}$, the total external potential of the system would consist of $\nu_{ext} = v^{(0)} + v^{(1)}$. The density can then be expanded in a perturbative series

$$\rho(\mathbf{r}, t) = \rho^{(0)}(\mathbf{r}) + \rho^{(1)}(\mathbf{r}, t) + \rho^{(2)}(\mathbf{r}, t) + \ldots, \tag{3.69}$$

where $\rho^{(1)}$, a component of $\rho(\mathbf{r}, t)$, depends linearly on $v^{(1)}$ and $\rho^{(2)}$ quadratically, etc. Since the perturbation is weak, we will only consider the linear term $n^{(1)}$ and in frequency space this reads

$$\rho^{(1)}(\mathbf{r}, \omega) = \int d^3\mathbf{r}' \chi_{KS}(\mathbf{r}, \mathbf{r}', \omega) \nu^{(1)}_{KS}(\mathbf{r}', \omega). \tag{3.70}$$

The linear density-density response function of the system, χ, sometimes known by other names in other disciplines, such as the reducible polarization function in the context of many-body perturbation theory, has been simplified in Equation 3.70 again through TD-DFT. The linear change of the density response function (χ_{KS}) of a fictitious Kohn-Sham system of non-interacting electrons, facilitates a much easier calculation than the fully interacting χ [98].

The expression for the potential ($\nu^{(1)}_{KS}$) in equation (3.28) is simply the linear change of the Kohn-Sham potential ν_{KS}, which includes all external perturbation powers due to non-linear dependence on the density. It can be calculated from the ν_{KS} definition

$$\nu^{(1)}_{KS}(\mathbf{r},\omega) = \nu^{(1)}(\mathbf{r},\omega) + \nu^{(1)}_{Hartree}(\mathbf{r},\omega) + \nu^{(1)}_{xc}(\mathbf{r},\omega). \tag{3.71}$$

Here $\nu^{(1)}$ is the variation of the external potential, the Hartree $v^{(1)}_{Hartree}$ and the exchange-correlation ($\nu^{(1)}_{xc}$) potentials to linear order, may be expanded with respect to the variation of the density as

$$\nu^{(1)}_{Hartree}(\mathbf{r},\omega) = \int d^3r' \frac{n^{(1)}(\mathbf{r}',t)}{|\mathbf{r}-\mathbf{r}'|}, \tag{3.72}$$

and

$$\nu^{(1)}_{xc}(\mathbf{r},\omega) = \sum dt' \sum d^3r' \frac{n^{(1)}(\mathbf{r}',t)}{|\mathbf{r}-\mathbf{r}'|} n(\mathbf{r}',t'), \tag{3.73}$$

respectively. An a side, the exchange-correlation kernel, f_{xc}, defined by

$$f_{xc}(\mathbf{r}t,\mathbf{r}'t') = \frac{\partial \nu_{xc}(\mathbf{r},t)}{\partial n(\mathbf{r}',t')}, \tag{3.74}$$

is a quantity well-known in several disciplines of theoretical physics: e.g. in electron gas evaluation, it is referred to as the local-field correction. Finally, combing above findings and a transformation to frequency space, the Dyson equation of TD-DFT follows,

$$\chi(\mathbf{r},\mathbf{r}',\omega) = \chi_{KS}(\mathbf{r},\mathbf{r}',\omega) + \int d^3x \int d^3x' \chi(\mathbf{r},x,\omega) \left[\frac{1}{|\mathbf{x}-\mathbf{x}'|} + f_{xc}(\mathbf{x},\mathbf{x}',\omega) \right] \chi_{KS}(\mathbf{x},\mathbf{r}',\omega).$$

(3.75)

Formally Equation 3.75 is an exact representation of the linear density response: i.e. were the exact Kohn-Sham potential known, the f_{xc} would follow, and the response function, χ, of the interacting system could be obtained through a self-consistent solution [98].

3.7 Basis Set Functions

In order to solve electronic structure problems, either within HF or DFT, a choice of the set of mathematical functions used to represent the one-electron orbitals, known as basis functions, needs to be made, in order that the wave function can be constructed. The one-electron wave functions are expanded into a generic basis set by the description of the orbitals $\phi_\alpha\rangle$, which is represented in real-space. In HF or DFT theory (Section 3.4 and 3.5 respectively), the HF or KS orbitals are expressed as linear combinations of basis functions,

$$\phi_j(\mathbf{r}) = \sum_{\alpha=1}^{N} c_{j\alpha}\chi_\alpha(\mathbf{r}), \tag{3.76}$$

where j is the wave function label that runs up M the dimension (or size) of the basis set, and $c_{j\alpha}$ is the expansion coefficient for the MO j.

The optimal description of the electron probability density, known as the basis set limit, is achieved with used of an infinite set of basis functions. This, however, is impractical and much work has gone into developing basis functions that allow the wave function to approach the limit efficiently.

There are three considerations to be made when considering the efficiency of a basis set in HF-SCF calculations, assuming any simplifying approximations do not involve empirical data.

i. The total number of basis functions needs to be kept to a minimum, since the number of two-electron integrals increases by $\sim N^4$ (depending on the method employed), where N is the number of basis function;

ii. The basis set leads to the efficient evaluation of the Fock (F_{lk}) and overlap integrals (S_{lk});

iii. The basis set is capable of describing the wave function of the molecule well enough to given chemically useful results, i.e. the function should have the

appropriate amplitudes in regions of space with high or low electron density probability.

In this section, we will discuss the functional forms of relevant basis sets used in this computational investigation.

3.7.1 Periodic systems

A system containing electrons in a unit cell, which is subject to Periodic Boundary Conditions (PBC), should have a wave function with the same periodicity as the unit cell. This condition of the wave function is sumarised by **Bloch's theorem** and the modified basis functions can be given by:

$$\phi_\alpha^k(\mathbf{r}) = e^{\mathbf{ik\cdot r}}\phi_\alpha^k(\mathbf{r}) \tag{3.77}$$

where k indicates the wave vector in the Brillouin zone.

3.7.2 Slater Type Orbitals

The atomic orbitals are well described by **Slater Type Orbitals** (STO): hydrogen-like atom functions combined through **Linear Combination of Atomic Orbitals** (LCAO) in accordance with the MO method, are exact solutions of the time-independent Schrödinger equation . Their general form is given by:

$$\chi_{\zeta,n,l,m}^{STO}(r,\theta,\phi) = NY_l^m(\theta,\phi)r^{n-1}e^{-\zeta r}, \tag{3.78}$$

where r is the distance from the nucleus, n is the principle quantum number, and ζ is the Slater exponent . The terms N , $Y_{l,m}(\theta,\phi)$, and $r^{n-1}e^{-\zeta r}$ are the normalisation constant, the spherical harmonic function, and the radial function respectively. The Slater exponent is defined as $\zeta = \frac{Z^*}{n} = \frac{Z-S}{n}$, where Z is the nuclear charge, Z^* the effective nuclear charge, and S is the screening constant.

At long range they possess exponential decay reproducing the overlap between atoms and the charge and spin function at the nucleus, and at short range a cusp at the position of the nuclei. They satisfy points *i.* and *iii.*, but not *ii.*, in Section 3.7, since analysis of the integral e^{-r} is not computationally straight forward.

3.7.3 Gaussian Type Orbitals

STO basis sets can be approximated using as linear combinations of **Gaussian Type Orbitals** (GTO), which is useful since the integrals of GTO functions are analytical. In addition, aside from evaluating matrix elements and the energy, properties gained from the derivative of the energy, such as polarisabilities, frequencies, and forces, can also be gained with good accuracy and reasonable computational cost.

A single Gaussian function (or primitive GTO) has the following spherical form:

$$\chi^{GTO}_{\zeta,n,l,m}(r,\theta,\phi) = NY^m_l(\theta,\phi)r^{n-1}e^{-\zeta r^2}. \tag{3.79}$$

The dependence of GTO functions on $e^{-\zeta r^2}$ is a disadvantage, as the GTO-type $1s$ hydrogenic AO has no cusp at the nucleus (GTO functions have a zero slope, i.e. $df(x)/dx = 0$) and the tail of the wave function is also poorly represented.

The *Gaussian Product Theorem* guarantees that the product of two GTO with different centres, is the same as a finite sum of Gaussians with a point between that of the two centres. In general, three times as many GTOs are required to reproduce the same level of accuracy in as one STO. So in order to alleviate the problem of using three times as many GTO functions to achieve the desired accuracy, several GTOs are often grouped together to form a **contracted Gaussian function** (χ) from a fixed linear combination of a number of original primitive Gaussian functions (g):

$$\chi_j = \sum_i d_{ji} g_i, \tag{3.80}$$

where d_{ji} is the contracted Gaussian function coefficient. The spatial orbitals are then expanded in terms of contracted Gaussians:

$$\psi_i = \sum_j c_{ji}\chi_j \tag{3.81}$$

Using contracted rather that primitive Gaussians reduces the number of unknown coefficients c_{ji} to be determined. The GTO is treated as a single function in the molecular calculation, and the greater the number of primitive Gaussian functions used in the contracted Gaussian, the better the STO approximation will be.

Contracted Gaussian functions vary by the number of primitive Gaussians used

to construct them, and their choice is dependent on the chemistry of the modelled molecular system. For instance, valence orbitals are be better described by multiple contracted Gaussian functions, e.g. *double zeta* uses two sets of contracted Gaussians. *Polarised functions* often enhance a basis set by including an AO with an angular momentum (l) one more than the valence electron orbital occupies, and *diffuse functions* are used to improve the basis set in excited state calculations.

3.7.4 Plane-Wave Basis Sets

In addition to atom centred functions, a suitable basis set choice for crystalline solids is given by non-localised basis sets formed using Plane waves (PW). These are independent of ionic nuclear positions, which allows for an uniform unbiased description of the electronic structure throughout the system, and a simpler calculation of the quantum mechanical forces.

The general form of a PW basis function demonstrates that Bloch's theorem (Section 3.7.1) is automatically satisfied, and any function in real space can be written as the Fourier transform (FT) in reciprocal space (g),

$$u_{\mathbf{k}}(\mathbf{r}) = \int e^{\mathbf{ig}\cdot\mathbf{r}} \tilde{u}_{\mathbf{k}}(\mathbf{g}) d\mathbf{g} \tag{3.82}$$

where $u_{\mathbf{k}}(\mathbf{r}) = u_{\mathbf{k}}(\mathbf{r} + \mathbf{a}_i)$ with $\mathbf{a}_i$) being any lattice vector.

3.7.4.1 PW Advantages and Disadvantages

PW basis sets take full advantage of fast Fourier transform (FFT) techniques and transform efficiently between real and reciprocal space. This is a major advantage when evaluating kinetic and potential integrals terms, since the one-electron Hamiltonian of these terms are diagonal in real space and local in reciprocal space respectively. Computationally, this operation scales to $M \log M$, where M is the number of PWs. Therefore certain integrals and other operations, such as the energy and derivatives of the energy (e.g. forces, stress) can be carried out with relatively little computational cost.

Not being an atom centred method, all regions of space and equally represented by PW basis sets with the same level of accuracy, and all basis functions are mutually orthogonal and therefore do not exhibit the Bsis-Set Superposition Error (BSSE). PW basis sets are also converge towards a target wave function in a guaranteed smooth and monotonic manner [101].

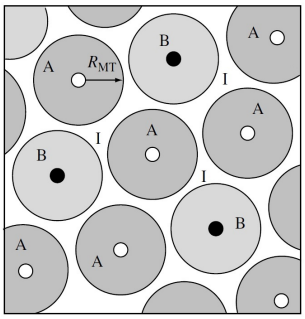

Figure 3.3: A schematic representation of a system partitioned into atomic spheres (shaded areas) with radii R_{MT} and interstitial region (I). These two regions represent different electron densities and an can be approximated better by the use of two different choices of basis functions in accordance with the augmented basis set method. Figure reproduced from reference [101].

Very high cutoff energies are required for simulating core electrons, as these wave functions vary rapidly close to the nucleus. Localised basis set are much better in this respect and that is why pseudopotentials are often used in conjunctions with PW basis sets [101]. This is particularly prevalent for H, first-row elements, and transition metals [101].

3.7.5 Augmented Basis Sets

The shortcomings in the asymptotic behavior of of Gaussian type orbitals, in that these functions fall off too quickly ($\sim e^{-\alpha r^2}$), means that it is important to consider the augmentation of a standard bases when investigating the properties of a system that are sensitive in the region of electron density where r (the radius from the nucleus) is large [102]. One can partition a system of condensed matter into two regions for wave function analysis: atomic spheres and interstitial regions (see Figure 3.3). The solutions are symmetric inside the the sphere and matched to the set of interstitials at the surface, where the atomic sphere meets the interstitial, in both amplitude and derivative [101]. The strategy of the basis function being augmented in the interstitial regions and represented with atomic-like function inside the sphere is known as *augmentation*.

One such example includes the hybrid Guassian and plane waves (GPW) method, where atom-centred Gaussian-type basis functions are used to describe the wave functions, and a PW auxiliary basis describes the density. Since FFTs and regular grids are generally a well established feature of PW codes, the density, which is represented as PWs, can efficiently solve both the Poisson equation and the Hartree energy and in a time that scales linearly, by exploiting FFTs. The GPW method employs real space grids in their choice of basis functions [103].

Chapter 4

Computational Method

The computational codes we propose to use for the investigation of the ground-state and the defects of topaz and their UV-Vis spectra are the CRYSTAL code [104], and the QUICKSTEP implementation [103] within the CP2K program package.

4.1 GULP

One unit cell (non primitive) of hydroxyl aluminium silicate contains four formula units of $Al_2SiO_4(OH)_2$. Although this is not an exceptionally large number of atoms, in a periodic three-dimensional array, 44 atoms is a sizable computational calculation for accurate *ab initio* quantum mechanical codes.

Structural details, however, can also be approximated using simple interatomic potential methods, that do not consider explicit electrons, but rather expresses the energy as a function of interatomic distances and angles. The GULP (the General Utility Lattice Program) code [60] was employed for interatomic potential calculations, employing potentials taken from previous studies (see Section 4.1.1 for details). Although the goal of this investigation was to apply previously derived potentials to the hydroxyl aluminium silicate system, the nature of the H disorder and its interaction with other defects, such as fluorine, contained within the host lattice, are subtle and define its properties.

4.1.1 Interatomic Potentials

Since aluminosilicates have already been extensively studied [105, 106], the potentials used for simulation of the silicate framework all come from the literature and are given in Table 4.1.1. The majority of the potentials come from works done by Catlow 1988 [106], but the Al−F and Al−O potentials, used to describe the bonding

interactions of the octahedrally coordinated Al^{3+} ion, where developed and fitted by Jackson and Valerio [61] for the same $Al_2SiO_4F_2$ structure studied here. The shell model was used to describe the oxygen (core 0.84819 and shell −2.84819) and fluorine ions and the covalent nature of Si−O bonds required the inclusion of 3-body bond-bending terms.

The short-range interactions are described with a Buckingham potential. It consists of a repulsive exponential part and an attractive dispersive r^{-6} term [60]:

$$A \cdot \exp\left(-\frac{r}{p}\right) - C \cdot r^{-6} \tag{4.1}$$

Interaction	Potential	A (eV)	ρ (Å)	C (eV Å^6)
(a) Short range potentials for F^-- and OH^--topaz				
$Si_{core}-O_{shell}$	Buckingham	1283.900	0.320	10.660
$Al_{core}-O_{shell}$	Buckingham	1460.300	0.299	0.000
$F_{shell}-O_{shell}$	Buckingham	464.540	0.336	22.100
$F_{sheel}-OH_{shell}$	Buckingham	464.540	0.336	22.100
$*F_{shell}-H_{core}$	Buckingham	415.000	0.2463	0.000
$O_{shell}-O_{shell}$	Buckingham	22764.300	0.149	27.880
$Si_{core}-F_{shell}$	Buckingham	1773.415	0.257	0.000
$Al_{core}-F_{shell}$	Buckingham	1773.415	0.257	0.000
$F_{shell}-F_{shell}$	Buckingham	4350.000	0.275	15.830
$Al_{core}-OH_{core}$	Buckingham	1142.678	0.299	0.000
$OH_{core}-OH_{core}$	Buckingham	22764.300	0.149	27.880
$H_{core}-OH_{core}$	Buckingham	311.970	0.250	0.000
$OH_{core}-O_{shell}$	Buckingham	22764.300	0.149	0.000
$OH_{core}-Si_{core}$	Buckingham	983.557	0.321	0.000
$H_{core}-O_{shell}$	Buckingham	1400.000	0.250	0.000
(b) Other potential types				
O−Si−O	Harmonic	$k_b = 2.097\,\text{eV rad}^{-2}$	$\theta_0 = 109.47°$	
$H_{core}-H_{core}$	Morse	$D = 7.052\,\text{eV}$	$a = 2.198\,\text{eV}^{-2}$	$r_0 = 0.948\,\text{eV}$
$F_{core}-F_{shell}$	Harmonic	$Y = -1.378\|e\|$	$k = 24.36\,\text{eV}^{-2}$	
$O_{core}-O_{shell}$	Harmonic	$Y = -2.84819\|e\|$	$k = 74.92\,\text{eV}^{-2}$	

Table 4.1: Potentials used in the GULP calculations of this investigation were taken from Jackson and Valerio [61], with the exception of the $F_{shell}-H_{core}$ Buckingham potential taken from [107]

The Morse potential was used here to model the $H_{core}-OH_{core}$ interaction and models the convergence and the limiting behaviour of a bond stretching towards infinity and the dissociation energy by including the dissociation energy in its definition

$$D((1 - \exp(-a(r - r_\theta))^2)^2 - 1) \tag{4.2}$$

4.1.2 Partial Occupancy

As mentioned in Section 2.2, topaz contains disordered F^-/OH^- solid solution in the $8d$ Wyckoff positions. This feature is challenging to model explicitly, but interatomic potentials enable the definition of partial occupation of the lattice sites. Furthermore, the orientational disorder of the OH^- ions needs to be represented.

In a hydroxyl saturated topaz, there are four possible OH−HO orientations that may exist (see Figure 2.1(a) in Section 2.2). Occupation of both sites is unstable, since this would lead to a H···H separation that is too short. Gulp can provide two methods for approaching the issue of disorder.

4.1.2.1 Mean Field Approach

The first method for handling disorder is the mean-field approach. It is an approximate approach where all atoms are assigned an occupancy factor, o_i, where $0 < o_i < 1$. The product of the relevant occupancies scales all interactions [60]:

$$U_{ij}^{m-f} = o_i o_j U_{ij} \tag{4.3}$$

$$U_{ijk}^{m-f} = o_i o_j o_k U_{ijk}. \tag{4.4}$$

For the majority of structures, the mean field model returns a reasonable result to compare to crystallography, since this experimental method returns averages anyway. However, for systems where thermodynamic data is required, such as the excess enthalpy of two phases mixing, these are typically over estimated since the stabilisation caused by distortions in the local structure are omitted [108].

4.1.2.2 Sampling Configurational Space

The alternative approach would be to assume the system is in thermodynamic equilibrium (which may not always be the case) and to construct a supercell of material with the required stoichiometry consistent with the composition required, and then to search the configurational landscape for the most stable configurations. Even though some notable examples have used this method, e.g. disordered alumina polymorphs, this is still a highly demanding method due to the sheer numbers of possibilities to consider, that increase with a factorial dependence on the correlation length.

As already mentioned, both hydroxyl and fluoro-/hydroxyl- structures have the same crystal structure and therefore both have four formula units of $Al_2SiO_4(OH)_2$ and $Al_2SiO_4(F,OH)_2$ respectively in their crystallographic unit cells. This means that even before creating a supercell, there are eight H positions to assign to one of two positions (H1 and H2). To generate all the unique configurations, we constructed a number generator, written in python (see Appendix B.1), the results of which were piped through a bash script that generated the structurally unique GULP input files to submit for calculation (see Appendix B.2). The total number of input files generated was 256 and 6305 for hydroxyl-pure ($Al_2SiO_4(OH)_2$) and mixed ($Al_2SiO_4(F,OH)_2$) topaz respectively. In order analyse the results from all these inputs, another scripted was created to tabulate and sort results, and also determine final configurations and probe local structures.

4.2 Quantum Mechanical DFT Calculations

Quantum mechanical DFT calculations were performed using two codes: CRYSTAL and CP2K.

4.2.1 CRYSTAL

4.2.1.1 Hamiltonian and Computational Parameters

Periodic Density Functional Theory (DFT) calculations were performed using the CRYSTAL06 [104] and CRYSTAL09 [109, 110] versions of the CRYSTAL code. The calculations employed the hybrid exchange functional PBE0, which contains 25% exact HF exchange in combination with the GGA exchange and correlation functional proposed by Perdew-Burke-Ernzerhof [111]. A number of parameters that control the accuracy of the calculations have been selected in this work; making reference to the CRYSTAL input keywords that activated them. The accuracy for the numerical integration of the DFT potential was controlled by selecting the large integration grid (keyword **LGRID**). This grid has high accuracy as it consists of atom-centred grids with 75 radial and 434 angular points, and is recommended for calculations containing second-row and third-row atoms (transition metals), especially when numerical derivatives of energy or related properties and gradients have to be computed, such as in geometry optimisations [104].

The percentage of Fock/Kohn-Sham matrices mixing during the SCF cycle to ensure convergence was set to 70%; keyword **FMIXING**. Eigenvalue level shifting was also used, as it reduces the coupling between filled and unoccupied orbitals

during the SCF procedure (keyword **LEVSHIFT**) using the absolute value of 1 E_h (recommended for complex cases where convergence is difficult). Results of a Mulliken population analysis have been collected for each system investigated using the keyword **PPAN**. Reciprocal space integration has been performed using a finite mesh of $8 \times 8 \times 8$ k-points for the orthorhombic system respectively, using the Pack-Monkhorst scheme [112]. Results are well converged with respect to denser k-point grids. The SCF convergence threshold on the total energy was set to 10^{-7} E_h of the total energy (keyword **TOLDEE**). The default value of the tolerances **TOLINTEG** were modified to 7 7 7 7 18: these numbers correspond to the overlap integrals threshold for the calculation and selection of two electron Coulomb and exchange integrals. Geometry optimizations have been performed to determine the equilibrium structures, i.e. the lattice parameters and atomic positions, for each chemical system investigated. Geometry optimizations were only considered complete when successive restarts showed no further change in both the unit cell parameters and fractional coordinates [104].

The majority of defects considered were open shell, i.e. they contain at least one unpaired electron. In these cases, spin polarised calculations have been performed. The keyword **SPINLOCK** was used to drive the SCF process towards a defined open shell state, by locking the difference in the number of alpha and beta electrons ($n_\alpha - n_\beta$) for a given number of SCF cycles. In more challenging cases, i.e. those systems which contained multiple defect species with more than one unpaired electron, such as two dopant Cr^{3+} d^3 ions, an additional alteration to the orbital occupation was required before the SCF process, in order to encourage relaxation into the required electronic configuration. The keywords **EIGSHIFT** and **FDOCCUP** were used to, shift the selected orbitals of the *d*-shell in energy to force the specified orbital occupation, and define the occupation of the partially occupied *d*-shell in the initial guess calculation, respectively.

Basis Sets

In CRYSTAL, the wave function and the electronic density are obtained within the LCAO approximation. The basis sets used to describe the one-electron crystalline atomic orbitals, are expanded from Gaussian-type localised atomic orbital functions.

The basis sets chosen for each atom-type investigated were taken from the recent literature and the online database provided by the CRYSTAL authors. An all-electron basis set was employed for all atoms (Al [113], Si [114], O [115], F [116], H [117], Cr [118, 119], and P [120, 121]). The basis sets were at least of double valence plus polarisation quality for each element, i.e. Al^{3+}, Si^{4+}, O^{2-}, F^{-}, H^{+}, Cr^{3+}, and

P^{4+}, and have been used for the study of several pure and doped aluminosilicate and aluminophosphate materials.

4.2.2 CP2K

Defect calculations performed using CRYSTAL were repeated using the CP2K computational package [122]. Calculation type included *ab initio* static calculations and molecular dynamics (MD) TD-DFT simulations: static calculations were performed for comparison with CRYSTAL results and for the calculation of the wavefunction and atomic positions required as an initial guess for MD TD-DFT simulations using hybrid functionals. The MD TD-DFT simulations were performed in order to calculate the UV-Vis spectra of a number of open shell defects in topaz.

The Quickstep module [103] in CP2K was used for the density functional implementation. The hybrid GPW scheme was utilised as an efficient method for calculating the Kohn-Sham matrix, as it allows for the electron density to be represented as either Guassians (primary basis) or by plane waves (auxiliary basis). The GPW scheme has the advantage of using only a small number of Guassian basis functions to represent the wavefunction accurately. Representing the density as a plane wave basis set or on a regular grid, exploits fast Fourier techniques to efficiently compute the electrostatic (Hartree) energy efficiently. A 400 Ry cut-off for the plane wave density has been applied.

The optimisation of the wavefunction used the orbital transformation (**OT**) Conjugate Gradients (**CG**) minimiser method, to avoid the diagonalisation of the Hamiltonian matrix and guarantee convergence. The Perdew-Burke-Erzenrhof hybrid functional [111], with 25% HF exchange (**PBE0**), was employed, together with the Goedecker-Teter-Hutter (GTH) pseudopotentials [123–125]. Screening thresholds for hybrid calculations, of $\epsilon_{Schwarz} = 10^{-7}$ and $\epsilon_{Schwarz_Forces} = 10^{-6}$ for static calculations and increased to $\epsilon_{Schwarz} = 10^{-8}$ and $\epsilon_{Schwarz_Forces} = 10^{-8}$ for *ab initio* MD simulations, were employed.

Molecularly optimised basis sets were employed. The atoms silicon, oxygen, fluorine, hydrogen and phosphorus were described using a standard triple-ζ basis with two sets of polarisation functions (TZV2P-MOLOPT-GTH), whereas for aluminium and chromium a double-ζ basis with one set of polarisation functions (DZVP-MOLOPT-GTH) was used [126]. The auxiliary density matrix method (ADMM) [127] was used to aid the computation of the Hartree-Fock exchange, in this large and demanding system of topaz with high-quality basis sets. The auxiliary basis functions for aluminium, silicon, oxygen, fluorine, hydrogen and phosphorus were described with a polarised contracted (to double-ζ quality) basis functions of

6-31G standard (cpFIT3), whilst chromium was described using again a double-ζ single polarisation function (DZV-ADMM). Atoms were given i their ionic state for the initial set up.

k-points are currently unavailable in CP2K, so to simulate similar accuracies as in other methods, larger units cell have to be selected [128]. Unfortunately, with the nature of our problem, it was not computationally viable to extend the cell larger than $2 \times 1 \times 1$ times the unit cell. Geometry and cell optimisations employed the Broyden-Fletcher-Goldfarb-Shanno (**BFGS**) algorithm with a 0.0016 Å maximum displacement and 300 bar pressure tolerance, for convergence criteria and full atomic relaxation. Initial geometries for ground state calculations were taken from optimised CRYSTAL calculated structures. The CP2K optimised geometry and wavefunction were used as an initial for the MD TD-DFT calculations.

Ab initio MD time-dependent DFT simulations using hybrid functionals [129] were preformed in order to obtain calculated UV-Vis absorption spectra of potentially optically active defects in topaz. All simulations were performed in a NVE ensemble using the same $2 \times 1 \times 1$ supercell defined before for static calculations. An electric field pulse of $5 \times 10^9\,\mathrm{W\,cm^{-2}}$ intensity was applied to the initial step. Given that the defect cell of topaz is orthogonal, the MD simulations were performed three times per spectra, with the polarisation direct of the electric field directed parallel to one of the x-, y- or z-axes. A time step of 0.15 a.u. was employed and simulations ran for approximately $4000 - 6000$ time steps (see captions of calculated spectra for actual number of time steps recorded).

For analysis of the real time propagation simulations, configurations were stored at every 0.15 a.u. time step. Optical spectra from time-propagation calculations were obtained by combining the dipole moments of the three polarised MD TD-DFT simulations through the td.general/multipole utility package of the Octopus computational code [130]. The magnitude of the dipole moment as a function of propagated time is converted into the intensity as a function of the energy via a Fourier transform. Following a unit conversion of the energy [eV] into wavelengths [nm], the spectra resembled an absorption spectra.

Chapter 5

Pure Topaz

5.1 Introduction

The composition of pure topaz, as discussed in Section 2.1, is $Al_2SiO_4(OH,F)_2$. Even in the absence of impurities or defects, the structure of topaz includes a degree of natural disorder, in the form of the F/OH anion solid solution, whereby F^- and OH^- groups are randomly distributed onto the same lattice site. This is otherwise known as fractional occupation. The long range ordering of F^- and OH^- groups, if any, has not yet been established in the literature, either by experiment or computational efforts. It is widely assumed that in natural topaz the F/OH anions order randomly, and any ordering of anions that may occur does so on a short range scale. Pockets of localised high F/OH anion concentrations have been observed and are referred to as zoning.

In addition to the variation in chemical composition due to F/OH disorder, the topaz structure can also accommodate orientational disorder of the OH groups, with the H occupying either of two nonequivalent sites. Depending on localised structural and electronic factors, the H atom can migrate between the extremes of these two lattice sites, in order to find the optimum orientation and lowest energy configuration.

In this chapter, the first aim will be to verify to what extent F^-/OH^- anion mixing and the preferred orientation of H atoms has on the structural and electronic properties of topaz. Here we will compare the computational data of pure topaz structures calculated using the codes GULP, CRYSTAL and CP2K, with those of literature experimental and computational data. We will also demonstrate the merits of using both a mean field approach and configurational space sampling methods to discuss the disorder. The relative stability of different configurations for a variety of topaz compositions is discussed.

5.2 Fractional Occupation

Computationally, there are two methods for dealing with an atom in a system with fractional occupancy: the mean field approach, whereby the atom can occupy both sites simultaneously, but only with a fractional occupation; and the configurational space sampling method, where a single structural configuration is considered at a time and the atom with fractional occupancy is allocated only one of the possible sites in any given configuration. Both methods have their advantages and disadvantages. The mean field approach is considerably faster, as it integrates all possible configurations in a single calculation; however, it does not enable local structural relaxations around specific anion orderings, and can only be accessed via interatomic potentials, not quantum mechanical calculations.

In this section, we consider both the mean field and configurational sampling approaches within a classical computational method, as comparative methods for approaching fractional atomic occupation in put topaz. For this, the same pair potentials as Jackson and Valerio [61] used in their investigation of topaz were also employed, and also within the GULP code.

To begin, the labeling convention adopted in this investigation and used to distinguish between different structural configurations is outlined. The same labeling convention is then used throughout this thesis.

5.2.1 Labeling Convention

The labeling convention adopted here uses an 8-digit number to distinguish between unique structural configurations of varying compositions of topaz. The 8-digit label consists of the numbers 1, 2 and 3, which differentiate between F and OH population of the F/OH site. The numbers 1 and 2 are both given to represent the OH, and are associated with the two unique positions the H atom can adopt in the OH group (see Table 5.5 for fraction coordinates of H1 and H2). The number 3 represents a F^- ion on the OH/F site.

The order in which the numbers 1, 2 and 3 appear in the 8-digit labeling sequence, dictates the unique structural configuration of the topaz composition. The total number of orientations and configurations considered was limited to only those possible from one unit cell of topaz (cell dimensions given in Table 5.3): in one unit cell of topaz, there are four ($Al_2SiO_4(OH,F)_2$) formula units, so eight OH/F sites. In the structure of topaz, two OH/F groups are formally bonded to each Al atom in an octahedral site, but there is a 1 : 1 ratio between Al and F/OH ions, hence each Al can be assigned one F/OH group, as shown in Figure 5.1(a).

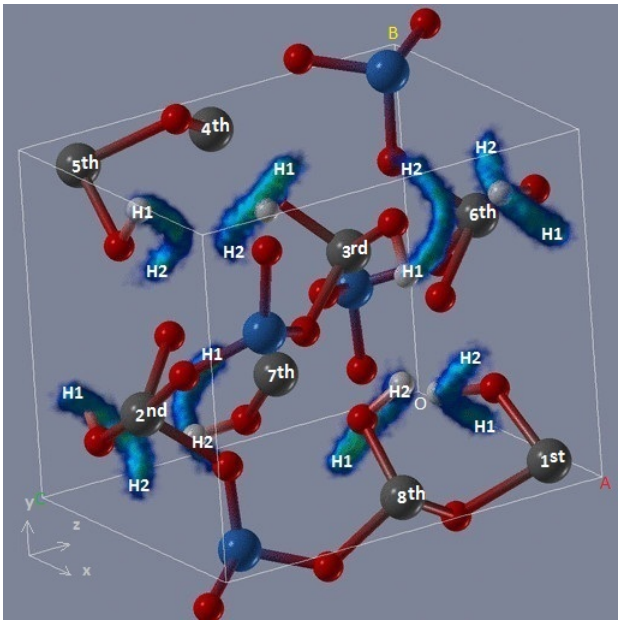

(a) H1 H2 labeling

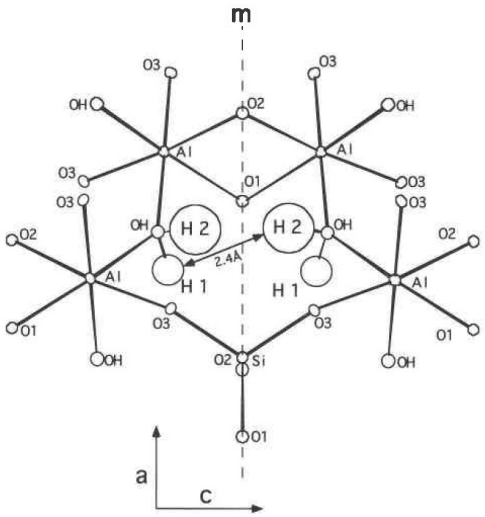

(b) H1 H2 positions

Figure 5.1: In (a) the labeling convention used in this investigation to distinguish between different structural configurations of pure topaz. The order in which the hydrogen atom labels, 1 and 2 for H1 and H2 respectively, are given is demonstrated here by the labeling of 1^{st}-8^{th} of Al atoms to which one of the OH groups has been assigned. The labeling convention is demonstrated on one unit of pure topaz-OH. For completeness, the number 3 has not been shown in this figure, as it is used to indicate where F^- ions are substituted in place of OH^- groups in topaz containing fluorine. Colour system: here Al atoms are depicted as grey spheres, Si blue, O red, and H are white. The blue/green cloud is used to show the time average path the H atom can move along between the two optimum positions. Therefore, the Al pairs that correspond to neighbouring OH pairs are $1-8$. $2-7$, $3-6$, $4-5$: NB Al6 has no formal bond to the OH group it is assigned in (a). Figure (b) is simply a reprint of 2.1(a) to emphasis the OH···OH pairings and the neighbour structural dependency.

The eight Al atoms, from which the ordering of the 8-digit structural label is derived, are labeled $1-8$. In Table 5.1 the fractional coordinates of the Al labeled $1-8$ along with there corresponding H 1 and 2 sites are also given. Figure 5.1(a) also shows the $3D$ representation of the two H (H1 and H2) positions. The ordering of the numbers 1, 2 and 3 in the 8-digit configuration label, combined with the unique structural and composition assignment each number holds, constitutes the labeling convention adopted here.[1]

[1]As an example of the use of the structural configuration label, if one takes the configuration 12312222: the first Al atom labeled 1 in Figure 5.1(a) would have an OH group in the location indicated where the H atom is in position 1; the second Al atom would have an OH with the H atom located in position 2; and the third Al atom would be bonded to an F atom. It should be noted that in every octahedral Al complex in topaz there are two F/OH groups: each F/OH group is also shared with another Al complex and so for the purposes of labeling, we consider one F/OH group per Al octahedral complex.

Fractional Coordinates									
no.	Al			H1			H2		
	x	y	z	x	y	z	x	y	z
1	0.905	0.132	0.080	0.438	0.223	0.118	0.552	0.282	0.201
2	0.405	0.383	0.911	0.938	0.292	0.874	0.052	0.215	0.806
3	0.608	0.632	0.411	0.076	0.723	0.374	0.956	0.782	0.306
4	0.108	0.883	0.580	0.576	0.792	0.618	0.456	0.715	0.701
5	0.108	0.883	0.911	0.576	0.792	0.874	0.446	0.725	0.796
6	0.608	0.632	0.080	0.076	0.723	0.118	0.946	0.792	0.191
7	0.405	0.383	0.580	0.938	0.292	0.618	0.042	0.225	0.691
8	0.905	0.132	0.411	0.438	0.223	0.374	0.542	0.292	0.296

Table 5.1: The fractional coordinates of the Al atoms and associated H1 and H2 sites, numbered $1-8$ according to the labeling convention employed here to distinguish structural configurations.

5.2.2 Comparison of Classical Methods

Fractional Occupancy

The lattice energies for topaz-F and topaz-OH, as calculated in this investigation and reference data taken from Jackson and Valerio [61], both using the GULP computational code, are given in Table 5.2. Our results for the mean field approach compare favourably with those computed by Jackson and Valerio [61], which only employed the mean field approach, even though the same numerical value was not reproduced, the general trends were. One explanation for this could involve different versions of the GULP code being used, or a different computational environment or setup for the GULP code.

The method of sampling configurational space did, however, highlight some disadvantages of using the mean field approach. In the configurational sampling results, the structural configuration with the lowest lattice energy for the topaz-OH ($Al_2SiO_4(OH)_2$) system is the case with equal fractional occupation of the H1 and H2 sites, 50 : 50 H1:H2 split. In contrast, the mean field approach predicted the most stable configurations of topaz-OH are those where there is 100% population of H into either H1 or H2 site occurs. The increase in lattice energies from either a 0 : 100 or 100 : 0 H1:H2 split to a 50 : 50 split in the mean field approach (+1.14 eV, see Table 5.2) suggests an increased level of inter-atomic interaction that is not seen in natural topaz. This point is further expanded by Figure 5.2(a), which demonstrates the difference in energy trends between the two classical methods, the mean field approach (labeled in the Figure as fractional occupancy) and the sampling of configurational space.

The second point to note from the configurational sampling data in Table 5.2, is

Topaz form	Lattice Energy eV		
	GULP [61]	GULP[a]	GULP[b]
$Al_2SiO_4F_2$	-275.39	-275.117	-275.116
$Al_2SiO_4(OH)_2$ (50:50 H1:H2)	-297.26	-297.281	-298.533
$Al_2SiO_4(OH)_2$ (100% H1)	-298.37	-298.418	-298.418
$Al_2SiO_4(OH)_2$ (100% H2)	-298.38	n/a[c]	n/a [c]]

[a]mean field approach
[b]sampling configurational space
[c]the optimised geometry of this configuration is 11111111, i.e. 100% H1

Table 5.2: Comparison of mean field and configurational space sampling approaches used in GULP to calculate the lattice energy. Reference data supplied by Jackson and Valerio [61].

that the structural configuration of topaz-OH where 100% of the H atoms occupy the H2 site is not a stable configuration. This can be explained by considering the interatomic distances between neighbouring OH groups (see Figure 5.1(b) and Table 5.7). The interatomic distance between two neighbouring Hs in sites H1···H1 is 2.7277 Å, H1···H2 is 2.4413 Å (cf 2.43(7) Å from Northrup *et al.* [18]), and for H2···H2 it is 1.6669 Å. Both the H1···H1 and H1···H2 interatomic distance are of comparable separation, whereas the H2···H2 separation is much smaller, therefore two neighbouring H atoms in site H2 are likely to adjust to reduce steric repulsion.

To demonstrate this model of neighbouring H atoms only adopting either H1···H2 or H1···H1 configurational structural pairings, an investigation of all possible structural configurations within one unit cell of topaz-OH was conducted, and the optimised lattice energies are shown in Figure 5.2(a). Even though all (+200) configurations and orientations of H on H1 and H2 sites were considered for topaz-OH, occurring in one unit cell, the final optimised set of geometries show that the stable configurations only consist of structures consisting of $\geq$ 50% concentrations of H occupation split onto the H1 site: i.e. some H initially with a H2 position became H1 during geometry optimisation. The difference in lattice energy between configurations of topaz-OH with 100% of H situated on the site H1 and 50 : 50 split between the sites H1 and H2, is only 0.12 eV for the method of sampling configurational space (see Table 5.2), where structural configurations with 50 : 50 H1:H2 split are the most stable. This can be explained by examining the distance between nearest neighbouring pairs of H (see Figure 5.1(a)): the interatomic distance between H1···H2 is greater then H1···H1. Therefore, with reduced steric hindrance in configurations with greater concentrations of H1···H2 pairs, the energy of the system can be reduced.

In the mean field approach, when the fractional weight of H1 and H2 are both

50%, there is the greatest percentage of H2···H2 interaction, which causes the most stable set of configurations in natural to be predicted the lease stable by this computational method. Formally under the mean field approach method, the topaz-OH structure with initial H positioning on only H2 sites becomes a structure containing only H1 following geometry optimisation. This is the same also for the sampling of configurational space method. A structure of H populating site H2 100% of the time has been shown to be unstable by either method.

Examining the stable configurations of topaz-OH more closely, for which the 8-digit configurational labels are listed in Figure 5.3 and Table 5.4, the presence of short-range ordering patterns among the H sites is evident. This is confirmed by Northrup *et al.* [18] in their experimental investigation of the H location in topaz-OH, where they predicted from reasoned geometrical arguments that the most stable structural model would be the case were each H site would be one-half occupied, i.e. evenly split between H1:H2 occupation. This model is captured by results from sampling the configurational space (see Figure 5.2(a)). Table 5.4 also shows that phases with medium/long-range disordered H···H pairings have lower symmetries and therefore fewer structural constraints within a geometry optimisation. The mean field approach always has full symmetry and consequently more structural constraints performing optimisations.

5.2.2.1 The Solid Solution in Pure Topaz

Continuing then just with the configurational space sampling method, combined with the pair potential approach as used in the GULP code, the sampling was extended over all possible structural configurations of H1:H2 ordering and F^-/OH^- solid solution compositions, within one unit cell of topaz. The relative lattice energy range for all stable structural and composition configurations[2] are shown in Figure 5.2(b). Here the base line of the x-axis represents the linear relationship between the two extreme pure analogues of topaz, i.e. the pure hydroxy ($Al_2SiO_4(OH)_2$) and flouride ($Al_2SiO_4F_2$) topaz analogues. The thermodynamic effect of creating the F^-/OH^- solid solution in topaz, is given by the enthalpy of mixing,

$$\Delta E = E_x - \left(\frac{x}{100}\right) E_{\mathrm{F}} - \left(\frac{1-x}{100}\right) E_{\mathrm{OH}}. \tag{5.1}$$

[2]Following the geometry optimisation of all +7000 configurations, which are the result of considering all the different structural (H1/H2) and conformational (F/OH) options present in one unit cell of topaz, the number of possible configurations reduced following geometry optimisations to a small list of stable and therefore likely topaz structures. These are now compared for their relative stability.

As shown in Figure 5.2(b), the F/OH mixing process in topaz is favourable, as the trend of stable structures lies below the x-axis. For the case of maximum entropy change, where the F:OH content is split 50 : 50, the change in enthalpy is also the greatest. Therefore, the mixing of $F-/OH^-$ anions is as expected a favourable process in topaz.

Furthermore, an investigation into the favoured positioning of the H atom as a function of the increased F content in topaz, shows that it is the [H2] position that is favoured as the F concentration increases (see Figure 5.2(c)). This is because when an OH group is adjacent to a F group, i.e. there are OH···F pairings, the preferred orientation of the H atom is in the H2 position. This local order of OH···F pairings is observed in 100% of all stable configurations of topaz containing both OH^- and F^- anions. In summary, adjacent OH···OH groups prefer either a H1···H2 or a H1···H1 orientation, and adjacent OH···F groups prefer the configuration H2···F (see Figure 5.1(a), Section 5.2.1 for which numbered atoms make an adjacent pair, and Table 5.4 for labels of stable topaz-FOH configurations).

5.2.3 Comparison of Ab Initio Methods

The Relative Stability of Structural Configurations

Following the reduction from the total number of possible configuration resulting from all the F/OH and H1/H2 combinations through geometry optimisation with pair potentials within the GULP code, the most stable structural configurations in one unit cell of topaz were carried forward for analysis with *ab initio* codes. In Figure 5.3, the stable structural configurations for topaz-OH ($Al_2SiO_4(OH)_2$) as predicted by GULP were reoptimised using the *ab initio* codes CRYSTAL and CP2K, both at the DFT-Perdew-Burke-Erzenrhof (PBE)0 level. Here the relative total energies of stable configurations are compared. Good agreement is shown in both the numerical stabilisation energies and the general trend of stable structures between the two *ab initio* codes.

The most stable configuration for topaz-OH, as predicted by *ab initio* techniques, is the one labeled 12121212 (or 21212121). In this configuration, the H atoms have the longest range ordering, expanding the previously seen most favoured H1···H2 orientation ordering of nearest neighbour pairs of H, to the secondary nearest neighbour pair also. Northrup *et al.* [18] predicted that the most stable configuration of topaz-OH would be the case where neighbouring H pairings arrange in a diagonal configuration (as in the case of H1···H2 pairing). Energetically, we have also shown, through calculations subject to PBC, that longer range ordering of the H positions

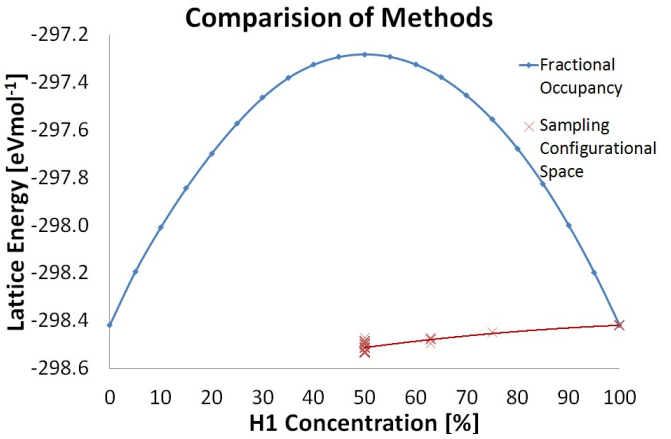

(a) Mean field approach vs sampling configurational space method of the H occupation of H1:H2 sites in topaz-OH.

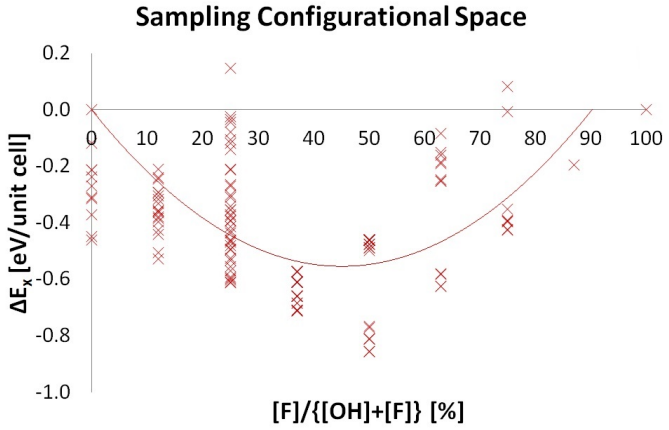

(b) Sampling of different structures across configurational space and varying the F:OH composition in pure topaz.

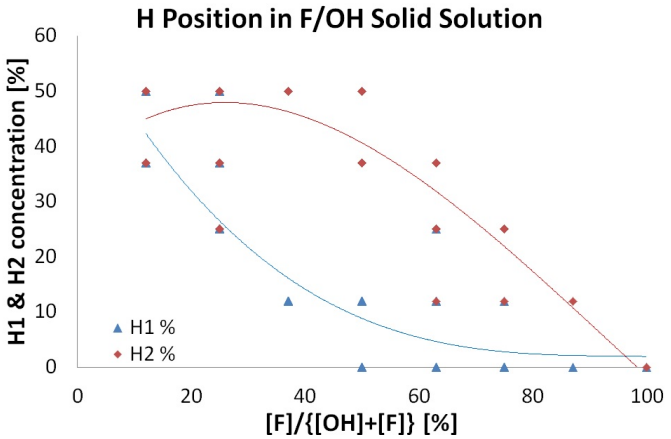

(c) H1 and H2 Concentrations across Varying F:OH Solid Solution in Topaz.

Figure 5.2: Results from the configurational space sampling method, shown in respect to the (a) fractional occupancy method (mean field approach), (b) the relative energy of different configurations of topaz with varying F:OH concentration with respect to the linear projection of the expected solution energy from topaz-OH and topazF, and (c) the H1 and H2 concentrations across varying F/OH solid solution in one unit cell of topaz.

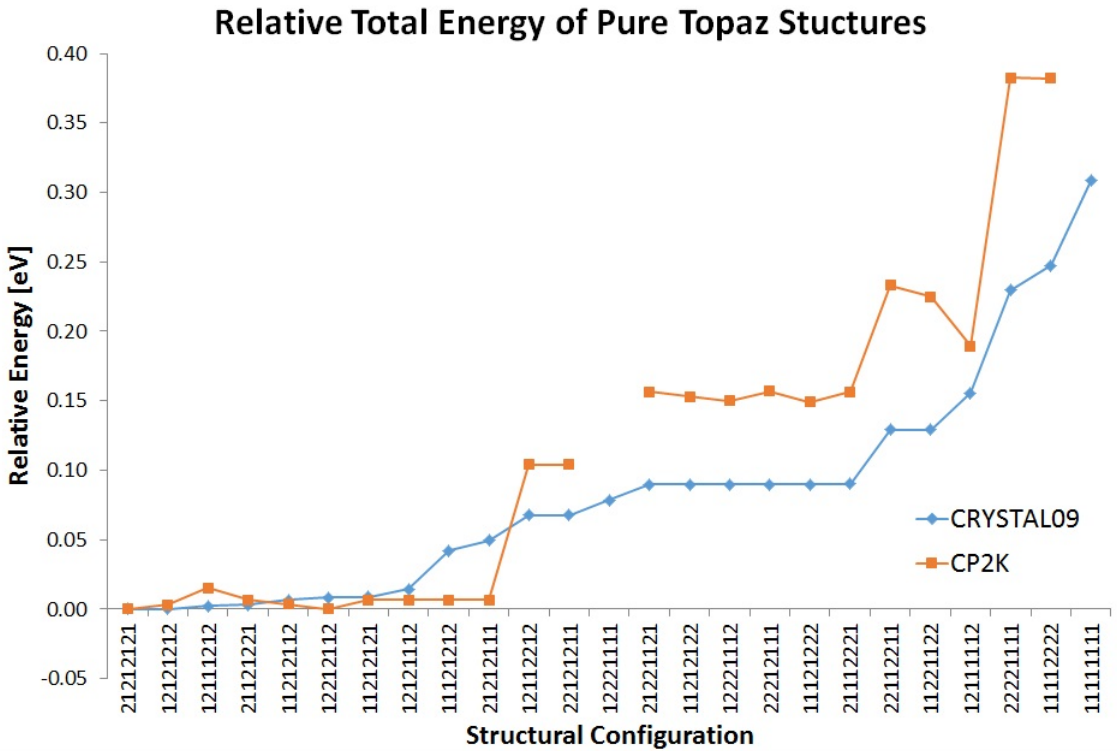

Figure 5.3: Relative total energies of stable topaz-OH configurations for CRYSTAL and CP2K optimised sructures.

in topaz is favourable.

5.3 Structure

This section explores the structural differences of changing the topaz composition (F/OH ratio) and the effect of altering configurations within a particular topaz composition.

5.3.1 Lattice Parameters

Calculated lattice parameters for pure forms of fluoro- and hydroxy- aluminium silicates were compared to experimental and calculated literature values, and are given in Table 5.3. The potentials used for both forms of the aluminium silicate reproduce the lattice parameter within an accuracy of approximately 2% and 1% for fluoro- and hydroxy- forms of topaz, and this is consistent with calculations made by Jackson and Valerio [61] also given in Table 5.3. Also presented are the lattice parameters obtained with CRYSTAL and CP2K codes. Our calculations with *ab initio* techniques show even better agreement of $< 1\%$ to the experimental lattice

parameters than those of the pair potencials.

Lattice Parameter	Experimental (Ref. [18])	GULP Calculated[a] (Ref. [61])	GULP Calculated	CRYSTAL Calculated	CP2K Calculated
		(a) $Al_2SiO_4F_2$			
a [Å]	4.6521	4.694	4.737	4.6801	4.644
b [Å]	8.8013	8.746	8.727	8.8121	8.766
c [Å]	8.4042	8.491	8.527	8.4474	8.417
		(b) $Al_2SiO_4(OH)_2$ (H1:H2 50:50)			
a [Å]	4.7203	4.686	4.696	4.7556	4.729
b [Å]	8.9207	8.934	8.948	8.9231	8.873
c [Å]	8.4188	8.505	8.483	8.3967	8.420

[a]Reference data calculated using the mean field approach method, i.e. the partial atomic occupancy method.

Table 5.3: The calculated lattice parameters of pure topaz-F ($Al_2SiO_4F_2$) and topaz-OH ($Al_2SiO_4(OH)_2$) using the configurational space method, from GULP, CRYSTAL and CP2K calculations. Literature data provided for reference (cited within).

The lattice parameters for all the topaz-OH ($Al_2SiO_4(OH)_2$) configurations, the topaz-F composition ($Al_2SiO_4F_2$) and for a number of mixed F/OH topaz compositions (12.5 : 87.5, 50 : 50 and 87.5 : 12.5), as predicted by CRYSTAL calculations, are provided in Table 5.4 (the corresponding CP2K lattice calculated parameters are given for reference in Appendix C.1). The mirror plane of the *Pbnm* orthorhombic space group is violated, at least locally, and so the symmetry is topaz bearing high concentrations of OH is reduced. Northrup *et al.* [18] were not able to resolve the symmetry of topaz-OH using X-ray diffraction data, but postulated the possibility of long-range H ordering and suggested that the symmetry may reduce to $Pbn2_1$. For the structural configurations of topaz-OH that were identified by this investigation as unique and stable configurations, the space groups are also provided in Table 5.4.

For the comparison of *ab initio* method performance, the relative energy of different topaz-OH configurations as a function of unit cell volume is given in Figure 5.4 (lattice parameters calculated from CP2K calculations are provided in Table C.2). This Figure highlights a correlation between stability and lattice spacing corresponding to long-range ordering of H positions. Lower energy configurations are able to pack atoms together more tightly. CP2K calculated topaz-OH cell volumes are between $1-2\%$ lower than those calculated by CRYSTAL. The break down of each lattice parameter as a function of the relative stability of each topaz-OH configuration are given in Figure 5.5. Both codes reproduce the same lattice parameter trends with respect to the stability of structural configurations, but CP2K calculated a and b lattice parameters are on average 0.5% lower then that of CRYSTAL

Struct.	Space Group		Lattice Parameters							
Config.	IGR	Symbol	a [Å]	b [Å]	c [Å]	α	β	γ	Vol. [Å^3]	ρ[g cm^{-3}]
(a) $Al_8Si_4O_{16}(OH)_8$ (Topaz-OH)										
11112222	19	$P2_12_12_1$	4.7340	8.9494	8.4340	90.000	90.000	90.000	357.32	3.345
22221111	19	$P2_12_12_1$	4.7284	8.9547	8.4392	90.000	90.000	90.000	357.33	3.345
11221122	14	$P2_1/c$	4.7538	8.9122	8.4332	90.508	90.000	90.000	357.27	3.345
22112211	14	$P2_1/c$	4.7536	8.9120	8.4328	89.501	90.000	90.000	357.23	3.345
11121222	1	$P1$	4.7515	8.9209	8.4154	90.267	90.068	89.991	356.70	3.350
11212122	1	$P1$	4.7514	8.9205	8.4160	90.269	89.926	89.997	356.70	3.350
12112212	1	$P1$	4.7486	8.9274	8.4169	89.940	90.014	90.153	356.82	3.349
12221112	1	$P1$	4.7515	8.9207	8.4154	90.265	90.068	89.995	356.70	3.350
21112221	1	$P1$	4.7515	8.9201	8.4150	89.733	89.932	89.994	356.65	3.351
21221121	1	$P1$	4.7514	8.9205	8.4156	90.269	89.925	89.998	356.69	3.351
22121211	1	$P1$	4.7485	8.9271	8.4163	89.935	90.013	90.156	356.77	3.350
22212111	1	$P1$	4.7519	8.9209	8.4154	89.736	89.936	89.995	356.73	3.350
12121212	14	$P2_1/c$	4.7556	8.9233	8.3962	90.000	90.141	90.000	356.30	3.354
21212121	14	$P2_1/c$	4.7556	8.9231	8.3967	90.000	89.855	90.000	356.31	3.354
12221111	14	$P2_1/c$	4.7483	8.9265	8.4150	90.058	90.022	89.841	356.67	3.351
12212112	14	$P2_1/c$	4.7515	8.9239	8.4033	90.000	90.000	90.000	356.32	3.354
21121221	33	$Pna2_1$	4.7520	8.9236	8.4055	90.000	90.000	90.000	356.44	3.353
11121212	33	$Pna2_1$	4.7552	8.9237	8.3951	89.998	90.146	90.002	356.23	3.355
11212121	33	$Pna2_1$	4.7542	8.9239	8.3991	90.004	89.855	89.998	356.34	3.354
12111212	33	$Pna2_1$	4.7556	8.9235	8.3941	90.001	90.153	90.000	356.22	3.355
12121112	33	$Pna2_1$	4.7554	8.9236	8.3943	89.996	90.151	90.001	356.21	3.355
21212111	33	$Pna2_1$	4.7549	8.9244	8.3963	89.997	89.854	90.001	356.29	3.354
11212112	1	$P1$	4.7512	8.9239	8.4076	90.003	90.002	89.999	356.47	3.353
12111112	7	Pc	4.7089	8.9478	8.5003	90.000	90.076	90.000	358.16	3.337
11111111	62	$Pnma$	4.6723	8.9735	8.5622	90.000	90.000	90.000	358.99	3.329
(b) $Al_8Si_4O_{16}(OH)_7F$										
32221112	1	$P1$	4.7329	8.9263	8.4193	89.922	89.885	89.742	355.69	3.369
31212122	1	$P1$	4.7400	8.9190	8.4074	90.104	89.837	89.868	355.42	3.372
(c) $Al_8Si_4O_{16}(OH)_4F_4$ (Topaz-FOH)										
23323223	33	$Pna2_1$	4.6921	8.9100	8.4077	90.000	90.000	90.000	351.50	3.438
23332321	1	$P1$	4.7055	8.8903	8.4188	89.869	90.069	90.343	352.18	3.431
(d) $Al_8Si_4O_{16}(OH)_1F_7$										
23333333	1	$P1$	4.6821	8.8401	8.4430	89.987	90.053	90.213	349.46	3.486
(e) $Al_8Si_4O_{16}F_8$ (Topaz-F)										
33333333	62	$Pbnm$	4.6793	8.8126	8.4470	90.000	90.000	90.000	348.32	3.507

Table 5.4: The CRYSTAL calculated lattice parameters and unit cell dimensions of stable configurational structures of pure topaz.

(the c parameter is on average 0.15% higher in CP2K then in CRYSTAL).

This can be explained by considering the structure of topaz as a close packed double-*hcp* (*dhcp*) structure of three distinct layers (A, B and C) of large anions O and F with the small Al and Si cations sitting in interstitially between layers [131]. The A layer accommodates six oxygens, which are not quite coplanar because the a lattice is too small to accommodate them, and the B and C layers consist of four flouro/hydroxy groups and two oxygens. The layers are ordered $ABAC$ and are stacked parallel to the b-axis [22]. Even though there is a slight overestimation of the b lattice parameter by CRYSTAL, in that the interaction between ionic layers are not as well reproduced by the local basis set of CRYSTAL than they are by the

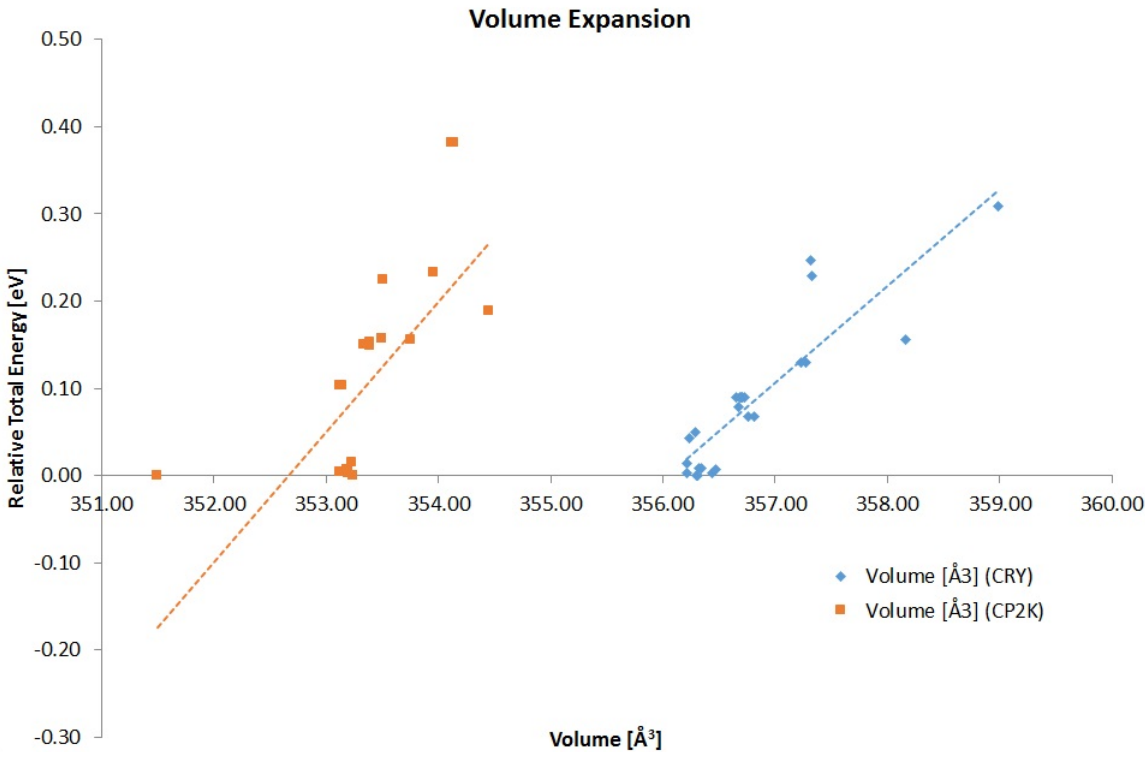

Figure 5.4: Volume expansion for CRYSTAL and CP2K calculated pure structures of topaz-OH.

mixed basis set of CP2K, there is still very good agreement between the two codes.

5.3.2 Fractional Coordinates

The CRYSTAL calculated fractional coordinates for the pure fluoro- and hydroxy-analogues of topaz ($Al_2SiO_4F_2$ and $Al_2SiO_4(OH)_2$ respectively) are given in Table 5.5 along with experimental literature data taken from Northrup *et al.* [18]. The agreement between literature and computational fractional coordinates is good, with $< 0.5\%$ difference for structural atomic positions. However, discrepancies increase for atomic positions in the F/OH solid solution. In addition, with the reduced symmetry caused by the H atoms, the structural O are able to relax along the z-axis.

5.3.3 Bond Distances

The CRYSTAL calculated and literature experimental Al−X and Si−X bond distances (where X is an anion) of pure fluoro- and hydroxy- analogues of topaz ($Al_2SiO_4F_2$ and $Al_2SiO_4(OH)_2$ respectively) are given in Table 5.6. The percentage difference between computational and experimental distances are also given for

(a) Lattice Parameter a

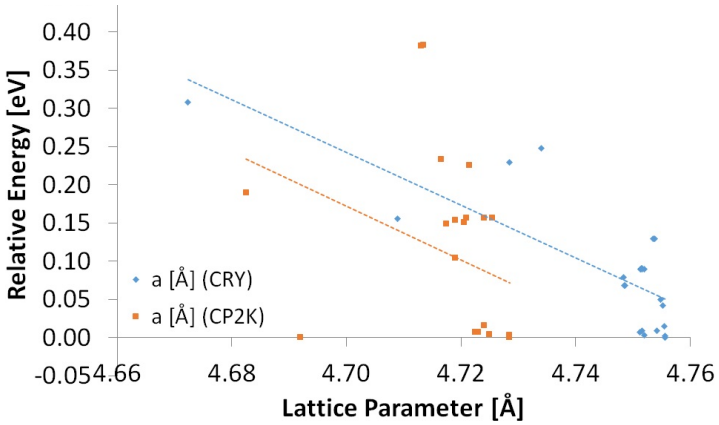

(b) Lattice Parameter b

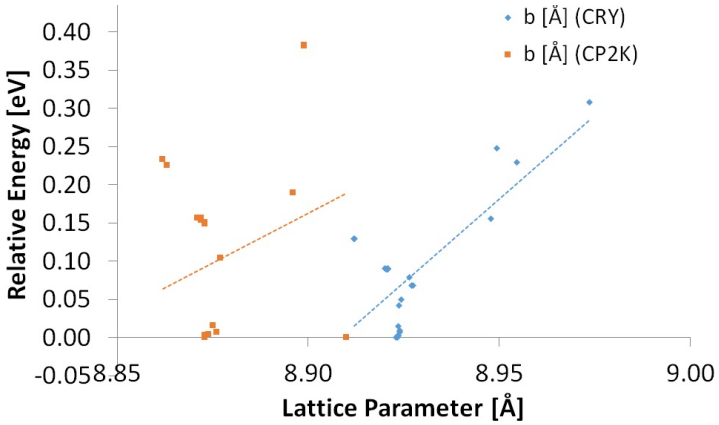

(c) Lattice Parameter c

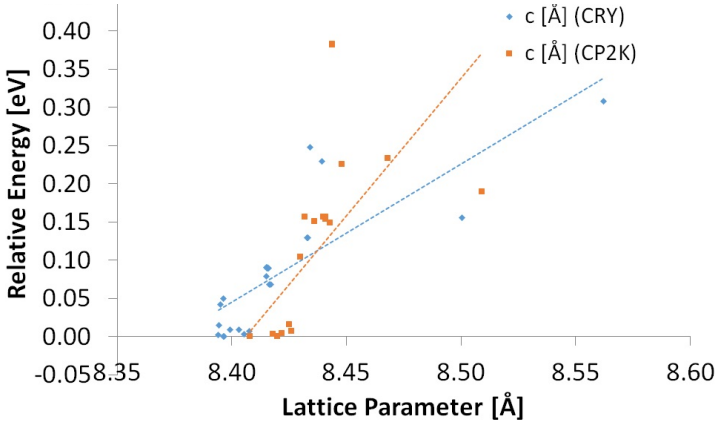

Figure 5.5: Lattice parameter expansion for CRYSTAL and CP2K calculated pure structures of topaz-OH.

	Reference [18]			CRYSTAL		
	x	y	z	x	y	z
(a) $Al_2SiO_4F_2$						
Al	0.90303	0.1309	0.08283	0.900938	0.129820	0.083745
Si	0.39723	0.94035	0.25	0.395366	0.939846	0.250000
O1	0.7036	0.0321	0.25	0.701190	0.032600	0.250000
O2	0.4577	0.756	0.25	0.460899	0.755264	0.250000
O3	0.2101	0.9892	0.0924	0.207755	0.988765	0.092665
F	0.5982	0.2525	0.0561	0.600224	0.252202	0.052534
(b) $Al_2SiO_4(OH)_2$						
Al	0.90499	0.1321	0.07984	0.906275	0.131420	0.081896
Si	0.40189	0.94045	0.25	0.404571	0.941844	0.243502
O1	0.7104	0.0262	0.25	0.713833	0.026249	0.251072
O2	0.4439	0.7561	0.25	0.450219	0.757319	0.243279
O3	0.2141	0.9929	0.0943	0.214767	0.994231	0.088885
OH	0.5906	0.2507	0.0659	0.590966	0.253482	0.070849
H1$*$	0.443	0.199	0.088	0.428657	0.168075	0.079895
H2$*$	0.607	0.281	0.151	0.543705	0.279494	0.179347

Table 5.5: Fractional coordinates of pure (a) topaz-F and (b) topaz-(OH).
$*$ The H-sites are only partially occupied: the most stable structural configurations assign half the H to H1 and half to H1. All other atoms have 100% occupation.

each bond, and the majority of calculated bond distances are shown to be $< 1\%$ off the literature value. The bond distance that less well reproduced by calculation, i.e. $> 1\%$ difference to experimental values, is the $Al{-}O2_{struct.}$ in topazOH. The bond could be due to the increased separation between anionic layers in the *dhcp* structure of topaz to accommodate more atoms.

The variation in Al−F/OH bond length as a function of the F/OH content in topaz is shown in Figure 5.6. As the concentration of [F] increases in topaz, the length of the bond Al−F/OH. The rate of decrease in bond length is more acute for Al−F than of Al−OH, but Al−OH bond lengths in any topaz analogue tend to be shorter than those of Al−F.

Table 5.7 records the calculated and literature experimental bond distances and angles of the H1 and H2 atomic positions within topaz-OH. The bond distances here show a greater discrepancy between computational and literature acquired bond distances. As already shown (in Section 5.2.2.1), only a single structural configuration of topaz can be used at any one time in a computational investigation to ensure a realistic model. The disadvantage that this approach presents is that long-range ordering of both F/OH groups and H positions occurs periodically, where experimentally there is little proof of this occurring. The bond distances acquired ex-

		Reference [18]		CRYSTAL			
		Topaz-F	Topaz-OH	Topaz-F	Δ[%]	Topaz-OH	Δ[%]
Al	O1	1.892	1.946	1.892	0.00	1.931	-0.77
	O2	1.896	1.945	1.901	0.26	1.972	1.39
	O3	1.885	1.922	1.901	0.85	1.912	-0.52
	O3a	1.896	1.926	1.890	-0.32	1.910	-0.83
	F/OH	1.798	1.834	1.810	0.67	1.844	0.55
	Fa/OHa	1.788	1.826	1.792	0.22	1.856	1.64
Mean	(Al−O)	1.892	1.935	1.896	0.21	1.931	-0.19
	(Al−(F/OH))	1.793	1.830	1.801	0.45	1.850	1.09
Si	O1	1.636	1.645	1.648	0.73	1.654	0.55
	O2	1.645	1.657	1.655	0.61	1.661	0.24
	O3 × 2	1.640	1.651	1.650	0.64	1.665	0.82
Mean	(Si−O)	1.640	1.651	1.651	0.67	1.660	0.54

Table 5.6: Bond distances [Å] Al−O and Si−O in pure topaz-F and topaz-OH (lowest energy configuration 21212121) calculated using CRYSTAL. Reference experimental data are taken from Northrup *et al.* [18].

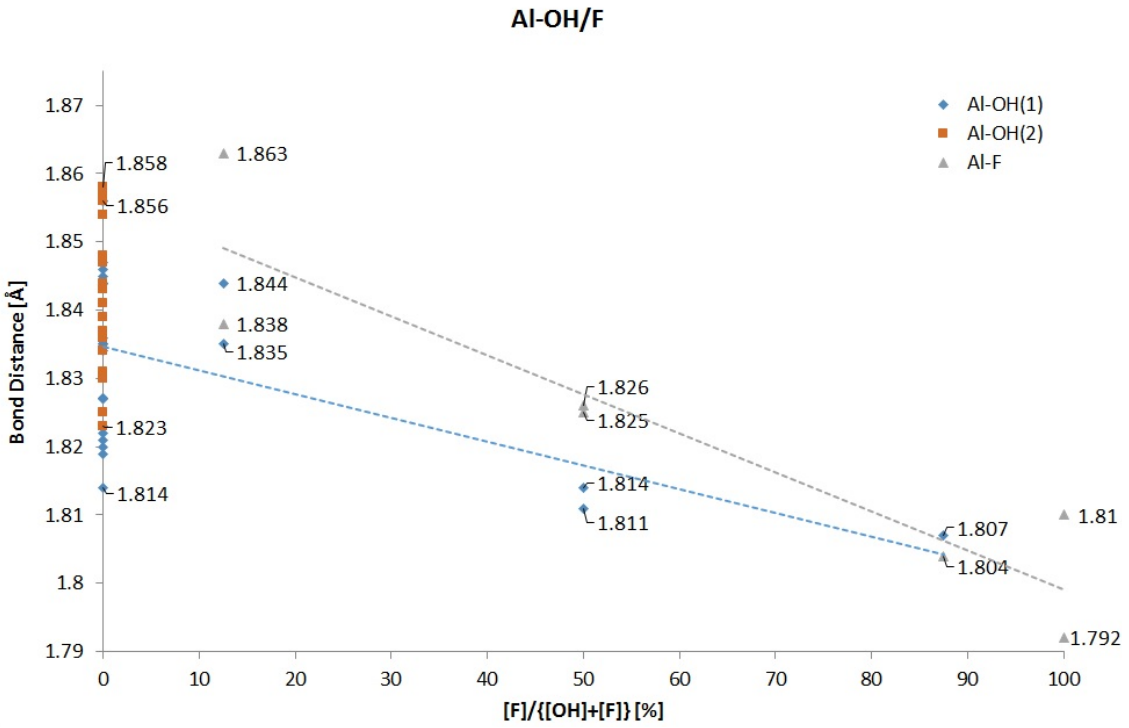

Figure 5.6: The Al−OH and Al−F bond distance in pure topaz of varying F/OH concentrations. (NB: bond lengths Al−OH labeled 1 and 2 do not refer here to the H1 and H2 positions, but simply to the 1^{st} and 2^{nd} longest Al−OH bond distance within one structure).

		Distance			Angle	
		Ref. [18]	CRYSTAL		Ref. [18]	CRYSTAL
H1	OHa	0.86	0.917			
	OHb	2.156	2.157	OHa-H1-OHb	112	103.232
	O1	-	2.334	OHa-H1-O1	-	92.274
	O2	2.330	2.961	OHa-H1-O2	129	123.553
	O3	2.129	2.6772	OHa-H1-O3	152	143.907
	Al	2.07	2.2487	Al-OHa-H1	109	103.598
	H2a	2.43	2.3185	Ala-OHa-H1	94	73.851
H2	OHb	0.78	0.9661			
	O1	2.459	2.4751	OHb-H1-O1	130	108.589
	O2	2.290	2.444	OHb-H1-O2	114	116.902
	O3	-	2.3931	OHb-H1-O3	-	92.260
	OHa	2.377	2.1818	OHb-H1-OHa	153	151.414
	Al	2.02	2.3197	Al-OHa-H2	92	106.257
	H1a	2.43	2.3185	Ala-OHa-H2	118	113.191

Table 5.7: Bond distances [Å] Al−O and Si−O in pure topaz calculated using CRYSTAL. Reference experimental data are taken from Northrup *et al.* [18].

perimentally may then the average culmination of many influencing configurations. The calculated bond distances given Table 5.7 were of the most stable CRYSTAL topaz-OH configuration 21212121.

5.4 Band Gaps and Density of States

The calculated band gaps for various compositions and configurations of pure topaz, with a range of F/OH disorder, are given in Table 5.8. The values indicate that defect-free topaz is colourless, as expected, for an ionic closed shell solid corresponds to a large band gap insulator. The configurational disorder does effect the band gap, for up to ∼0.3 eV, but it cannot by itself be responsible for optical observations in the visible. Defects are required for colour, but also configurational space is important and needs to be accounted for. For this reason, of the inherent structural disorder that exists within topaz, that MD-TD-DFT calculations were performed instead of static excited state TD-DFT calculations, in order to capture the time-average location of the H atom within the lattice framework, when the system was perturbed in order to model its excited state.

The band gap can be established experimentally by one of two ways: by taking twice the value of the activation energy, or by calculating from the optical absorption edge of the UV-Vis portion of the spectrum [132]. The absorption edge of topaz prior to irradiation, given by Nassau and Prescott [12], is reported as 0.3 μm (300 nm

or 4.13 eV). Taran *et al.* [2] reported the absorption edge in Brazilian topazes (mainly pink or Imperial topaz, i.e. an high Cr content) appears in the UV range at wavelength λ <350 nm (3.54 eV). Shlygin *et al.* gave the fundamental adsorption edge of blue topaz at T =10 K as ≈8.5 eV (146 nm) [133]. Jackson [134] quoted the band gap of pure colourless topaz-F ($Al_2SiO_4F_2$) as 3.35 eV (370 nm).

When comparing the electronic structure computational techniques with respect to calculating the band gaps of pure topaz, CRYSTAL band gaps fair 1.2 eV higher then those calculated using CP2K. The quality of geometry optimisation between classical and *ab initio* techniques was considered, by taking the optimised structure from the GULP lattice optimisations and initiating a single-point energy calculation in CRYSTAL: the settings for the single-point energy calculation were the same as for the CRYSTAL calculations, where the geometry had been allowed to relax. The resulting calculated band gaps for GULP were ∼1.8 eV smaller than those obtained with CRYSTAL after geometry optimisation (see Figure 5.7(a) and 5.7(b)).

A geometry optimisation technique that allows the system to properly relax and find the global minimum is important in predicting the correct electronic properties of the material. Using GULP primarily in a brute force approach to eliminate unfeasible structural configurations is valuable both in application and computational resource. It can not, however, be relied upon to predict geometrical structure, and more robust techniques need to be sourced instead.

Since CP2K performs geometry optimisations using FFT on a real-space grid, the code does not take advantage of simplifications of utilising symmetry operations in reciprocal, space as CRYSTAL does, and so the symmetry of configurations maybe lost or lowered during geometry reoptimisation of the CRYSTAL structures. Also, CP2K only samples a single k point and in order to increase this to a comparable amount as achieved with another code, the system size must be increased by the same amount as the k points sampled by the other code, i.e. for the number of k points sampled within the CRYSTAL Fock/KS matrix to be 8, an $8 \times 8 \times 8$ supercell would need to be constructed within CP2K in order to have the same level of k sampling. For the topaz system, a supercell of that size would have been too computationally expensive, and therefore the additional contributions to the bottom of the conduction band in the density of states as calculated by CP2K could be due to an unresolved structural optimisation.

In terms of trends, both CRYSTAL and CP2K band gaps follow the same trends: both increase as the F concentration in the F/OH disorder increases (see Figure 5.8(a)); and, comparing topaz-OH configurations, both decrease in relative stability as the band gap increases (see Figure 5.8(b)).

(a) GULP optimised structure, single-point calculation in CRYSTAL

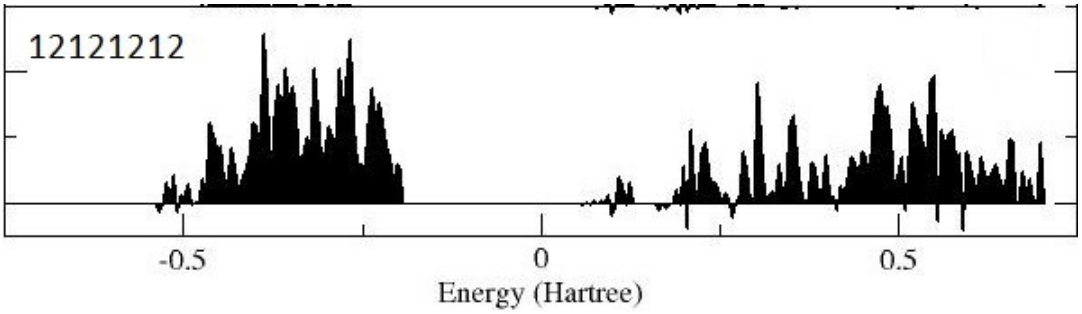

(b) CRYSTAL

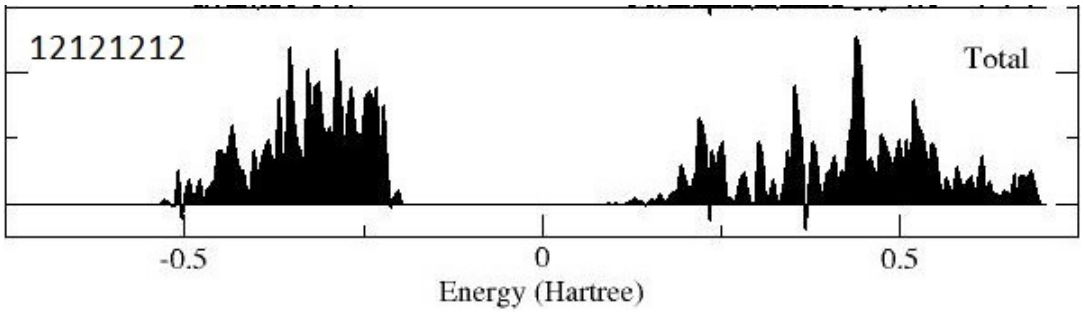

(c) CP2K

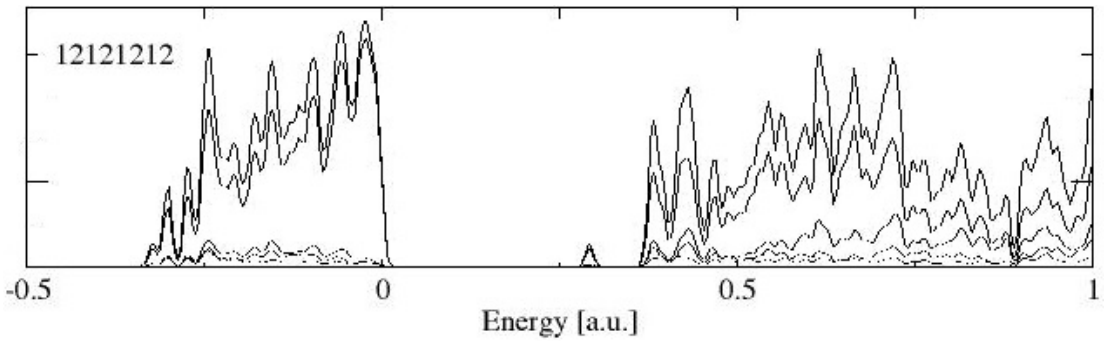

Figure 5.7: The total density of states for GULP, CRYSTAL and CP2K optimised 21212121 configuration of pure topaz-OH. (For the complete set of total densities of states for all 10 stable topaz-OH configurations for all three calculation methods are given in Appendix C.2).

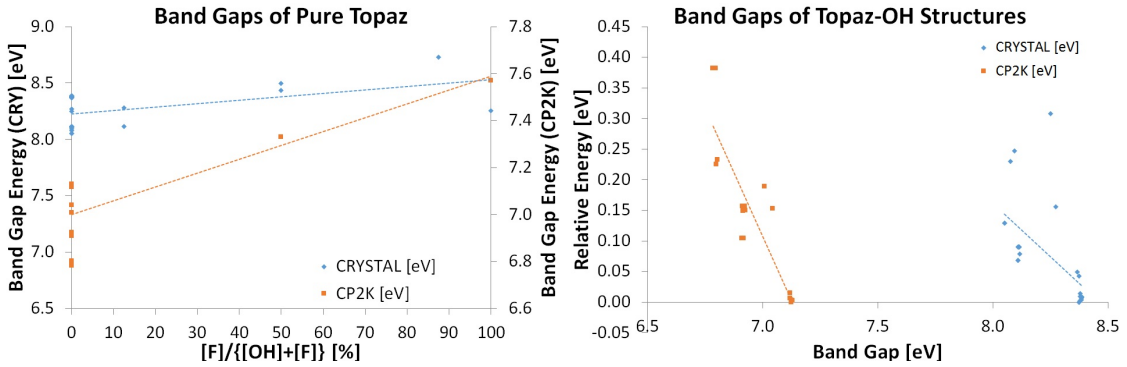

(a) Varying [F] (b) Varying Topaz-OH Configuration

Figure 5.8: Analysis of CRYSTAL and CP2K calculated pure topaz band gaps with respect to, (a) the F:OH composition, and (b) the relative energy of different topaz-OH configuration (total densities of states are given Appendix C.2.

5.5 Conclusion

In this chapter, we have explored the benefits of using the mean field approach and the method of sampling configurational space for dealing with structures that include atoms with fractional occupation. A labelling convention was introduced to distinguish between different structural and composition configurations in one unit cell of topaz. It was shown that, despite the computational cost, a brute force approach of sampling all configurational space of the different configurations of topaz-OH, this method is a better representation of the energetic stability and structural properties.

Structurally, the configurations with the greatest stability had the highest number of H1···H2 nearest neighbour interactions. Extending the method of sampling configurational space to topaz with F substitution on F/OH sites, the enthalpy of mixing was shown to be favourable for the case of maximum entropy (i.e. topaz-FOH 50 : 50 mixture). Structurally it was found that when the [F] increased, the H in the pairings of OH···F also preferred the H2 position.

The classical method of using pair potentials was found to be useful in reducing the total number of configurations to consider to just that were stable. Both *ab initio* methods compared favourably to literature data and predicted the same configurational structural stability and structural trends. The band gaps computed by all computational methods tended to overestimate the experimental mean, but are able to provide an interesting analysis of the impact of F/OH and configurational disorder on the band gap.

Composition	Band Gap [eV] Configuration	CRYSTAL	CP2K
$Al_8Si_4O_{16}(OH)_8$	11112222	8.093	6.784
	22221111	8.076	6.796
	11221122	8.051	6.799
	22112211	8.051	6.804
	11121222	8.112	6.915
	11212122	8.115	7.042
	12112212	8.109	6.917
	12221112	8.113	6.925
	21112221	8.111	6.921
	21221121	8.114	6.913
	22121211	8.109	6.909
	22212111	8.110	6.915
	12121212	8.374	7.129
	21212121	8.373	7.123
	12221111	8.118	7.123
	12212112	8.386	7.123
	21121221	8.385	7.119
	11121212	8.374	7.119
	11212121	8.380	7.119
	12111212	8.380	7.119
	12121112	8.380	7.119
	21212111	8.366	7.119
	11212112	8.385	7.123
	12111112	8.273	7.008
	11111111	8.250	-
$Al_8Si_4O_{16}(OH)_7F$	32221112	8.113	-
	31212122	8.279	-
$Al_8Si_4O_{16}(OH)_4F_4$	23323223	8.496	7.332
	23332321	8.437	-
$Al_8Si_4O_{16}(OH)F_7$	23333333	8.729	-
$Al_8Si_4O_{16}F_8$	33333333	8.256	7.570

Table 5.8: GULP, CRYSTAL and CP2K calculated band gap of pure topaz of varying composition and structural configuration.

Chapter 6

Pink Topaz

6.1 Introduction

As discussed in Section 2.6.1, the pink colouration of certain topazes is known to be due to chromium ion impurities found in trace quantities within the crystal structure, and isomorphically substituted onto aluminium octahedral sites. Some sources have argued that chromium-clustering is likely to occur within topaz [2, 52], and therefore the concentration of the chromium defect sites may have an effect on the colour observed.

In this chapter, a brief introduction into the interpretation electronic spectra of transition metal ions using group theory arguments is presented first, followed by the findings from our chromium-based defect calculations of topaz. Here our aim is to compare structural stabilities, defect formation energies, spin localisations, densities of state and optical absorption spectra, of chromium ion(s) substitution into three different topaz environments, using both ground and excited state computational methods. All calculations have been performed with DFT methods, using the PBE0 hybrid exchange functional.

6.2 Interpreting Electronic Spectra of Trivalent Chromium

In this section, we use arguments of group theory to understand the electronic spectra of trivalent chromium (Cr^{3+}), by understanding the symmetry of the bonds and orbitals of its crystalline environment within topaz, and predict which electronic transitions are symmetry allowed.

Spectra can be recorded in (*i*) emission and (*ii*) absorption; we only focus on

the latter. *Absorption spectra* are obtained when a substance is placed in the path of the light source, and the spectrometer records the portion of the electromagnetic spectrum the substance has absorbed. In the electronic spectra of transition metal complexes, there are two main types of electronic transitions: $d-d$ transfer, where electronic transfer occurs between d-orbitals of differing energy; and charge transfer (CT), which involves the transfer of electrons from the metal to the ligand and vice-versa.

The following principles need consideration when interpreting electronic absorption spectra:

i. The *Franck-Condon Principle* assumes that since electronic transitions occur within a very short time interval, the atoms in the structure will not have had time to appreciably relax, and therefore the same molecular configuration (and symmetry) still applies to the excited state as was present in the ground state at the point of absorption.

ii. *Selection rules* linked to local symmetry control the probability of transitions between different states to occur.

The effect of a crystal field on a free ion is to split the valence degenerate orbitals into a subset of different energies. In the case of a transition metal ion complex, the five degenerate d orbitals would be split according to the strength of the crystal field. The electronic transitions will occur in the spectral region spanning the near infrared, visible and UV region.

	cm^{-1}	nm	eV
Ultraviolet (UV)	$50000-26300$	$200-380$	$6.20-3.26$
Visible (Vis)	$26300-12800$	$380-780$	$3.26-1.59$
Near Infrared (NIR)	$12800-5000$	$780-2000$	$1.59-0.62$

The number of configurations electrons can adopt when populating orbitals are referred to as **microstates** and are labelled with the total angular and spin momentum of the occupied states. The process of obtaining the electron angular momenta associated with spin and orbital motions is called **Russell-Saunders coupling**.

The possible values of L (total orbital angular quantum number) and S (total spin quantum number) arising from the orbital and spin angular momenta of two individual electrons are

$$L = l_1+l_2, l_1+l_2-1, \cdots, |l_1-l_2| \text{ and } S = s_1+s_2, s_1+s_2-1, \cdots, |s_1-s_2|. \quad (6.1)$$

For the example of a d^3 electronic configuration, as for the Cr^{3+} ion, the possible values are $L = 6, 5, 4, 3, 2, 1, 0$ and $S = \frac{3}{2}, \frac{1}{2}$.

In a free ion, the microstates of a given electronic configuration have the same energy. However, in molecular and crystalline substances, the relative spatial ordering of electrons in the microstates corresponds to different energies [135].

The values of L and S are transformed into a term symbol,

$$^{(2S+1)}L \tag{6.2}$$

where values of L are denoted by an uppercase letter,

Total Orbital Momentum

L	0	1	2	3	4	5
	S	P	D	F	G	H

and the $(2S + 1)$ term is the spin **multiplicity**. Table 6.1 illustrates some of the lower energy term symbols arising from the d^3 configuration.

d^n	m_l					L	$(2S+1)$	Term	Crystal Field States/Substates
	2	1	0	-1	-2				
d^3	↑	↑	↑			3	4	^4F	$^4A_{2g}(F)$, $^4T_{1g}(F)$, $^4T_{2g}(F)$
d^3	↑	↑			↑	3	4	^4P	$^4T_{1g}(P)$
d^3	↑	↑↓				3	2	^2G	$^2A_{1g}(G)$, $^2T_{1g}(G)$, $^2T_{2g}(G)$, $^2E_g(G)$
d^3	↑↓	↑				3	2	^2H	$^2E_g(H)$, $2 \times ^2T_{1g}(H)$, $^2T_{2g}(H)$

Table 6.1: The crystal field components of the ground and some excited states for the d^3 configuration. The term symbols for a free ion with $3d^3$ electronic configuration are ^4F, ^4P, $^2(H, G, F, D, D, P)$. Only the most relevant term symbols are provided here, along with their microstate (m_l) configuration and respective crystal field substates. Note all states have parity g as, even though some term symbols have a value for L other than 3, they all arise from a d orbital.

An octahedral crystal field environment splits the d orbitals into two subsets t_{2g} and e_g: analogously the term D splits into the states T_{2g} and E_g.[1] The F term splits into the states T_{1g}, T_{2g}, and A_{2g} (here the F term arises from d and not f orbitals, and in an octahedral environment the lowest state term is A_{2g}) and so forth [136, 137].

Hund's rules can be used to determine the term symbol with the lowest energy (or the ground state term). These are as follows:

i. the term with the greatest multiplicity, i.e. the highest value of S, has the lowest energy;

[1]Here, upper case nomenclature signifies the states and lower case the orbitals

ii. the greatest value for the total orbital angular quantum number L, i.e. where the orbitals are filled with highest possible positive values of m_l first, has the lowest energy;

For the d^3 configuration of a trivalent chromium, the lowest energy is term ^4F, since it has the highest value for the spin multiplicity ($S = 4$) and for L.

The other terms possible from the d^3 configuration, ^2H, ^2G, ^2F, $2 \times ^2 D$ and ^2P (some of which are shown in Table 6.1), are possible excited states. Of these, the most important is ^4P [137]. Not all energy levels arising from term symbols are observed in the electronic spectra as electronic transitions are bound by selection rules (see Section 6.2.1). An illustration of the microstates of octahedral Cr^{3+} is given in Figure 2.13(c).

6.2.1 Selection Rules and Intensities

When an electron transitions from one state into another, defined by wave functions ψ_i and ψ_j, the strength of coupling is measured by the *transition dipole moment*, which is defined by the integral

$$P = \int \psi_f P \psi_i d\tau \tag{6.3}$$

where P is the perturbation that causes the electronic transition. In the case of UV-Vis spectra, this is the electronic dipole moment μ. Hence the probability of the transition, proportional to its intensity in the measured spectrum is

$$\boldsymbol{\mu} = \int \psi_f \boldsymbol{\mu} \psi_i d\tau \tag{6.4}$$

A large dipole moment corresponds to an intense transition and zero dipole moment corresponds to a forbidden one.

In spectroscopy, *allowed* transitions correspond to transitions with a nonzero transition dipole moment, and consequently nonzero absorption band intensity. *Forbidden* transitions occur in spectra for complexes where the symmetry may have lowered from that previously assumed. Selection rules define which transitions are allowed and forbidden. Since μ is the electronic dipole (1^{st} order tensor), group theory arguments indicate that the selection rules ate UV-Vis spectra are $\Delta S = 0$, $\Delta L = \pm 1$.

6.2.1.1 Spin Selection Rules

Electronic transitions between states with differing multiplicity are forbidden.
The orientation of electronic spins cannot change for a spin-allowed transition, the result of incident electromagnetic radiation, i.e.

$$\Delta S = 0 \tag{6.5}$$

For example ${}^4A \rightarrow {}^4T$ is allowed, but ${}^4A \nrightarrow {}^2T$ is forbidden.

6.2.1.2 The Laporte Selection Rule

If a molecule has centre of symmetry, then electronic transitions can not occur within the same p or d sub-shell.
In other words, a change in parity must accompany transitions for centrosymmetric complexes.

$$g \leftrightarrow u \quad g \nleftrightarrow g \quad u \nleftrightarrow u \tag{6.6}$$

Since orbitals s, p, d and f have parities g, u, g and u, there must be a change in the orbital momentum quantum number l to satisfy the Laporte selection rule, i.e.

$$\Delta L = \pm 1 \tag{6.7}$$

For centrosymmetric octahedral complexes, the $d - d$ ligand-field transitions have parity $g - g$ and so therefore forbidden. This accounts for their relatively weak intensities compared with CT bands that correspond to the transition from a d AO of the metal to an empty p state on the anions . The relaxation of the Larporte selection rule occurs when the centre of symmetry inversion is slightly destroyed, either by intrinsic asymmetry of the structure or by a vibration that distorts the i centre. In any case, a $d - d$ transition that is Laporte-forbidden tends to be more intense than a transition that is spin-forbidden.

6.2.2 Optical Spectra of Trivalent Chromium

The t_{2g}^3 is the expected ground state electronic configuration for a d^3 complex in an octahedral crystal field environment. The spectra of topaz containing trivalent chromium contain two bands with intermediate intensities at about 410 and 580 nm (see Figure 2.13(b)). These are the HOMO-LUMO $d - d$ transitions of the chromium(III) metal ion in the complex. The difference in energy between these

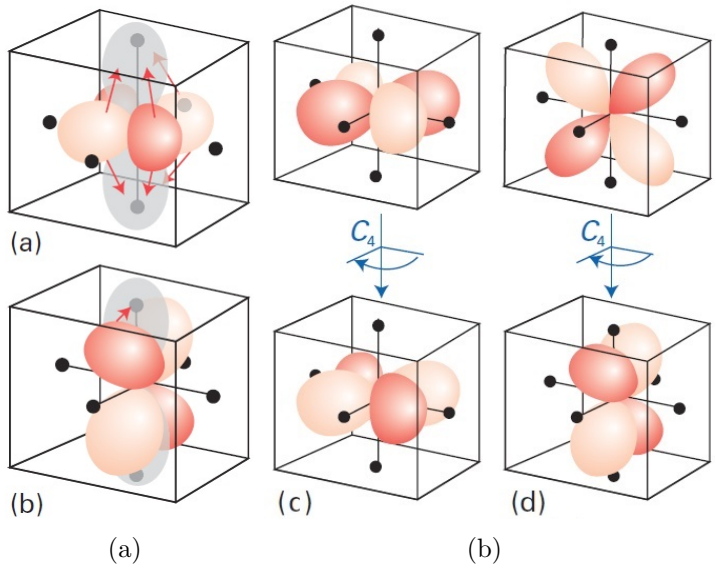

Figure 6.1: Molecular orbital arguments to explain the two $d-d$ electronic absorption bands in the UV-Vis spectra. (a) and (b) show the reallocation of electron density accompanying the two transitions $d_{xy} \rightarrow d_{z^2}$ and $d_{zx} \rightarrow d_{z^2}$ respectively. (c) and (d) represent the d_{xy}, and the d_{xz}/d_{yz} being transformed into a negative of itself and one of the other d-orbitals, respectively, under the C_4 operation of the O_h point group. Figures reproduced from reference [135].

two spectroscopic bands can be explained using molecular orbital theory.

These absorption bands have energies close to 3 eV, which corresponds to the typical ligand-field splittings in transition metal complexes [135]. The excitation can therefore be identified as $t_{2g}^3 \rightarrow t_{2g}^2 e_g^1$. This can be achieved by an electron transferring from one of the three degenerate t_{2g} orbitals, d_{xy} or d_{yz} or d_{zx}, to one of the two degenerate e_g orbitals, d_{z^2} or $d_{x^2-y^2}$. Comparing two of these type transitions, the $d_{xy} \rightarrow d_{z^2}$ and $d_{zx} \rightarrow d_{z^2}$ transitions for instance, the increase in electron-electron repulsion in the former is much greater than in the latter: since the relocation of an electron from the xy-plane to the z-axis increases the electron density of an already electronically populated orbital direction; whereas an electron transferring from the zx-plane to the z^2-axis is simply a redistribution of an electron that already populates that direction (see Figure 6.1(a)) [135]. The other orbital transitions fall into one of these two groups, and therefore there is a split, by the presence of electron-electron repulsion, into the components of the ligand-field transition with different energies.

The ground state spectroscopic term ^4F splits into $^4T_{1g}$, $^4T_{2g}$ and ^4A_g states in an octahedral ligand-field environment. These symbols are the irreducible representation of the O_h point group; A_g indicates the totally symmetrical ground state for three electrons in each of the t_{2g} orbitals.

The terms symbols arising from the excited quartet states of $t_{2g}^2 e_g^1$ and $t_{2g}^1 e_g^2$ are

$^4T_{1g}(F)$ and $^4T_{2g}(F)$, and $^4T_{1g}(P)$ respectively [135, 137].

$$\begin{array}{ll} (t_{2g})^3(e_g)^0: & {}^4A_{2g}(F),\ {}^2E_g(G),\ {}^2T_{1g}(G),\ {}^2T_{2g}(G) \\ (t_{2g})^2(e_g)^1: & {}^4T_{1g}(F),\ {}^4T_{2g}(F),\ {}^2T_{2g}(H) \\ (t_{2g})^1(e_g)^2: & {}^4T_{1g}(P) \end{array}$$

Therefore, the three bands observed in the spectrum of Cr^{3+} are $^4A_{2g}(F) \rightarrow^4 T_{1g}(F)$ (υ_1) and $^4A_{2g}(F) \rightarrow^4 T_{2g}(F)$ (υ_2) for the $t_{2g}^3 \rightarrow t_{2g}^2 e_g^1$ spin allowed transition, and $^4A_{2g}(F) \rightarrow^4 T_{1g}(P)$ (υ_3) for the $t_{2g}^3 \rightarrow t_{2g}^1 e_g^2$ spin allowed transition. When the octahedral symmetry of the Cr^{3+} complex is lowered, the spin allowed band splits into two components. The $^4A_{2g}(F) \rightarrow^4 T_{1g}(P)$ generally occur within the UV-Vis region of the spectra [137].

6.3 Chromium Substitution in Topaz

As discussed in Section 2.6.1, trace quantities of substitutional Cr^{3+} are responsible for the pink colour of Imperial topazes, which are stabilised by substitution into lattice sites rather than interstitial positions. In topaz, there are only two possible cationic sites: the octahedral Al^{3+} site and the tetrahedral Si^{4+} site. It has been shown by Jackson and Valerio [62] that chromium(III) substitution onto octahedral aluminium sites is energetically favourable to substitution onto tetrahedral silicon sites. This investigation of chromium-based defects in topaz only considers the case where chromium isomorphically substitutes onto aluminium sites.

The isomorphic substitution of a chromium(III) ion (Cr^{3+}) onto the octahedral site of a structural aluminium ion (Al^{3+}) yields a charge neutral defect, whose formation reaction can be written as:

$$[AlO_4(OH,F)_2]^{7-} + Cr^{3+} \longrightarrow [Cr^{\times}_{Al}O_4(OH,F)_2]^{7-} + Al^{3+} \tag{6.8}$$

The octahedral environment yields a high spin $t_{2g}^3 e_g^0$ stable electronic configuration for Cr^{3+}. Hence, we first examine if different OH/F octahedral substitutions around the Cr^{3+} ion affect the electronic energy levels of the d orbital, and consequently the energy of $d-d$ electronic transitions. All defect calculations are performed using three composition analogues of topaz (topaz-OH, topaz-FOH and topaz-F), in order to best represent all the different environments of Cr^{3+} within the topaz crystal. In the case of the $Cr^{\times}_{Al}$ isomorphic defect substitution this is more significant, since two of the six ligands in the octahedral complex are the interchange-

able fluor/hydroxy species. Therefore, there are three different coordination environments to consider for the chromium complex ($[Cr^{\times}_{Al}O_4(OH)_2]^{7-}$, $[Cr^{\times}_{Al}O_4(OH,F)]^{7-}$ and $[Cr^{\times}_{Al}O_4F_2]^{7-}$). We aim to understand to what extent the different coordination environments promote stabilisation, and alter band structure and UV-Vis properties.

Cluster model calculations of chromium defect ions in pink topaz, as introduced by references [2, 52], suggested that chromium ions form stable clusters after migration promoted by annealing or other conditions. We have therefore considered both isolated Cr^{3+} ions and pairs of Cr^{3+} in adjacent Al sites to compare stability and electronic properties of these cases.

6.3.1 Labeling Convention

The substitution of two chromium(III) ions into the topaz structure generates two further variables to consider in addition to the chemical composition of the host topaz structure. These are the relative position of the two chromium(III) ions within the host crystal structure, and the relative spin orientation of the two ions.

Regarding the structural configuration of the two adjacent chromium ions, after the first chromium substitution onto the aluminium site with fractional coordinates $(-0.297, 0.369, -0.418)$ is accomplished, there are four other octahedral aluminium sites immediately surrounding the primary defect site (see Figure 6.2(a)). Of these four secondary sites, two are *edge-sharing* octahedra linked by structural oxygens, and two are *corner-sharing* octahedra linked by the interchangeable F/OH groups. Edge-sharing chromium octahedra are labeled **ES1** and **ES2** with fractional coordinates $(-0.299, 0.365, -0.077)$ and $(-0.203, -0.369, 0.418)$ respectively, whilst corner-sharing octahedra are labeled **CS1** and **CS2** and have fractional coordinates at $(-0.049, 0.135, 0.423)$ and $(0.450, 0.135, 0.423)$ respectively (see Figure 6.2(b)).

In the case of topaz-OH and topaz-F, the choice of linking ions for corner-sharing chromium octahedra is simple, there is only one choice in either case. For the mixed-anion topaz-FOH, however, we need to further consider whether the two octahedra occupied by Cr are linked via F^- or OH^- ion. For the low energy configuration 23323223 (see Section 5.2.3) selected to form the pure topaz-FOH supercell prior to chromium ion defect substitution, in the **CS1** structural configuration the chromium octahedra are linked via a F^- ion; and in the **CS2** configuration, the linkage is via an OH^- species.

In respect to the spin coupling between the two Cr^{3+} ions, each with high-spin d^3 ($S = 4$) state, the two neighbouring Cr ions can couple in a ferro- or antiferromagnetic fashion. We identify them with **P** (i.e. $Cr(\uparrow\uparrow\uparrow)Cr(\uparrow\uparrow\uparrow)$) and **A** (i.e. $Cr(\uparrow\uparrow\uparrow)Cr(\downarrow\downarrow\downarrow)$) to indicate parrallel or antiparallel spins.

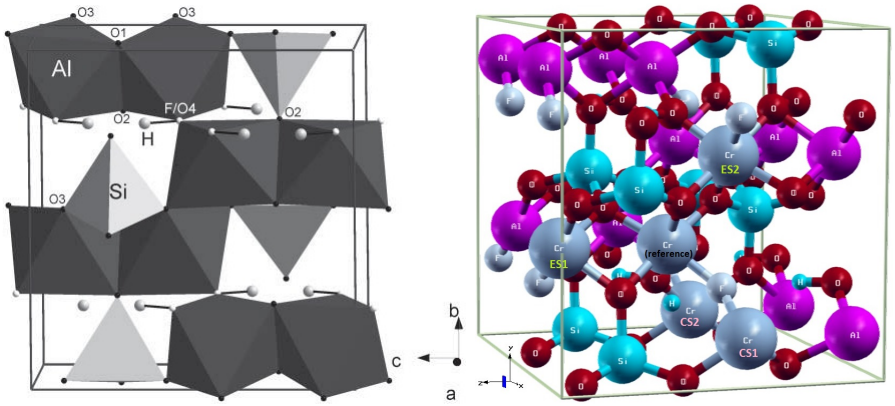

(a) (b)

Figure 6.2: Figures (a) highlights the anion linkages between octahedra and tetrahedra in a single unit cell of topaz, as given in reference [138]; and (b) depicts a supercell of topaz-FOH containing the primary chromium(III) defect (labeled *reference* in black) and four additional secondary chromium sites , adjacent to the first. Two of the secondary substitution sites are *edge-sharing* octahedra (in green and labeled **ES1** and **ES2**), and the other two are *corner-sharing* octahedra (in pink and labeled **CS1** and **CS2**).

To summarise, for the single isomorphic substitution of a chromium(III) ion into the supercell ($2 \times 1 \times 1$) structure of topaz ($Al_{15}Cr^{\times}_{Al}Si_8O_{32}(OH,F)_{16}$) there are 3 chromium defect systems considered here, i.e. one for each of the three base lattices, topaz-OH, topaz-FOH and topaz-F; for the double chromium(III) system there are 24 defect configurations to consider, i.e. the four unique structural configurations (**ES1**, **ES2**, **CS1** and **CS2**), plus two spin configurations (**P** and **A**), and three F:OH concentrations (0 : 100, 50 : 50 and 100 : 0). For a double chromium defect the structural and electronic configuration labels we employ to distinguish the different configurations at a given F:OH concentration are: **A-CS1**, **A-CS2**, **A-ES1**, **A-ES2**, **P-CS1**, **P-CS2**, **P-ES1** and **P-ES2**.

6.4 Defect Formation Energy

The defect formation energy equations employed here to calculate the isomorphic substitution of a single or double chromium(III) defect into the topaz supercell structure, are given by the reactions

$$Al_{16}Si_8O_{32}(OH,F)_{16} + \tfrac{1}{2}\,Cr_2O_3 \longrightarrow Al_{15}Cr^{\times}_{Al}Si_8O_{32}(OH,F)_{16} + \tfrac{1}{2}\,Al_2O_3, \quad (6.9)$$

and

$$Al_{16}Si_8O_{32}(OH,F)_{16} + Cr_2O_3 \longrightarrow Al_{14}(Cr^{\times}_{Al})_2Si_8O_{32}(OH,F)_{16} + Al_2O_3. \quad (6.10)$$

A fully optimised corundum structure of Al_2O_3 and Cr_2O_3 has been used, the latter in the ferromagnetic state: they both used the same calculation set up, basis sets and functional as in the defect calculations.

The defect formation energies are calculations as

$$\begin{aligned}\Delta H_f(\mathrm{Cr}) =& E_{tot}(\mathrm{Al_{15}Cr^{\times}_{Al}Si_8O_{32}(OH,F)_{16}}) + \tfrac{1}{2}E_{tot}(\mathrm{Al_2O_3}) \\ &- E_{tot}(\mathrm{Al_{16}Si_8O_{32}(OH,F)_{16}}) - \tfrac{1}{2}E_{tot}(\mathrm{Cr_2O_3}),\end{aligned} \tag{6.11}$$

and

$$\begin{aligned}\Delta H_f(2\,\mathrm{Cr}) =& E_{tot}(\mathrm{Al_{14}(Cr^{\times}_{Al})_2Si_8O_{32}(OH,F)_{16}}) + E_{tot}(\mathrm{Al_2O_3}) \\ &- E_{tot}(\mathrm{Al_{16}Si_8O_{32}(OH,F)_{16}}) - E_{tot}(\mathrm{Cr_2O_3}).\end{aligned} \tag{6.12}$$

6.4.1 Formation Energy of Isolated Chromium(III) Defect

The calculated defect formation energies (Equation 6.11) from this investigation are reported in Table 6.2, and compared with the earlier study by Jackson and Valerio [62]. Their method of calculation was to use interatomic potentials within the GULP code, together with computational reference data for an Cr^{3+} substitution onto an Al^{3+} site, provided by reference [62] where effective potentials were employed within the GULP code [60] via a Mott-Littleton approach [59] to perform lattice energy minimisations. The substitution energy of Cr^{3+} at the Al^{3+} site was calculated by Jackson and Valerio [61, 62] in two alternative ways; in one, referred to as the substitution energy, they employed the energy of isolated Cr^{3+} and Al^{3+}; while in the solution energy considers Al^{3+} and Cr^{3+} in binary fluoride lattices, corresponding to the chemical process $\mathrm{CrF_3 + Al_{Al} \longrightarrow Cr_{Al} + AlF_3}$, whose energy is calculated as

$$E_{sol}(\mathrm{Al^{3+} \rightarrow Cr^{3+}}) = -E_{latt}(\mathrm{CrF_3}) + E_{subs}(\mathrm{Al^{3+} \rightarrow Cr^{3+}}) + E_{latt}(\mathrm{AlF_3}). \tag{6.13}$$

Here $E_{latt}(\mathrm{CrF_3})$ and $E_{latt}(\mathrm{AlF_3})$ represent lattice energies for the metal fluoride solids AlF_3 and Al^{3+}.

The calculated defect energies for both *ab initio* and classical approaches (given in Table 6.2) suggest that the substitution of Cr^{3+} onto an Al^{3+} site in topaz is a favourable process. In addition, the data also suggests that the substitution of Cr^{3+} into a F-rich environment is more favourable than into an OH-rich or a mixed FOH topaz environment. The trend is not reproduced in the CP2K calculations. The CP2K calculations suffers from only sampling the single k-point used by the code. This is despite implementing recommended calculation criteria for flourinated

Defect Formation Energy, ΔH_f(Cr), [eV]				
Lattice	CRYSTAL	CP2K	E_{sol} [62]	E_{sub} [62]
Topaz-OH	-2.86	-2.44	1.62	-4.93
Topaz-FOH	-2.70	-2.34	-	-
Topaz-F	-3.96	-2.41	-2.27	-6.02

Table 6.2: Defect formation energy for a single isomorphic chromium(III) substitution into a $2 \times 1 \times 1$ supercell of topaz, calculated according to Equation 6.11, using the computational codes CRYSTAL and CP2K and literature data [62].

system in CP2K [139]. The numerical values for the CRYSTAL and CP2K calculated defect formation energies, for the topaz-OH and topaz-FOH analogues, are, however, in good qualitative agreement.

6.4.2 Formation of Chromium(III) Clusters

The formation energy of two Cr^{3+} in neighouring sites is given in Table 6.3. We define the stabilisation energy (ΔH_{stab}) as the energy of such Cr^{3+} dimers relative to two isolated Cr^{3+} sites in the same host lattice (defined by the F/OH ratio):

$$\Delta H_{Stab.}\left((2\mathrm{Cr}) - 2\,(\mathrm{Cr})\right) = \Delta H_f(2\,\mathrm{Cr}) - 2\Delta H_f(\mathrm{Cr}). \tag{6.14}$$

Negative values for $\Delta H_{stab.}$ indicate stability in forming the Cr^{3+} cluster relative to the isolated Cr^{3+} defect formation.

The most significant effect on the energy of Cr^{3+} clusters is the number of F/OH ions in the coordination environment of the two Cr^{3+} ions. Only in the fully hydrated topaz ($Al_2SiO_4(OH)_2$) do we observe negative values of $\Delta H_{stab.}$, corresponding to a stability in forming Cr^{3+} clusters. By increasing the F content, the clustering of Cr^{3+} ions becomes progressively less stable, and is not expected to occur at all in F-only topaz analogues (cf energies of +1.4 eV for the formation of Cr^{3+} clusters given in Table 6.3). This finding confirms the experimental models of Taran *et al.* [2] and Tarashchan *et al.* [52], who suggested the clustering of chromium ions in topaz occurs predominantly in hydroxyl rich topaz analogues (see Section 2.7).

Both the relative position and spin of the two Cr^{3+} ions has an effect the energy. These factors are also interconnected via an atomic bridge. For Cr^{3+} ions to form a cluster, the ions must be either bonded or connected via bridging species X. The bridging angle, Cr−X−Cr, determines the type of preferred electronic exchange. In the CS1 chromium(III) cluster configuration in the OHrich topaz analogue, the

		Solution Energy, [eV] $\Delta H_f(2\,\mathrm{Cr})$				Stabilisation Energy, [eV] $\Delta H_{Stab.}\,((2\mathrm{Cr}) - 2\,(\mathrm{Cr}))$			
		(**P**)		(**A**)		(**P**)		(**A**)	
Config.	[F] %	CRY	CP2K	CRY	CP2K	CRY	CP2K	CRY	CP2K
ES1	0	-5.6958	-4.7644	-5.7654	-4.8910	0.0270	0.1197	-0.0426	-0.0069
ES1	50	-5.3563	-4.5709	-5.4009	-4.6258	0.0494	0.1051	0.0049	0.0501
ES1	100	-6.5769	-4.1348	-6.6189	-4.1817	1.3363	0.6933	1.2943	0.6464
ES2	0	-5.6681	-4.9167	-5.7687	-4.9539	0.0547	-0.0326	-0.0459	-0.0698
ES2	50	-5.3563	-4.5865	-5.3908	-4.6041	0.0494	0.0895	0.0150	0.0718
ES2	100	-6.4598	-4.1369	-6.4904	-4.1607	1.4534	0.6912	1.4228	0.6674
CS1	0	-5.7630	-	-5.7464	-	-0.0402	-	-0.0236	-
CS1	50	-5.3805	-	-5.3816	-	0.0252	-	0.0242	-
CS1	100	-6.4878	-	-6.4921	-	1.4254	-	1.4211	-
CS2	0	-5.7026	-	-5.7196	-	0.0202	-	0.0032	-
CS2	50	-5.3747	-	-5.3870	-	0.0311	-	0.0188	-
CS2	100	-6.4878	-	-6.4916	-	1.4254	-	1.4216	-

Table 6.3: Formation energy of chromium(III) clusters in topaz as a function of the [F]:[OH] composition, structural configuration and spin, calculated with CRYSTAL and CP2K. Here P refers to parallel spins (i.e. ferromagnetic coupling scheme) and A to antiparallel spins (i.e. antiferromagnetic coupling scheme)

ground state is ferromagnetic; in all the other cases the two Cr ions are stable when the d^3 spins are antiparallel (A).

Further clustering of two Cr^{3+} ions with antiparallel spin is more stable when they are in edge-sharing (ES) than corner-sharing octahedra, i.e. when they are closer. Results obtained with both CRYSTAL and CP2K reproduce these trends and yield comparable numerical values of the stabilisation energy. Further structural details of the crystalline environment are given in Section 6.5.2.

6.5 Structural Analysis

The aim in this section is to demonstrate the structural changes that effect the energy of a single and double chromium ion isomorphic substitution in topaz.

6.5.1 Lattice Parameters

Tables 6.4 and 6.5 document the calculated lattice parameters (a, b and c) and cell angles (α, β and γ), and cell volumes and densities of single and double chromium(III) substitution into the three topaz analogues, topaz-OH, topaz-FOH and topaz-F, from CRYSTAL and CP2K calculations respectively. For reference, the calculated cell dimensions of the pure topaz analogues for the respective calculation methods are also given.

CRYSTAL									
[F] [%]	config.	a [Å]	b [Å]	c [Å]	alpha	beta	gamma	Volume [$Å^3$]	Density [$g\,cm^{-3}$]
(a) Pure Topaz (Supercell $2 \times 1 \times 1$)									
0		9.511	8.924	8.394	90.00	89.85	90.00	712.45	3.355
50		9.381	8.912	8.407	90.00	90.00	90.00	702.86	3.438
100		9.359	8.813	8.447	90.00	90.00	90.00	696.65	3.507
(b) Single Chromium(III) Substitution									
0		9.524	8.942	8.411	89.95	89.84	89.94	716.30	3.395
50		9.397	8.929	8.421	89.99	89.95	89.96	706.58	3.479
100		9.373	8.834	8.467	90.01	89.98	89.99	701.02	3.544
(c) Double Chromium(III) Substitution with Parallel Spin									
0	P-ES1	9.544	8.955	8.424	89.93	89.84	89.96	720.01	3.435
0	P-ES2	9.537	8.962	8.429	89.92	89.82	89.90	720.42	3.433
0	P-CS1	9.544	8.953	8.425	89.96	89.86	89.96	719.89	3.435
0	P-CS2	9.541	8.955	8.427	89.96	89.86	89.96	720.04	3.435
50	P-ES1	9.416	8.946	8.428	89.95	89.92	90.02	709.95	3.521
50	P-ES2	9.414	8.945	8.439	89.99	89.97	89.96	710.59	3.518
50	P-CS1	9.407	8.948	8.438	89.97	89.93	89.98	710.29	3.519
50	P-CS2	9.406	8.950	8.438	89.98	89.90	89.99	710.25	3.519
100	P-ES1	9.386	8.856	8.481	90.00	90.00	90.02	704.87	3.584
100	P-ES2	9.387	8.852	8.484	90.01	89.96	89.98	704.91	3.584
100	P-CS1	9.382	8.853	8.486	90.00	90.02	89.99	704.83	3.584
100	P-CS2	9.382	8.853	8.486	90.00	89.98	90.00	704.81	3.584
(d) Double Chromium(III) Substitution with Antiparallel Spin									
0	A-ES1	9.547	8.957	8.418	89.93	89.84	89.98	719.80	3.436
0	A-ES2	9.537	8.960	8.429	89.89	89.81	89.91	720.26	3.434
0	A-CS1	9.544	8.953	8.425	89.97	89.86	89.97	719.96	3.435
0	A-CS2	9.542	8.955	8.427	89.96	89.86	89.95	720.02	3.435
50	A-ES1	9.418	8.948	8.430	89.98	89.91	90.01	710.34	3.519
50	A-ES2	9.416	8.943	8.438	89.96	89.97	89.97	710.46	3.518
50	A-CS1	9.408	8.948	8.439	89.97	89.93	89.98	710.38	3.519
50	A-CS2	9.406	8.949	8.438	89.99	89.90	89.98	710.35	3.519
100	A-ES1	9.388	8.857	8.475	90.00	90.00	90.03	704.73	3.585
100	A-ES2	9.388	8.849	8.484	89.97	89.94	89.99	704.76	3.584
100	A-CS1	9.383	8.853	8.486	90.00	90.02	89.99	704.86	3.584
100	A-CS2	9.382	8.853	8.486	90.00	89.98	90.00	704.84	3.584

Table 6.4: CRYSTAL calculated lattice parameters (a, b, and c), cell angles (α, β, and γ), volumes, and densities of (a) pure topaz, and (b) single and (c)-(d) double chromium(III) (parallel and anti-parallel spins respectively) isomorphic substitution defect(s) in the $2\times1\times1$ topaz supercell.

The cell dimensions of the topaz doped with chromium(III) are shown to expand, as expected, following the incorporation of a larger ion. Cell volumes vary by between 0.53-0.63% and −0.38-0.94%, and 0.48-0.58% and 0.32-0.72% for pure to single Cr substitution and a single to double Cr topaz system for CRYSTAL and CP2K calculations respectively. The variation in cell expansions depending largely on the F/OH content.

The expansion of the cell in terms of the individual lattice parameters, a, b and c, show that for either the single or double chromium(III) topaz system the b lattice parameter (parallel to the y-axis) undergoes the greatest expansion, followed by either the c (parallel to z-axis) or the a (parallel to x-axis) lattice parameter. Structurally, this corresponds to the distance between anion layers and the Crankshaft chains of AlO_4(OH,F) octahedra and SiO_4 tetrahedra in topaz, which both lie perpendicular to the b lattice parameter (see Section 2.2), expanding their separation, since this direction has the weakest inter-atomic interactions and the lowest energy barrier.

CP2K								
[F] [%]	config.	a [Å]	b [Å]	c [Å]	alpha	beta	gamma	Volume [$Å^3$]
(a) Pure Topaz								
0		9.451	8.886	8.421	90.00	89.92	90.00	707.19
50		9.384	8.910	8.408	89.86	90.00	90.00	703.00
100		9.282	8.776	8.399	89.94	90.04	89.98	684.08
(b) Single Chromium(III) Substitution								
0		9.477	8.886	8.446	89.98	90.12	90.06	711.31
50		9.338	8.879	8.450	89.98	89.92	90.01	700.60
100		9.316	8.781	8.441	89.99	90.00	90.00	690.51
(c) Double Chromium(III) Substitution with Parallel Spin								
0	P-ES1	9.460	8.914	8.494	89.99	90.19	89.95	716.32
50	P-ES1	9.358	8.898	8.456	89.97	90.09	90.02	704.09
100	P-ES1	9.329	8.799	8.459	89.99	90.01	90.01	694.32
(d) Double Chromium(III) Substitution with Antiparallel Spin								
0	A-ES1	9.490	8.908	8.454	90.04	90.14	89.95	714.65
50	A-ES1	9.361	8.898	8.448	89.98	90.06	90.01	703.72
100	A-ES1	9.331	8.803	8.452	89.97	90.01	90.02	694.23

Table 6.5: CP2K calculated lattice parameters (a, b, and c), cell angles (α, β, and γ), and volumes of (a) pure topaz, and (b) single and (c)-(d) double chromium(III) (parallel and anti-parallel spins respectively) isomorphic substitution defect into the $2 \times 1 \times 1$ supercell of topaz.

6.5.2 Bond Distances

The localised structural changes to topaz incorporating one or two chromium(III) ion defects can be seen by examining the bond distances, bond angle, interatomic

separations at the octahedral site where isomorphic substitution occurred.

6.5.2.1 Single Chromium(III) Substitution

Table 6.6 compares the bond distances of the six ligands involved in the chromium octahedral complex and compares them to the same bond distances in the pure topaz analogue system. The Cr−F/OH bond distances undergo a greater expansion then the Cr−O_{STRUCT} bond distances (between 3.7−5.0% change to 3.2−3.4% expansion for the bonds respectively), and increases with respect to the pure system more as the [F] content increases. The Cr−F bond distance in the topaz-FOH analogue increases significantly more than the Cr−OH distance.

[F]	(a) Pure Topaz											
0	Al-OH	1.844	Al-OH	1.856	Al-O1	1.931	Al-O2	1.972	Al-O3a	1.910	Al-O3b	1.912
50	Al-OH	1.813	Al-F	1.825	Al-O1	1.928	Al-O2	1.944	Al-O3a	1.883	Al-O3b	1.918
100	Al-F	1.810	Al-F	1.792	Al-O1	1.892	Al-O2	1.901	Al-O3a	1.890	Al-O3b	1.901
[F]	(b) Single Chromium(III) Substitution											
0	Cr-OH	1.917	Cr-OH	1.918	Cr-O1	1.998	Cr-O2	2.008	Cr-O3a	1.975	Cr-O3b	1.998
50	Cr-OH	1.886	Cr-F	1.922	Cr-O1	1.970	Cr-O2	1.989	Cr-O3a	1.957	Cr-O3b	2.002
100	Cr-F	1.897	Cr-F	1.886	Cr-O1	1.956	Cr-O2	1.962	Cr-O3a	1.957	Cr-O3b	1.964

Table 6.6: Bond distances for (a) pure and (b) a single chromium substitution in topaz.

Mulliken population analysis (see Table 6.7) indicated that as the [F] content increases in topaz, the amount of spin localised on the Cr^{3+} defect (see Figure 6.3) marginally decreases, and the remaining spin is redistributed onto the surrounding F ions. The increase in the Cr−F/OH bond distances from the pure analogue of topaz as the F content increases, i.e. +3.9% to +4.0% to +5.2% for OH-, FOH- and F-rich topaz respectively, can be attributed to the increased electron-electron repulsion of the same spin for neighbouring atomic species.

[F]	Single Chromium(III) Substitution Mulliken $\alpha - \beta$ Spin Analysis													
0	CR	2.970	O	-0.006	O	-0.004	O	0.002	O	0.000	O	-0.001	O	0.004
50	CR	2.962	O	0.002	F	0.006	O	-0.002	O	-0.001	O	0.003	O	0.002
100	CR	2.958	F	0.008	F	0.009	O	0.000	O	0.002	O	0.004	O	-0.003

Table 6.7: Mulliken analysis for the $\alpha-\beta$ spin on the chromium defect ion and the six surrounding ligands.

6.5.2.2 Double Chromium(III) Substitution

The bond distances Cr−$O_{struct.}$ and Cr−F/OH, defect separation distances Cr···Cr, and bridging angles Cr−(O/OH/F)−Cr for topaz containing clusters of two Cr^{3+} ions, are analysed here with respect to the stabilisation energy for introducing a

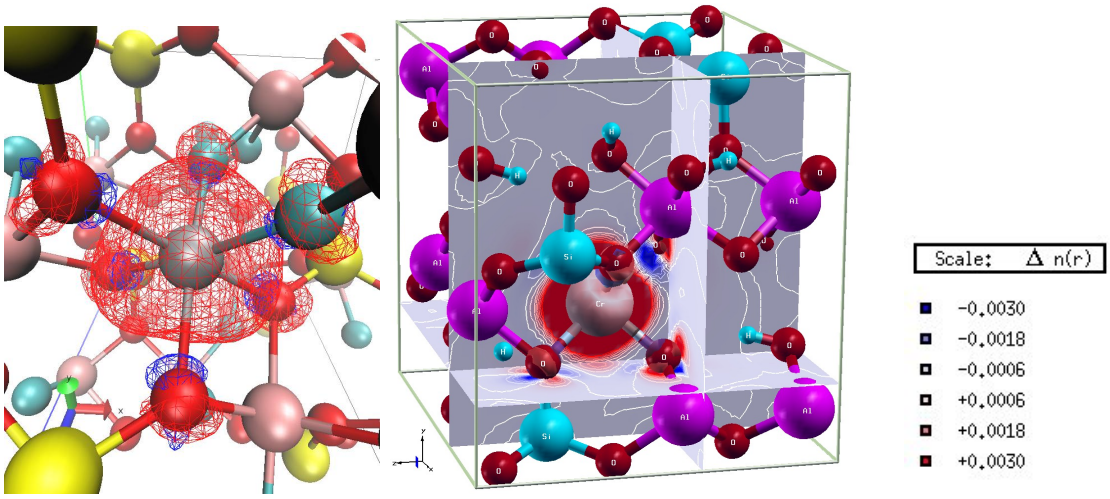

(a) CP2K (b) CRYSTAL (c) Isovalue scale (CRYSTAL)

Figure 6.3: Spin density of single substituted chromium in the topaz: (a) and (b) are CP2K and CRYSTAL calculated spin density projections onto the 3-dimensional topaz crystal geometry. The (c) chart conveys the isovalue colour scale used to distinguish spin density directions for the CRYSTAL calculation. Since the same spin localization pattern was observed across all three topaz compositions considered, only the spin density projection for topaz-OH has been included in this figure. Isothermal spin density were performed using an isovalue of 0.003.

secondary Cr^{3+} defect to the crystal structure (see Equation 6.14). Mulliken population analysis and isothermal $\alpha - \beta$ spin density plots are also included in Table D.1 (see Appendix D.2) and Figure 6.7 respectively.

Bond Distances Cr−$O_{struct.}$: Figure 6.4 shows the stabilisation energy as a function of the Cr−$O_{struct.}$ bond distance percentage expansion from the pure topaz crystal. Across the different topaz analogues sampled, the bond distance expansion increases with increasing F content. Between different configurations of the same composition, the Cr−$O_{struct.}$ bond distance decreases in all three analogues of topaz as the configuration becomes more stable in the antiferromagnetic scheme. Whereas in the ferromagnetic scheme, the Cr−$O_{struct.}$ bond distance increases as the configuration becomes more stable for topaz-OH and topaz-FOH, but decreases for topaz-F. As previously seen in the case of an isolated Cr ion in topaz (Section 6.5.2.1), the Mulliken population analysis for topaz with two Cr ions (see Table D.1) suggests that the topaz-OH analogue is much better at localising or containing the unpaired spin to only the defect Cr ion than analogues with an increased F content.

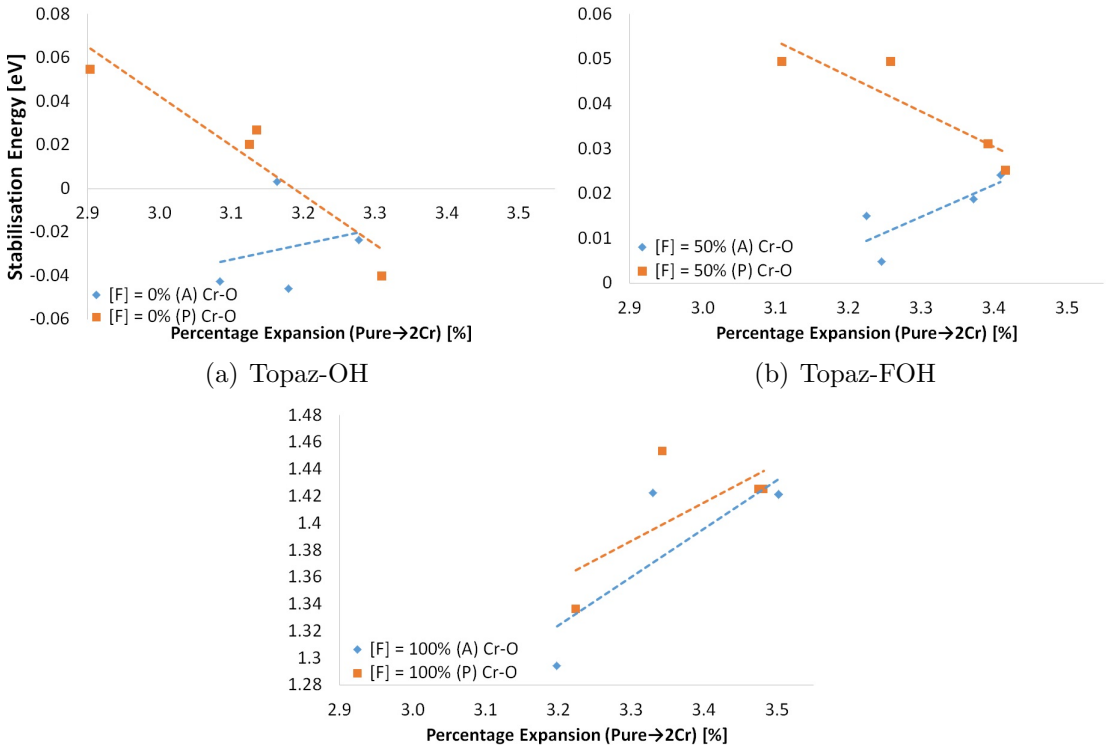

(a) Topaz-OH

(b) Topaz-FOH

(c) Topaz-F

Figure 6.4: The average bond distance percentage expansion between chromium and structural oxygens ($Cr{-}O_{struct}$), in systems (a) topaz-OH, (b) topaz-FOH and (c) topaz-F, going from the pure topaz crystal to accommodating two chromium ions.

Bond Distances Cr−F/OH: Figure 6.5 shows the Cr−F/OH bond distance percentage expansion when a pure topaz crystal incorporates two chromium ions in a substitution reaction. Once again, the Cr−F/OH bond expansion increases as the F content increases: the Cr−OH bond increases on average by $\sim 4\%$ and the Cr−F bond by $\sim 5\%$. Mulliken population analysis (see Table D.1) shows that when there are F^- ions present, there is also an increase in the delocalisation of unpaired d^3 spin from the Cr defect ion onto the F^- ion ligands (for visual representation of this characteristic, see Figure 6.7). Analogous to the single Cr^{3+} substitution in topaz, the increase in electron-electron repulsion resulting from the delocalised of unpaired defect spin, also increases bond lengths between the defect transition metal and the F/OH ions in the complex.

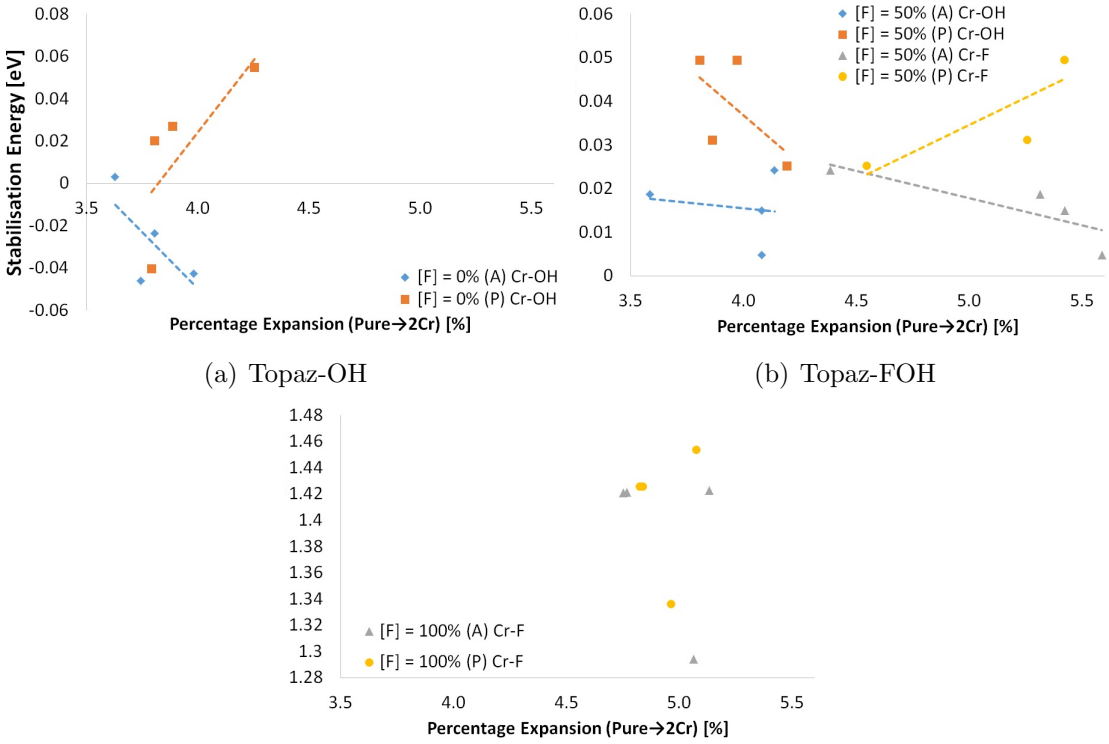

(a) Topaz-OH

(b) Topaz-FOH

(c) Topaz-F

Figure 6.5: Chromium and fluoro/hydroxyl bond distance percentage expansion (Cr−F/OH) in (a) topaz-OH, (b) topaz-FOH and (c) topaz-F, for a pure system going to a double chromium defect system.

Bond Distance for Atoms Linking Chromium Octahedra: Trends observed in the expansion of the bond distances for Cr−$O_{struct.}$ and Cr−F/OH, in Figures 6.4 and 6.5 respectively, are also observed for the bond distance for the atoms linking the chromium(III) octahedra, i.e. those involved in the bridging angles Cr−(O/OH/F)−Cr, given in Figure 6.6. Here the bond distance percentage expansion with respect to the analogue of topaz follows the following trend:

$$\text{Cr}-\text{O}_{\text{struct.}} < \text{Cr}-\text{OH} < \text{Cr}-\text{F}. \tag{6.15}$$

The ferromagnetic (i.e. parallel) electron spin configuration, which are generally less energetically stable, tends to display increased bond distances in comparison to its antiferromagnetic counterpart.

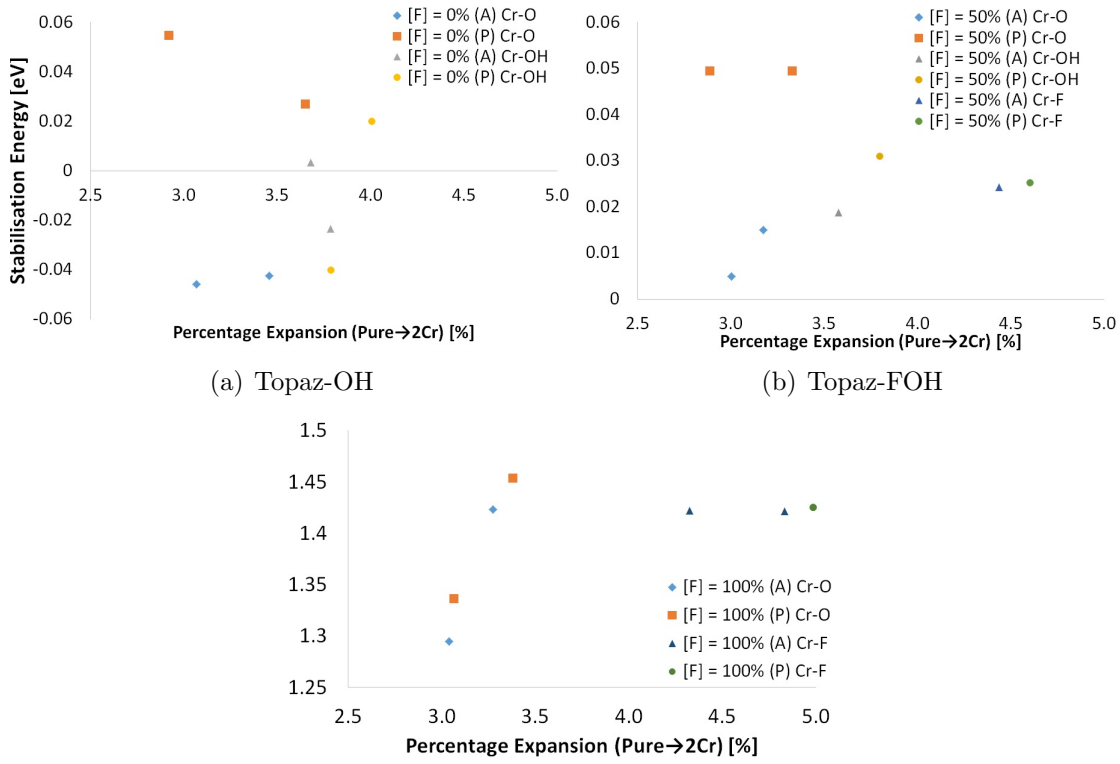

(a) Topaz-OH

(b) Topaz-FOH

(c) Topaz-F

Figure 6.6: Chromium octahedra linking oxygen Cr−O bond distance percentage expansion, from a pure system to a two chromium defect system, in the analogues (a) topaz-OH, (b) topaz-FOH and (c) topaz-F.

Interatomic Separation Cr···Cr and Bridging Angle Cr−(O/F/OH)−Cr: Table 6.8 shows the separation of two chromium(III) ions in adjacent lattice positions, and Table 6.9 shows the bridging angle Cr−(O/F/OH)−Cr between the two chromium defects (for reference, the equivalent angles in pure host and single chromium substituted topaz are also supplied). The separation between the two Cr defects decreases as the bridging-angle also decreases, bringing the two metal defects closer together.

The Cr···Cr separation is effected by both spin and structural configurations. Edge-sharing clusters with antiparallel spins (**A-ES**) have a smaller Cr···Cr separation then clusters with parallel spins (**P-ES**). Since there is no other atoms in the direct space between the two Cr ions in edge-sharing configurations, the defect separation is close enough for direct exchange electronic interaction to occur. Direct exchange is more favourable for the **A-ES** configuration (see Section 6.4.2). Qualitatively, this can be observed in the $(\alpha - \beta)$ isothermal spin density plots in Figures 6.7(a) and 6.7(b), where the contours of the spin density from the Cr defects can be observed to overlap.

Corner-sharing clusters have greater separations and consequently larger bridg-

ing angles when the Cr ions have antiparallel spins. According to the Goodenough-Kanamori rules of superexchange [140, 141], when cations that are next-to-nearest neighbours and coupled through the overlap of the covalent orbitals of a non-magnetic ion, if the bridging cation-anion-cation angle approaches 180° the favoured spin configuration is antiferromagnetic, and if it approaches 90° then a ferromagnetic configuration is preferred. Energetically we can apply the rules of superexchange corner-sharing Cr clusters, i.e. antiferromagnetic scheme is prefered, and direct exchange in edge-sharing Cr octahedra, i.e. ferromagnetic arranged spins are favoured. Larger bridging angles in the **A-ES** configurations are an attempt by the structure to increase the amount of superexchange possible.

The spin density plots of Figure 6.7 also highlight the spin coupling of the bridging atoms. In antiferromagnetic systems, the *p*-orbital of the bridging O^-/F^- anion is polarise, such that the opposite spin to the spin state of the Cr is available for coupling. In ferromagnetic systems, the *p*-orbital of the anion has to deform, so that covalent bonding can occur between itself and the Cr cation.

	Interatomic Cr···Cr Separation [Å]							
[F]	P-ES1	A-ES1	P-ES2	A-ES2	P-CS1	A-CS1	P-CS2	A-CS2
0	2.885	2.852	2.935	2.915	3.461	3.465	3.533	3.537
50	2.832	2.835	2.904	2.883	3.529	3.534	3.486	3.491
100	2.847	2.820	2.904	2.885	3.530	3.531	3.529	3.531

Table 6.8: The separation of two chromium defect ions.

6.6 Band Gap Analysis

In this section we discuss the calculated band gaps and density of states of chromium(III) transition metal defects in topaz.

6.6.1 Single Chromium Substitution

The band gaps and densities of states for the single chromium substitution in topaz are given in Table 6.10 and Figure 6.8 respectively for computational techniques CRYSTAL and CP2K. The densities of states indicate additional electronic states within the band gap which are due to the chromium defect. In the CRYSTAL density of states, the three t_{2g} levels can be made out at the top of the valence band for the alpha spins, and at the bottom of the conduction band the two e_g levels for the alpha spins. Similarly for the beta spins, the three and two t_{2g} and e_g levels respectively can be made out, but at much higher energies. The defect d^3

Cr−(O/F/OH)−Cr Angle [°]					
[F] [%]	Config.	ES (a)	ES (b)	Config.	CS
Pure Topaz					
0	(ES1)	94.98	95.16	(CS1)	136.40
50	(ES1)	95.80	94.73	(CS1)	142.91
100	(ES1)	95.85	95.28	(CS1)	147.53
0	(ES2)	96.90	96.90	(CS2)	138.79
50	(ES2)	95.59	97.62	(CS2)	139.82
100	(ES2)	97.30	97.30	(CS2)	147.53
Single Chromium Substitution					
0	(ES1)	93.36	93.93	(CS1)	132.06
50	(ES1)	94.54	93.66	(CS1)	137.97
100	(ES1)	94.81	94.305	(CS1)	143.59
0	(ES2)	95.92	95.82	(CS2)	139.06
50	(ES2)	94.65	96.28	(CS2)	139.17
100	(ES2)	96.70	96.35	(CS2)	143.72
Double Chromium Substitution					
0	A-ES1	91.06	91.69	A-CS1	130.36
0	A-ES2	94.53	94.53	A-CS2	136.62
0	P-ES1	92.21	92.79	P-CS1	130.09
0	P-ES2	95.25	95.25	P-CS2	135.66
50	A-ES1	91.71	91.14	A-CS1	135.64
50	A-ES2	93.28	94.93	A-CS2	136.05
50	P-ES1	91.70	91.09	P-CS1	134.88
50	P-ES2	94.10	95.74	P-CS2	135.11
100	A-ES1	92.57	92.26	A-CS1	140.01
100	A-ES2	94.80	94.80	A-CS2	139.91
100	P-ES1	93.67	93.13	P-CS1	139.46
100	P-ES2	95.56	95.56	P-CS2	139.41

Table 6.9: The angle between the two chromium defect ions: Cr−(O/F/OH)−Cr. For reference, the equivalent angles are given for pure topaz and topaz with a single Cr substitution.

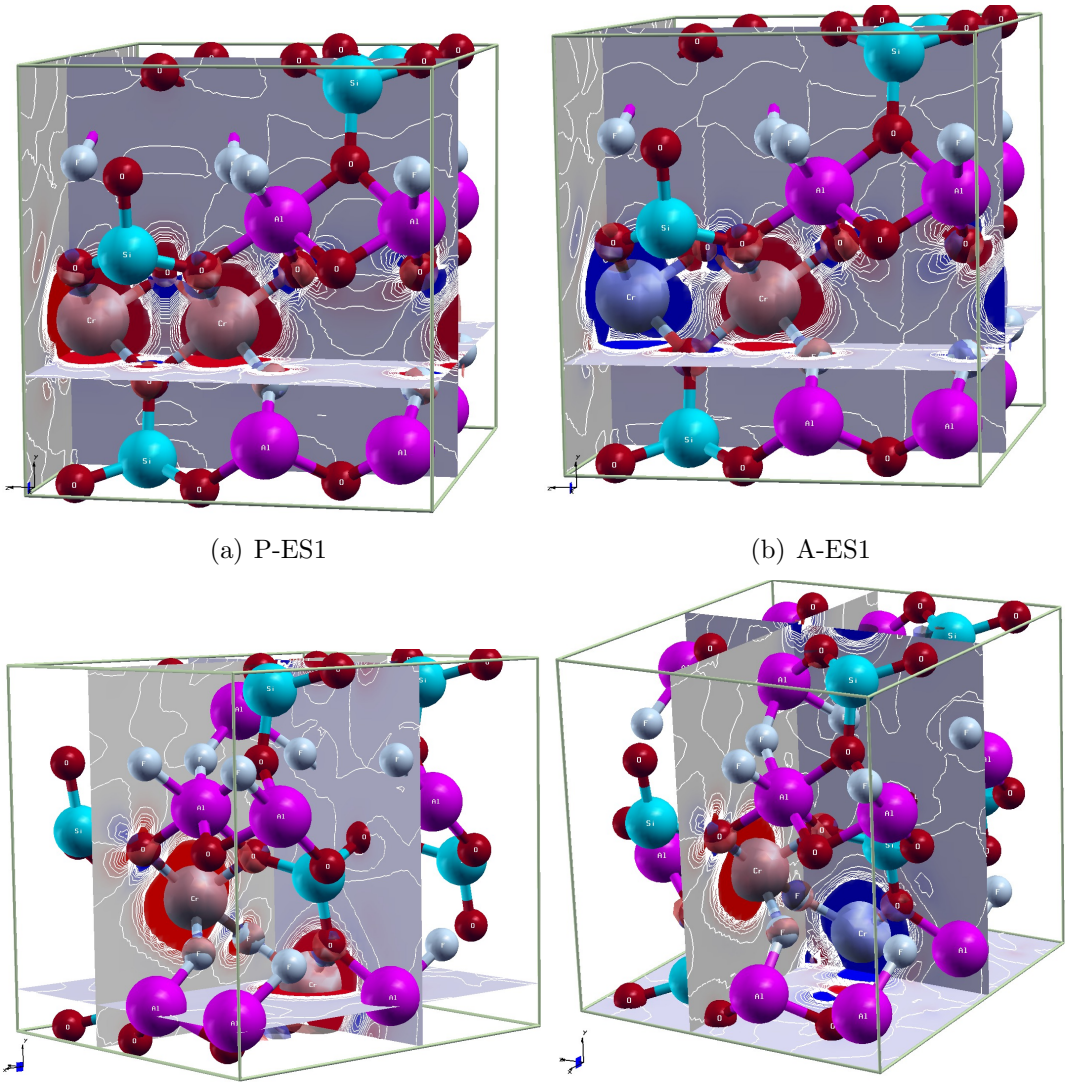

(a) P-ES1 (b) A-ES1

(c) P-CS2 (d) A-CS2

Figure 6.7: The $\alpha - \beta$ isothermal spin density plots for clustered chromium(III) from CRYSTAL calculations: (a) and (b) for configurations P-ES1 and A-ES1, and (c) and (d) for P-CS2 and A-CS2 respectively. Isothermal spin density were performed using an isovalue of 0.003. The corresponding isothermal chart is given in Figure 6.3(c). Isothermal spin plots for all configurations on the topaz-F host crystal are given in Appendix D.1.

electrons were placed in the alpha spin for the calculation and it is clear that the fundamental transition $t_{2g} \rightarrow e_g$ occurs between alpha spin statse. Similar band gap characteristics can be seen in the CP2K replicated density of states. The difference in energies for the $t_{2g} \rightarrow e_g$ transition for each of the Cr defect in topaz are too small to observe qualitatively, so Table 6.10 is included to compare the differences in the HOMO-LUMO transition for the pure analogues of topaz and with the introduction of a Cr defect.

The calculated minimum $d - d$ transition given in Table 6.10 shows an overestimation by the *ab initio* method, which can be expected when using large amounts of HF exchange. The band gaps for both the pure and Cr defected topaz lie outside the region of a visible electronic transition. The band gap, however, has shown to be reduced by the presence of the chromium(III) defect in topaz. On average, CRYSTAL calculated band gaps from pure topaz to a single chromium substitution fell by on average 1.9 eV and for CP2K by 1.5 eV. The amount the band gap reduces by is dependent on the topaz composition: largest reductions occur in topaz-FOH for both CRYSTAL and CP2K.

6.6.2 Double Chromium Substitution

The summary of the calculated band gaps for clusters of chromium, consisting of two Cr^{3+} ions in topaz, for all the electronic and structural configurations considered for the two defect ions in adjacent lattice positions, are given in Table 6.11. With the exception of the configuration A-ES2 for topaz-OH in CRYSTAL, the addition of a secondary chromium(III) defect ion into a topaz system already containing an isolated chromium(III) ion, has the effect of reducing the band gap and the energy required for the $t_{2g} \rightarrow e_g$ electronic transition further, then from pure topaz to a topaz system containing a single isolated Cr defect. The amount the band gaps reduces by, is 0.3 eV and 1.3 eV on average for CRYSTAL and CP2K calculated methods respectively. Although the overall trend predicted by both is the same, the 1.0 eV difference in the methods respective estimated band gap reduction for the scheme outlined in Equation 6.14, suggests that the k-point sampling of CP2K would need to be increased before further comparisons of band gap trends could be made. This would, however, require considerable computational resources to expand the unit cell twice more in each direction.

The amount by which the $d - d$ transition is altered depends again largely on the topaz composition, and the structural and electron configurations adopted. The antiferromagnetic scheme has a band gap between 0.1 and 0.6 eV larger than the ferromagnetic scheme, for any of the considered structural configurations, with the

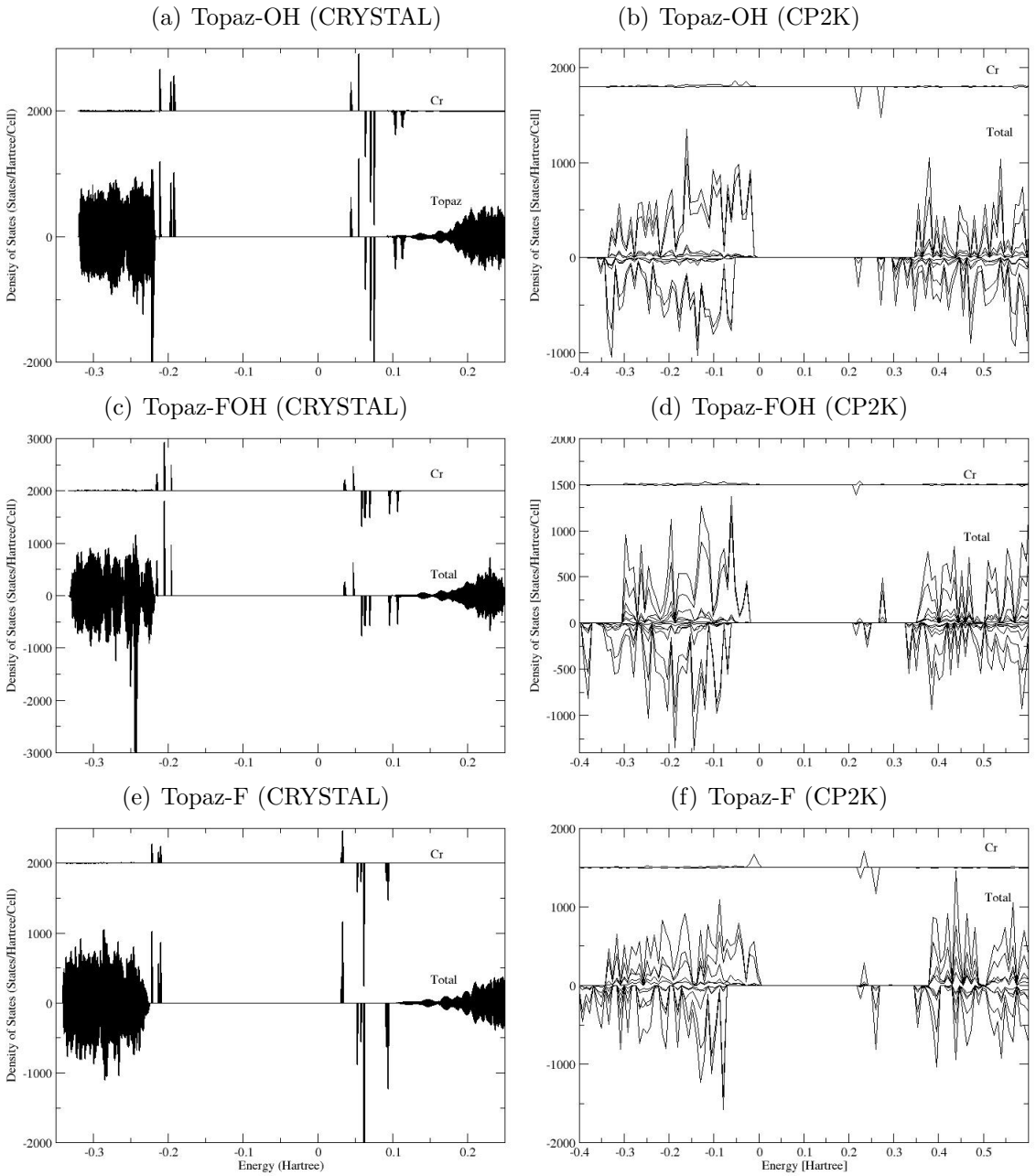

Figure 6.8: Density of states from CRYSTAL and CP2K calculations for a single chromium(III) substitution in topaz: (a) and (b) for topaz-OH, (c) and (d) for topaz-FOH, and (e) and (f) for topaz-F, for calculation methods repectively.

exception of **ES1** for topaz-FOH. For the energetically favoured configurations as found in Section 6.4.2, which are **P-ES** in OH-rich and **A-CS** in F-rich topaz, when chromium clusters form in an OH-rich topaz environment, the band gap is reduced considerably more than the lesser change experienced in a F-rich environment.

6.7 UV-Vis Analysis

In this section, we report the results of our MD-TD-DFT calculated UV-Vis spectra of isolated and clustered chromium(III) in topaz. We assign spectral features where possible with reference to literature experimental and computational data (additional reference spectral data provided in Appendix D.4).

6.7.1 Single Chromium Substitution

Following on from successful static ground state defect calculations, the optimised chromium(III) topaz system undergoes an energy perturbation, and the resultant fluctuating dipole moment is calculated as a function of time. Following a Fourier transform, the intensity as a function of the dipole moment is transformed into the intensity as a function of energy. Conversion from energy (eV) to wavelength (nm) produces the simulated absorption spectra via this method. Since topaz is orthorhombic, three separate simulations of the Cr defect topaz system, with the initial energy perturbation dipole directed parallel to one of the three axis, was required in order to produce one absorption spectrum: an already costly computational exercise made even more expensive.

To demonstrate the necessity for increased numbers of time steps in simulating UV-Vis absorption spectra, Figure 6.9(d) shows the evolution of the spectral peak resolution as the total number of MD steps propagated. As the total number of progressive MD steps increases, absorption intensities at lower energies are resolved, i.e. those with long wavelengths. Secondary to long simulations times are that if there are unforeseen errors in the simulation, such as the selection of the timestep causing noise in the spectrum, these can only be identified after large numbers of MD steps have already been simulated and peaks begin to be defined.

In Figures 6.10 and 6.11, the UV-Vis spectra of isolated and clustered chromium(III) substitution are given for all three topaz analogues studied for defect calculations. Absorption spectral features are difficult to identify, as firstly the absorption bands are not clearly defined, and secondly the method does not provide information regarding the energy or the spectroscopic states to or from which the electronic transitions occurs.

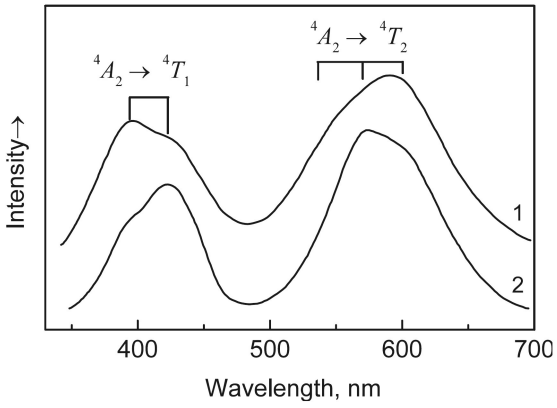

(a) Selective Ion Excitation

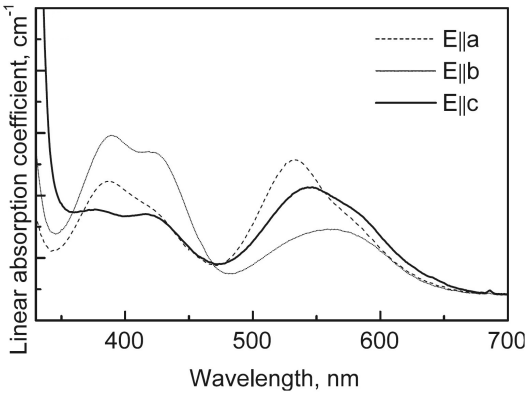

(b) UV-Vis

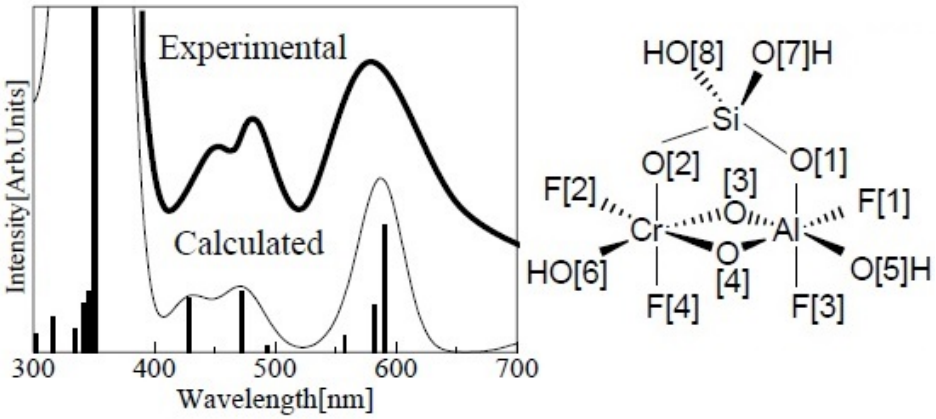

(c) CI method

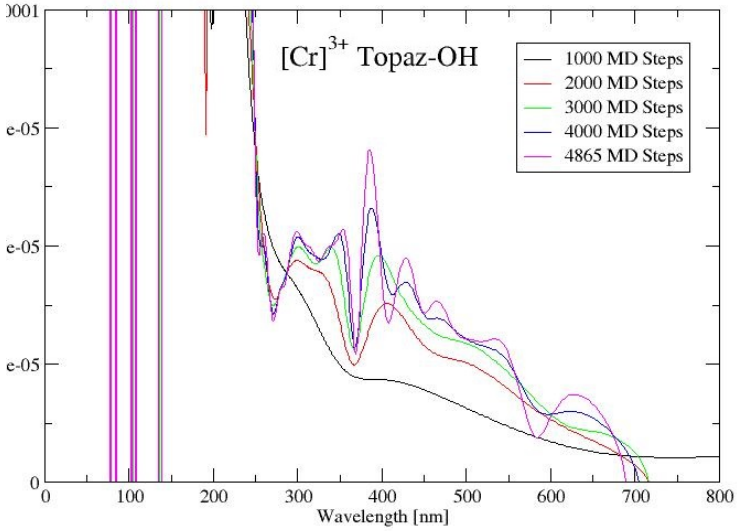

(d) MD-TDDFT

Figure 6.9: A comparison of experimental and computational literature UV-Vis absorption spectra of isolated chromium(III) in topaz: (a) shows the selective ion excitation spectra of an Cr^{3+} ion; (b) polarised experimental UV-Vis absorption spectra of pink topaz; (c) computationally obtained UV-Vis spectra in the CI method using the molecular model as shown to simulate the pink topaz crystal; and (d) the MD-TD-DFT computational method used here and showing the progression of peak development as a function of the accumulation of successive MD steps. (a) and (b) taken from reference [52] and (c) from [3].

(a) Cr^{3+} Topaz-OH

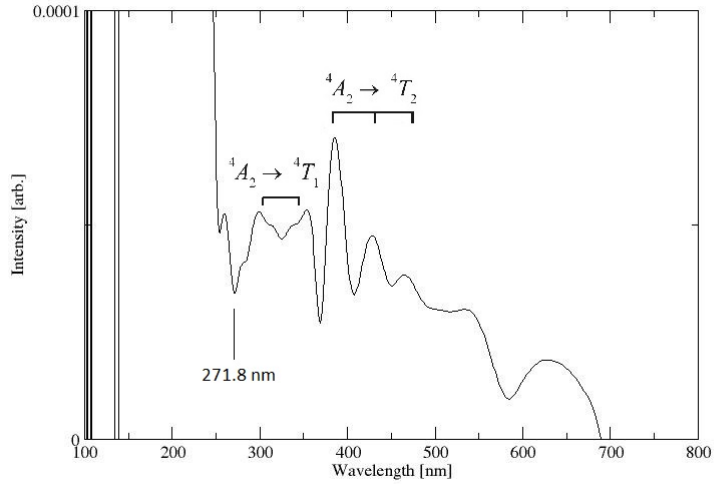

(b) Cr^{3+} Topaz-FOH

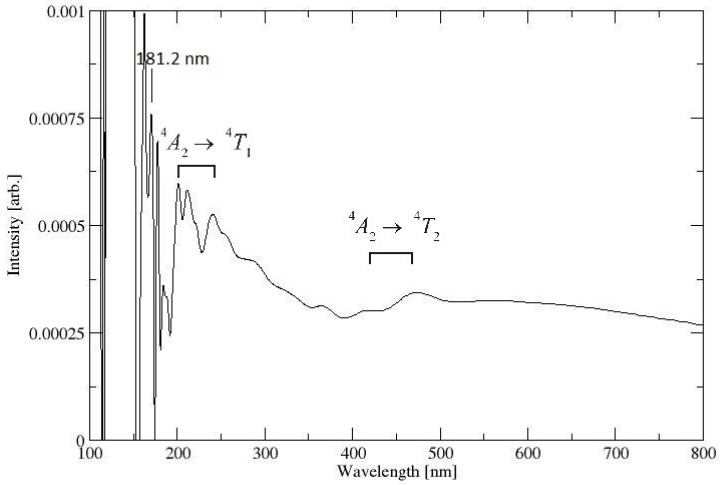

(c) Cr^{3+} Topaz-F

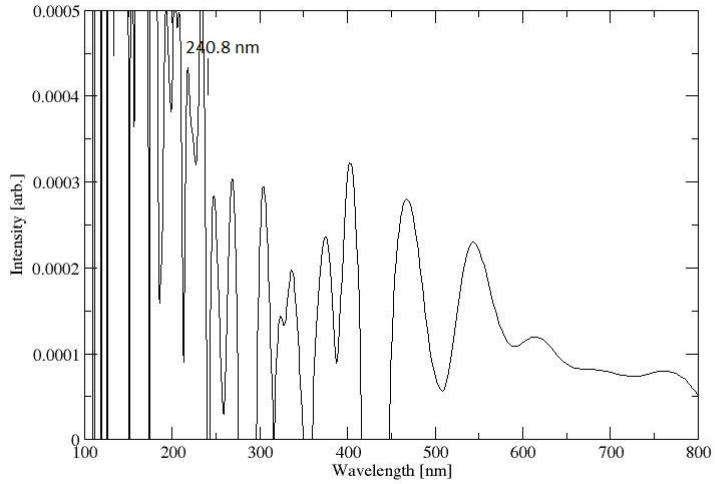

Figure 6.10: UV-Vis absorption spectra of single substituted chromium(III) in (a) topaz-OH, (b) topaz-FOH, and (c) topaz-F. The CT band is labelled (given again in Table 6.12) and the t_{2g}-e_g transitions have been assigned. The total number of MD steps simulated to generate each spectra are 4865, 5510, and 6006 respectively.

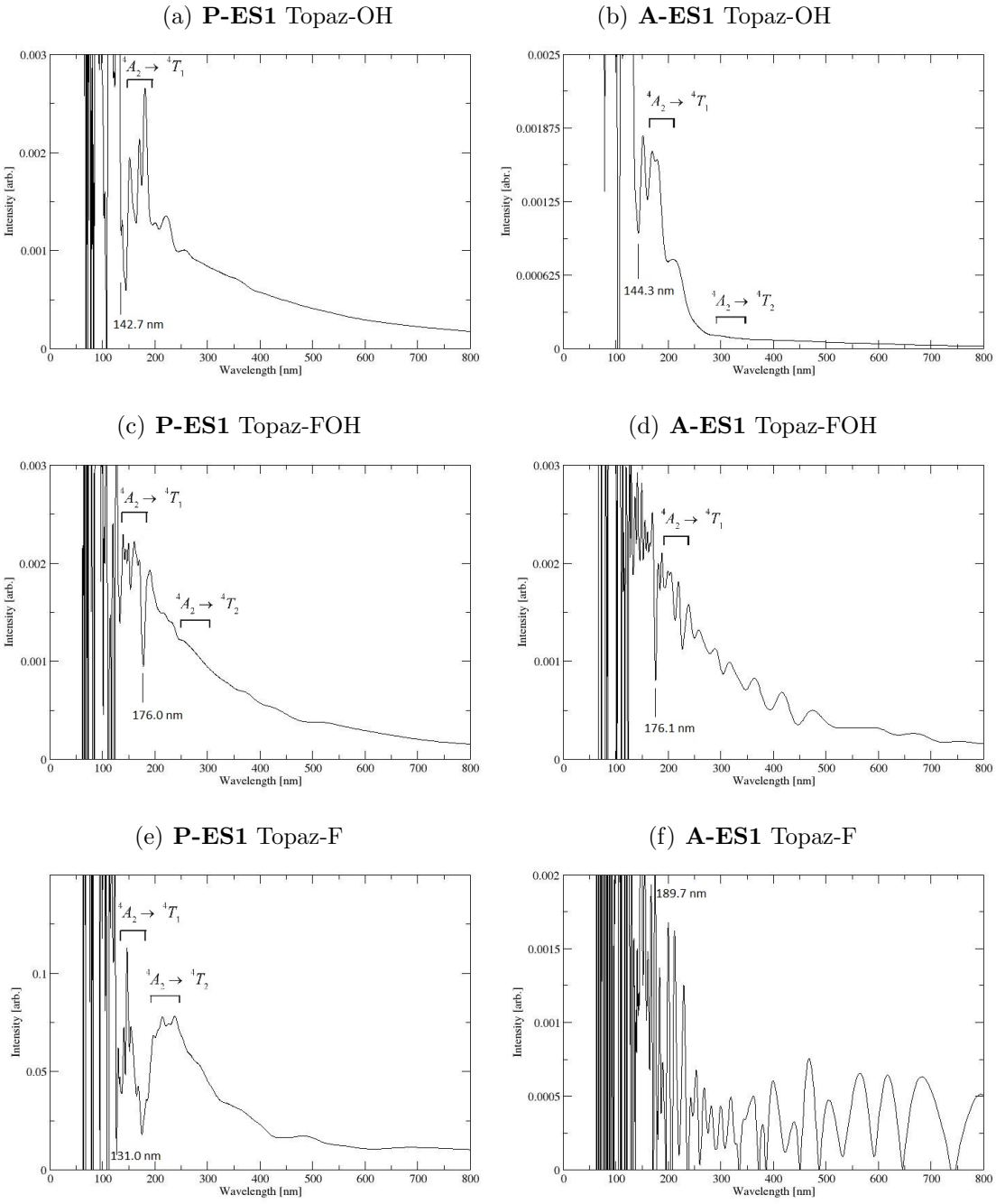

Figure 6.11: UV-Vis absorption spectra of clustered chromium(III), with parallel and antiparallel spins for two chromium(III) ions in a **ES1** structural configuration, for (a)-(b) topaz-OH, (c)-(d) topaz-FOH, and (e)-(f) topaz-F. The CT band is labelled (given again in Table 6.12) and the t_{2g}-e_g transitions have been assigned. The total number of MD steps simulated to generate each spectra are 3981 and 2397, 4686 and 4880, and 5399 and 5663 respectively.

However, visually assignment of expected spectral features have been made. The high energy wall of the CT band can be identified in all simulated UV-Vis spectra of Figures 6.10 and 6.11, and the corresponding energies to the wavelengths are given in Table 6.12. In comparison to the static band gaps calculated, given in Tables 6.10 and 6.11 for isolated and cluster chromium in topaz, the simulated CT-band in general are much larger than their static counterparts. The chromium cluster systems are generally shown by this method to have a larger band gap than the isolated chromium system. Spectral features, such as the $t_{2g} \rightarrow e_g$ transitions ($^4A_2 \rightarrow ^4T_2$ and $^4A_2 \rightarrow ^4T_1$), as seen in Figure 6.9(a) and discussed in Section 6.2.2, have been assigned to calculated the spectra in Figures 6.10 and 6.11, which have been deemed to have completed enough simulation steps in order to resolve those parts of the spectrum. Some spectra, such as the isolated Cr in topaz-F and the **A-ES1** configuration in F-rich and mixed topaz have unresolved spectra with too much noise: peak assignment therefore could not be made. Since the CT band has shifted up in energy for these systems containing Cr, the optical transitions may also be shifted up into the UV part of the spectrum. Therefore, the comparison with experimental UV-Vis spectra (see Figure 6.9(b)) is difficult as the absorption edge and subsequent optical transitions are shifted up in energy.

6.8 Conclusion

In this chapter, we have investigated the stability of a $Cr^{\times}_{Al}$ defect in topaz-OH, -FOH and -F. We have demonstrated that a single defect chromium(III) ion substitution into topaz prefers a F-rich octahedral environment, but when forming a chromium cluster, of two adjacent chromium(III) ions, the defect system prefers a OH-rich topaz environment. This finding supports experimental models detailed by Taran *et al.* [2] and Tarashchan *et al.* [52]. Mulliken population analysis showed the localisation of $(\alpha - \beta)$ spin on the chromium(III) ions is the greatest in a OH-rich topaz environment than when F in present, since the Cr d^3 unpaired electrons can redistribute and stabilise onto F^- ions. This is favourable for systems with isolated chromium(III) ions, but not when clustering occurs. Goodenough-Kanamori rules of superexchange can be applied to explain these observations.

Additional electronic and structural considerations were considered for the two chromium(III) ion cluster in topaz. The antiferromagnetic coupling scheme, where the two chromium(III) ions have the d^3 spins aligned in an antiparallel fashion (i.e. $Cr(\uparrow\uparrow\uparrow)Cr(\downarrow\downarrow\downarrow)$), were found to be more stable for corner-sharing chromium octahedra, whereas the ferromagnetic coupling scheme (i.e. $Cr(\uparrow\uparrow\uparrow)Cr(\uparrow\uparrow\uparrow)$)

for edge-sharing chromium octahedra.

Lattice parameters, bond distances and Cr−(OH/F/O)− bridging angles were also calculated and trends as a function of defect or stabilisation energies were made. Local structural trends were heavily dependent on the local and/or crystal composition, and the electronic and structural configuration of the defect system.

Numerically, the calculated band gaps were overestimated for pink topaz, in that they did not fall within the visible part of the spectrum. This is a known problem for computational methods that use high percentages of HF exchange. However, introducing Cr into topaz does decrease the band gap and creating a cluser reduces it further. The magnitude of these changes are all subject to the local composition environment, the coordination and structural effects, and the electronic configuration. A ferromagnetic scheme in most cases reduced the band gap further.

UV-Vis absorption spectra were simulated using a MD-TD-DFT method. The calculated CT absorption band did not improve upon the static calculations made of the band gap. Since the CT band was shifted higher in energy, it was assumed that optical transitions, if there were any, were also translated higher in energy. Together with an absence in electronic information of electronic transitions and the spin states involved, the assignment of peaks within the spectra was difficult.

For systems with Both CRYSTAL and CP2K computational methods provide both similar numerical values for the energy of defect formation and the energy required to stabilise two defect species, and trends in stability when electronic, structural, and conformational variables are changed.

Single Chromium Band Gap [eV]				
	Pure Topaz		Single Cr Defect	
[F] [%]	CRYSTAL	CP2K	CRYSTAL	CP2K
0	8.37	7.12	6.48	5.65
50	8.50	7.33	6.35	5.72
100	8.26	7.57	6.60	6.01

Table 6.10: Calculated band gaps for a single chromium substitution in topaz from CRYSTAL and CP2K calculations with band gaps from pure topaz for comparison.

Chromium Clusters Band Gap [eV]								
	Edge-Sharing Octahedra					Corner-Sharing Octahedra		
[F]		(**P**)		(**A**)			(**P**)	(**A**)
%	Config.	CRYSTAL	CP2K	CRYSTAL	CP2K	Config.	CRYSTAL	CRYSTAL
0	ES1	6.243	4.015	6.325	4.703	CS1	6.121	6.221
50	ES1	5.134	4.283	5.034	4.550	CS1	5.974	6.179
100	ES1	6.406	4.323	6.531	5.023	CS1	6.151	6.498
0	ES2	5.932		6.519		CS2	5.925	6.344
50	ES2	5.890		6.307		CS2	5.890	6.268
100	ES2	6.383		6.560		CS2	6.151	6.496

Table 6.11: Calculated band gaps for a double chromium substitution in topaz from CRYSTAL and CP2K calculations. (The densities of states for chromium clustering in topaz-F for CRYSTAL and CP2K calculations are given in Figures D.2 and D.3 in Appendices D.1 and D.3 respectively).

Single Chromium Band Gap [eV]						
[F]	Isolated Cr^{3+}		Cr^{3+} Clusters (ES1)			
			(P)		(A)	
	[nm]	[eV]	[nm]	[eV]	[nm]	[eV]
0	271.765	4.563	144.265	8.595	142.745	8.687
50	181.152	6.845	176.050	6.536	131.005	7.045
100	240.784	5.150	189.730	7.043	125.593	6.307

Table 6.12: The charge transfer bands calculated via MD-TD-DFT simulations. Numbers given in again respective spectra in Figures 6.10 and 6.11. Given in wavelengths [nm] and the corresponding energy [eV].

Chapter 7

Phosphorus Defects in Topaz

7.1 Introduction

From the list of potential defects to effect the colour of topaz, the literature research discussed in Chapter 2 indicates that a class of defects involves phosphorus ions. The two most commonly invoked P-based defects centres can be described as a *phosphate* $[PO_4]^{4-}$ and a *phosphite* $[PO_3]^{2-}$ molecular ion, eventually with an electron (e^-) trapped on P^{5+} to yield a neutral $P^{\times}_{Si}$ replacement at the Si site. In this chapter, we investigate how these defect centres form in topaz, their relative stability within different F/OH environments, any unique geometrical structures, electronic configurations, and their effect on band gaps, which can give rise to distinguishing features in UV-Vis spectra.

7.1.1 Formation of Phosphorus in Topaz

In order for natural topaz to contain phosphorus, it needs to be present in surrounding minerals at the point of crystallisation. P can however be generated artificially from Si, via a nuclear decay reaction. This occurs by bombarding the topaz crystal with neutron (^1_0n) radiation. Following β^- decay, a phosphorus atom is formed on the site of a ^{30}Si isotope. This involves the decay of a neutron into a proton, emitting in the process an electron and an electron antineutrino ($^1_0n- >^1_1 p + e^- + \bar{\upsilon}_e$)). The P_{Si} process via β^- decay can be summarised by:

$$^{30}_{14}\mathrm{Si} + ^{1}_{0}\mathrm{n} \longrightarrow ^{31}_{14}\mathrm{Si} \xrightarrow{\beta^-} ^{31}_{15}\mathrm{P} + \mathrm{e}^- + \bar{\upsilon}_\mathrm{e} \tag{7.1}$$

The natural abundance of ^{30}Si is 3.1%, and the half-life of ^{31}Si is 157.3 min (∼2.6 h).

Therefore, the formation of P via Equation 7.1.1 is not a lengthy process, and if phosphorus in some chemical form is partly or wholly responsible for the blue colouration in topaz, the experimental observation that topaz turns almost instantly blue upon irradiation supports the evident. The abundance of ^{31}Si indicates that even at high neutron fluxes, the concentration of P is not likely to reach saturation, given the trace quantities of defect required to cause an optical change. Therefore, the colour intensity of irradiated topaz is proportional to the dose of neutron radiation to which the crystal has been exposed.

The quantum chemical approach we employed to investigate P-based defects in topaz was a a static aproach and focused on the initial and final electronic and structural configuration, rather than a dynamic approach involved bombard cells of atoms with high energy neutron particles and monitoring the defects created. As a result, more of an emphasis was given to electronic of the P defect in its equilibrium state, and how the band gap and optical features were affected, once the excess energy liberated in the nuclear decay of Equation 7.1.1 has been dissipated.

The large excess of energy is likely to generate a wide range of P-based sites; even if these require a large formation energy when calculated relative to defect-free topaz, their generation is a non-thermal process, hence chemical equilibrium rules do not apply, and we assume that both phosphate and phosphite ions are generated. Thermal annealing processes, instead can be described with the quantum chemical methods. For simplicity, in our discussion, we assume that the $[PO_4]^{4-}$ centre is formed first, via the nuclear reaction at Si, with the electron liberated in Equation 7.1.1 and trapped on P^{5+} to yield P^{4+}. The reduced P^{4+} can relax by releasing one of its oxygen neighbours with a 3+ charge state. The $[PO_3]^{2-}$ centre forms by displacement of one of the tetrahedral oxygens into a vacancy position.

$$\begin{aligned} [P^{\times}_{Si}O_4]^{4-} \longrightarrow\ & [P^{\times}_{Si}O_3V^{\times}_{O}]^{4-} + O^{\times}_{i} \\ & [P^{\bullet}_{Si}O_3V^{\times}_{O}]^{4-} + O'_{i} \\ & [P^{\bullet}_{Si}O_3V^{\bullet}_{O}]^{4-} + O''_{i} \end{aligned} \tag{7.2}$$

The oxygen released occupies an interstitial site of the topaz lattice and can be located at different distances from the original P ion. These interstitial sites are therefore likely to have different energies and migration of the oxygen between sites may represent one of the possible mechanisms for thermal annealing observed in topaz.

To describe this thermal relaxation in the form of O^- migration, we performed calculations with different local configurations of $[P^{\bullet}_{Si}O_3V^{\bullet}_{O}]^{4-} + O''_{i}$ in a double cell

$(2 \times 1 \times 1)$ of topaz. There are four structural oxygens that are bonded to the phosphorus when substituted onto the silicon tetrahedral site, and eight possible interstitial sites within a $2\times1\times1$ topaz supercell[1]. A total of 32 defect configurations were therefore considered for each composition of topaz (OH-, FOH- and F-topaz). The labeling notation used here to distinguish different starting defect configurations is outlined in Appendix E.1.

7.2 Defect Energy

Even though P is likely formed following nuclear reaction and irradiation of topaz, we still employ a chemical reaction to investigate its formation energy, and compare relative stablities of different configurations.

The chemical reaction scheme employed to calculate the defect formation energy of $[PO_4]^{4-}$ in a $2 \times 1 \times 1$ supercell of topaz is:

$$Al_{16}Si_8O_{32}(OH,F)_{16} + PO_4 \longrightarrow Al_{16}Si_7P^{\times}_{Si}O_{32}(OH,F)_{16} + SiO_4, \tag{7.3}$$

where PO_4 is an isolated molecule ion of P^{4+} oxidation state. This is an highly unstable chemical species, which will reflect in the calculated reaction energies, but provides a suitably simple way to charge and mass balance the reaction of P sites.

Here we propose that the formation of phosphite-like ions ($[PO_3]^{2-}$) from phosphate ($[PO_4]^{4-}$), occurs via an O displacement from the tetrahedral species, and an interstitial O is formed. These can be described by cells with identical compositions in the following way, i.e.

$$Al_{16}Si_7P^{\times}_{Si}O_{32}(OH,F)_{16} \longrightarrow Al_{16}Si_7O_{28}[P^{\times}_{Si}O_3V^{\bullet\bullet}_{O}]O''_{i}(OH,F)_{16}, \tag{7.4}$$

hence the two calculated energies are directly comparable.

We define the formation energy of $[PO_4]^{4-}$ and $[PO_3]^{2-} + O^{2-}_{i}$ centres as

$$\begin{aligned}\Delta H_f([PO_4]^{4-}) =& E_{tot}(Al_{16}Si_7P^{\times}_{Si}O_{32}(OH,F)_{16}) + E_{tot}(SiO_4) \\ &- E_{tot}(Al_{16}Si_8O_{32}(OH,F)_{16}) - E_{tot}(PO_4)\end{aligned} \tag{7.5}$$

and

$$\begin{aligned}\Delta H_f([PO_3]^{2-}) =& E_{tot}(Al_{16}Si_7O_{28}[P^{\times}_{Si}O_3V^{\bullet\bullet}_{O}]O''_{i}(OH,F)_{16}) \\ &- E_{tot}(Al_{16}Si_7P^{\times}_{Si}O_{32}(OH,F)_{16})\end{aligned} \tag{7.6}$$

[1]The location of the interstitial sites within topaz, were given by Jinan *et al.* [142], and are reproduced for reference in Appendix E and Table E.3.

respectively. Negative values of ΔH_f indicate stable configurations.

The calculated formation energies for both CRYSTAL and CP2K calculations are given in Table 7.1. The defect centre $[PO_4]^{4-}$ was given the initial electronic configurations of $[P^{\times}_{Si}O_4]^{4-}$ corresponding to the one electron localised on P, and a total of one unpaired electron in the unit cell. Calculations containing the $[PO_3]^{2-}$ ion were started with an interstitial oxide (O^{2-}) ion and tricoordinated P ion with one electron localised in the vacant O site. The number of unpaired electrons in the unit cell is the same for the phosphate as for the phosphite configuration. It is unclear where the two unpaired electrons on the O^{2-} interstitial will localise following optimisation, but it is hoped that the SCF cycle will converge towards a stable electronic configuration and reveal the defect energy landscape.

The optimisation of defect systems $[PO_4]^{4-}$ and $[PO_3]^{2-} + O''_i$ yielded some interesting stable electronic configurations. In $[PO_4]^{4-}$ defect systems, the unpaired electron remained mainly localised on the phosphorus ion, but with noticeable contributions on the four oxygens of the $[PO_4]^{4-}$ ion, as can been seen in the $(\alpha - \beta)$ spin density plots of Figure 7.2. Tables 7.3 and 7.4 report the $(\alpha - \beta)$ Mulliken population analysis from CRYSTAL and CP2K results, respectively.

For the $[P^{\times}_{Si}O_3V^{\bullet\bullet}_O]^{2-} + O''_i$ defect, a number of different stable electronic configurations emerged following optimisation. These can be summarised by the following reaction schemes:

$$[P^{\bullet}_{Si}O_3V^{\bullet}_O]^{2-} + [O''_i]^{2-} \xrightarrow{+O_{STRUC}} [P'_{Si}O_3V^{\bullet\bullet}_O]^{3-} + [O'_2]^{-} \quad = O_2^- \tag{7.7}$$

$$[P^{\bullet}_{Si}O_3V^{\bullet}_O]^{2-} + [O''_i]^{2-} \xrightarrow{+2\,O_{STRUC}} [P'_{Si}O_3V^{\bullet\bullet}_O]^{3-} + [O'_3]^{-} \quad = O_3^- \tag{7.8}$$

$$[P^{\bullet}_{Si}O_3V^{\bullet}_O]^{2-} + [O''_i]^{2-} \longrightarrow [P'_{Si}O_3V^{\bullet}_O]^{4-} + [O_i] \quad = e^-_V \tag{7.9}$$

$$[P^{\bullet}_{Si}O_3V^{\bullet}_O]^{2-} + [O''_i]^{2-} \longrightarrow [P^{\times}_{Si}O_3O_iV^{\bullet\bullet}_O]^{4-} \quad = [PO_4]^{4-} \tag{7.10}$$

In most calculations, the phosphorus was found in the form of a phosphite ion ($[PO_3]^{2-}$) with two electrons in an unshared electron pair, directed towards the vacant O site. These are given in reactions Equations 7.7 and 7.8. The interstitial oxygen in these cases has a $1-$ charge, and does not remain isolated, but rather forms a O_2^{3-} superoxide ions, with one of the lattice oxygens $[O^-_i + O^{2-}_O \longrightarrow (O^{3-}_2)]$ (i.e. Equation 7.7); or an ozonide (O_3^{5-}) ion, with two lattice oxide ions (Equation 7.8). All these molecular ions have have one unpaired electron. The neighbouring structural oxygens in peroxide/ozonide ions aid the stabilisation of the extra spin (see Equations 7.7 and 7.8). Often calculations have converged in an electronic state where the interstitial O is charge neutral (in triplet state), while the extra electron is

Config.	CRYSTAL			CP2K		
$\frac{[F]}{[F+OH]}$	0%	50%	100%	0%	50%	100%
(a) $\Delta H_f([PO_4]^{4-})$						
	-1.376	-1.267	-2.470	0.448	0.359	0.531
(b) $\Delta H_f([PO_3]^{2-})$						
V1i1	4.115	4.327	-			
V1i2	-	4.261	-	4.779		
V1i3	4.193	4.296	6.408			
V1i4	-	-	9.040			
V1i5	4.192	4.301	-			
V1i6	4.100	4.483	8.805			5.539
V1i7	4.133	4.366	-			
V1i8	4.460	4.401	-			
V2i1	4.244	4.456	-			
V2i2	4.145	4.344	-			
V2i3	4.420	4.594	8.812			
V2i4	3.968	-	6.553	4.414		5.208
V2i5	4.284	4.609	-			
V2i6	-0.718	-	-	-0.192		
V2i7	-	-	-			
V2i8	-	4.813	-			
V3i1	4.223	4.602	6.324			
V3i2	4.346	4.480	-			
V3i3	4.444	4.171	-		4.767	
V3i4	-	-	-			
V3i5	4.676	4.828	-			
V3i6	4.404	4.596	6.633			
V3i7	4.075	4.454	-			
V3i8	4.591	4.770	-			
V4i1	-	4.254	6.245			-0.049
V4i2	4.440	4.608	-			
V4i3	4.414	4.615	-			
V4i4	-	-	-			
V4i5	4.666	4.731	-			
V4i6	4.300	-	6.415			
V4i7	4.099	4.094	-		4.439	
V4i8	4.636	4.707	-			

Table 7.1: Defect energies of P-based defects, (a) $[PO_4]$ and (b) $[PO_3]+O_i$, in topaz. The labeling convention used to distinguish different starting phosphite configurations is outlined in Appendix E.1.

located in the O vacancy next to P, as an open-shell defect (Equation 7.9). Others showed still the recombination or migration of the oxygen interstitial back into the vacancy site next to the P in order to regenerate the phosphate ion ($[PO_4]^{4-}$) with one additional electron localised in P (Equation 7.10). These electronic configurations are confirmed by the $(\alpha - \beta)$ spin density plots of Figures 7.3, 7.4 and 7.5, and the Mulliken population analysis in Tables 7.4 and 7.3. (The complete $(\alpha - \beta)$ spin density plots of all optimised structural phosphate configurations, for topaz-OH, -FOH and -F, calculated by CRYSTAL are given in Appendix E.3).

In other defect electronic configurations, the unpaired electron was trapped on the site of the oxygen vacancy and creating an F-centre, and another case saw the recombination of displaced defect species. These are given in Equations 7.9 and 7.10 respectively.

Each configuration can be differentiated by the final defect type and local configuration of the host lattice, an unique energy penalty and a characteristic signature in the band gap. Typical formation energies of the $[PO_3]^{2-}$ electronic configurations given by Equation 7.6, described by Equations 7.7-7.10, are summarised in Table 7.2, along with the defect formation energy for $[PO_4]^{4-}$ given by Equation 7.5. For each defect type, these are the lowest formation energies reported in Table 7.1). The products are labelled as in Equations 7.7-7.10.

	Defect Formation Energy, $\Delta H_f([PO_3]^{2-})$ [eV]							
	CRYSTAL					CP2K		
$\frac{[F]}{[F+OH]}$	O_3^-	O_2^{-a}	O_2^{-b}	e_V^-	$[PO_4]^{4-}$	O_3^-	O_2^-	$[PO_4]^{4-}$
0%	4.075	4.223	3.968	-	-0.718	4.779	4.414	-0.192
50%	4.094	4.171	4.253	-	-	4.439	4.767	-
100%	6.553	6.245	6.553	8.805	-	5.208	5.539	-0.049

[a] Mulliken spin evenly shared between two oxygens.

[b] Mulliken spin unevenly shared between two oxygens [65 : 35, 70 : 30 and 60 : 40].

Table 7.2: Formation energies of different defect states of P-containing defects in topaz.

The creation of interstitial oxygen species, such as superoxide and ozonide ions, in phosphorus doped topaz is shown to be a highly endothermic process ($\sim$4 eV), and therefore unlikely to occur via chemical doping methods. However, β-decay and neutron bombardment could provide the extremely high energies required for such defect formations, and hence their presence cannot be excluded. Once the phosphite ion has been created by removal of an O^{2-} ion, the interstitial oxygen has many local minima available, which may prevent defect recombinations. Both the O_3^- and O_2^- defects form more easily in a OH-rich environments; topaz-F is less likely

to stabilise these defects. In Table 7.2, the formation energy for the O_2^- defect is divided into two columns, corresponding to slightly different electronic states: one where the spin is split evenly between the two oxygens, and the other were there is unequal distribution. OH-rich topaz environments favour a more polarised spin distribution, but as the F content increases the evenly spread distribution of spin becomes preferable. This difference is likely due to formation of local H-bonding interactions between OH^- and O_2^{3-} ions in close proximity in OH-rich environments.

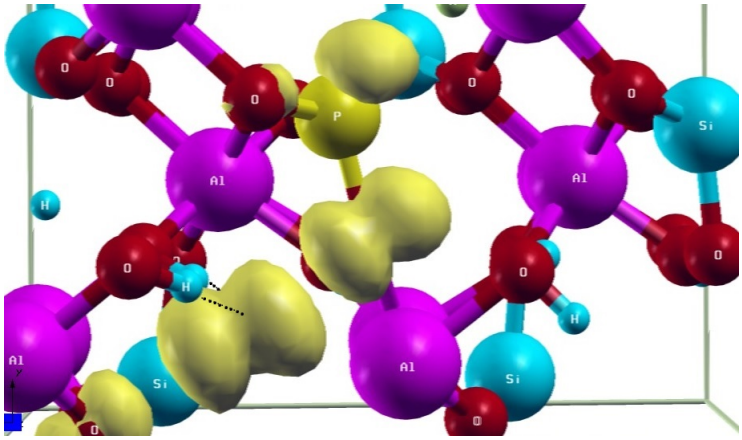

Figure 7.1: Depicting the H-Bonding (indicated by ···) in superoxide/ozonide defects prevalent in phosphite-containing topaz.

The stabilisation of the O_2^- defect in topaz is a confirmation of literature experimental models proposed in references [7, 14, 22] and discussed in Section 2.4. Our results did not indicate the presence of a polaron, i.e. an O^- centre, as proposed by references [6, 8, 37, 38] and also discussed in Section 2.4, at least associated with P defects. However, from Mulliken analysis (see Tables 7.3 and 7.4) the unpaired spin in the defect centres we identified as O_3^- shows a significant localisation of the unpaired spin on one oxygen, usually the O_i, and could therefore be interpreted as a polaron defect stabilised by the two neighbouring structural oxygens. This is more prevalent in mixed F/OH topaz than in either OH- or F-rich topaz.

Defects	[F]	Config.	Elect.	Mulliken Population Analysis						Total
Energy [eV]	[%]	Label	Config.	Atom	Spin	Atom	Spin	Atom	Spin	Charge
4.779	0	V1i2	O_3^-	O_i	0.620	$O_{STRUC.}$	0.480	$O_{STRUC.}$	0.035	1.134
4.414	0	V2i4	O_2^-	O_i	0.019	$O_{STRUC.}$	0.701	$O_{STRUC.}$	0.441	1.160
-0.192	0	V2i6	$[PO_4]^{4-}$	P_{Si}	0.728	O_i	0.269	$O_{STRUC.}$	0.073	1.070
4.767	50	V3i3	O_2^-	O_i	0.637	$O_{STRUC.}$	0.523	-	-	1.160
4.439	50	V4i7	O_3^-	O_i	0.667	$O_{STRUC.}$	0.478	$O_{STRUC.}$	0.031	1.176
5.539	100	V1i6	O_2^-	O_i	0.560	$O_{STRUC.}$	0.607	-	-	1.167
5.208	100	V2i4	O_3^-	O_i	0.032	$O_{STRUC.}$	0.656	$O_{STRUC.}$	0.484	1.171
-0.049	100	V4i1	$[PO_4]^{4-}$	P_{Si}	0.879	$O_{STRUC.}$	0.107	$O_{STRUC.}$	0.103	1.089

Table 7.3: Detailed Mulliken population analysis for configurations of $[PO_3]^{2-}$ defect from CP2K calculations.

CRYSTAL calculations showed that F-rich topaz was also able to localise the extra unpaired electron on the oxygen vacancy neighbouring the phosphorus defect, creating an e_V^- species, i.e. an F-centre and a possible colour centre. This, however, is over 2 eV higher in energy relative to stabilising the extra spin on O_i, a relaxation that only requires electronic, not ionic diffusion. The e_V centre is therefore an unlikely candidate to play much of a role in the defect chemistry of P-topaz, but for the conditions that govern the creation of the phosphorus defect in topaz, would still mean that this defect configuration was still possible and may in fact play a role in the defect chemistry of topaz.

Finally, following optimisation of all the different structural combinations possible from a $[PO_3]^{2-} + O_i^{2-}$ system in topaz, it was shown that the recombination of O_i^{2-} back into the $[PO_3V_O]^{2-}$ centre, i.e. the reformation of the $[PO_4]^{4-}$ centre, is not only possible but the most favourable outcome. This, however, requires oxygen migration in order for recombination of defects to occur. Migration of the interstitial oxygen species depends on steric factors and requires the overcoming of energy barriers: annealing could be the process via which recombination occurs.

The above configurations have been studied systematically using the code CRYSTAL. A selection of calculations, based on the lowest energy of each identified electronic configuration, have been repeated with CP2K, and we note that there is good qualitative agreement between CRYSTAL and CP2K (see Table 7.2, and Figures 7.2, 7.3, 7.4 and 7.5). The energy trends observed above, together with the unique defect electronic configurations, are replicated in both methods.

7.3 Structural Analysis

In this section, we discuss the structural features connected with the unique defect electronic structures established in Section 7.2.

7.3.1 Lattice Parameters

The CRYSTAL calculated lattice parameters for the topaz containing $[PO_4]^{4-}$ defects are presented in Table 7.5, while results for the $[PO_3]^{2-}$-based defect are summarised in Figures 7.6 and 7.7. The corresponding CP2K lattice parameters are given in Appendix E.2 in Table E.2.

Structral	Elect.	Mulliken Population Analysis						Total	Bond Distance	
Config.	Config.	Atom	Spin	Atom	Spin	Atom	Spin	Charge	$P-O_i/O$ [Å]	O_i-O [Å]
					Topaz-OH					
V1i1	O_3^-	O_i	0.665	$O_{STRUC.}$	0.219	$O_{STRUC.}$	0.111	0.995	3.894	2.007
V1i3	O_3^-	O_i	0.679	$O_{STRUC.}$	0.201	$O_{STRUC.}$	0.118	0.998	3.998	2.003
V1i5	O_3^-	O_i	0.654	$O_{STRUC.}$	0.247	$O_{STRUC.}$	0.089	0.990	4.255	1.992
V1i6	O_3^-	O_i	0.548	$O_{STRUC.}$	0.287	$O_{STRUC.}$	0.076	0.911	1.606	1.982
V1i7	O_3^-	O_i	0.683	$O_{STRUC.}$	0.198	$O_{STRUC.}$	0.114	0.995	4.408	2.022
V1i8	O_3^-	O_i	0.650	$O_{STRUC.}$	0.227	$O_{STRUC.}$	0.110	0.987	4.212	1.991
V2i1	O_3^-	O_i	0.665	$O_{STRUC.}$	0.229	$O_{STRUC.}$	0.100	0.994	3.783	2.015
V2i2	O_3^-	O_i	0.698	$O_{STRUC.}$	0.165	$O_{STRUC.}$	0.138	1.001	1.575	2.045
V2i3	O_3^-	O_i	0.659	$O_{STRUC.}$	0.242	$O_{STRUC.}$	0.092	0.993	4.158	1.996
V2i4	O_2^-	O_i	0.328	$O_{STRUC.}$	0.638	-	-	0.966	1.555	1.944
V2i5	O_3^-	O_i	0.641	$O_{STRUC.}$	0.260	$O_{STRUC.}$	0.092	0.993	4.288	1.977
V2i6	$[PO_4]^{4-}$	P_{Si}	0.596	O_i	0.270	$O_{STRUC.}$	0.038	0.904	2.171	-
V3i1	O_3^-	O_i	0.532	$O_{STRUC.}$	0.003	$O_{STRUC.}$	0.386	0.921	3.462	1.943
V3i2	O_3^-	O_i	0.659	$O_{STRUC.}$	0.243	$O_{STRUC.}$	0.088	0.990	1.631	1.989
V3i3	O_3^-	O_i	0.661	$O_{STRUC.}$	0.246	-	-	0.907	4.047	1.990
V3i5	O_3^-	O_i	0.678	$O_{STRUC.}$	0.208	$O_{STRUC.}$	0.108	0.994	4.275	2.000
V3i6	O_3^-	O_i	0.660	$O_{STRUC.}$	0.230	$O_{STRUC.}$	0.101	0.991	1.657	1.995
V3i7	O_3^-	O_i	0.677	$O_{STRUC.}$	0.204	$O_{STRUC.}$	0.123	1.004	4.299	2.010
V3i8	O_3^-	O_i	0.674	$O_{STRUC.}$	0.202	$O_{STRUC.}$	0.118	0.994	4.198	2.005
V4i2	O_3^-	O_i	0.656	$O_{STRUC.}$	0.248	$O_{STRUC.}$	0.087	0.991	1.652	1.987
V4i3	O_3^-	O_i	0.667	$O_{STRUC.}$	0.239	$O_{STRUC.}$	0.083	0.989	4.043	1.994
V4i5	O_3^-	O_i	0.674	$O_{STRUC.}$	0.221	$O_{STRUC.}$	0.098	0.993	4.329	2.001
V4i6	O_3^-	O_i	0.637	$O_{STRUC.}$	0.261	$O_{STRUC.}$	0.089	0.987	1.657	1.983
V4i7	O_3^-	O_i	0.669	$O_{STRUC.}$	0.231	$O_{STRUC.}$	0.098	0.998	4.276	1.996
V4i8	O_3^-	O_i	0.673	$O_{STRUC.}$	0.207	$O_{STRUC.}$	0.114	0.994	4.195	2.008
					Topaz-FOH					
V1i1	O_3^-	O_i	0.778	$O_{STRUC.}$	0.121	$O_{STRUC.}$	0.107	1.006	4.034	2.084
V1i2	O_3^-	O_i	0.762	$O_{STRUC.}$	0.130	$O_{STRUC.}$	0.115	1.007	1.516	2.067
V1i3	O_3^-	O_i	0.771	$O_{STRUC.}$	0.106	$O_{STRUC.}$	0.132	1.009	3.904	2.089
V1i5	O_3^-	O_i	0.777	$O_{STRUC.}$	0.140	$O_{STRUC.}$	0.085	1.002	4.144	2.062
V1i6	O_3^-	O_i	0.767	$O_{STRUC.}$	0.118	$O_{STRUC.}$	0.102	0.987	1.629	2.081
V1i7	O_3^-	O_i	0.776	$O_{STRUC.}$	0.121	$O_{STRUC.}$	0.109	1.006	4.292	2.083
V1i8	O_3^-	O_i	0.778	$O_{STRUC.}$	0.140	$O_{STRUC.}$	0.082	1.000	4.155	2.064
V2i1	O_3^-	O_i	0.780	$O_{STRUC.}$	0.123	$O_{STRUC.}$	0.102	1.005	3.900	2.091
V2i2	O_3^-	O_i	0.768	$O_{STRUC.}$	0.112	$O_{STRUC.}$	0.129	1.009	1.497	2.106
V2i3	O_3^-	O_i	0.784	$O_{STRUC.}$	0.121	$O_{STRUC.}$	0.098	1.003	4.074	2.087
V2i5	O_3^-	O_i	0.767	$O_{STRUC.}$	0.128	$O_{STRUC.}$	0.111	1.006	4.107	2.070
V2i8	O_3^-	O_i	0.793	$O_{STRUC.}$	0.121	$O_{STRUC.}$	0.090	1.004	4.257	2.091
V3i1	O_3^-	O_i	0.761	$O_{STRUC.}$	0.116	$O_{STRUC.}$	0.129	1.006	3.888	2.091
V3i2	O_3^-	O_i	0.772	$O_{STRUC.}$	0.133	$O_{STRUC.}$	0.098	1.003	1.601	2.070
V3i3	O_2^-	O_i	0.598	$O_{STRUC.}$	0.391	-	-	0.989	2.950	1.956
V3i5	O_3^-	O_i	0.784	$O_{STRUC.}$	0.125	$O_{STRUC.}$	0.095	1.004	4.209	2.070
V3i6	O_3^-	O_i	0.775	$O_{STRUC.}$	0.140	$O_{STRUC.}$	0.086	1.001	1.643	2.066
V3i7	O_3^-	O_i	0.758	$O_{STRUC.}$	0.136	$O_{STRUC.}$	0.117	1.011	4.174	2.062
V3i8	O_3^-	O_i	0.780	$O_{STRUC.}$	0.120	$O_{STRUC.}$	0.104	1.004	4.218	2.077
V4i1	O_2^-	O_i	0.727	$O_{STRUC.}$	0.205	-	-	0.932	3.587	2.023
V4i2	O_3^-	O_i	0.780	$O_{STRUC.}$	0.141	$O_{STRUC.}$	0.083	1.004	1.594	2.059
V4i3	O_3^-	O_i	0.772	$O_{STRUC.}$	0.133	$O_{STRUC.}$	0.098	1.003	4.017	2.081
V4i5	O_3^-	O_i	0.782	$O_{STRUC.}$	0.125	$O_{STRUC.}$	0.097	1.004	4.167	2.073
V4i7	O_3^-	O_i	0.769	$O_{STRUC.}$	0.131	$O_{STRUC.}$	0.110	1.010	4.180	2.117
V4i8	O_3^-	O_i	0.775	$O_{STRUC.}$	0.132	$O_{STRUC.}$	0.097	1.004	4.202	2.073
					Topaz-F					
V1i3	O_2^-	O_i	0.452	$O_{STRUC.}$	0.539	-	-	0.991	3.403	1.956
V1i4	eV^-	P_{Si}	0.067	V_O	0.605	-	-	0.672	4.070	1.441
V1i6	eV^-	P_{Si}	0.071	V_O	0.561	-	-	0.632	4.335	1.454
V2i3	eV^-	P_{Si}	0.069	V_O	0.634	-	-	0.703	2.939	1.431
V2i4	O_3^-	O_i	0.376	$O_{STRUC.}$	0.610	$O_{STRUC.}$	0.033	1.019	1.540	1.930
V3i1	O_2^-	O_i	0.472	$O_{STRUC.}$	0.521	-	-	0.993	4.555	1.948
V3i6	O_2^-	O_i	0.477	$O_{STRUC.}$	0.518	-	-	0.995	3.783	1.943
V4i1	O_2^-	O_i	0.456	$O_{STRUC.}$	0.535	-	-	0.991	4.475	1.956
V4i6	O_2^-	O_i	0.496	$O_{STRUC.}$	0.498	-	-	0.994	3.756	1.948

Table 7.4: Detailed Mulliken population analysis for configurations of $[PO_3]^{2-}$ defect from CRYSTAL calculations.

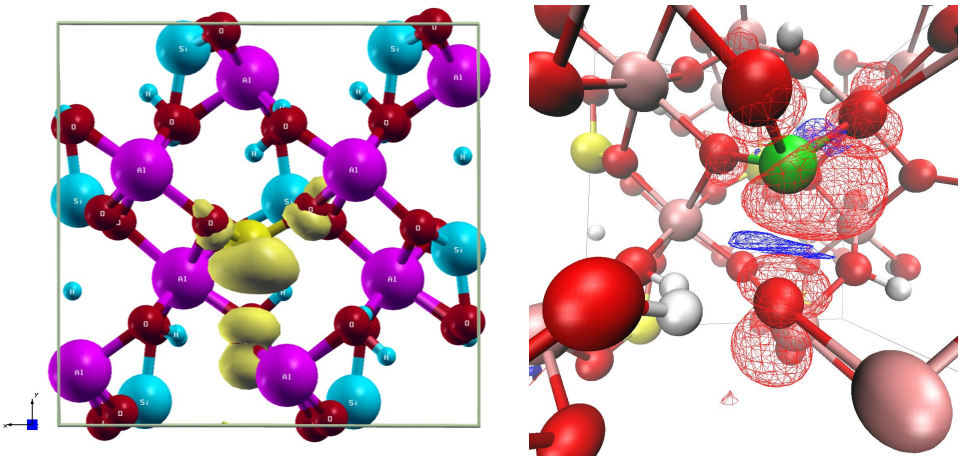

(a) $[PO_4]^{4-}$ Topaz-OH (CRYSTAL)

(b) $[PO_4]^{4-}$ Topaz-OH (CP2K)

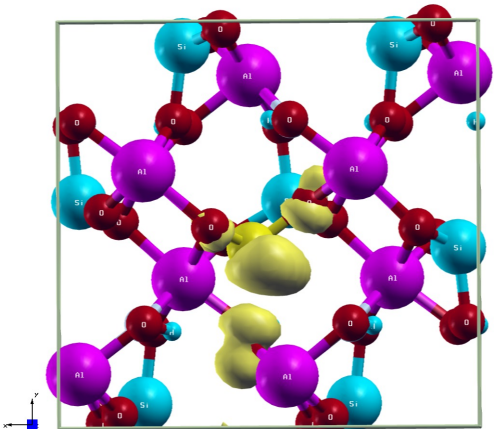

(c) $[PO_4]^{4-}$ Topaz-FOH (CRYSTAL)

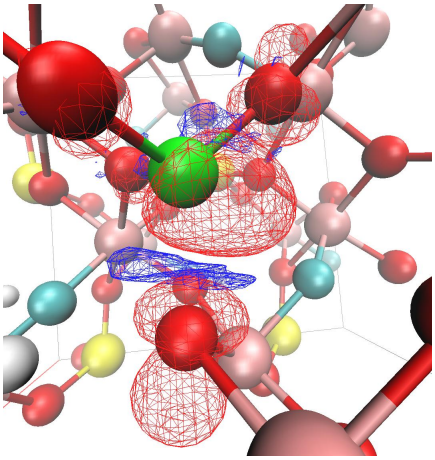

(d) $[PO_4]^{4-}$ Topaz-FOH (CP2K)

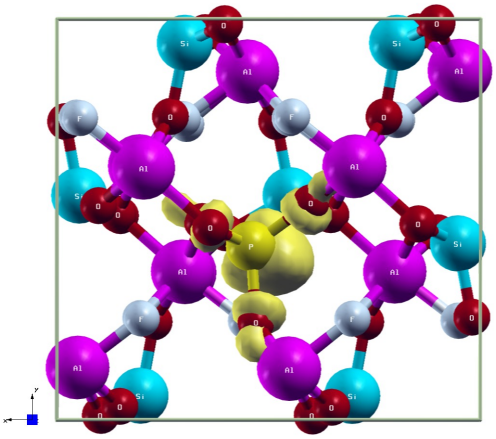

(e) $[PO_4]^{4-}$ Topaz-F (CRYSTAL)

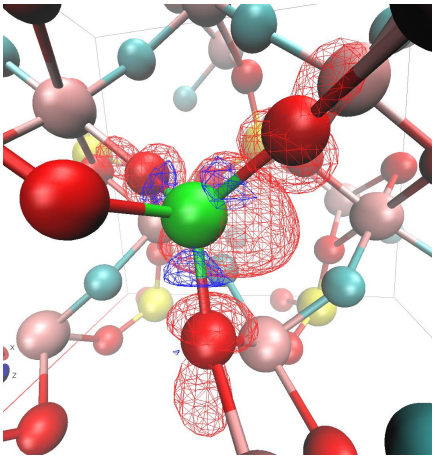

(f) $[PO_4]^{4-}$ Topaz-F (CP2K)

Figure 7.2: Spin density projections on 3-dimensional crystal representation for phosphorus substitution, from both CRYSTAL (figures (a), (c), and (e)) and CP2K (figures (b), (d), and (f)) calculations, in topaz-OH, topaz-FOH, and topaz-F (pairs (a)-(b), (c)-(d), and (e)-(f) respectively).

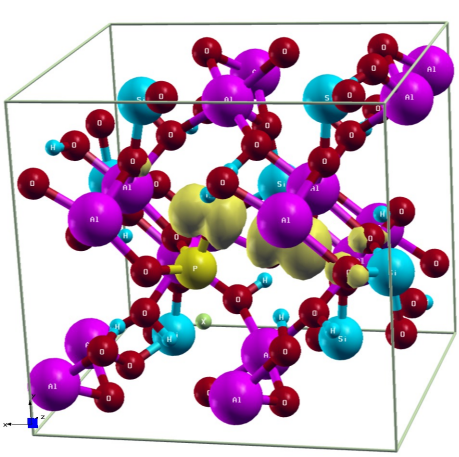

(a) $[PO_3]^{2-}$ (V2i4) (CRYSTAL)

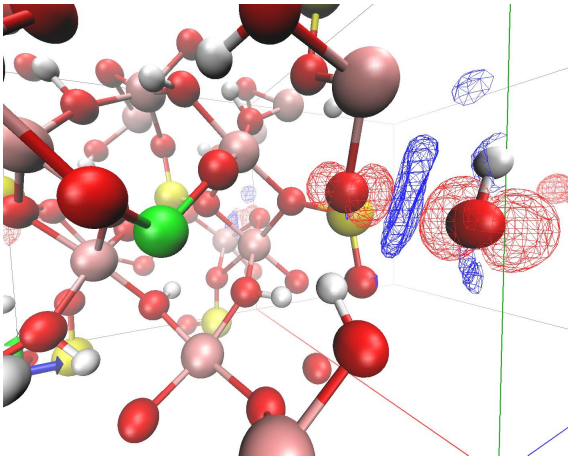

(b) $[PO_3]^{2-}$ (V2i4) (CP2K)

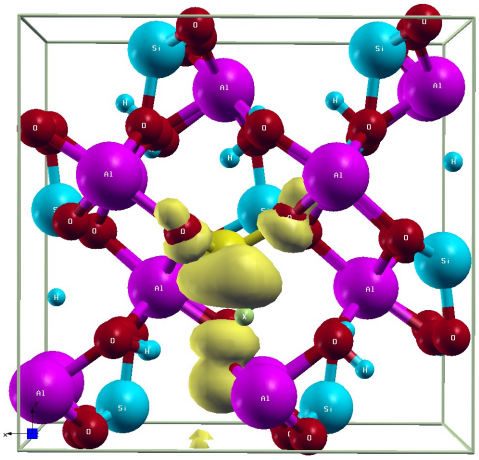

(c) $[PO_3]^{2-}$ (V2i6) (CRYSTAL)

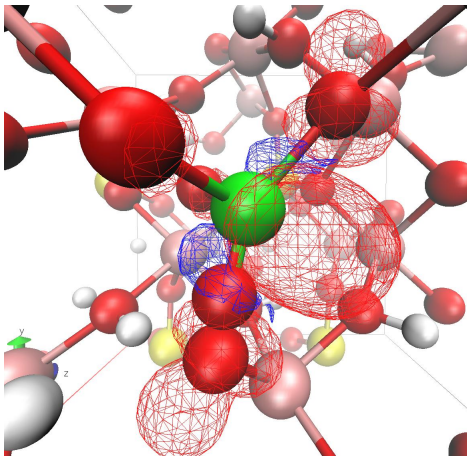

(d) $[PO_3]^{2-}$ (V2i6) (CP2K)

Figure 7.3: Spin density projections on 3-dimensional crystal representation for the two stable electron configurations of a phosphorus substitution in topaz-OH with oxygen displacement. Both CRYSTAL and CP2K optimisations are represented in (a) and (c), and (b) and (d) figures respectively.

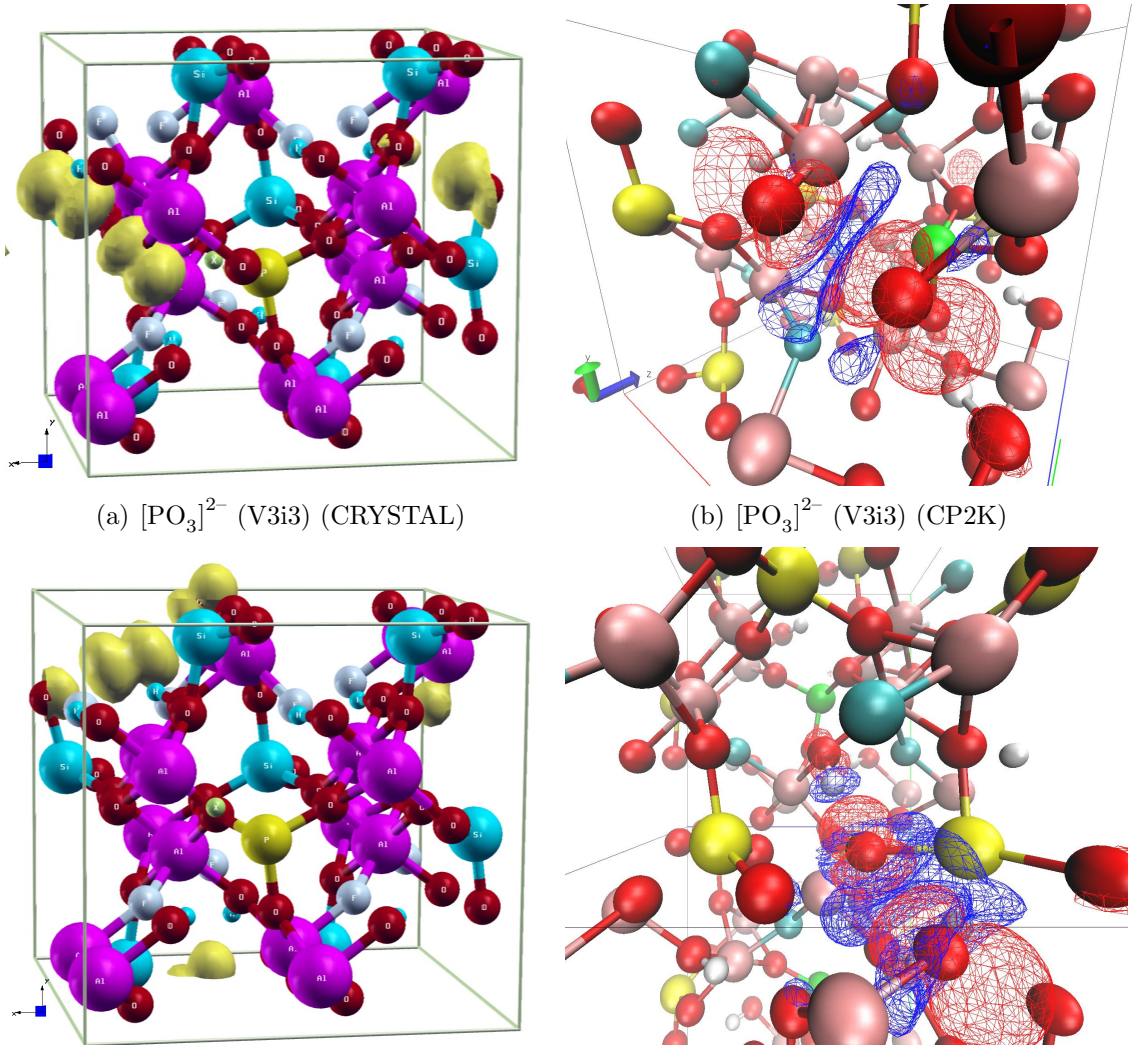

(a) $[PO_3]^{2-}$ (V3i3) (CRYSTAL)

(b) $[PO_3]^{2-}$ (V3i3) (CP2K)

(c) $[PO_3]^{2-}$ (V4i7) (CRYSTAL)

(d) $[PO_3]^{2-}$ (V4i7) (CP2K)

Figure 7.4: Spin density projections on 3-dimensional crystal representation for the two stable electron configurations of a phosphorus substitution in topaz-FOH with oxygen displacement. Both CRYSTAL and CP2K optimisations are represented in (a) and (c), and (b) and (d) figures respectively.

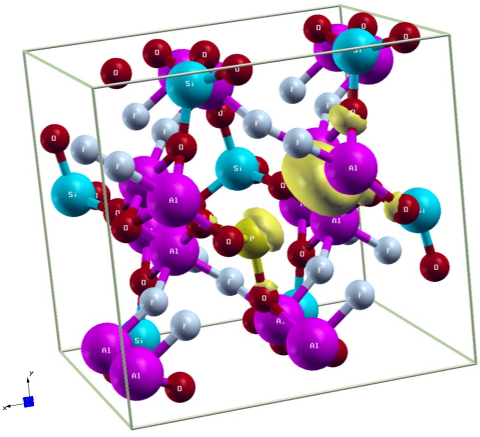

(a) $[PO_3]^{2-}$ (V1i6) (CRYSTAL)

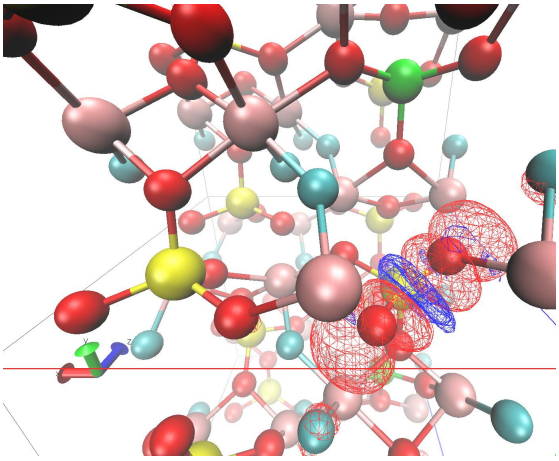

(b) $[PO_3]^{2-}$ (V1i6) (CP2K)

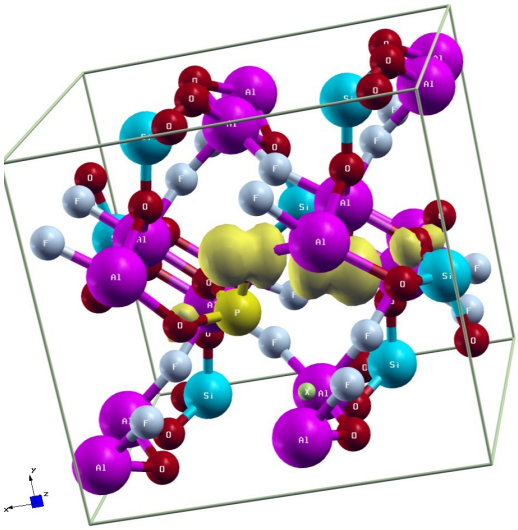

(c) $[PO_3]^{2-}$ (V2i4) (CRYSTAL)

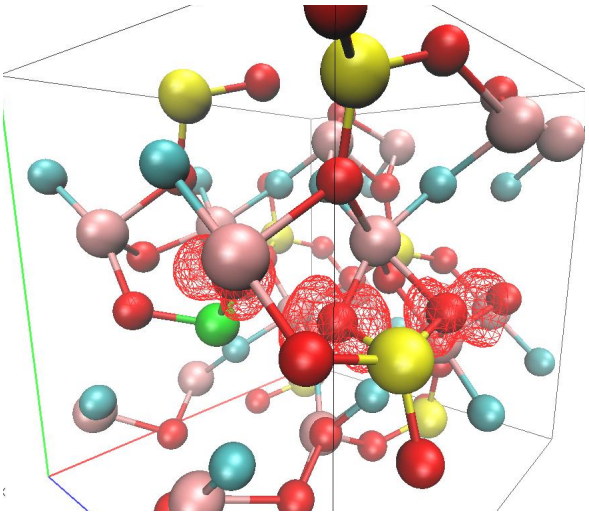

(d) $[PO_3]^{2-}$ (V2i4) (CP2K)

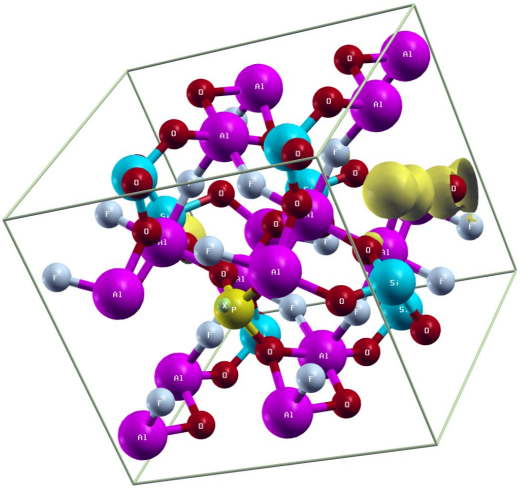

(e) $[PO_3]^{2-}$ (V4i1) (CRYSTAL)

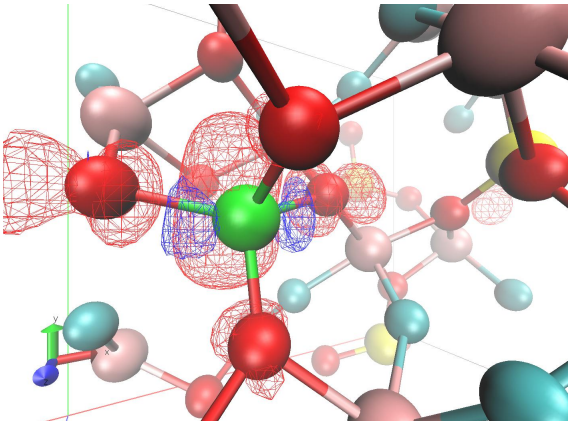

(f) $[PO_3]^{2-}$ (V4i1) (CP2K)

Figure 7.5: Spin density projections on 3-dimensional crystal representation for the two stable electron configurations of a phosphorus substitution in topaz-F with oxygen displacement. Both CRYSTAL and CP2K optimisations are represented in (a), (c) and (e), and (b), (d) and (f) figures respectively.

CRYSTAL Lattice Parameters								
[F] [%]	a [Å]	b [Å]	c [Å]	alpha	beta	gamma	Volume [$Å^3$]	Density [$g\,cm^{-3}$]
(a) Pure Topaz (for reference)								
0	9.5113	8.9235	8.3942	90.00	89.85	90.00	712.45	3.355
50	9.3807	8.9119	8.4074	90.00	90.00	90.00	702.86	3.438
100	9.3585	8.8126	8.4470	90.00	90.00	90.00	696.65	3.507
(b) $[PO_4]^{4-}$								
0	9.4457	9.0294	8.4077	90.00	89.95	89.82	717.08	3.340
50	9.3253	9.0071	8.3870	90.00	89.96	90.10	704.45	3.438
100	9.3543	8.8486	8.4356	89.78	89.42	90.06	698.19	3.506

Table 7.5: $[PO_4]^{4-}$ Defect Lattice Parameters in Topaz-OH, Topaz-FOH, and Topaz-F. Pure lattice parameters of the host lattice provided for reference.

In all structural and electronic configurations of P-containing defect in topaz, an expansion of lattice parameters is observed. This is surprising as the P^{5+} ion is smaller than Si^{4+}. In figure 7.6, the defect formation energy is plotted as a function of the volume of expansion. Generally, the more stable the defect configuration, the less the system as a whole expands. Here the topaz lattice expands by an additional $0.8 - 2.5\%$, and the host lattice that undergoes the least change is FOH < OH < F. The pure topaz-FOH has the highest degree of disorder within the structure and can therefore accommodate additional defects without large alterations to the dimensions. Figure 7.7 divides the volume into its constituent parameters and shows the defect energy as a function of the percentage change in lattice parameters. The lattice parameters increase in the axis $x \parallel a$ and $z \parallel c$, but decease for $y \parallel b$. This trend is more strong in OH-containing analogues of topaz. (For reference, all the corresponding calculated lattice parameters, cell angles and volumes, for the $[PO_3]^{2-}$ defect in topaz, are given in Appendix E.2 and Tables E.1 and E.2 for CRYSTAL and CP2K respectively).

7.3.2 Bond Distances

The defect energy of forming the $[PO_3]^{2-} + O_i^{2-}$ system from a $[PO_4]^{4-}$ defect centre, is given as a function of the $O_i{-}O_{STRUCT}$ bond distance in Figure 7.8, and the values are summarised (from Table 7.4) for all unique electronic configurations in Table 7.6. Here it can be seen that as the O−O bond order of unique defect species decreases, i.e. $O_2 > O_2^- > O_3^-$, the bond distance as expected increases.

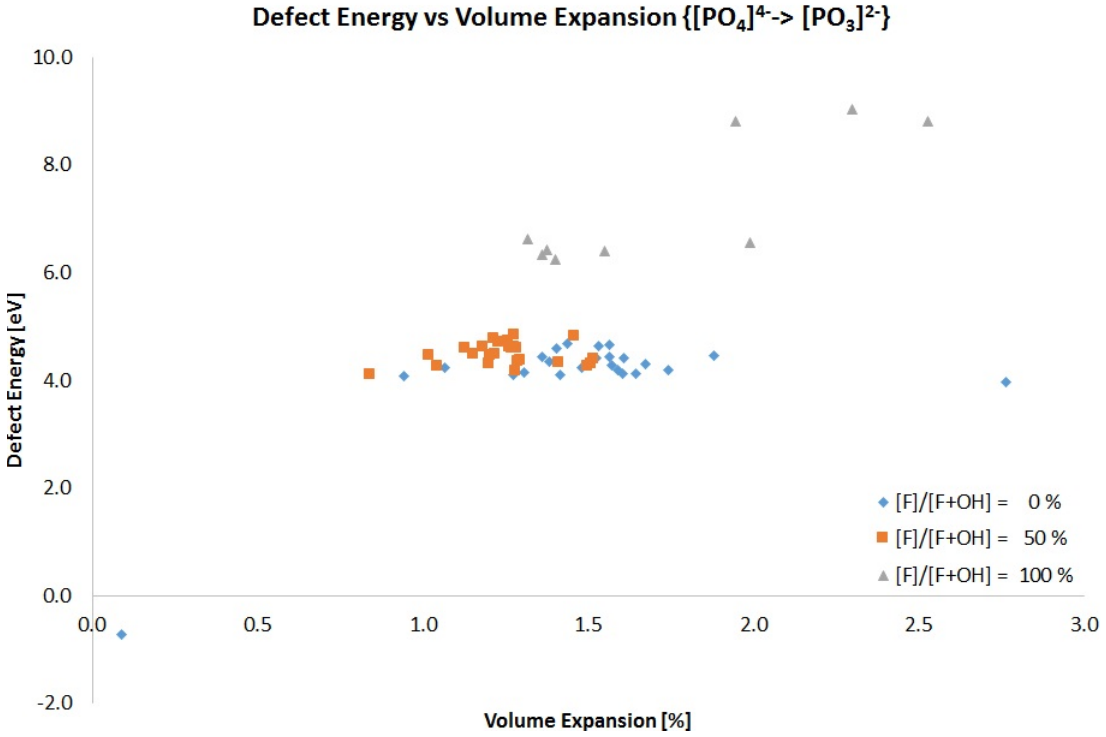

Figure 7.6: The defect energy [eV] as a function of the total cell volume expansion [%] in the reaction scheme $[PO_4]^{4-} \longrightarrow [PO_3]^{2-} + O_i^{2-}$.

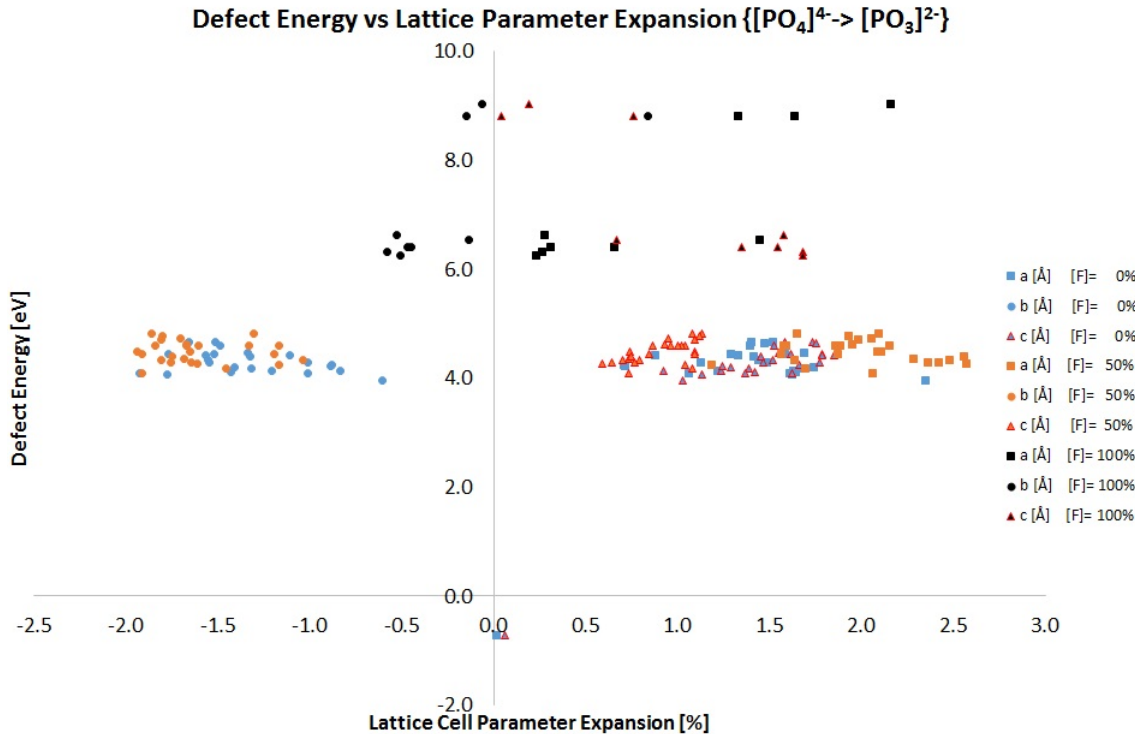

Figure 7.7: The defect energy [eV] as a function of the all three lattice parameters (a, b, and c) in the total effect of cell expansion [%] in the reaction scheme $[PO_4]^{4-} \longrightarrow [PO_3]^{2-} + O_i^{2-}$.

Bond Distance [Å]			
[F]	O_2^-	O_3^-	e_V^-
0	1.944	1.997	
50	1.990	2.079	
100	1.947	-	1.442

Table 7.6: The average $O_i - O_{STRUCT}$ bond distance in $[PO_3]^{2-}$ defect systems.

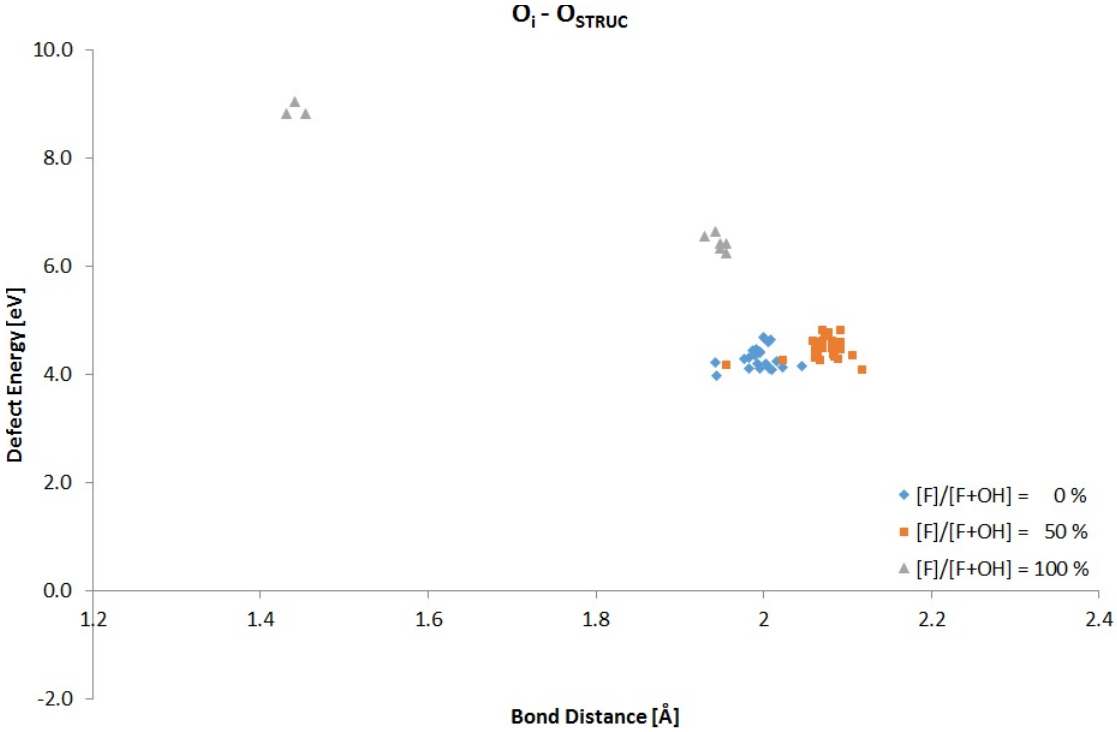

Figure 7.8: The defect energy [eV] for the defect system $[[PO_3]^{2-} + O_i]$ with respect to the interstitial oxygen and the bonding structural oxygen separation [Å], in topaz-OH, topaz-FOH, and topaz-F host lattices.

7.4 Density of States and Band Gap

The total and projected defect atomic density of states for the defect $[PO_4]^{4-}$ in topaz as calculated by CRYSTAL, are given in Figure 7.9, and the total density of states of the defect $[PO_3]^{2-}$ are given in Figure 7.10 (for reference, the projected atomic densities of states calculated using CRYSTAL and the density of states calculated using CP2K, are both provided and given in Appendix E.4 and Figures E.5 and E.5 respectively). Both sets of projected densities of states, for the phosphate and phosphite ions (given in Figure 7.9 and Figure 7.10 respectively), show that the electronic defect states within the band gap are due to the defect species onto which the electron has been localised.

A summary of calculated CRYSTAL and CP2K band gaps are given in Table 7.7, and the defect energy[2] is given as a function of the CRYSTAL calculated band gap in Figure 7.11. The combination of Figure 7.11 and Table 7.7 shows that there are three main groups of band gap energies for P-based defects in topaz: the stable phosphate ($[PO_4]^{4-}$) ion at $\sim$5.0 eV, and the unstable F-centre (e_V^-) and superoxide/ozonide (O_2^-/O_3^-) ions at $\sim$3.8 eV and $\sim 5.9 - 7.3$ eV respectively.

From Table 7.7, the band gap of topaz is shown to decrease significantly from the pure crystal due to the presence of phosphate ($[PO_4]^{4-}$) ions: by between $\sim 3.2 - 3.7$ eV for CRYSTAL calculations, depending on the OH/F environment, and ~ 4.4 eV for CP2K. The overestimation in the calculation of the wide band gap of pure topaz is inherent in hybrid computational methods: the electronic levels within a band gap, however, which are local states to the defect, are better represented by electronic structure calculations. Therefore, the difference in energies between defect states within the band gap can be considered as more reliable. In pure topaz, OH-rich topaz has the smallest band gap, and the trend in band gap size follows OH $<$ FOH $<$ F. In topaz containing phosphate ions (i.e. where the electron is localised on the P), the trend is reversed, i.e. band gap size is reversed, OH $>$ FOH $>$ F. Despite a $\sim$ 3 eV reduction in the CRYSTAL calculated band gaps ($\sim$ 4 eV for CP2K calculation) from a pure topaz crystal to one containing a $[PO_4]^{4-}$ defect, the band gap obtained from calculation does not indicate an optical transition, since violet light spans the wavelengths $380 - 450$ nm, which corresponds to $3.26 - 2.76$ eV (see Section A.1).

Defect electronic configurations of P-based defects in topaz, where the defect electron localises on the interstitial oxygen forming either superoxides (O_2^-) or ozonides (O_3^-) with neighbouring structural oxygens, form band gaps that are larger than those calculated for phosphate ions. There is little distinction between band gaps for O_2^- and O_3^- electronic configurations. There are, however structural changes that influence the band gap instead. Figure 7.12 shows the band gap energy for O_2^- and O_3^- ions in P-topaz as a function of the $P-O_i/O_{STRUC}$ separation (the values of band gaps and atomic separations for individual configurations are given in Tables 7.7 and 7.4 respectively). From Figure 7.12, we are able to observe that defect configurations of the phosphate ion are divided into two groups; those where the O_i is arranged in the same interstitial lattice channel as the P defect at distances of $\sim$1.6 Å, and those where O_i are found in a different interstitial channel away from P at $\sim$4.0 Å. The band gap is found to decrease, by an average of 0.24, 0.22 and 0.93 eV for OH-,

[2]Here the energy is described as the energy required to form either the phosphate ($[PO_4]^{4-}$) or the phosphite ($[PO_3]^{2-}$) defect species from the pure topaz crystal (Equation 7.3).

FOH- and F-host crystals, as the $P{-}O_i/O_{STRUC}$ decreases.

Despite the large energy penalty involved in the formation of F-centres (e_V^-) in topaz with P-based defects (see Tables 7.1 and 7.2), the band gaps calculated indicate this to be the most promising electronic defect in terms of causing colour in topaz (see table 7.7). These electronic defects, only found in the calculations of phosphite ions in topaz-F, have calculated band gaps of between $3.8 - 3.9\,\text{eV}$, which fall close to the violet range of visible light (see Section A.1). A possible mechanism of forming a blue colour centre in topaz could be the creation of F-centres on the oxygen vacancy of phospite ($[PO_3]^{2-}$) defect ions, which form follow a nuclear reaction and β-decay of a Si site to form a phosphate ($[PO_4]^{4-}$) ion, together with the displacement of one of the structural oxygens of the $[PO_4]^{4-}$ tetraherdral ion to an interstitial position (as in Equation 7.9). As previously mentioned, despite the extremely high energy penalty for the creation of an F-centre, an excess amount of very high energy is abundant for a β-decay reaction.

Trends for CP2K calculated band gaps for P-based defects in topaz did not follow those made by CRYSTAL. We attribute this the limitation in k-point sampling of this method.

7.5 UV-Vis Absorption Spectra

The UV-Vis spectra of all the unique electronic structural defects found from our static ground state calculations were calculated using the same method as for the chromium(III) defect in Chapter 6. These are given for reference in Appendix E.5. As with the Cr-based defects, the analysis of the corresponding UV-Vis spectra of P-based defects in topaz is difficult due to the lack of electronic information produced by the method. Clear absorption peaks are not easy to identify in these calculated spectra and so comparison with experimental data would be difficult to perform.

7.6 Conclusion

In this chapter, electronic structure calculations were performed on topaz-OH, -FOH and -F containing a $[PO_4]^{4-}$ defect, and a large number of structural configurations of the defect $[PO_3]^{2-} + O_i^{2-}$, also within these host lattices of topaz. A number of high energy but stable defect electronic structures emerged from geometry optimisations. These may form due to the high energies involved with the formation or doping of phosphorus in topaz via neutron bombardment. The defect electronic structures involved the stabilisation of the extra unpaired spin, required in order to make the

(a) $[PO_4]^{4-}$ Topaz-OH

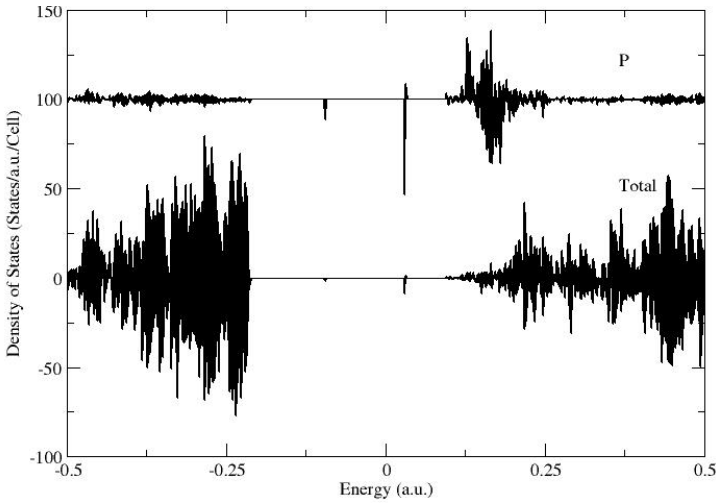

(b) $[PO_4]^{4-}$ Topaz-FOH

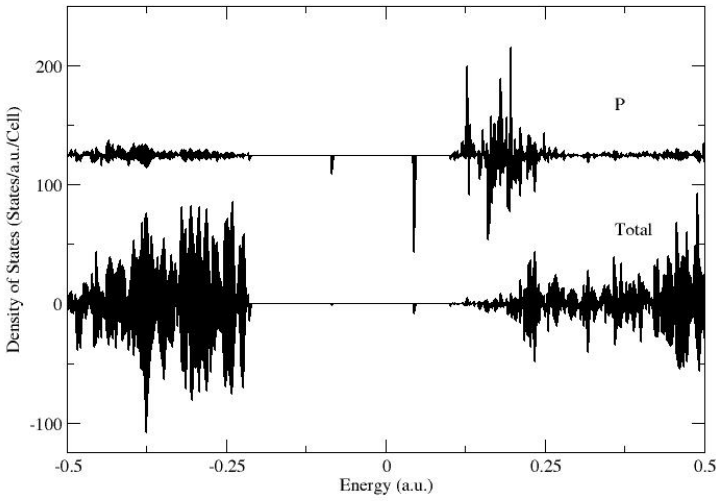

(c) $[PO_4]^{4-}$ Topaz-F

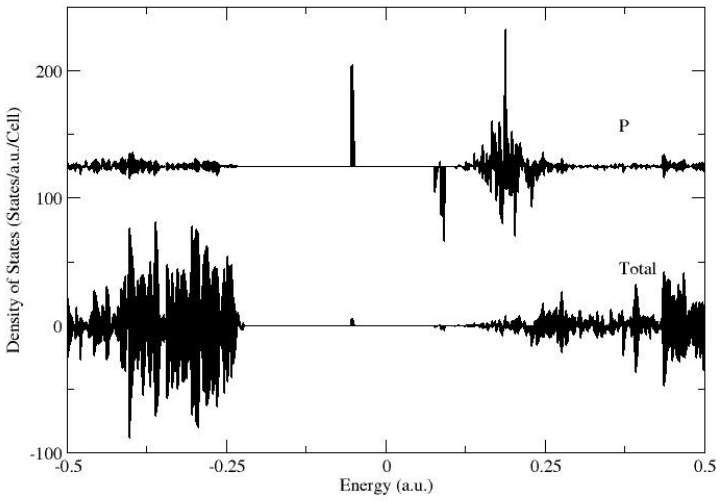

Figure 7.9: CRYSTAL calculated density of states for the $[PO_4]^{4-}$ defect in topaz-OH, topaz-FOH, and topaz-F crystal structures, shown in figures (a), (b) and (c) respectively.

(a) Topaz-OH

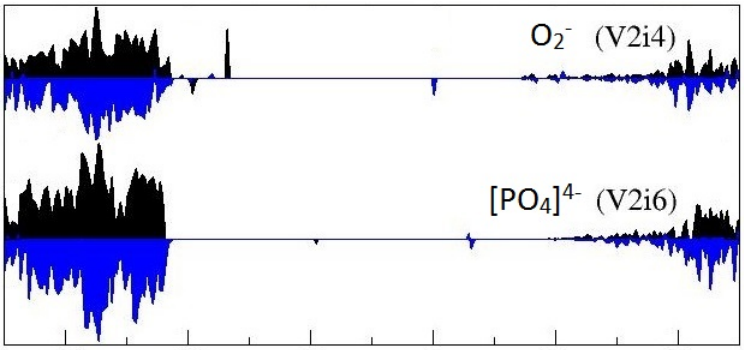

(b) Topaz-FOH

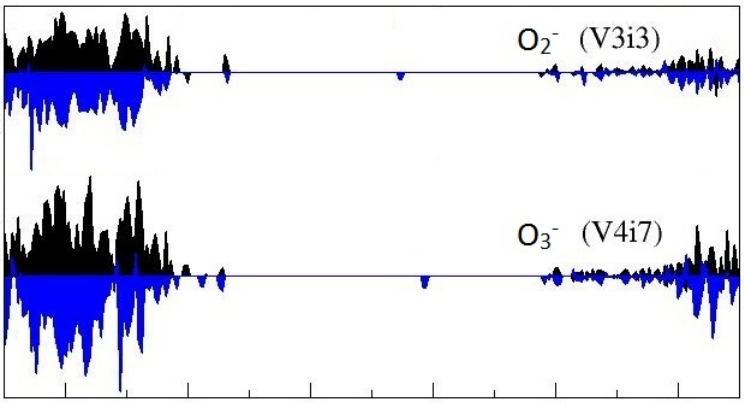

(c) Topaz-F

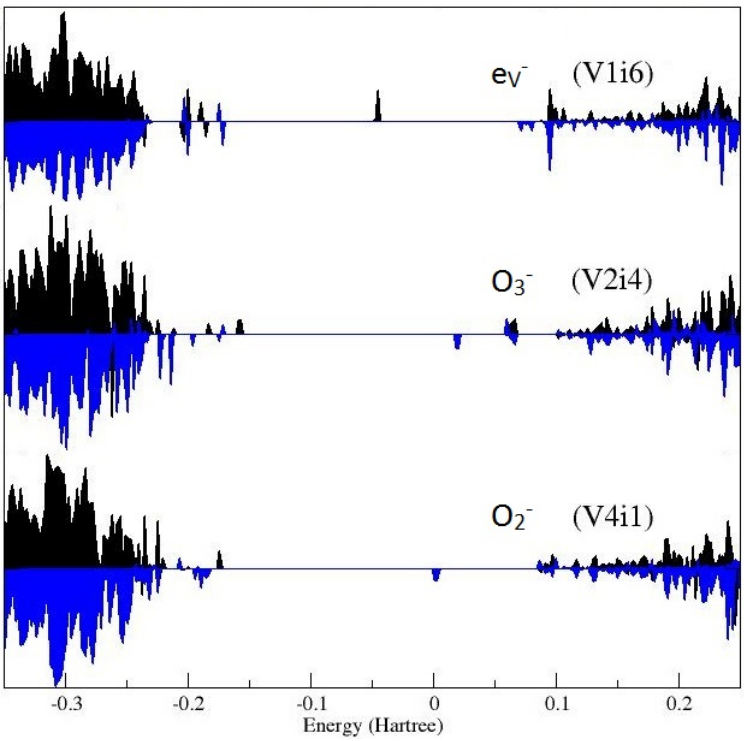

Figure 7.10: Total density of states for the $[PO_3]^{2-}$ defect in (a) topaz-OH, (b) topaz-FOH, and (c) topaz-F, as calculated using the CRYSTAL code. The total density of states including projections of individual defect ions for the $[PO_3]^{2-}$ defect configurations singled out here are given in Appendix E.4.

Defect Energy [eV]						
Config.	CRYSTAL			CP2K		
$\frac{[F]}{[F+OH]}$	0%	50%	100%	0%	50%	100%
(a) Pure Topaz						
	8.373	8.496	8.496	7.123	7.332	7.570
(b) $[PO_4]^{4-}$						
	5.197	5.052	4.807	2.723	-	-
(c) $[PO_3]^{2-}$						
V1i1	6.829	7.022	-			
V1i2	-	6.890	-	2.569		
V1i3	6.995	7.132	6.920			
V1i4	-	-	3.772			
V1i5	6.707	6.886	-			
V1i6	6.648	6.621	3.830			4.335
V1i7	6.736	6.976	-			
V1i8	6.861	7.143	-			
V2i1	6.936	6.840	-			
V2i2	6.688	6.505	-			
V2i3	7.078	7.136	3.863			
V2i4	6.491	-	5.935	2.225		4.079
V2i5	7.131	7.130	-			
V2i6	5.210	-	-	2.473		
V2i7	-	-	-			
V2i8	-	6.717	-			
V3i1	7.047	7.247	6.898			
V3i2	6.785	6.930	-			
V3i3	7.075	7.049	-		3.148	
V3i4	-	-	-			
V3i5	6.888	6.945	-			
V3i6	-	7.145	6.613			
V3i7	7.002	7.024	-			
V3i8	6.985	7.063	-			
V4i1	-	7.315	7.042			2.850
V4i2	-	6.885	-			
V4i3	6.850	7.088	-			
V4i4	-	-	-			
V4i5	6.771	6.999	-			
V4i6	6.831	-	-			
V4i7	6.889	7.223	-		3.509	
V4i8	6.946	6.956	-			

Table 7.7: The CRYSTAL and CP2K calculated band gaps of P-based defects in topaz, for (a) the $[PO_4]$ and (b) $[PO_3] + O_i$, in topaz. (The labeling convention used to distinguish different starting phosphite configurations is outlined in Appendix E.1).

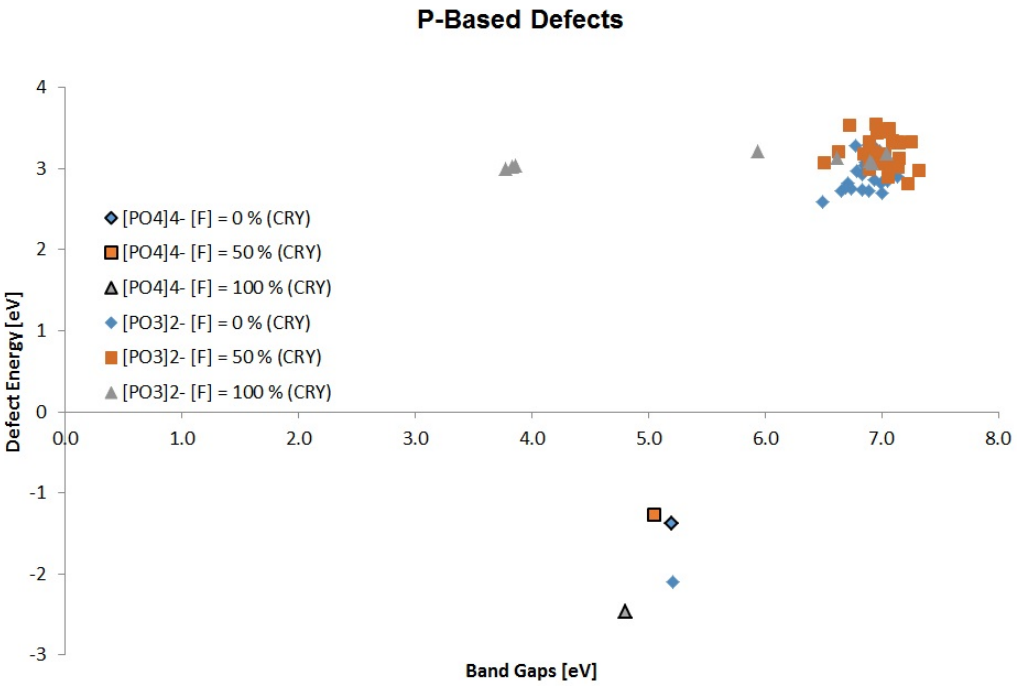

Figure 7.11: The defect energy [eV] as a function of the band gap energy calculated with CRYSTAL for P-based defect systems, in topaz-OH, -FOH, and -F host lattices. The energy given is that which is required to form either the phosphate ($[PO_4]^{4-}$) or the phosphite ($[PO_3]^{2-}$) defect species from the pure topaz crystal (Equation 7.3).

system charge neutral in the presence of a phosphorus defect, involved the formation of a superoxide (O_2^-), an ozonide (O_3^-) and an F-centre (e_V^-). It was also shown that the recombination of the oxygen interstitial back into the phosphorus tetrahedra, from which it was formed, was also possible. The latter was the most stable process and suggested that annealing of these defects could be possible. The ozonide could be reinterpreted as a polaron (O^-), and together with the prediction of the superoxide forming under high energy conditions and in the presences of a phosphorus atom within the crystal, these two defect models are supported by experimental literature models discussed in Chapter 5 and given by references [6, 8, 37, 38].

Structurally, the oxygen interstitial has predictable bond lengths with neighbouring structural oxygens, based on bond order and dependent on where the additional electron is localised in the structure and how many structural oxygens are involved with its stabilisation. The $O_i{-}O_{STRUC}$ in P-bearing topaz was found to follow the trend $O_2 > O_2^- > O_3^-$. Variations in the bond length occur due to different OH/F mixing in topaz.

The calculated band gaps of P-based defects in topaz were shown to significantly reduce the wide band gap of pure topaz. The order of the band gaps of phosphite based defects in topaz followed the trend: $O^{2-}/O^{3-} > [PO_4]^{4-} > e_V^-$. The band gaps of electronic defects O^{2-}/O^{3-} were shown to reduce as the interstitial oxygen

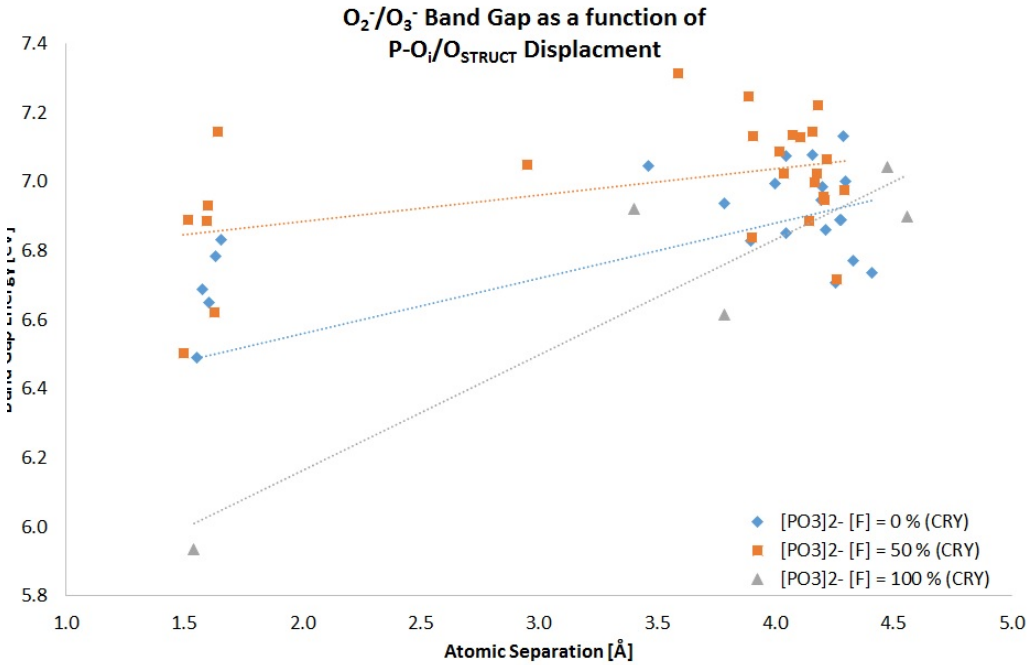

Figure 7.12: The band gap energy of P-based defects is topaz containing superoxide (O_2^-) and ozonide (O_3^-) ions are given as a function of the $P-O_i/O_{STRUC}$ separation.

became closer to the $[PO_3]^{2-}$ ion. The only electronic defect resulting from one of the phosphite ion configurations to indicate a possible change in the possibility of an optical appearance was the F-centre (e_V^-). This defect was only found in topaz-F.

UV-Vis spectra of phosphate and phosphite ions in topaz were performed. However, further analysis was not possible due to lack of electric information provided by the method and the proper convergence of peaks. Thheir result were, however, presented in Appendix E for reference.

Chapter 8

Silicon Based Intrinsic Defects in Topaz

8.1 Introduction

Another class of defects to emerge from the literature investigation of Chapter 2 as possible colour effecting centres, involved intrinsic defects centred about silicon ions. The most commonly described defect is the $[SiO_3]^{2-}$ ion species. In this section, we present the results of our extensive investigation of Si-based defects in topaz and provide analysis of their relative stabilities, structural and electronic characteristics. These results were performed using CRYSTAL calculations.

8.1.1 Defect Formulas

In an analogues way to the creation of phosphite ($[PO_4]^{4-}$) ions in topaz from phosphate ions ($[PO_3]^{2-}$) in Chapter 7, the removal of an oxide ion (O^{2-}) from the silicate ($[SiO_4]^{4-}$) tetrahedra to an interstitial position, can be given the reaction scheme

$$[SiO_4]^{4-} \longrightarrow [SiO_3V_O^{\bullet\bullet}]^{2-} + [O_i'']^{2-}. \tag{8.1}$$

As previously seen for P-based defects, there are 8 interstitial position in a $2 \times 1 \times 1$ unit cell of topaz into which the displaced oxide ion can be placed, and 4 tetrahedral oxides in the silicate from which to create the vacancy. Therefore, 32 defect configurations of $[SiO_3]^{2-} + O_i^{2-}$ for each of the three topaz compositions were considered, making a total of 96 defect calculations (see Appendix E and Section E.1 for the labeling convention, which is the same as for the phosphite ion configurations).

8.2 Defect Energy

Since the composition of topaz is the same before and after defect formation, the defect energy for the process given in Equation 8.1 is simply the difference between the total calculated energies of the two crystals:

$$\begin{aligned}\Delta H_f([\mathrm{SiO_3}]^{2-}) =& E_{tot}(\mathrm{Al_{16}[SiO_3V_O^{\bullet\bullet}][O_i'']Si_7O_{32}(OH,F)_{16}}) \\ &- E_{tot}(\mathrm{Al_{16}Si_8O_{32}(OH,F)_{16}})\end{aligned} \tag{8.2}$$

In order, however, to create an open shell system in which to study optically active defects, the oxygen that is extracted from the silicate tetradhedra leaves behind a vacancy with one unpaired electron, and created an interstitial oxygen with the other unpaired electron, i.e. Equation 8.1 becomes instead

$$[\mathrm{SiO_4}]^{4-} \longrightarrow [\mathrm{SiO_3V_O^{\bullet}}]^{3-} + [\mathrm{O_i'}]^{-}. \tag{8.3}$$

Full optimisation of the structure will provide an insight as to where these two electrons are likely to localise. In Table F.2 (of Appendix F.2), the calculated defect energies for optimised defect structural configurations are given together with their defect electronic configurations. The defect electronic configuration category is supported by the Mulliken analysis (also given in Table F.2) and the isovalue spin density plots in Figure 8.1.

As with our investigation of P-based defects in topaz in Chapter 7, the SCF process of optimising the electronic and geometrical structure of the $[\mathrm{SiO_3V_O^{\bullet}}]^{3-} + [\mathrm{O_i'}]^{-}$ defect in topaz, generates a variety of energetically unique electronic configurations. These are summarised by the following reaction schemes and their labels,

$$[\mathrm{SiO_3V_O^{\bullet}}]^{3-} + [\mathrm{O_i'}]^{-} \longrightarrow [\mathrm{Si^{\bullet}O_3O'}]^{4-} \qquad = [\mathrm{SiO}]^{2-} \tag{8.4}$$

$$[\mathrm{SiO_3V_O^{\bullet}}]^{3-} + [\mathrm{O_i'}]^{-} \xrightarrow{+\mathrm{O}} [\mathrm{SiO_3V_O^{\bullet}}]^{3-} + [\mathrm{O'O}]^{-} \qquad = [\mathrm{SiV}]^{-} + \mathrm{O}^{-}/\mathrm{O_2^{-}} \tag{8.5}$$

$$[\mathrm{SiO_3V_O^{\bullet}}]^{3-} + [\mathrm{O_i'}]^{-} \xrightarrow{+3\,\mathrm{O}} [\mathrm{SiO_3}]^{2-} + [\mathrm{O''O_3}]^{2-} \qquad = [\mathrm{O_4}]^{2-} \tag{8.6}$$

$$[\mathrm{SiO_3V_O^{\bullet}}]^{3-} + [\mathrm{O_i'}]^{-} \xrightarrow{+[_3\mathrm{O}]^{2-}} [\mathrm{SiO_3}]^{2-} + [\mathrm{O''O_3}]^{4-} \qquad = [\mathrm{O_4}]^{4-} \tag{8.7}$$

$$[\mathrm{SiO_3V_O^{\bullet}}]^{3-} + [\mathrm{O_i'}]^{-} \longrightarrow [\mathrm{Si^{\bullet}O_3V^{\bullet}}]^{4-} + \mathrm{O_2} \qquad = [\mathrm{SiV}]^{2-} + \mathrm{O_2} \tag{8.8}$$

The unique energies for the reaction schemes given in Equations 8.4-8.8, are sum-

marised in Table 8.1 together with Mulliken population analisys (see Table F.2 in Appendix F.2 for the complete list of energies and Mulliken analisys of all the $[SiO_3]^{2-}$ defects considered).

Mulliken Population Analysis for $[SiO_3]^{3-} + O_i^-$ Defect Configurations											
[F]	Config.	Defect E. [eV]	Elect.	Atom	Spin	Atom	Spin	Atom	Spin	Atom	Spin
(a) $[SiO]^{2-}$, (Equation 8.4)											
0	V1i4	6.546	$[SiO]^{2-}$	Si	0.613	O_i	0.953				
50	V2i6	6.699	$[SiO]^{2-}$	Si	0.807	O_i	0.901				
50	V3i4	8.115	$[SiO]^{2-}$	Si	0.782	O_i	0.857				
100	V4i4	6.597	$[SiO]^{2-}$	Si	0.846	O_i	0.846				
(b) $[SiV]^- + O^-$ or $[SiV]^- + [O_2]^-$, (Equation 8.5)											
100	V3i4	6.609	$[O_2]^-$	O_i	0.843	O	0.157	F	0.002	F	0.001
(c) $[O_4]^{2-}$, (Equation 8.6)											
0	V1i3	11.207	$[O_4]^{2-}$	O_i	1.435	O	0.271	O	0.139	O	0.137
50	V1i6	11.188	$[O_4]^{2-}$	O_i	1.520	O	0.250	O	0.097	F	0.017
100	V3i3	9.527	$[O_4]^{2-}$	O_i	1.626	O	0.287	F	0.036	F	0.033
(d) $[O_4]^{4-}$, (Equation 8.7)											
0	V2i3	11.324	$[O_4]^{4-}$	O_i	1.116	O	0.356	O	1.041	O	1.013
(e) $[SiV]^{2-}$, (Equation 8.8)											
100	V2i1	11.331	$[SiV]^{2-}$	Si	0.670	V_O	0.822				

Table 8.1: Mulliken population analysis for the energetically unique defect configurations of $[SiO_3]^{2-}$. (The labeling convention used to distinguish different starting $[SiO_3]^{2-} + O^{2-}$ configurations is the same as for the phosphite configurations in Chapter 7 and is outlined in Appendix E.1).

Several interesting oxygen based defects resulting form in a $[SiO_3]^{2-} + O^{2-}$ defect system in topaz: the $[O_4]^{2-}$ and the $[O_4]^{4-}$ species (Equations 8.6 and 8.7 respectively). These follow the removal of an O^- species from the silicate tetrahedra into an interstitial position. The oxide is stabilised by three anion species, one structural oxygen (O_{STRUCT}) and two OH/F species, in a trigonal-planar arrangement (see Figures 8.1(b), 8.1(e) and 8.1(g)). Polarisation of the spin occurs in the x-direction and towards the single structural oxygen. Mulliken analysis (in Table 8.1 or F.2) indicates that a larger proportion of spin from the oxide species delocalises on to the anion of $O_{STRUCT} > OH > F$ species.

Equations 8.4, 8.5 and 8.8 all refer to forming a $Si^\bullet$ radical, and either an $O^\bullet$ radical or an $e^\bullet$ F-centre. In the defect configurations of Equations 8.4 and 8.7, the silicate tetrahedra is reformed, by either elongation in the direction of the recombined oxygen ion (see Figures 8.1(a) and 8.1(c)), or a reformed distorted tetrahedra (see Figures 8.1(d) and 8.1(f)). For the defect configuration of Equation 8.8, the metasilicate ($[SiO_3]^{2-}$ ion has the additional electronic structure of the spin located on the Si ion, together with the interaction of the F-centre (e^-) from the vacancy po-

sition: the relocated interstitial oxygen combines with a structural oxygen in crystal to form an interstitial oxygen molecule (O_2).

As seen before with the phosphite chemistry in topaz in Chapter 7, the $[SiO_3]^{2-}$ + O^{2-} defect system in topaz also leads to the formation of either a superoxide (O^- or an oxide (O^{2-}) species (Equation 8.5). The formation of the oxide interstitial is stabilised by surrounding structural oxygens, which leads to the variation in choice of label here, since the defect is somewhere between an oxide and a superoxide. The other unpaired electron localises onto the Si atom and is stabilised by the vacancy.

The generation of each of these defects is highly unfavourable under normal reaction conditions, however the irradiation of materials generates a lot of energy so all of these defect states should be accessible. For defect centres labelled $[O_4]^{2-}$ and $[SiO]^{2-}$, the topaz analogue preferred for formation are OH > F > FOH and F > FOH > OH respectively: defect centre $[O_4]^{4-}$ only forms in topaz-OH, and O^- and $[SiV]^{2-}$ only form in topaz-F.

8.3 Structural Analysis

The defect energy $\Delta H_f([SiO_3]^{2-})$ (Equation 8.2) is given as a function of the percentage of [F] (i.e. $[F]/[OH]^+[F]$) as it increases in Figure 8.2, as a function of the volume expansion in Figure 8.3, as a function of the individual lattice parameter expansion in Figure 8.4, and the $Si-O_i$ atomic separation in Figure 8.5.

From Figure 8.2, it can be seen that there are two energy distinct defect electronic configurations in topaz-OH, and at least three in topaz-FOH and topaz-F. The defect energies recorded for these electronic configurations are much larger than those seen for defect energies of P-based defect in topaz. Only Under extreme conditions could these defects likely form.

The expansion of cell volumes and lattice parameters range from between $0 - 1.5\%$. These are unique for each type of defect electronic configuration. The creation of the $[SiV]^{2-}$ in topaz-F not only has a high energy penalty, increases causes up to 3% of unit cell expansion (for a complete listing of calculated cell parameters for all the structural configurations, refer to Appendix F.1). There is a variation in the expansion of the individual lattice parameters depending on the type of defect: from Figure 8.4, it is shown that the expansion due to the polarisation of the unpaired spin for the $[O_4]^{2-}$ defect in the x-direction, causes the $a \parallel x$ lattice parameter to increase more than the other axes.

In the Figure 8.5, a range of $Si-O_i$ separations given with respect to the defect formation energy, show that the a migration of O_i ions has very little effect on the

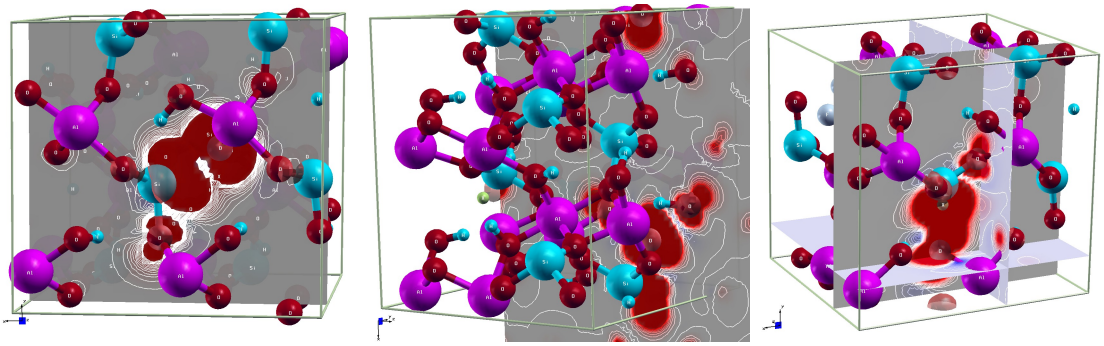

(a) (V1i4) Topaz-OH (b) (V4i7) Topaz-OH (c) (V2i6) Topaz-FOH

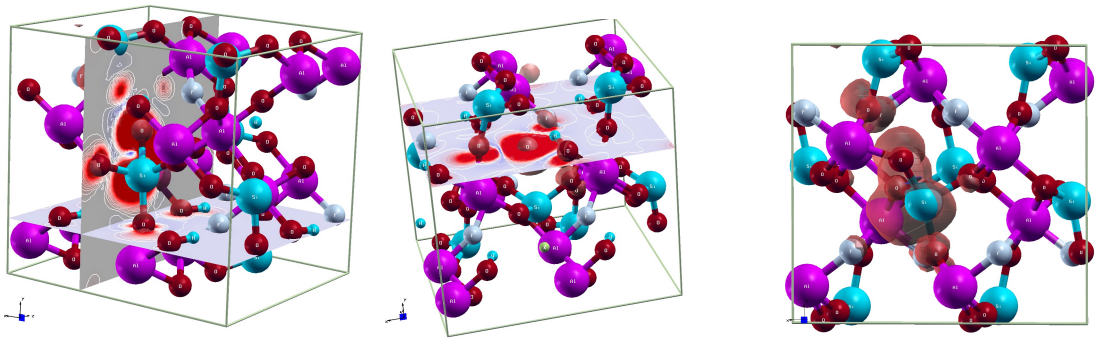

(d) (V3i4) Topaz-FOH (e) (V2i4) Topaz-FOH (f) (V4i4) Topaz-F

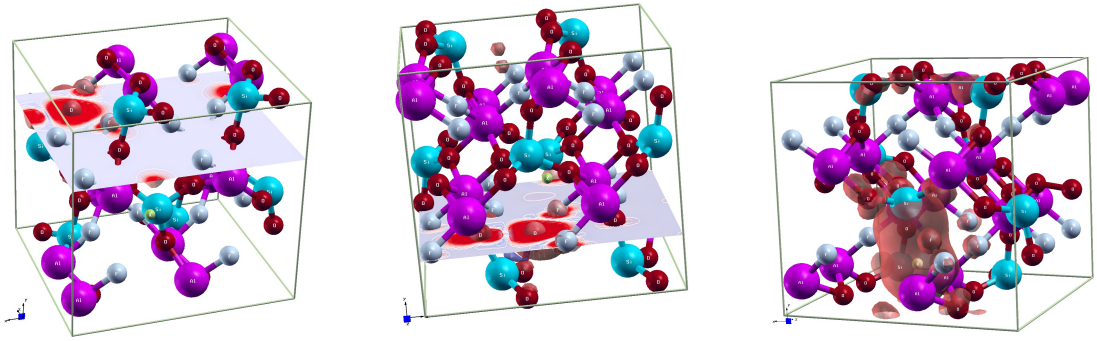

(g) (V4i7) Topaz-F (h) (V2i2) Topaz-F (i) (V2i1) Topaz-F

Figure 8.1: 3-Dimensional Spin Density of Silicon Based Intrinsic Defects in ((a)-(b)) topaz-OH, ((c)-(e)) topaz-FOH, and ((f)-(i)) topaz-F calculated using CRYSTAL.

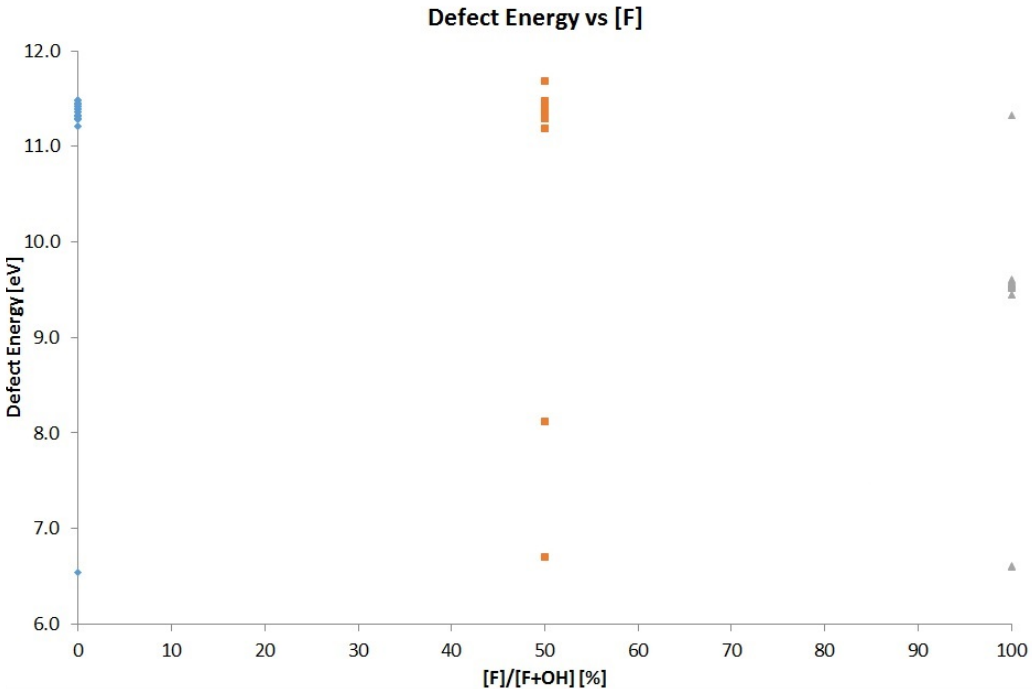

Figure 8.2: The defect energy [eV] as a function of the [F]:[OH] content [%] in the reaction scheme $[SiO_4]^{4-} \longrightarrow [SiO_3]^{2-} + O_i^{2-}$.

energy of the system and therefore migration is unlikely to change in the defect energy. Silicon based intrinsic defects in topaz could therefore act as the location within the cell where colour centres migrate to in order to stabilise.

8.4 Spin Densities and Band Gap Analysis

The analysis of energetically unique defect electronic configurations of Si-based intrinsic defects in topaz has yielded a wide range of defect types. The total densities of states for all the unique electronic configurations in all three topaz analogues are given in Figure 8.6 (also see Appendix F for projected atomic density of states). As has been shown by our $(\alpha - \beta)$ spin population analysis (see Figure 8.1), the unpaired spin of these open shell systems has localised onto one or both of the defect centres. These defect centres have then been shown to form defect states within the band gap, reducing the band gap and potentially altering the optical properties of the material. The unique electronic configurations established in Section 8.2 all display a unique characteristic arrangement of localised bands within the band gap.

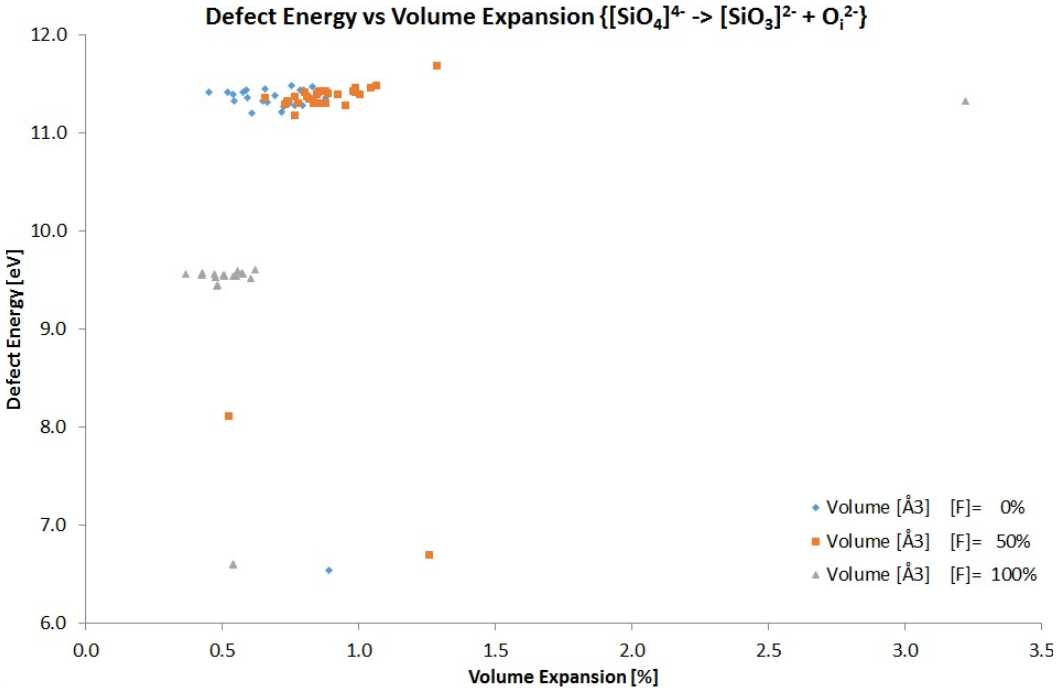

Figure 8.3: The defect energy [eV] as a function of the total cell volume expansion [%] in the reaction scheme $[SiO_4]^{4-} \longrightarrow [SiO_3]^{2-} + O_i^{2-}$.

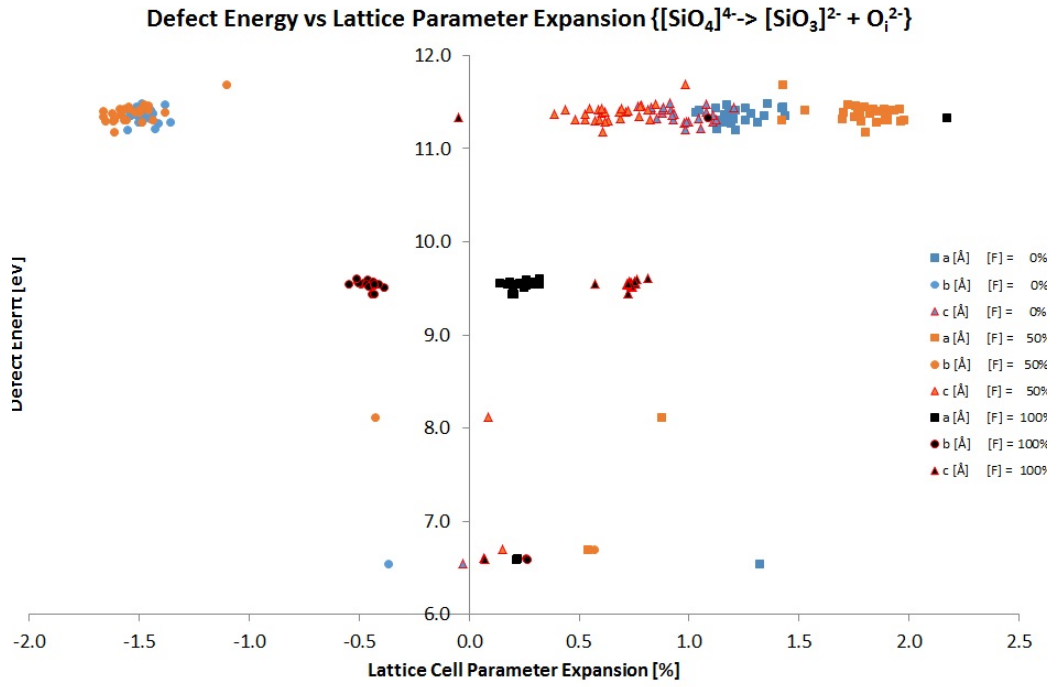

Figure 8.4: The defect energy [eV] as a function of the all three lattice parameters (a, b, and c) in the total effect of cell expansion [%] in the reaction scheme $[SiO_4]^{4-} \longrightarrow [SiO_3]^{2-} + O_i^{2-}$.

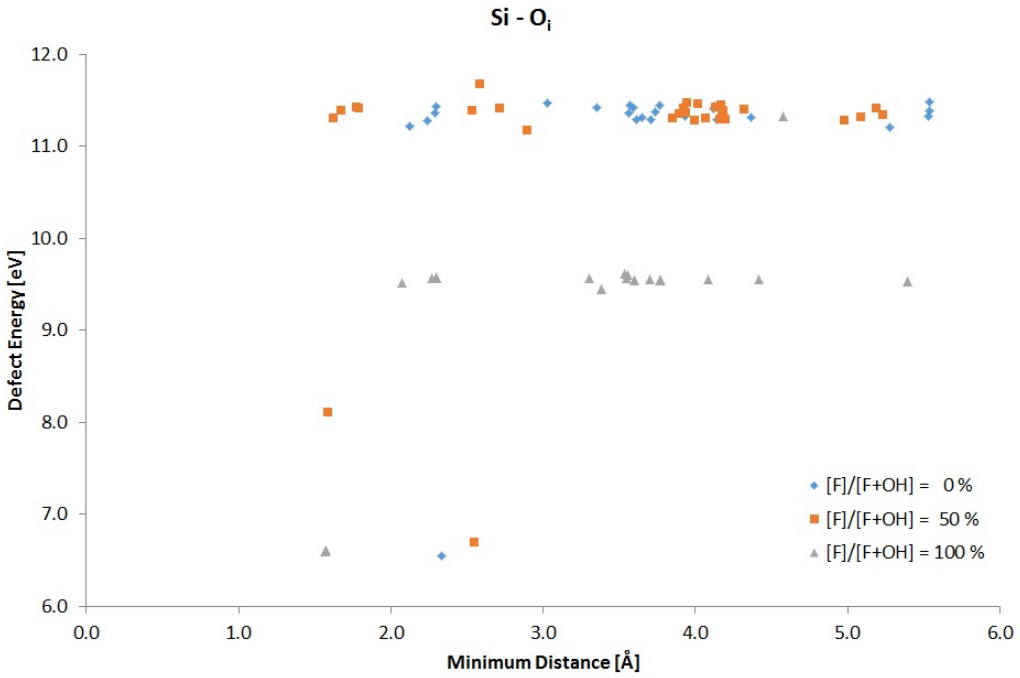

Figure 8.5: The defect energy [eV] as a function of the minimum separation Si−O$_i$ [Å] in the reaction scheme $[SiO_4]^{4-} \longrightarrow [SiO_3]^{2-} + O_i^{2-}$.

8.5 Conclusion

The calculated defect energy for the formation of Si-based intrinsic defects in topaz, are based on the creation of an oxygen vacancy from a silicate tetrahedra and its relocation into an interstitial site, i.e. $[SiO_3V_O]^{3-} + O_i^-$, generated an unexpectedly large number and variety of open shell defects. These included the formation of the following defect centres: $[Si^{\bullet}O_3O']^{4-}$, which is the recombination of displaced $[SiO_3V_O]^{3-}$ and O_i^- defects (i.e. $[SiO]^{2-}$); $[SiO_3V_O^{\bullet}]^{3-} + [O'O]^-$, where the O_i^- is stabilised primarily by one of the nearest O_{STRUCT}, and an F-centre in formed (i.e. $[SiV]^- + O^-$); $[SiO_3]^{2-} + [O''O_3]^{2-}$, where $3\,O_{STRUCT}$ are required for stabilisation of +2 electron spin (i.e. $[O_4]^{2-}$); $[SiO_3]^{2-} + [O''O_3]^{4-}$, where $3\,O_{STRUCT}$ are required for stabilisation of +4 electron spin ($[O_4]^4$); and $[Si^{\bullet}O_3V^{\bullet}]^{4-} + O_2$, which is the creation of an interstitial O_2 molecule, a silicon radical and an F-centre ($[SiV]^{2-} + O_2$).

The formation energy for these defect centres were found to be unfavourably high. Since formation occurs under extreme conditions, i.e. irradiation, an abundance of energy is in the system and for even the F-centre to be formed in topaz. The defect configurations that localise an unpaired electron(s) onto an interstitial oxygen, tend to structurally expend in the $x \parallel a$ direction, because the majority of delocalised spin from the interstitial is polarised onto a neighbouring oxygen in the same direction. The defects centres all contributed localised electronic bands into the band gap

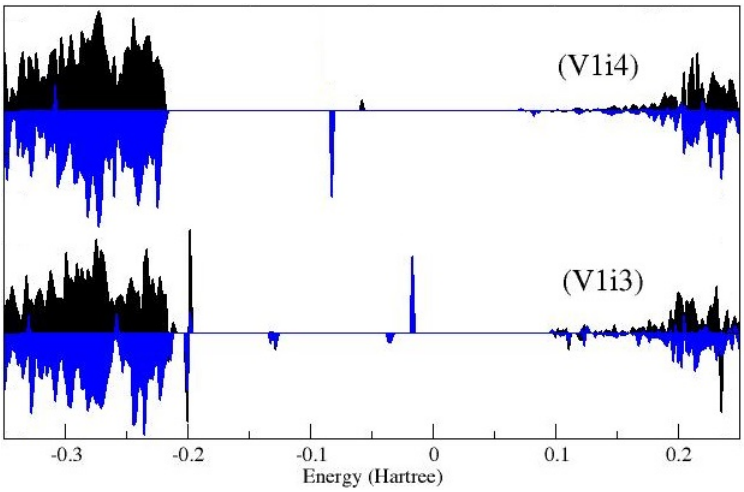

(a) Topaz-OH

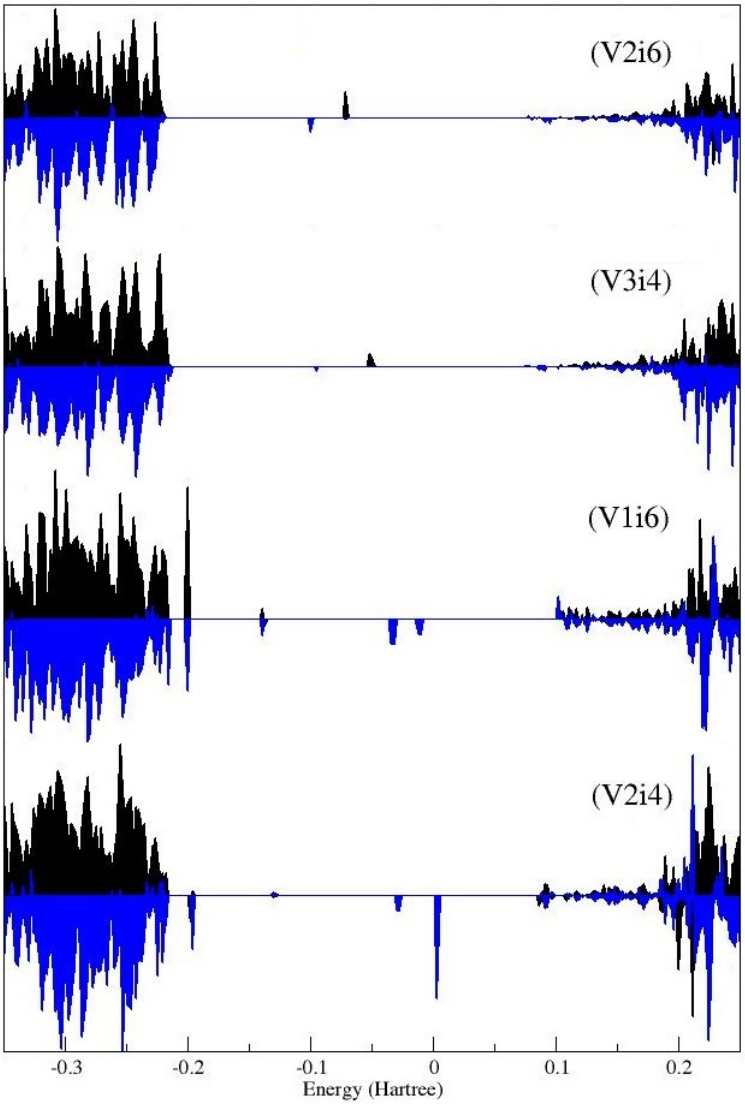

(b) Topaz-FOH

Figure 8.6: This figure is continued.

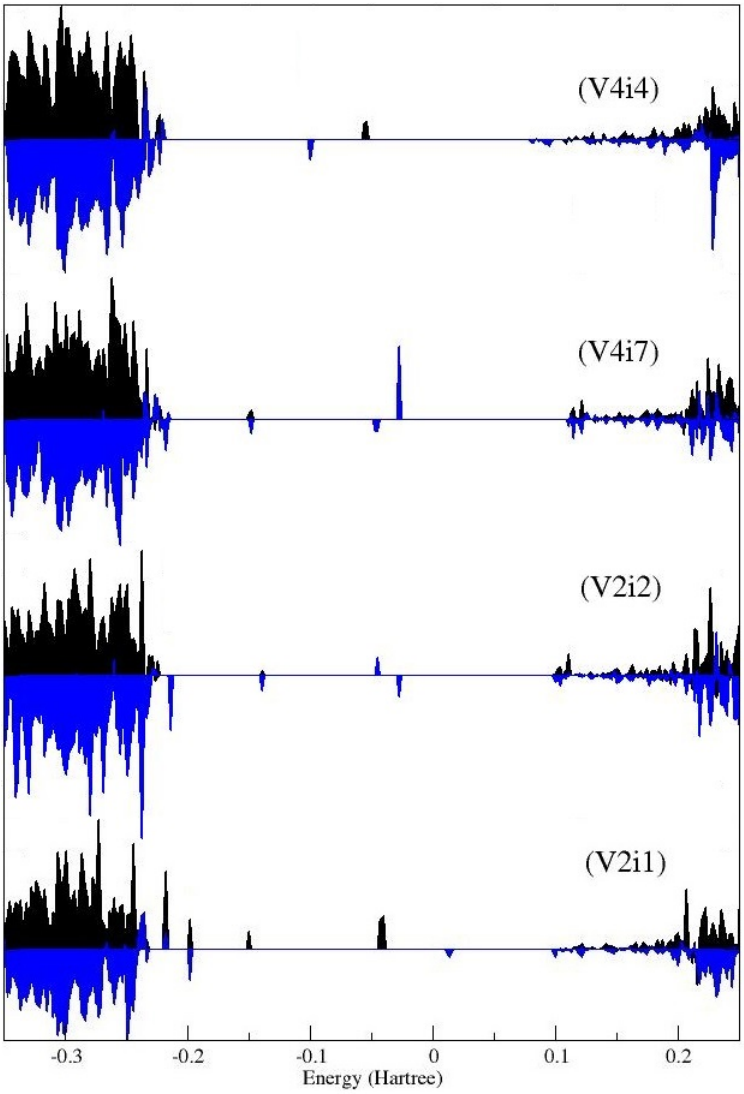

(c) Topaz-F

Figure 8.6: Total density of states for the $[SiO_3]^{2-}$ defect in (a) topaz-OH, (b) topaz-FOH, and (c) topaz-F, as calculated using the CRYSTAL code. The total density of states including projections of individual defect ions for the $[SiO_3]^{2-}$ defect configurations singled out here are given in Appendix F.3.

reducing the fundamental transition. Advanced techniques would determine which if any of these defect centres were optically active.

Chapter 9

Oxygen Based Intrinsic Defects in Topaz

9.1 Introduction

In this chapter, we discuss another the class of intrinsic defects within topaz, which involve the displacement of a neutral hydrogen atom from a structural hydroxide ($[OH]^{-}$) ion, leaving an open shell O^{-} ion. From our defect calculations in CRYSTAL, we presented the defect formation energies and structural trends, spin densities and densities of states, Mulliken population analysis, and optical absorption spectral trends for this defect system.

9.1.1 Defect Formulas

The displacement of a neutral H species from a cleaved hydroxide ion bond into an interstitial position the within topaz can be given as

$$[OH]^{-} \longrightarrow [O^{\bullet}V_{H}^{\times}]^{-} + H_{i}^{\prime}. \tag{9.1}$$

Prior to optimisation, there is a a single unpaired electron localised onto both defect species H_i and OV_H^- sites. Since the hydroxide ion is only present in topaz structures rich in OH, only two lattice hosts were considered here, the topaz-OH and the topaz-FOH.

The labeling convention adopted here s similar to those use in Chapters 7 and 8. Only one site from which to create a vacancy V_H from a hydroxide unit, but there are still 8 possible location within a $2 \times 1 \times 1$ supercell of topaz in which to insert an interstitial. The labels take the following form, e.g. OHi1 indicates that the H_i is

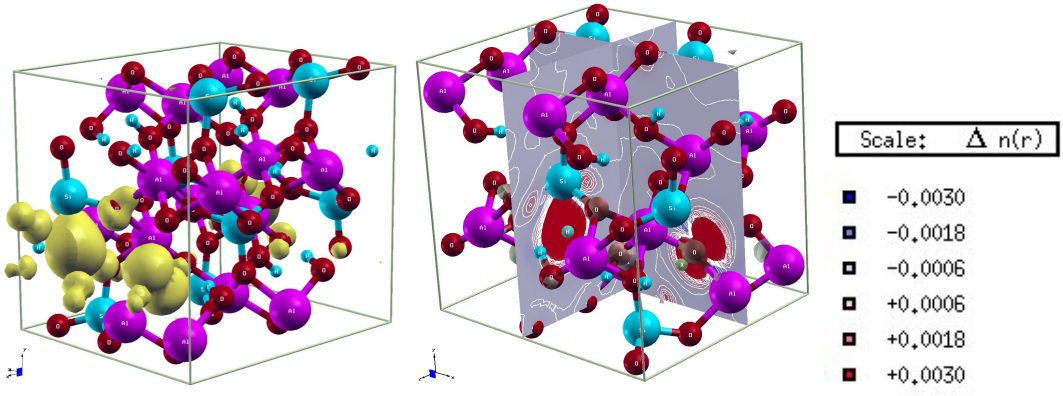

(a) *3D solid* (b) *2D planes* (c) Isovalue Thermoscale

Figure 9.1: 3-Dimensional spin density representations of oxygen based intrinsic defect, the displacement of hydroxyl group ($[\mathrm{OV_H}]^{-} + \mathrm{H_i}$). The $(\alpha - \beta)$ spin density is shown to be well localised around the $\mathrm{O_{(OH)}}$ and $\mathrm{H_i}$ defect species, ((a)) solid yellow and ((b)) isovalue plane contours. The isovalue scale for ((b)) is given in ((c)).

located one the interstitial site labelled 1 (see Table E.3 for the lattice coordinates of the interstitial positions).

9.2 Defect formation Energy and Mulliken Population Analysis

The defect formation energy of creating the $[\mathrm{OV_H}]^{-} + \mathrm{H_i}$ system in topaz, can be given as

$$\begin{aligned}\Delta H_f([\mathrm{OV_H}]^{-} + \mathrm{H_i}) =& E_{tot}(\mathrm{Al_{16}Si_8O_{32}(OH,F)_{15}[O^{\bullet}V_H][H_i']}) \\ &- E_{tot}(\mathrm{Al_{16}Si_8O_{32}(OH,F)_{16}}).\end{aligned} \tag{9.2}$$

The defect formation energies and Mulliken population analysis are presented in Table 9.1. The two unpaired spins are shown to remain localised on the two defect species, $\mathrm{H_i}$ and $\mathrm{OV_H^{-}}$, for all the structural configurations considered. Therefore there is only one electronic configuration possible for this type of defect.

The energy required to form the $[\mathrm{OV_H}]^{-} + \mathrm{H_i}$ defect system in the topaz analogues OH and FOH is $\sim 6.17 - 6.22\,\mathrm{eV}$ and $\sim 6.38 - 6.47\,\mathrm{eV}$ respectively. If we combine the Mulliken $(\alpha - \beta)$ spin population analysis in Table 9.1 together with the isothermal $(\alpha - \beta)$ spin density plots given in Figure 9.1, we can see that the spin on the $\mathrm{H_i}$ species is stabilised by the delocalisation of some of the unpaired spin onto surrounding oxygen ions. The redistribution of localised $\mathrm{H_i}$ spin is more extensive

in topaz-OH. This is demonstrated by there being less Mulliken spin found on the H_i in topaz-OH than for topaz-CeFOH, and may help explain why it is $\sim 0.21\,eV$ easier to create this defect system in topaz-OH than topazFOH.

Mulliken Population Analysis for $[OV_H]^- + H_i$ Defect Configurations						
Config.	Defect Energy	Elect. Config.	Atom	Spin	Atom	Spin
(a) Topaz-OH						
OHi1	6.199	$OV_H^- + H_i$	OV_H^-	0.939	H_i	0.783
OHi2	6.197	$OV_H^- + H_i$	OV_H^-	0.935	H_i	0.794
OHi3	6.213	$OV_H^- + H_i$	OV_H^-	0.940	H_i	0.784
OHi4	6.210	$OV_H^- + H_i$	OV_H^-	0.942	H_i	0.785
OHi5	6.173	$OV_H^- + H_i$	OV_H^-	0.940	H_i	0.775
OHi6	6.182	$OV_H^- + H_i$	OV_H^-	0.927	H_i	0.786
OHi7	6.217	$OV_H^- + H_i$	OV_H^-	0.940	H_i	0.781
OHi8	6.214	$OV_H^- + H_i$	OV_H^-	0.941	H_i	0.783
(a) Topaz-OH						
OHi1	6.413	$OV_H^- + H_i$	OV_H^-	0.953	H_i	0.807
OHi2	6.439	$OV_H^- + H_i$	OV_H^-	0.954	H_i	0.812
OHi3	6.438	$OV_H^- + H_i$	OV_H^-	0.953	H_i	0.810
OHi4	6.444	$OV_H^- + H_i$	OV_H^-	0.953	H_i	0.810
OHi5	6.377	$OV_H^- + H_i$	OV_H^-	0.950	H_i	0.835
OHi6	6.277	$OV_H^- + H_i$	OV_H^-	0.963	H_i	0.864
OHi7	6.466	$OV_H^- + H_i$	OV_H^-	0.954	H_i	0.814
OHi8	6.433	$OV_H^- + H_i$	OV_H^-	0.954	H_i	0.813

Table 9.1: Mulliken population analysis and defect energy for different structural configurations of $[OV_H]^- + H_i$.

9.3 Structural Analysis

The defect formation energy $\Delta H_f([OV_H]^- + H_i)$ is given as a function of the cell expansion in Figure 9.2 (for reference, the complete lattice parameters are given in Appendix G.1 Table G.1). As $\Delta H_f([OV_H]^- + H_i)$ increases in the topaz-FOH system, the cell volume is also shown to increase. The cell volume is shown to contract in stead for the topaz-OH system, whwn the $[OV_H]^- + H_i$ defect system is introduced. The expansion of the cell is divided into the individual component lattice parameters as a functional of $\Delta H_f([OV_H]^- + H_i)$ in Figure 9.3. There is little change in the individual lattice parameters with respect to the increase in the defect formation energy, except for the $c \parallel z$ lattice parameter in the topaz-FOH stsem, which expanses slightly as $\Delta H_f([OV_H]^- + H_i)$ increases.

The defect energy as a function of the atomic separation of the defect species is

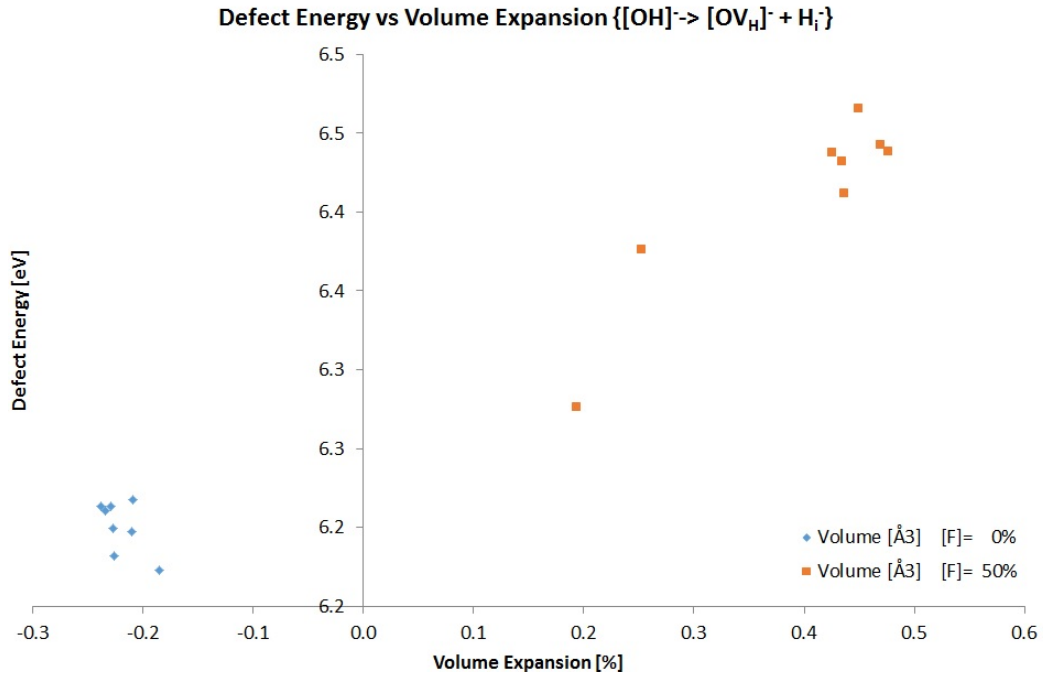

Figure 9.2: The defect energy [eV] as a function of the total cell volume expansion [%] in the reaction scheme $[\mathrm{OH}]^- \longrightarrow [\mathrm{OV_H}]^- + \mathrm{H_i}$.

$\mathrm{OV_H}-\mathrm{H_i}$ for topaz-OH and topaz-FOH are given in Figures 9.4 and 9.5 respectively. It is shown that the defect energy decreases as the $\mathrm{OV_H}-\mathrm{H_i}$ separation decreases, and there are a number of energy penalties before recombination takes place. This could indicate a mechanism for annealing, not seen before in this investigation with other the larger oxygen defect species (see Chapters 7 and 8). The H atom is small enough to migrate with relatively small energy penalties through the channels in topaz for the recombination of displaced ions to occur.

9.4 Band Gap Analysis

The CRYSTAL calculated total density of states for the $[\mathrm{OV_H}]^- + \mathrm{H_i}$ defect system in topaz-OH and topaz-FOH is given in Figure 9.6: for the atomic projections of the densities of state, see Appendix G.2. The fundamental band gaps are summaried along with $\Delta H_f([\mathrm{OV_H}]^- + \mathrm{H_i})$ in Table 9.2. Given that in the creation of the open shell $[\mathrm{OV_H}]^- + \mathrm{H_i}$ defect system a bond was required to be cleaved, the equal sharing of the two electrons between defect species $[\mathrm{OV_H}]^-$ and $\mathrm{H_i}$, would require one of the defects to localise the α radical and the other the β, so that multiplicity remains the same. Therefore, both the α and the β HOMO-LUMO transitions need to be examined, as both hold valence electrons easily available to under go electronic transition.

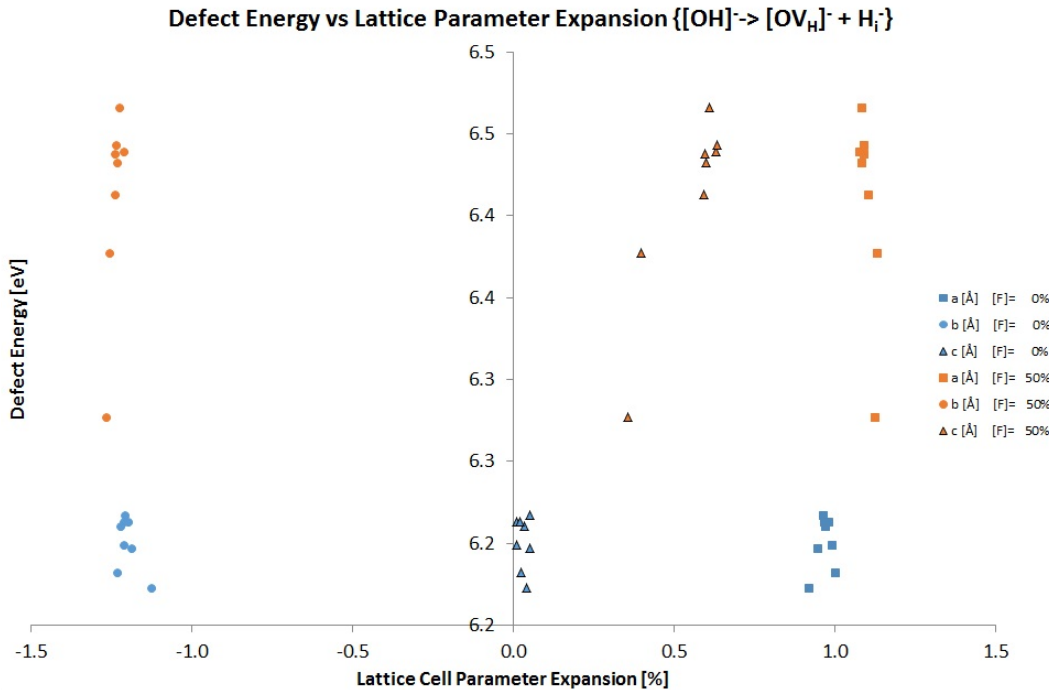

Figure 9.3: The defect energy [eV] as a function of the all three lattice parameters (a, b, and c) in the total effect of cell expansion [%] in the reaction scheme $[\mathrm{OH}]^- \longrightarrow [\mathrm{OV_H}]^- + \mathrm{H_i}$.

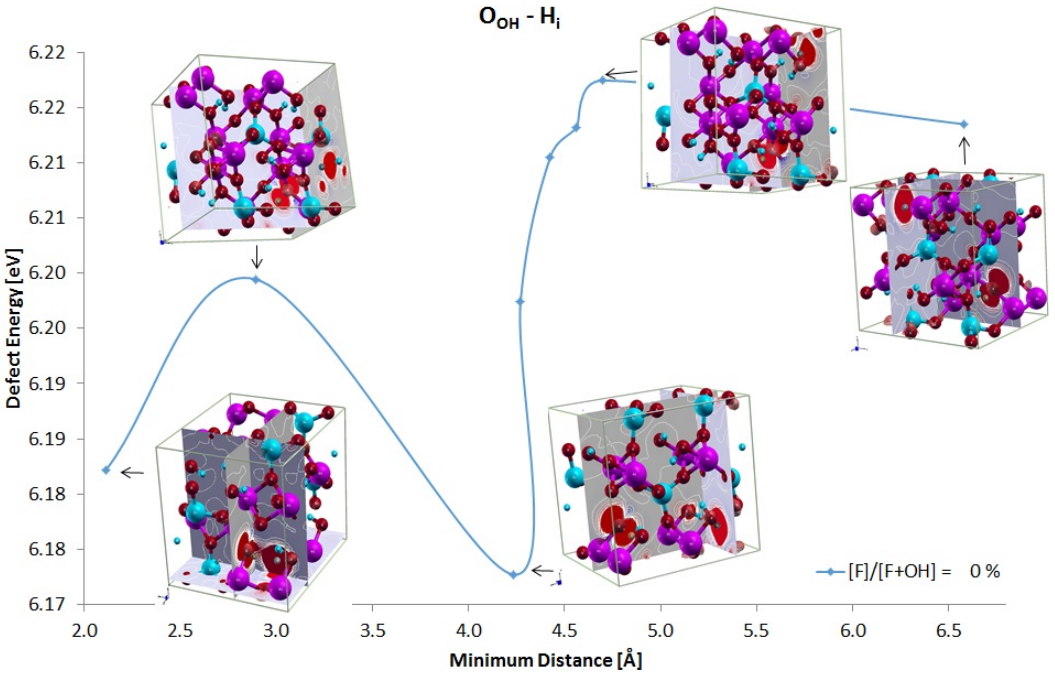

Figure 9.4: The defect energy [eV] as a function of the $\mathrm{O_{(OH)}}-\mathrm{H_i}$ minimum separation [Å] in the reaction scheme $[\mathrm{OH}]^- \longrightarrow [\mathrm{OV_H}]^- + \mathrm{H_i}$ in topaz-OH.

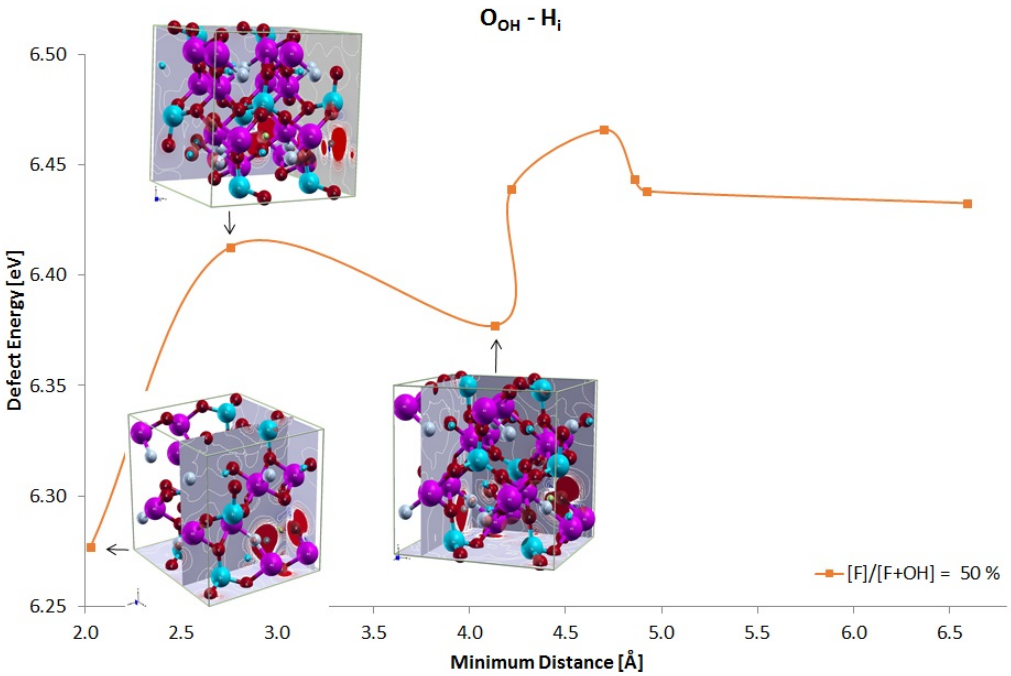

Figure 9.5: The defect energy [eV] as a function of the $O_{(OH)}-H_i$ minimum separation [Å] in the reaction scheme $[OH]^- \longrightarrow [OV_H]^- + H_i$ in topaz-FOH.

The total densities of state show that there are additional electronic states are found within the band gap that shorten the band gap of pure topaz. The projected density of states it is shown that these additional states are due to the defect species and the localisation of electrons onto them. From Table 9.2, it is shown that the band gaps $\alpha > \beta$, $\alpha_{FOH} > \alpha_{OH}$ and $\beta_{OH} \approx \beta_{FOH}$. There was found to be no strong correlation between the $\Delta H_f([OV_H]^- + H_i)$ and the band gap or the $O^-_{OH}-H_i$ separation and the band gap.

The introduction of the $[OV_H]^-+H_i$ defect system into topaz does reduce the band gap by ∼2.25 eV and ∼2.03 eV for α-band gaps in topaz-OH and -FOH respectively, and ∼5.07 eV and ∼4.94 eV for β-band gaps in topaz-OH and -FOH respectively. Despite the significantly large reduction in the calculated band gaps for the pure to the $[OV_H]^- + H_i$ defect system in topaz, the α HOMO-LUMO transitions are still to large to be considered as a transition within the visible region. However, the β HOMO-LUMO transitions are within the blue/violet range of the electromagnetic spectrum, and this defect system could therefore be considered as a candidate colour centre to produce a blue colour centre in topaz for further investigations of defect colour centres in topaz.

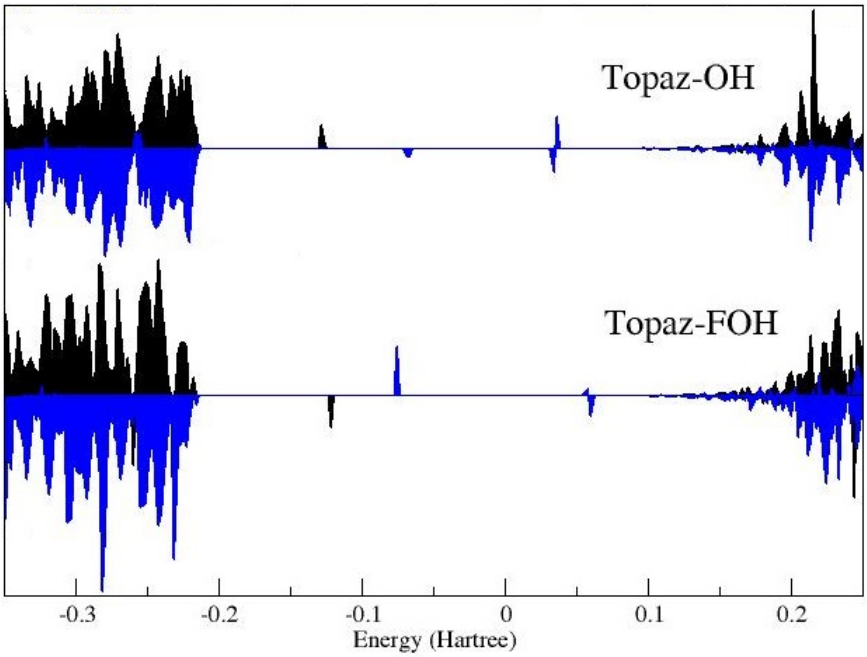

Figure 9.6: Total density of states for the $[OV_H]^- + H_i$ defect in topaz-OH and topaz-FOH, as calculated using the CRYSTAL code. The total density of states including projections of individual defect ions for the $[OV_H]^- + H_i$ defect configurations singled out here are given in Appendix G.2.

Calculated Band Gaps for the Defect System $[OV_H]^- + H_i$						
Config.	Band Gap [eV]					
	Topaz-OH			Topaz-FOH		
	Defect E. [eV]	(alpha)	(beta)	Defect E. [eV]	(alpha)	(beta)
OHi1	6.199	6.103	3.006	6.413	-	-
OHi2	6.197	6.118	2.995	6.439	6.466	2.835
OHi3	6.213	6.101	2.990	6.438	6.371	2.913
OHi4	6.210	6.088	2.959	6.444	6.329	3.008
OHi5	6.173	6.116	2.700	6.377	6.268	3.184
OHi6	6.182	6.101	3.304	6.277	6.073	3.557
OHi7	6.217	6.123	2.914	6.466	6.377	2.939
OHi8	6.214	6.083	2.982	6.433	6.389	2.927

Table 9.2: Calculated band gaps for the defect system $[OV_H]^- + H_i$ from CRYSTAL calculations.

9.5 Dynamic Excited State Optical Analysis

The UV-Vis spectra for the $[OV_H]^- + H_i$ defect system in topaz-OH and topaz-FOH are given in 9.7(a) and 9.7(a) respectively. As before, it is difficult to give analysis of the UV-Vis spectra, as the CP2K method does not provide chemical information on calculated absorptions. However, the defect configurations chosen for MD TD-DFT calculation and UV-Vis absorption spectra analysis were those

with the lowest energy, which happened to be those configurations where the $[OV_H]^-$ and H_i were almost recombined. During the process of reoptimisation of the defect structure to generate the wave function for the initial MD TD-DFT step, the defect species recombined in the topaz-OH system, and as a result the absorption spectra resembles a colourless crystal (see Figure 9.7(a)). The spectra for $[OV_H]^- + H_i$ in topaz-FOH is different: recombination of defect species has not occurred and the absorption spectra has an absorption valley around $335 - 442\,\text{eV}$ and absorption bands prevalent around 520 and 675 eV (cf. Figure 2.6).

9.6 Conclusion

The defect system $[OH]^- \longrightarrow [O^\bullet V_H^\times]^- + H_i'$ was investigated in the topaz-OH and topaz-FOH analogues, and findings from our defect energy analysis, Mulliken population study, $(\alpha - \beta)$ isothermal spin density plots, geometrical analysis, band gap and density of states analysis, and UV-Vis absorption spectra were presented here. It was found that through Mulliken analysis and spin density plots, there was only one electronic defect structure for this defect system setup: i.e. where the unpaired spins remained as two radicals on their respective cleaved defect species. Through analysis of the defect formation energy with respect to the $[OV_H]^-$ and H_i separation, an annealing mechanism was found likely to occur for this defect system, and the recombination of separated defects the most favourable outcome.

From isothermal plots and analysis of the density of states, it has been shown that defect electronic states are formed within the band gap, and a reduction in the band gap with respect to the pure topaz analogue does occur, as much as $\sim$2 eV for α-transitions and $\sim$5 eV for β-transitions. From our static ground state calculations, we predict that the $[OV_H]^-$ and H_i system produces a band gap in topaz of $\sim 2.70 - 3.5\,\text{eV}$, depending mainly on the structural configuration and less on the host topaz analogue. These band gaps indicate possible optical behaviour, since blue/violet light spans energies $2.5 - 3.26\,\text{eV}$, but further analysis using time-dependent methods would show whether $[OV_H]^-$ and H_i as a defect system is likely to produce optically transitions. UV-Vis spectra were also performed and presented.

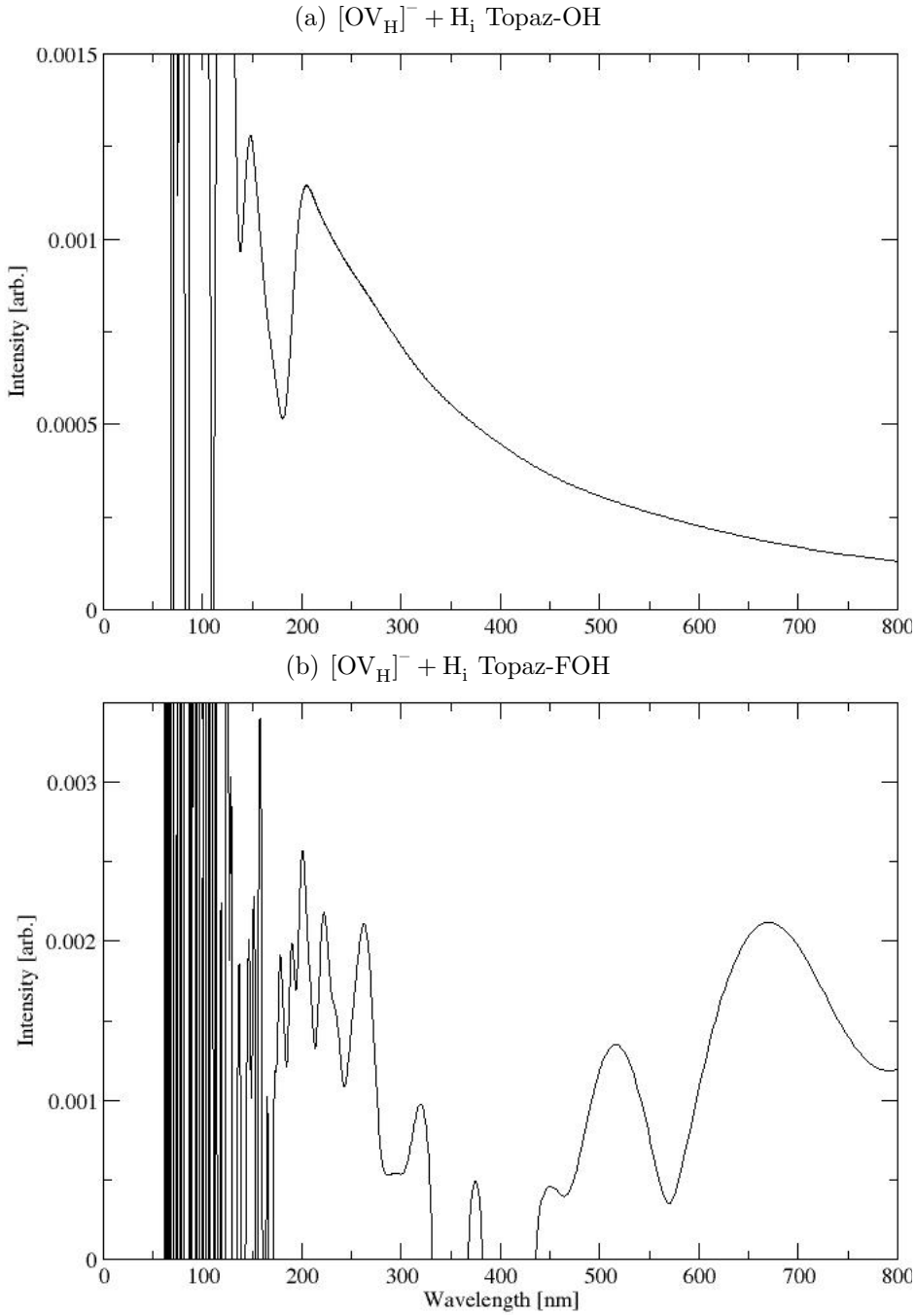

Figure 9.7: UV-Vis absorption spectra of the $[OV_H]^- + H_i$ open shell defect in ((a)) topaz-OH and ((b)) topaz-FOH. The total number of MD steps simulated to generate each spectra are 1631 and 5019 respectively.

Chapter 10

Conclusion

In this computational investigation of the radiation induce colour centres of blue topaz ($Al_2SiO_4(OH,F)_2$), we have examined the nature of the solid-solution inherent within the pure form of topaz, and investigated a number of likely and known defect centres in topaz. Our aim was to verify, by theoretical means, the structural and electronic properties of these defects, suggest possible mechanisms for their formation, compare their stability, predict optical properties where possible, and provide some additional discussion to the story of establishing the cause of blue colour in topaz

Our method combined the techniques of three computational codes: GULP, CRYSTAL and CP2K. The classical GULP code, with pair potentials for topaz prepared by Jackson [58, 61, 62], was primarily used to predict stable and relevant structural configurations of varying solid-solutions in topaz. In order to do this, both the mean field approach and configurational space sampling methods were exploited in GULP to address the problem of the H fractional occupancy within topaz. The out come was the reduction of +7000 structural configurations of topaz to consider, and a short list of only those which, theoretically at least, have any contribution of the topaz structure. A selection of the most stable of these structures of topaz, in analogues of only OH-, FOH- and F-rich topaz, were then optimised using electronic structure calculations in the *ab initio* codes CRYSTAL and CP2K. The combination of both codes was employed to demonstrate reliability of method. The *ab initio* codes both used the hybrid functional PBE0 (with 25% HF) and a full and auxiliary basis set description of the polarised atoms for the codes respectively. CP2K was employed to perform MD TD-DFT calculations, in order to generate the UV-Vis absorption spectra of the open shell defect systems topaz, for a direct comparison with experimental methods.

A review of current literature helped ascertain that the defect(s) responsible for

the particular optical property this investigation was concerned with was not well understood. A definitive answer to the precise form of the blue colour causing defect in topaz was not possible to establish, so instead the review uncovered a number of defects, possibly also colour centres, which may or may not to occur in topaz. Our aim then became to calculate the properties of as many of these defects as possible, to try and placate the lack of tangible understanding of these defect and their optical responsibility in topaz. The incorporation of defects was holistic in order to anticipate a discussion in mechanism of defect formation and (possible) annealing. The defects considered, included $[PO_4]^{4-}$, $[PO_3]^{2-}$, $[SiO_3]^{2-}$, O^- and O_2^- centres. In addition, the impurity responsible for pink topaz, the transition metal Cr^{3+} found in trace quantities, was used as a verification of computational data.

The natural disorder that exists within the pure structure of topaz ($Al_2SiO_4(OH,F)_2$), which incorporates both the lattice positions of OH that can adopt one of two lattice sites (H1 and H2), and the OH/F groups that are freely interchangeable, was important to establish to what extent their properties are influenced by these changing factors. It was found that configurations with long-range ordering of OH and F groups and generally with higher symmetry, were more stable and had an increased band gap. The factor that influences the structural configurations of pure topaz is the nature of how the OH/F pairs interact within the structure. Favourable pairings uncovered in this investigation, are the H1···H2 pairing in OH-rich topaz, less so H1···H2 but still a valuable contribution to the overall structure, but never H2···H2 as the interatomic separation is too low and steric hindrance high for the H ion to be mobile and switch positions. Band gaps were also effected by the extent of OH/F exchange.

The known colour centre for pink topaz, Cr^{3+}, was investigated using both *ab initio* methods. The chromium(III) transition metal defect ion was isomorphically substituted onto aluminium octahedral sites. It was found that isolated Cr^{3+} ions in the crystal favoured a F-rich host lattice, but that when clusters of Cr form in topaz in adjacent sites, the lattice environment preferred in the OH-rich crystal, which were supported by experimental models detailed by Taran *et al.* [2] and Tarashchan *et al.* [52]. Isolated Cr ions are stabilised by the redistribution of the d^3 unpaired electron spin onto the surrounding F̧ ions. Clusters of Cr have their d^3 spin contained better on the metal defect ion in an OH-rich topaz host, and this reduced the electronic repulsion of delocalised spin and enables clusters of Cr to form in topaz. Structurally, the clusters of Cr obeyed the Goodenough-Kanamori rules of superexchange: corner-shared octahedra prefer an antiparamagnetic erlectronic configuration and the Cr−O−Cr angle is above 135°. Since the ions are close enough for

direct exchange to occur between edge-sharing Cr octahedra, the antiparallel electronic configuration is again favourable. The calculated band gaps, although smaller than those calculated for the host crystal, were found to be too large for the optical range. The corresponding UV-Vis spectra suffered from being shifted up in energy due to the large band gaps calculated. This was compounded by the computational method not being able to provide any additional chemical information about the nature of the electronic transitions. Peaks were therefore assign visually.

The investigation into P-based defects in topaz yielded a considerable variety of defect configurations. Phosphorus is either naturally present within topaz or can be doped there artificially via a β-decay nuclear reaction at a ^{30}Si site. Phosphate ($[PO_4]^{4-}$) tetrahedra transform into phosphite ($[PO_3]^{2-}$) centres via the creation of an oxygen vacancy from adjacent to the P, and since we applied a holistic approach to defect formation, the displaced oxygen is placed into an interstitial position. Following the optimisation of the phosphite systems, a number of defect states were discovered yielding from this defect profile. In order of stability, these contained: a phosphate ion (the recombination of defects), a superoxide (O_2^-), an ozonide (O_3^-), and an F-centre (e_V^-). The presence of superoxide and the ozonide (which can also be interpreted as a polaron O^-) defects within topaz, confirms experimental models proposed by Schirmer *et al.* [37], da Silva *et al.* [6] and Krambrock *et al.* [7]. With unique defect formation energies, local structural characteristics and distinguishable band gaps, the only defect configuration to have a band gap close to the visible region was the F-centre, which was also the most unstable defect.

Intrinsic defects formed from silicate ($[SiO_4]_4^-$) or hydroxide (OH^-) were also studied. The reaction scheme $[SiO_3V_O]^{3-} + O_i^-$ generated a number of similar defects, but all unique energetically and optically: the $[Si^{\bullet}O_3O']^{4-}$, which is the recombination of displaced $[SiO_3V_O]^{3-}$ and O_i^- defects; the $[SiO_3V_O^{\bullet}]^{3-} + [O'O]^-$, where the spin in localised on the O_i^-, which is stabilised primarily by one of the nearest O_{STRUCT}, and on the vacancy forming an F-centre; the $[SiO_3]^{2-} + [O''O_3]^{2-}$, where $3\,O_{STRUCT}$ are required to stabilise O_i and the 2 unpaired spins; the $[SiO_3]^{2-} + [O''O_3]^{4-}$, where $3\,O_{STRUCT}$ are required to stabilisation 4 electron spin; and the $[Si^{\bullet}O_3V^{\bullet}]^{4-} + O_2$, which is the creation of an interstitial O_2 molecule, a silicon radical and an F-centre. As with the defect configurations resulting from the phosphite ion, the formation energy of these silicon based defects are all highly unfavourable processes. However, in the abundance of an excess in energy, as experienced in irradiation conditions, these defect states should be accessible. Ground state calculations showed that electronic states resulting from localised unpaired spin on defect species form within the band gap reducing its size.

The final defect type investigated involved the cleaving of the hydroxide (OH^-) ion. A number of structural configurations were considered, but only one electronic configuration was found, $[OH]^- \longrightarrow [O^{\bullet}V_H^{\times}]^- + H_i'$. Since multiplicity needs to be maintained in the formation of $[OV_H]^-$ and H_i radical species, both α- and β-electronic states have valence unpaired electrons. The calculated band gaps for α-transition were shown to be 6.1 and 6.4 eV, and for and β-transitions 3.0 and 3.1 eV, for OH- and FOH-topaz respectively. Therefore, an increase in the [OH] content in topaz containing the $[OV_H]^-$ and H_i radical species, decreases the band gap. In an OH-rich topaz, the unpaired spin is able to be stabilised by surrounding anions, much more than for F-containing topaz. The cell volume was shown to expand for FOH-topaz, whereas for OH-topaz it decreased. The energy profile with respect to the $[OV_H]^-$ and H_i radical ion separation, shows evidence of a potential annealing mechanistic pathway.

10.1 Future Work

The goal of determining the precise form of the blue colour centre in topaz by computationally method is still an objective worth perusing. The defect calculations of this investigation can, of course, be built on, but the objective of such an investigation would be more important to establish.

If the main concern is computing data that can be directly comparable to experiment, then the focus should be on the finding (or writing) robust excited state techniques to can calculate optical absorption spectra. EPR parameters, band gaps, structural information, annealing properties, neutron bombardment simulations, are other comparable computable information about the defect system with experiment. If, however, the focus is comparing methods for the calculation of excited state spectra, then codes that implement the CI method, static TD-DFT, or dynamic TD-DFT method, would be interesting to compare.

If alternatively the direction is one of application, then there are a variety of possibilities. Expanding the number of defect types, to include a larger variety of transition metals (in both interstitial and substitution positions), intrinsic defects (such as Frenkel and exchange), the polaron species, or the smoky quartz defect centre, would all be likely candidates before revisiting the literature. The size of the supercell could be expanded to model the defect concentrations more realistically. The chemistry of topaz as a nano particulate or as a surface could also be examined for application as a dosimeter. Collaboration with an experimental groupthat investigate topaz, could give more direction and ideas to other possible defect models.

Appendix A

Additional Information for Literature Review

A.1 Unit Conversion of Energy

The conversion of units of energy for photons in the visible spectrum (eV) into their respective wavelengths of visible light (nm) is given in Table A.1.

Colour	Wavelength [nm]	Energy [eV]
Violet	$380 - 450$	$3.26 - 2.76$
Blue	$450 - 495$	$2.76 - 2.50$
Green	$495 - 570$	$2.50 - 2.18$
Yellow	$570 - 590$	$2.18 - 2.10$
Orange	$590 - 620$	$2.10 - 2.00$
Red	$620 - 750$	$2.00 - 1.65$

Table A.1: Conversion table for the energy [eV] and wavelength [nm] of (emitted) visible light.

A.2 Complementary Colour of Pink

The complementary colours are those colours our eyes perceive when the reference colour is removed from white light (see Figure A.1).

(a) Pink (b) Red

Figure A.1: Complementary colour experiment: stare at one of the coloured dots for a minute and then look away next at the white space. One should observe for (a) a green and for (b) a blue afterimage.

Appendix B

Additional Information for Computational Method

The additional information provided in Appendix B supports the discussion on the computational method presented in Chapter 4.

B.1 Number Generator

The 8-digit number generator script written in python, created from this investigation is given below in the gray box. The python script was used in conjunction with another script written in bash in order to generate input files for GULP calculations of pure topaz (see Section B.2). The python script is used as follows:

```
[user ]$: python script.py 11213221
```

The 8-digit number is made up of three unique numbers that each present either an OH orientation (1 = OH1 and 2 = OH2), or an F ion (3 = F). There are 8-digits in the unique number as there are eight locations within one unit cell of topaz where OH/F is located: i.e. in the example above, there is an OH1 in the 1^{st}, 2^{nd}, 4^{th} and 8^{th} positions; an OH2 in the 3^{rd}, 6^{th} and 7^{th} positions; and an F in the 5^{th} position. The factional coordinates of each of these eight positions is given in Section 5.2.1.

The number generator works by finding all the combinations of arranging those 8-digits into the eights positions and then presenting only the unique one in the output. This way the concentration of each species, OH1, OH2 and F could be controlled at the initial stage of the calculation.

```
importsys
test = list()
arg = sys.argv[1]
forxinarg :
test.append(x)
lex = list()
copy = list()
results = list()
myPos = "bf"
forxinrange(len(test)) :
lex.append(0)

j = 1
iflen(lex) > 0 :
lex[0] = j
foriinrange(len(lex)) :
iftest[i - 1]! = test[i] :
j = j + 1
lex[i] = j

defSwap(i, j) :
globalcopy
globallex
myTemp = copy[i]
copy[i] = copy[j]
copy[j] = myTemp
myKviTemp = lex[i]
lex[i] = lex[j]
lex[j] = myKviTemp

defGetNextPermutation() :
globallex
i = len(lex) - 1

whilelex[i - 1] >= lex[i] :
i = i - 1
ifi == 0 :
returnFalse
j = len(lex)
```

```
whilelex[j-1] <= lex[i-1]:
j = j-1
Swap(i-1, j-1)
i = i+1
j = len(lex)
whilei < j:
Swap(i-1, j-1)
i = i+1
j = j-1
returnTrue

defMoveNext():
globalmyPos
globalcopy
ifmyPos == "bf":
forxintest:
copy.append(x)
lex.sort()
myPos = "is"
elifmyPos == "is":
iflen(copy) < 2:
myPos = "al"
elifGetNextPermutation() == False:
myPos = "al"
returnmyPos! = "al"

##Mainloophere
pointless = 0
whileMoveNext()! = False:
results.append(list(copy))

output = ""
#output+ = "("
forxinresults:
output+ = ""
foryinx:
output+ = str(y)
#output+ = ")"
printoutput
```

B.2 GULP Input File Generation Script from Unique Number Generated

A bash script was written to convert the set of unique configurations, generated from the original 8-digit number created by the number generator in Section B.1, and build a GULP input files. The whole script is too large to include here, but in essence the script was designed to take any one of the unique 8-digit configuration numbers and convert them into the fractional coordinates of the particular anion species at that site, then build an input file based on the unique structural configuration and composition for a GULP calculation. The script was executed in the following manor:

```
[user ]$: ./script.sh 11213221
```

Appendix C

Supporting Information for Pure Topaz

The additional information provided in Appendix C supports the results and discussion on pure topaz as presented in chapter 5.

C.1 Lattice Paramters

The CP2K calculated lattice parameters and cell angles and volumes for the all teh stable structural configurations of pure hydroxyl- analogue of topaz are given in Table C.2, along with the pure flouro- analogue of topaz and the 50 : 50 F/OH mixed topaz analogue.

C.2 Total Density of States

The total density of states for stable structural configurations of pure topaz-OH ($Al_2SiO_4(OH)_2$) calculated by GULP, CRYSTAL and CP2K are given respectively in Figures C.1, C.2 and C.3. Comparative total densities of states of topaz with varying F/OH contents for CRYSTAL and CP2K calculations are given in Figures C.4 and C.5 respectively.

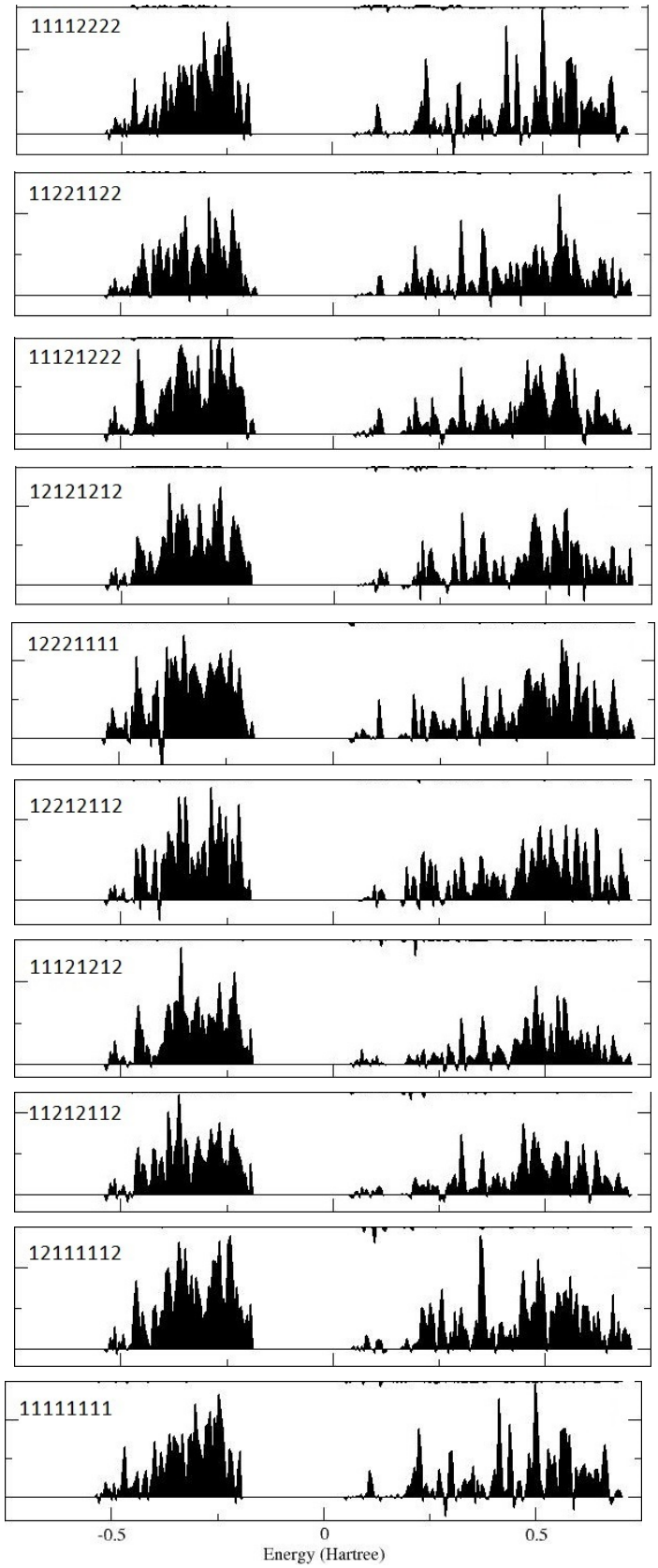

Figure C.1: The total density of states for the GULP optimised structures of pure topaz-OH for the structural configurations indicated within the figures.

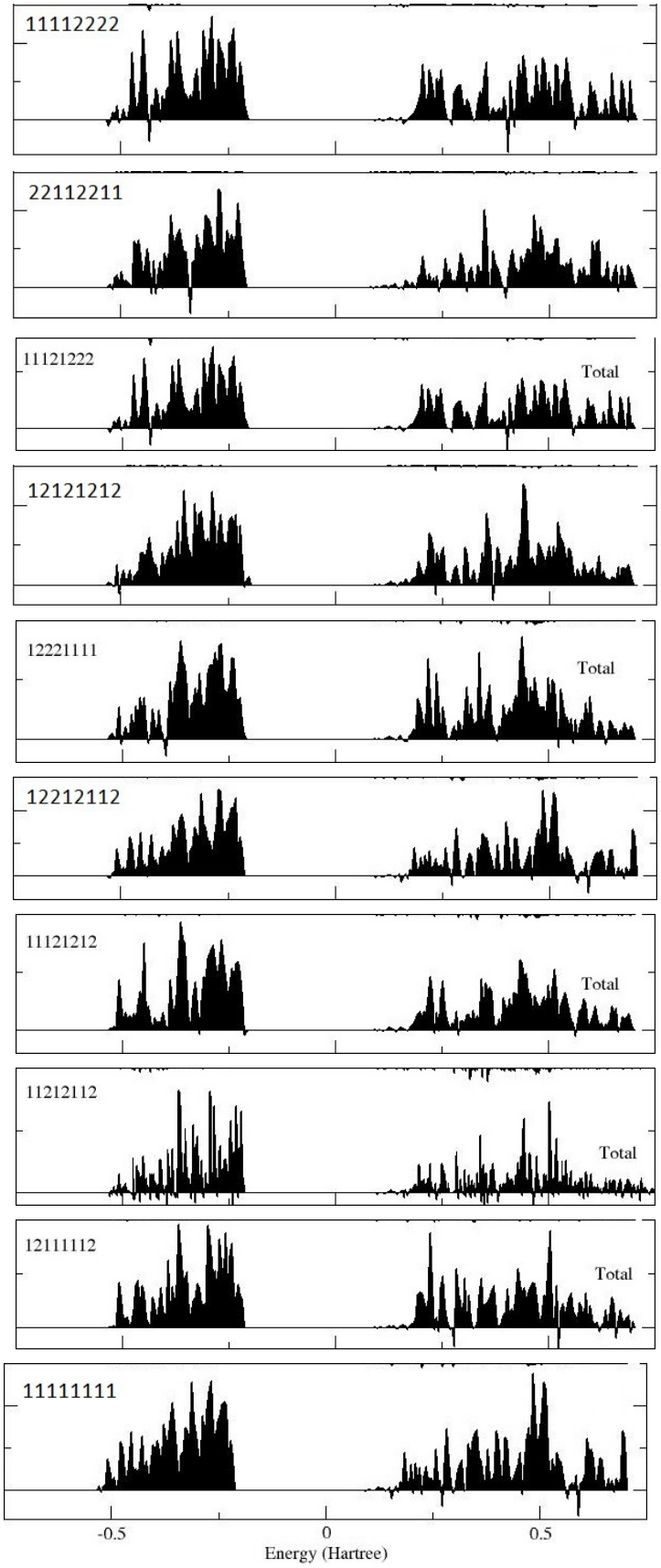

Figure C.2: CRYSTAL calculated total density of states for the unique structural configurations of pure topaz-OH, which are indicated according to the convention set out in Section 5.2.2.1 within the figures.

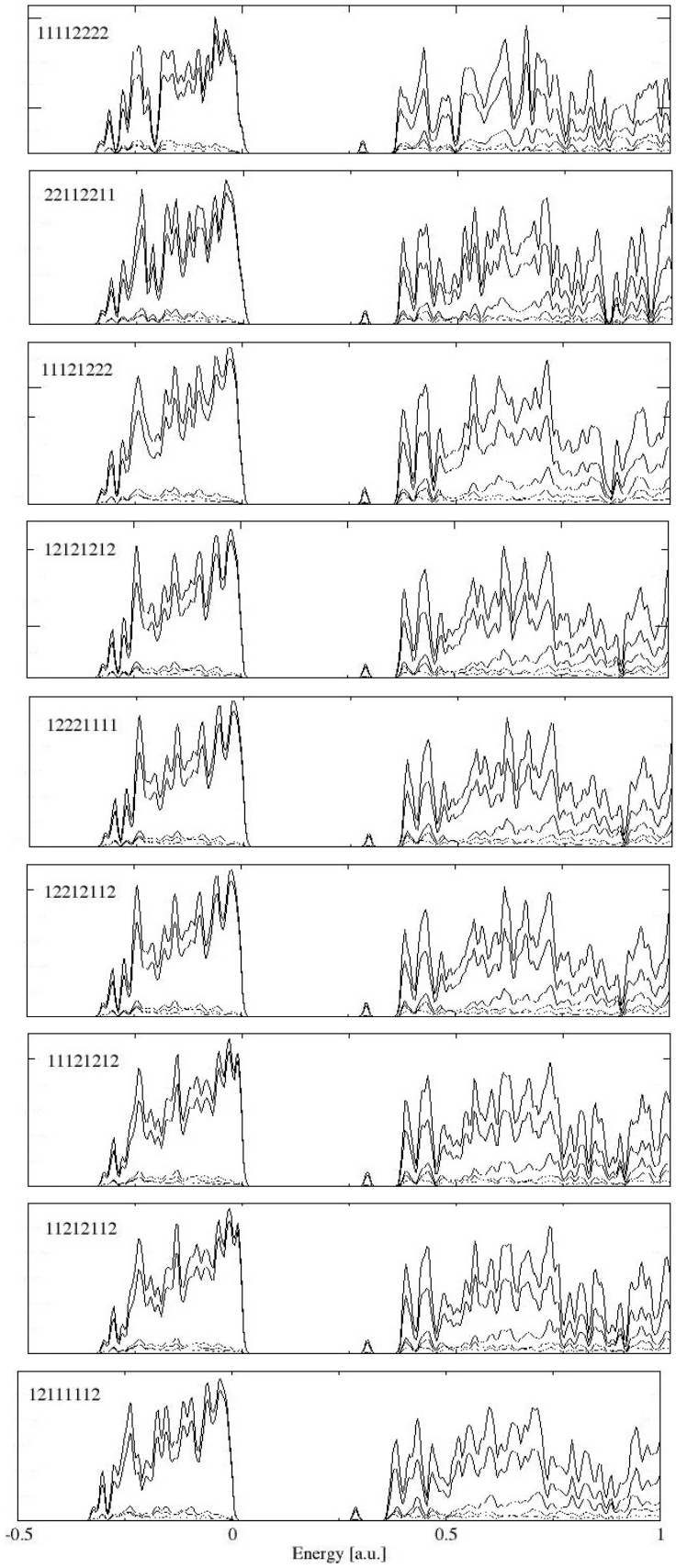

Figure C.3: CP2K calculated total density of states for the unique structural configurations of pure topaz-OH, which are indicated according to the convention set out in Section 5.2.2.1 within the figures.

(a) $Al_8Si_4O_{16}(OH)_8$ (Topaz-OH)

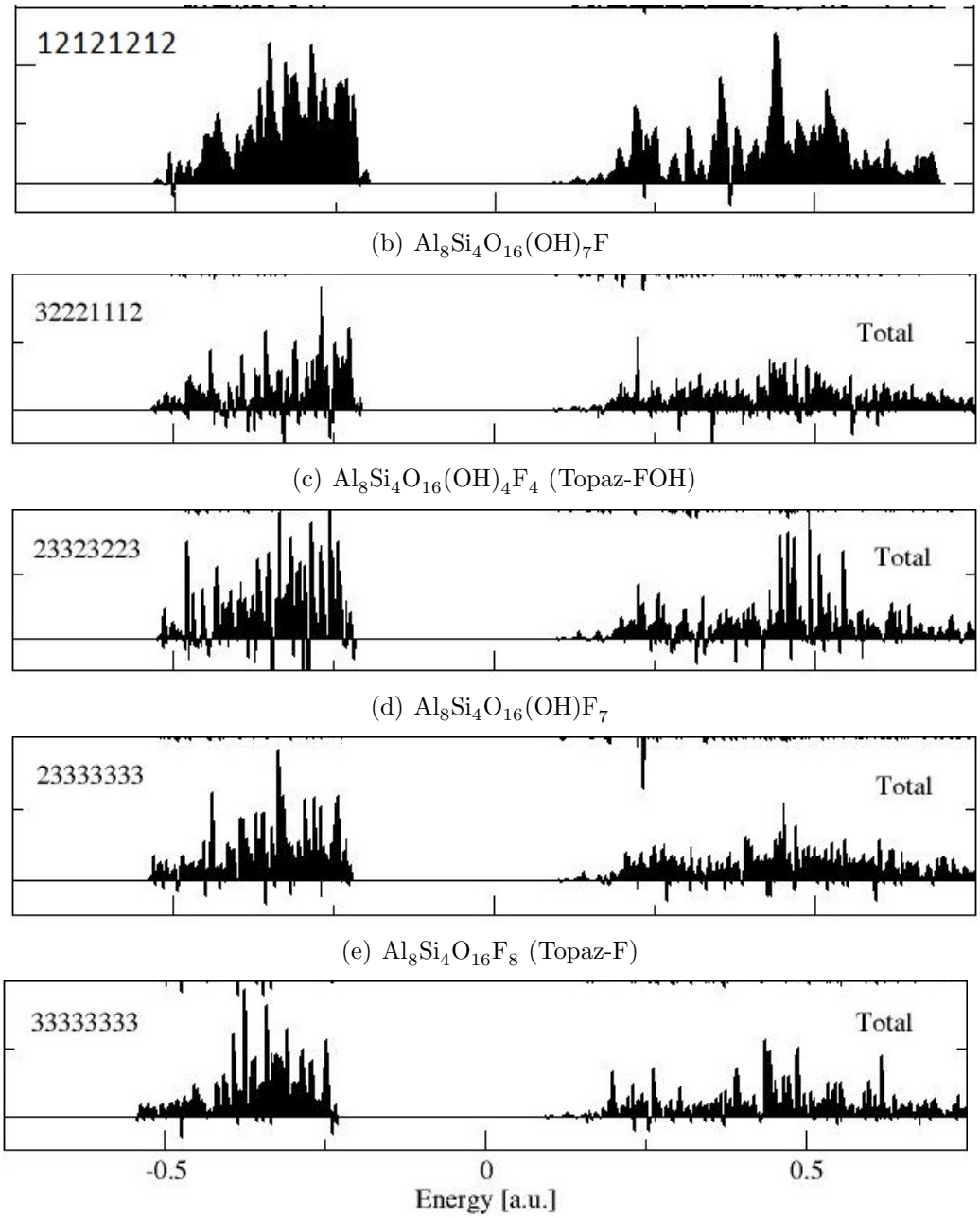

Figure C.4: Total density of states for CRYSTAL optimised pure topaz structures of varying fluoride/hydroxy concentrations.

(a) $Al_2SiO_4(OH)_2$

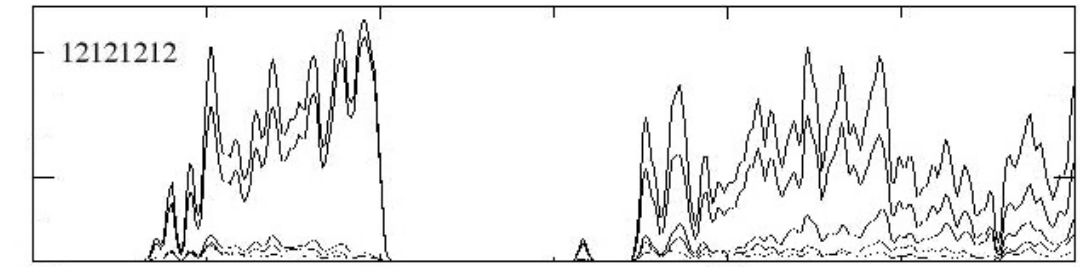

(b) $Al_2SiO_4(OH)F$

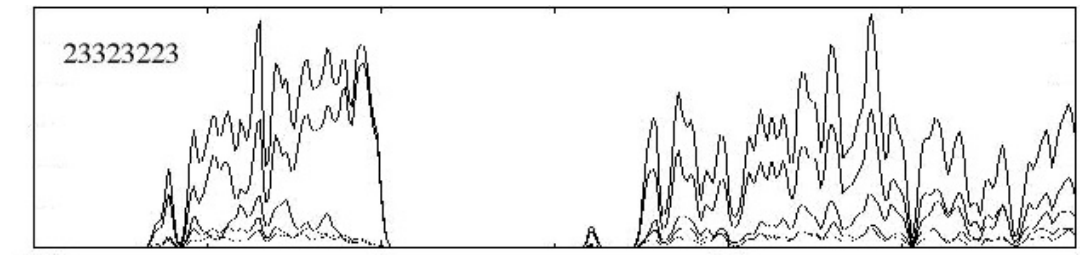

(c) $Al_2SiO_4F_2$

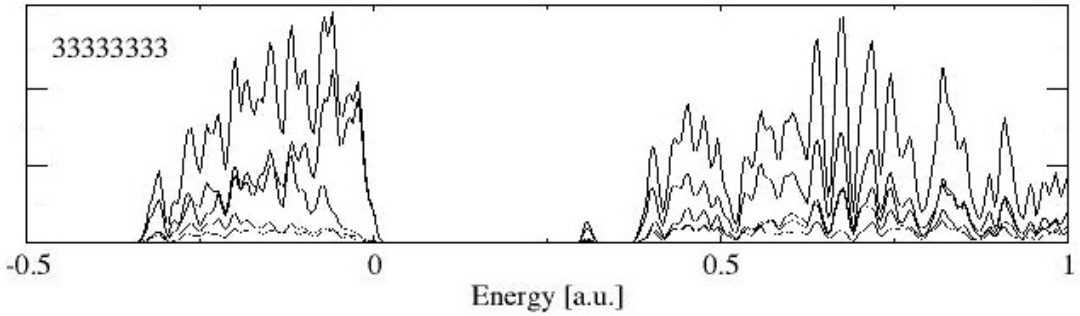

Figure C.5: Density of states for CP2K optimised pure topaz-OH.

Structural Config.	a [Å]	b [Å]	c [Å]	alpha	beta	gamma	Vol. [Å^3]
(a) $Al_8Si_4O_{16}(OH)_8$ (Topaz-OH)							
11112222	4.713	8.899	8.444	90.001	89.991	90.005	354.12
22221111	4.714	8.899	8.444	90.001	90.006	89.996	354.14
11221122	4.722	8.863	8.448	90.008	90.363	90.009	353.51
22112211	4.717	8.862	8.468	90.001	89.705	90.023	353.96
11121222	4.718	8.873	8.443	90.011	89.967	90.193	353.39
11212122	4.719	8.872	8.441	90.008	90.009	90.186	353.39
12112212	4.719	8.877	8.430	89.886	90.027	90.007	353.13
12221112	4.721	8.873	8.436	90.018	89.985	90.184	353.34
21112221	4.724	8.871	8.441	90.010	89.968	90.200	353.75
21221121	4.721	8.872	8.440	90.021	90.014	90.189	353.50
22121211	4.719	8.877	8.430	89.886	90.028	90.007	353.14
22212111	4.726	8.872	8.432	90.019	90.041	89.799	353.50
12121212	4.729	8.873	8.418	90.006	90.066	90.012	353.19
21212121	4.729	8.873	8.420	90.037	89.920	90.029	353.24
12221111	4.729	8.873	8.420	90.037	89.919	90.029	353.24
12212112	4.729	8.873	8.420	90.038	89.919	90.029	353.24
21121221	4.723	8.876	8.426	90.019	90.003	89.991	353.19
11121212	4.723	8.876	8.426	90.010	90.007	89.991	353.19
11212121	4.723	8.876	8.426	90.010	90.007	89.991	353.19
12111212	4.724	8.875	8.425	90.005	90.019	89.988	353.23
12121112	4.723	8.876	8.426	90.010	90.007	89.991	353.19
21212111	4.723	8.876	8.426	90.010	90.007	89.991	353.19
11212112	4.725	8.874	8.422	90.010	89.995	89.987	353.12
12111112	4.683	8.896	8.509	89.968	90.085	90.005	354.45
11111111	4.692	8.910	8.408	90.000	89.856	90.000	351.50
(c) $Al_8Si_4O_{16}(OH)_4F_4$ (Topaz-FOH)							
23323223	4.692	8.910	8.408	89.856	90.000	90.000	351.50
(e) $Al_8Si_4O_{16}F_8$ (Topaz-F)							
33333333	4.644	8.766	8.417	90.046	90.003	90.015	342.63

Table C.1: The CP2K calculated lattice parameters and unit cell dimensions of stable configurational structures of pure topaz.

Appendix D

Supporting Information for Chromium Based Defects in Topaz

The additional information provided in Appendix D supports the results and discussion on chromium based defect in topaz as presented in chapter 6.

D.1 CRYSTAL Spin Density and Density of States

Figures D.1 and D.2 show the CRYSTAL calculated ($\alpha - \beta$) spin localisation on 3D spin density plots and the densities of states for the different structural and electronic configurations possible for two defect chromium(III) ions to be adjacent to one another within the unit cell.

D.2 Mulliken Analysis

The Mulliken population analysis for $\alpha - \beta$ spins in clustered chromium(III) as calculated by CRYSTAL are given in Table D.1. As the F content increases, the total $\alpha - \beta$ spin on the Cr defect slightly reduces and the localised spin on the surrounding F ion increases.

D.3 CP2K Spin Density and Density of States

Figure D.3 shows the CP2K calculated densities of states for A- and P-ES configurations in topaz-OH, -FOH and F.

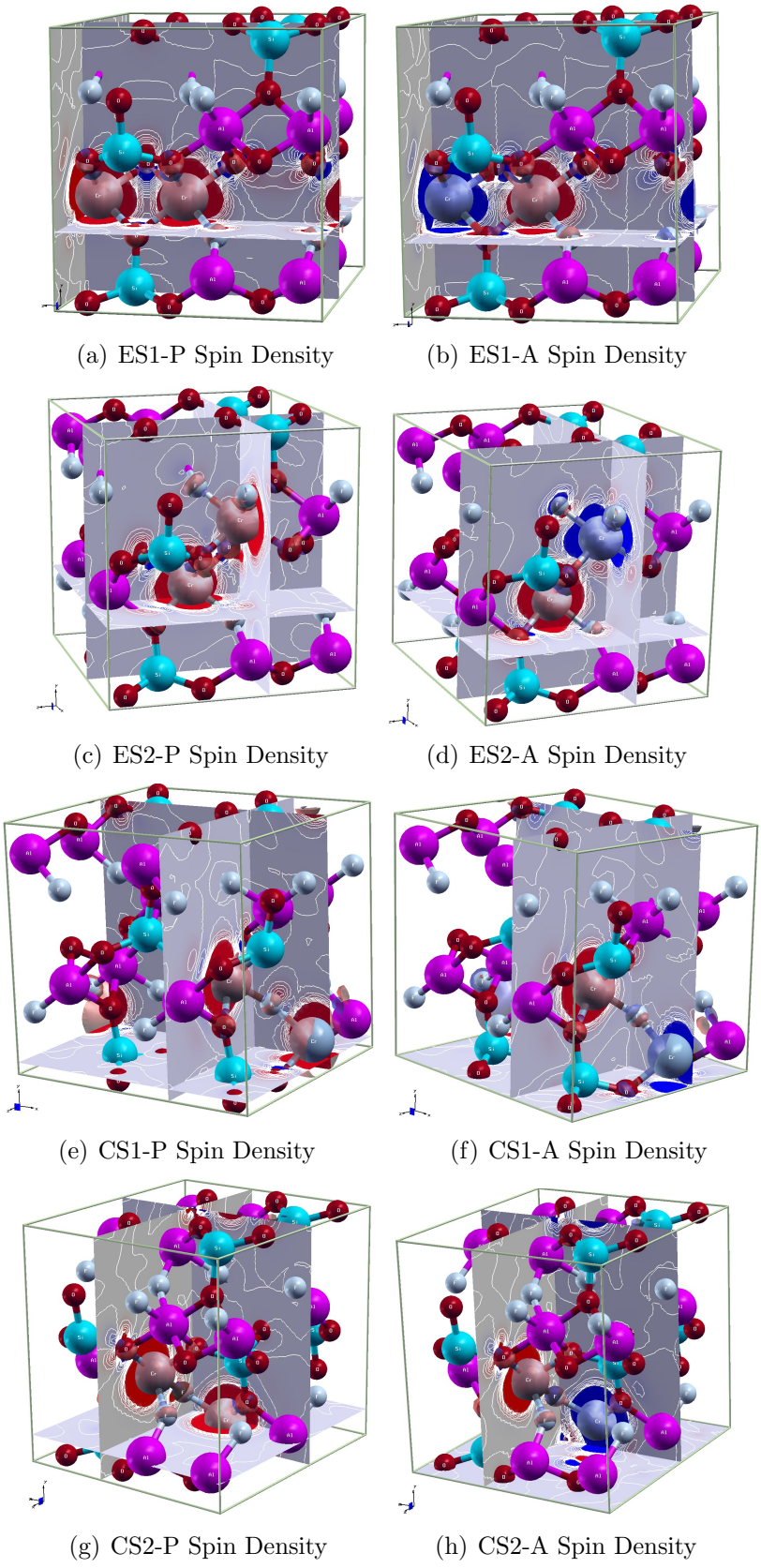

(a) ES1-P Spin Density (b) ES1-A Spin Density

(c) ES2-P Spin Density (d) ES2-A Spin Density

(e) CS1-P Spin Density (f) CS1-A Spin Density

(g) CS2-P Spin Density (h) CS2-A Spin Density

Figure D.1: The $(\alpha - \beta)$ spin densities 3D plots of clustered chromium for all eight structural and electronic configurations considered. The example given here is topaz-F.

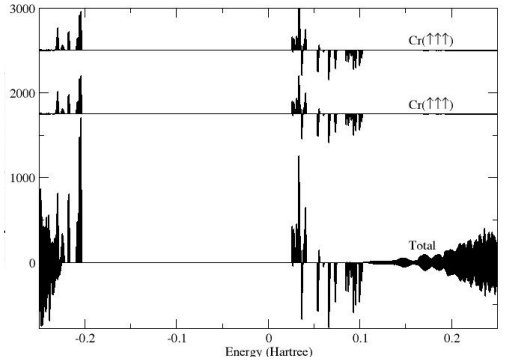

(a) ES1-P Density of States

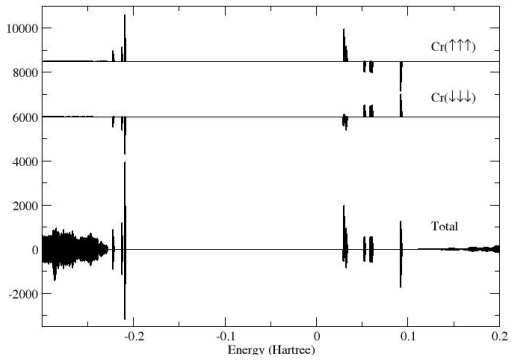

(b) ES1-A Density of States

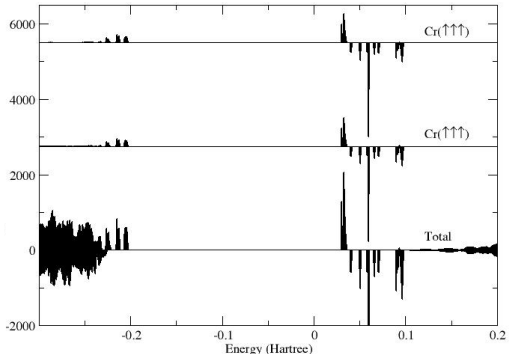

(c) ES2-P Density of States

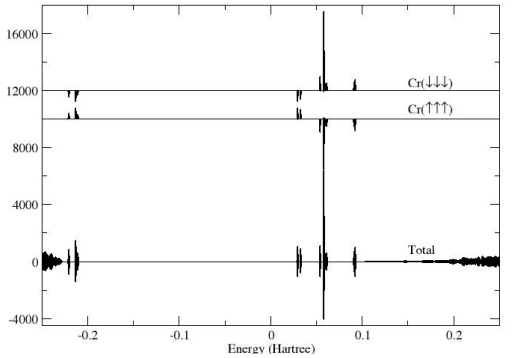

(d) ES2-A Density of States

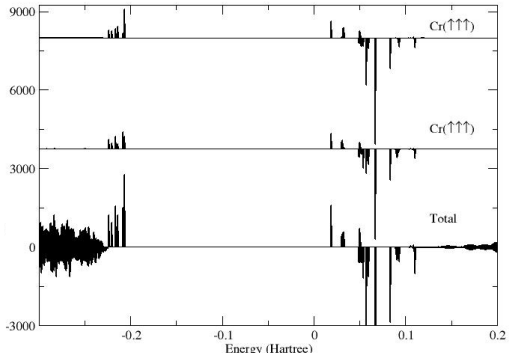

(e) CS1-P Density of States

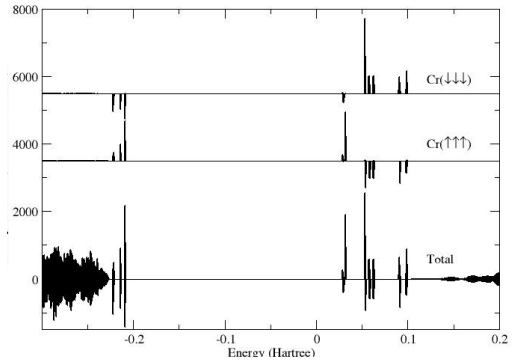

(f) CS1-A Density of States

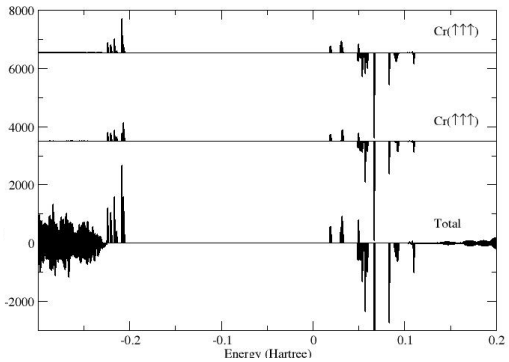

(g) CS2-P Density of States

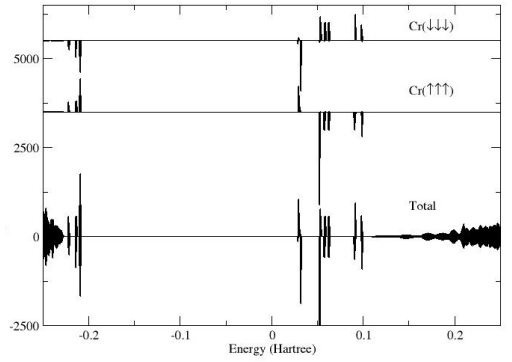

(h) CS2-A Density of States

Figure D.2: Density of states for chromium clusters for all eight structural and electronic configurations considered in topaz-F.

Config.	[F]	Mulliken $\alpha - \beta$ Spin Analysis Cr	OH/F[a]	OH/F[b]	O1	O2	O3a	O3b
	Double Chromium(III) Substitution Antiferromagnetic (A) Configuration							
A-ES1	0	2.962	-0.007	-0.004	0.001	-0.003	-0.002	0.004
		-2.952	-0.004	0.006	0.001	-0.003	-0.003	0.001
A-ES1	50	2.950	0.001	0.005	-0.004	-0.002	0.002	0.002
		-2.95	-0.001	-0.006	-0.004	-0.002	0.002	0.000
A-ES1	100	2.946	0.006	0.009	0.000	0.000	0.003	-0.003
		-2.946	-0.006	-0.009	0.000	0.000	0.003	-0.003
A-ES2	0	2.964	-0.007	-0.005	0.002	0.000	-0.003	0.003
		-2.964	0.007	0.005	-0.002	0.000	-0.003	0.003
A-ES2	50	2.954	0.001	0.006	-0.003	-0.001	0.006	-0.001
		-2.952	-0.001	-0.005	-0.003	-0.001	0.006	-0.001
A-ES2	100	2.951	0.008	0.008	0.000	0.002	0.008	-0.008
		-2.951	-0.008	-0.008	0.000	-0.002	0.008	-0.008
A-CS1	0	2.966	0.001	-0.004	0.002	0.000	-0.002	0.003
		-2.958	0.001	-0.004	-0.001	-0.002	0.000	-0.003
A-CS1	50	2.959	0.001	0.001	-0.001	0.000	0.002	0.001
		-2.958	-0.001	0.001	-0.003	-0.001	0.000	0.001
A-CS1	100	2.956	-0.001	0.009	0.001	0.003	0.003	-0.003
		-2.956	-0.001	-0.007	0.000	-0.002	-0.004	0.001
A-CS2	0	2.966	-0.007	-0.007	0.002	-0.001	-0.002	0.004
		-2.957	0.005	-0.007	-0.002	-0.003	0.000	-0.001
A-CS2	50	2.956	0.000	0.006	-0.002	-0.002	0.003	0.003
		-2.955	0.000	-0.005	-0.003	-0.002	0.000	0.003
A-CS2	100	2.956	0.007	0.001	0.000	0.002	0.004	-0.001
		-2.956	-0.008	0.001	-0.001	-0.003	-0.003	0.003
	Double Chromium(III) Substitution Ferromagnetic (P) Configuration							
P-ES1	0	2.970	-0.006	-0.004	0.005	0.004	-0.001	0.004
		2.961	-0.006	0.004	0.004	0.000	0.005	0.002
P-ES1	50	2.967	-0.001	0.005	-0.003	-0.001	0.001	0.004
		2.964	-0.001	0.005	0.004	0.001	0.001	0.003
P-ES1	100	2.955	0.008	0.010	0.003	0.011	0.004	-0.002
		2.955	0.009	0.008	0.003	0.003	0.011	-0.002
P-ES2	0	2.980	-0.008	-0.008	0.001	-0.001	0.003	0.003
		2.980	-0.008	-0.008	0.003	0.001	0.003	-0.001
P-ES2	50	2.967	-0.001	0.005	-0.003	-0.001	0.001	0.004
		2.964	-0.001	0.005	0.004	0.001	0.001	0.003
P-ES2	100	2.958	0.007	0.009	0.000	0.002	0.005	0.005
		2.958	0.009	0.007	0.005	0.002	0.000	0.005
P-CS1	0	2.976	-0.020	-0.004	0.003	0.000	-0.002	0.003
		2.970	-0.020	0.003	0.003	0.000	-0.001	0.004
P-CS1	50	2.964	0.001	0.009	-0.001	-0.001	0.002	0.003
		2.962	0.001	0.009	-0.001	0.001	0.002	0.001
P-CS1	100	2.960	0.014	0.009	0.001	0.002	0.002	-0.002
		2.960	0.014	0.007	-0.001	0.002	-0.001	0.004
P-CS2	0	2.972	-0.005	-0.003	0.002	0.000	-0.001	0.004
		2.963	-0.003	-0.004	0.002	-0.001	0.002	0.003
P-CS2	50	2.966	0.000	0.005	-0.003	-0.002	0.003	0.002
		2.965	0.000	0.006	-0.002	-0.001	0.003	0.001
P-CS2	100	2.959	0.007	0.014	-0.001	0.002	0.004	-0.001
		2.960	0.014	0.009	0.001	0.002	-0.002	0.002

[a]Atomic species are OH for topaz-OH and -FOH, and F for topaz-F.
[b]Atomic species are OH for topaz-OH, and F for topaz-FOH and -F.

Table D.1: Mulliken analysis for the $\alpha - \beta$ spin on the two chromium defect ions and the six surrounding ligands. Data calculated using the CRYSTAL method.

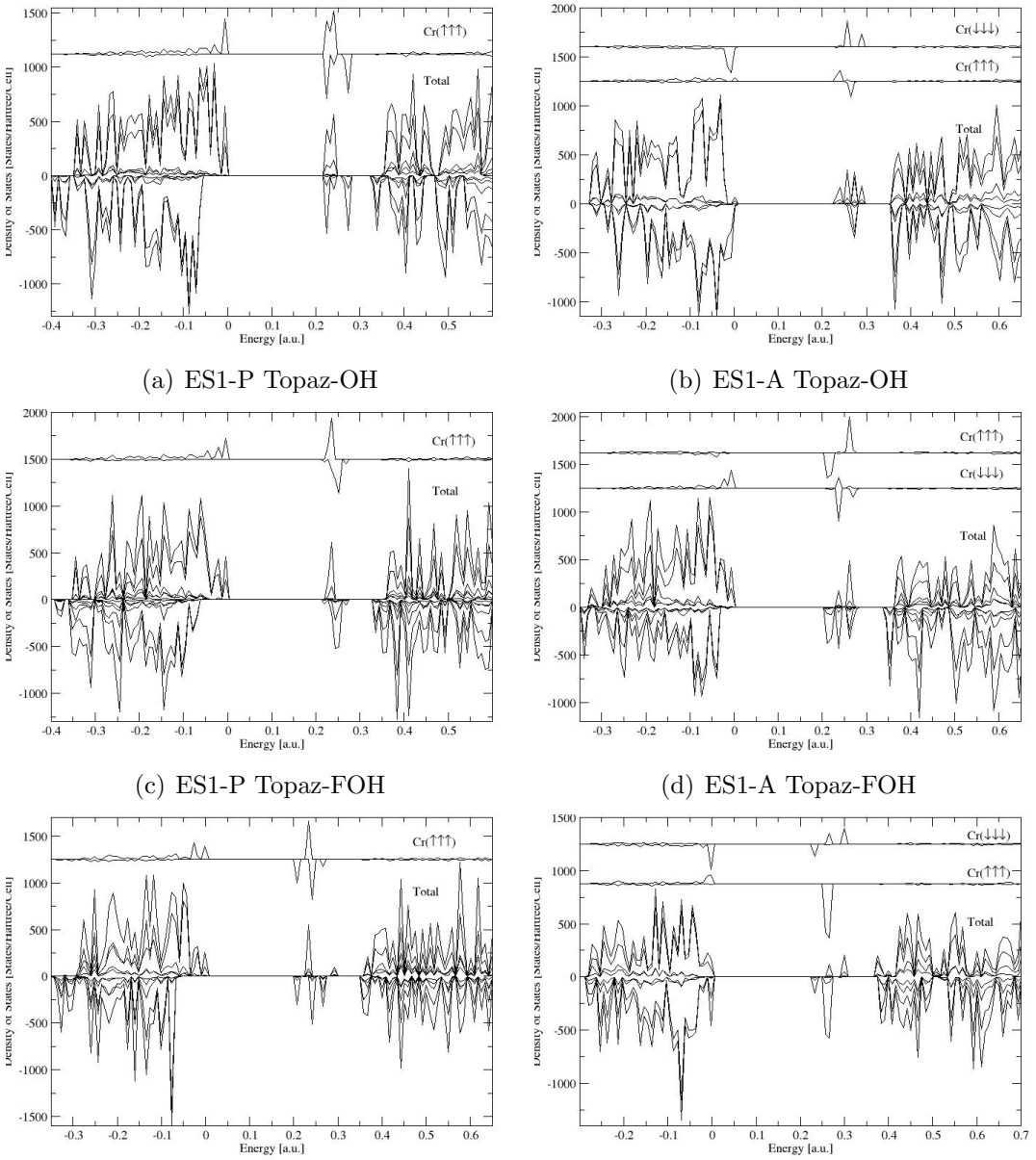

(a) ES1-P Topaz-OH

(b) ES1-A Topaz-OH

(c) ES1-P Topaz-FOH

(d) ES1-A Topaz-FOH

(e) ES1-P Topaz-F

(f) ES1-A Topaz-F

Figure D.3: The CP2K calculated density of states, with total and defect ion projections (chromium, the ghost vacancy site, and the interstisial oxygen), of double chromium defect in topaz. The unqiue electron configurations are labeled.

D.4 UV-Vis Absorption Spectra

Figure D.4 shows the UV-Vis spectra of isolated chromium in topaz-OH, -FOH and -F, with a longer wavelength range sampled then just visible light, and the development of the spectra as a function of larger numbers of sequential MD simulation steps. Since no information regarding the electronic transitions are provided by CP2K in calculating these absorption spectra, the features expected in an optical absorption spectra can be guessed at: such as the onset of the CT band and the $d-d$ transitions. In addition, absorption is observed at longer wavelengths [nm] outside the visible region. This could indicated addition vibrational frequencies occurring in the IR. Only with the progressive MD simulation can longer wavelengths and the lower energy electronic excitations be resolved.

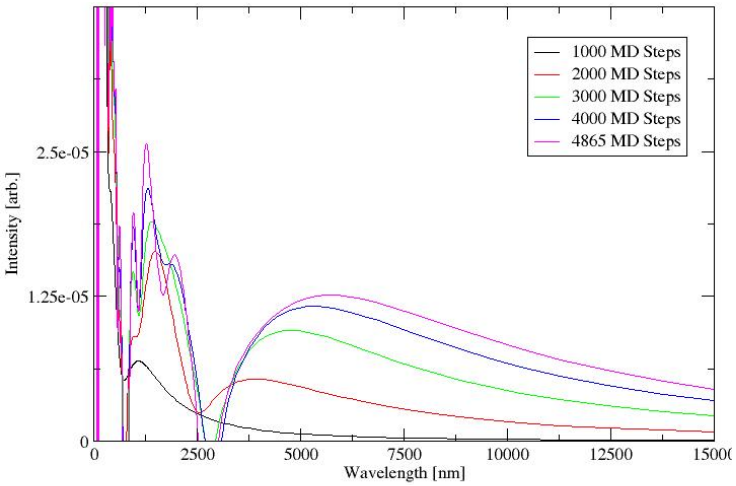

(a) Cr^{3+} Topaz-OH

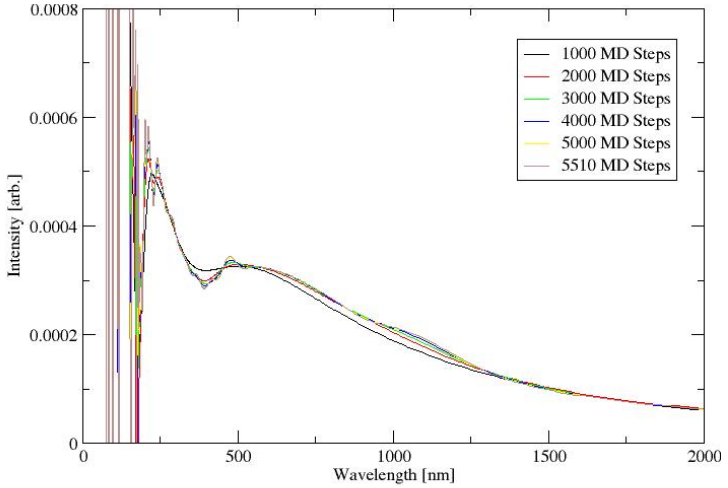

(b) Cr^{3+} Topaz-FOH

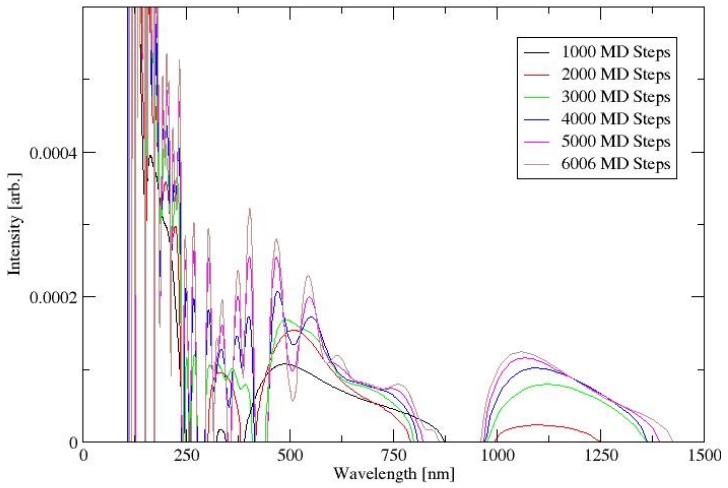

(c) Cr^{3+} Topaz-F

Figure D.4: Absorption spectra of single substituted chromium.

Appendix E

Supporting Information for Phosphorous Based Defects in Topaz

The additional information provided in Appendix E supports the results and discussion on phosphorous based defect in topaz as presented in chapter 7.

E.1 Defect Configuration Labels

The labeling convention adopted in this investigation to distinguish between different configurations for the combination of defects resulting from forming $[PO_3]^{2-}$ and O_i in topaz is illustrated in Figure E.1. There are four tetrahedrally coordinated structural oxygen sites adjacent to the substituted phosphorous from which a vacancy can be created. These are labeled V1, V2, V3, and V4 respectively. In pure high symmetry topaz, the structural oxygens here labeled V3 and V4 are symmetry equivalent. We have considered both of these sites as independent when introducing defects in the topaz system. A constant chemical composition is maintained for every vacancy created, an interstitial is formed. There are eight interstitial sites within the $2 \times 1 \times 1$ supercell we have created to examine defects in topaz that are labeled in Figure E.1 by numbers $1 - 8$. The fractional coordinates of each of the eight positions in a $2 \times 2 \times 2$ supercell of topaz are given in Table E.3. Therefore the labeling convention adopted is as follows: for an oxygen vacancy and interstitial at site 4 and 7 respectively would be referred to as defect configuration V4i8.

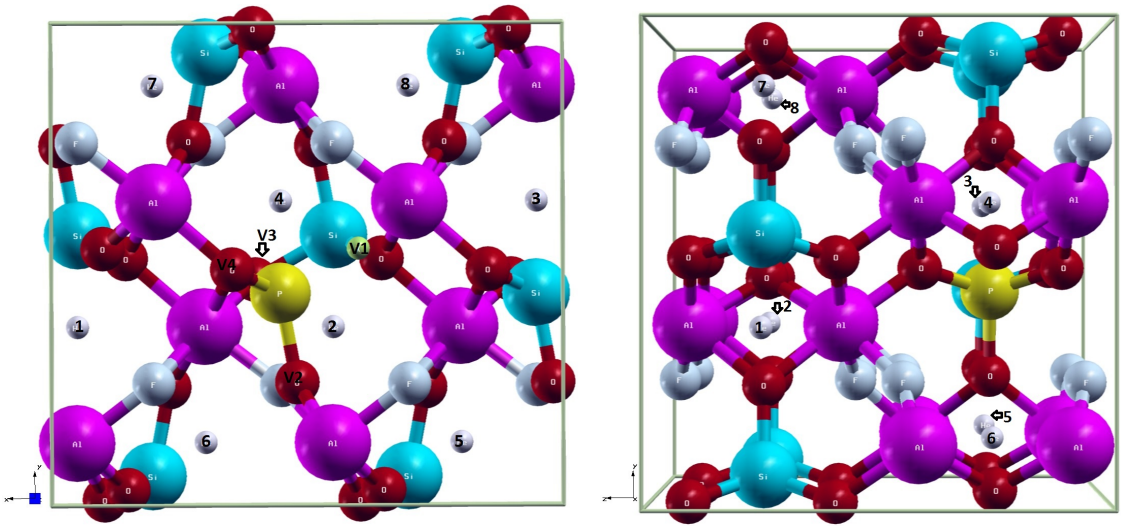

(a) xy-plane (b) zy-plane

Figure E.1: Key for labeling convention for the distinction of locations of an oxygen vacancy from phosphate tetrahedra ($[P^{\times}_{Si}O_4]^{4-}$) and the resulting oxygen interstitial (O_i^{2-}) in topaz containing $[PO_3]^{2-}$.

E.2 Lattice Parameters

The values of the lattice parameters for topaz including the defect $[PO_3]^{2-}$ as calculated by CRYSTAL are given in Table E.1. These include the cell dimensions (a, b, and c), cell angles (α, β, and γ), volumes and densities for the defect configurations investigated here (see Appendix E.1 for defect labeling convention) that were successfully optimised. The corresponding lattice parameters for CP2K calculated phosphorous based defect centres in topaz are given in Table E.2, together with their corresponding pure host lattice parameters.

The lattice parameters for the interstitial sites in topaz are given in Table E.3. These are lattice sites that fall between the crankshaft chains of topaz (AlO_4(F,OH) octahedra linked with SiO_4 tetrahedra in a zig-zag like fashion) and run parallel to the c-axis (see Figures 2.1 and E.1), creating channels where interstitials can form.

E.3 Spin Density Representations

In this section, all 3-dimensional ($\alpha - \beta$) spin density representations of successfully optimised $[PO_3]^{2-}$ defect configurations in topaz are presented here. Figures E.2, E.3, and E.4 give the spin density projections for the $[PO_3]^{2-}$ system in topaz-OH, topaz-FOH, and topaz-F. The gaps in the table indicate configurations that were unsuccessful or unstable for completing a ground state geometry optimisation. (For

defect configuration labeling nomenclature in this section, please see Appendix E.1).

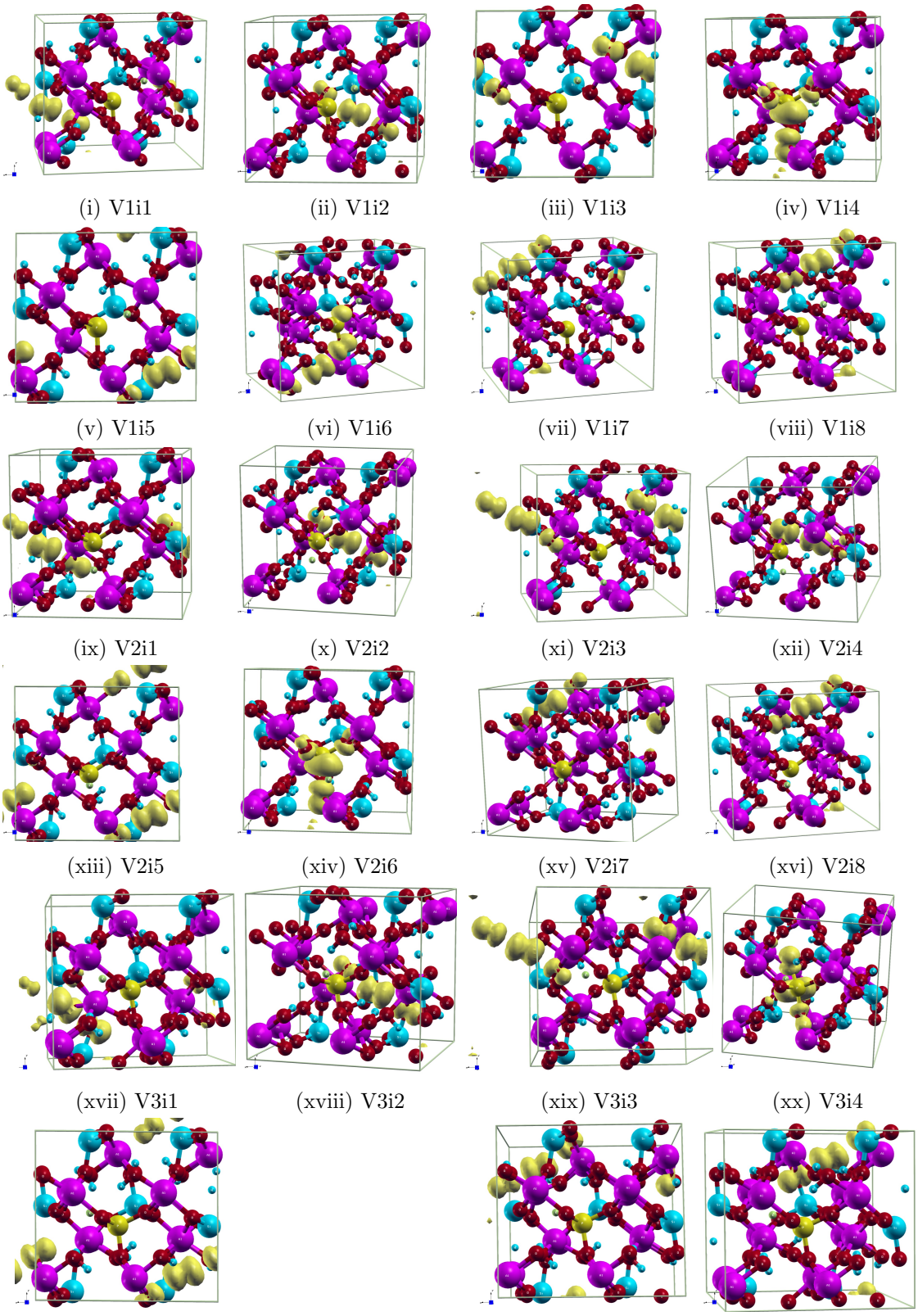

Figure E.2: This figure is continued.

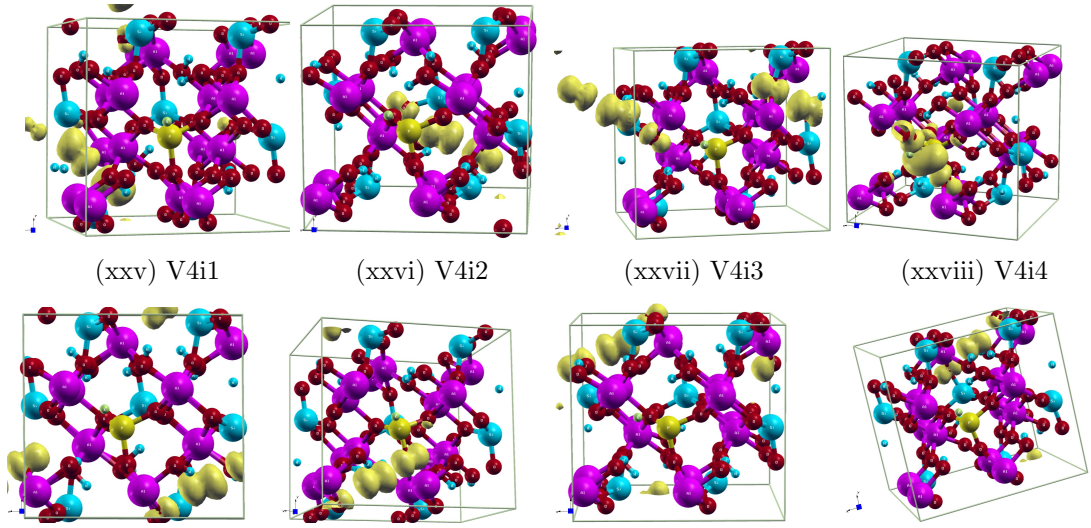

(xxv) V4i1 (xxvi) V4i2 (xxvii) V4i3 (xxviii) V4i4

(xxix) V4i5 (xxx) V4i6 (xxxi) V4i7 (xxxii) V4i8

Figure E.2: $(\alpha - \beta)$ spin density projections of the $[PO_3]^{2-} + O_i$ defect in topaz-OH. Spin density indicated by the yellow shapes and the isovalue used was 0.005.

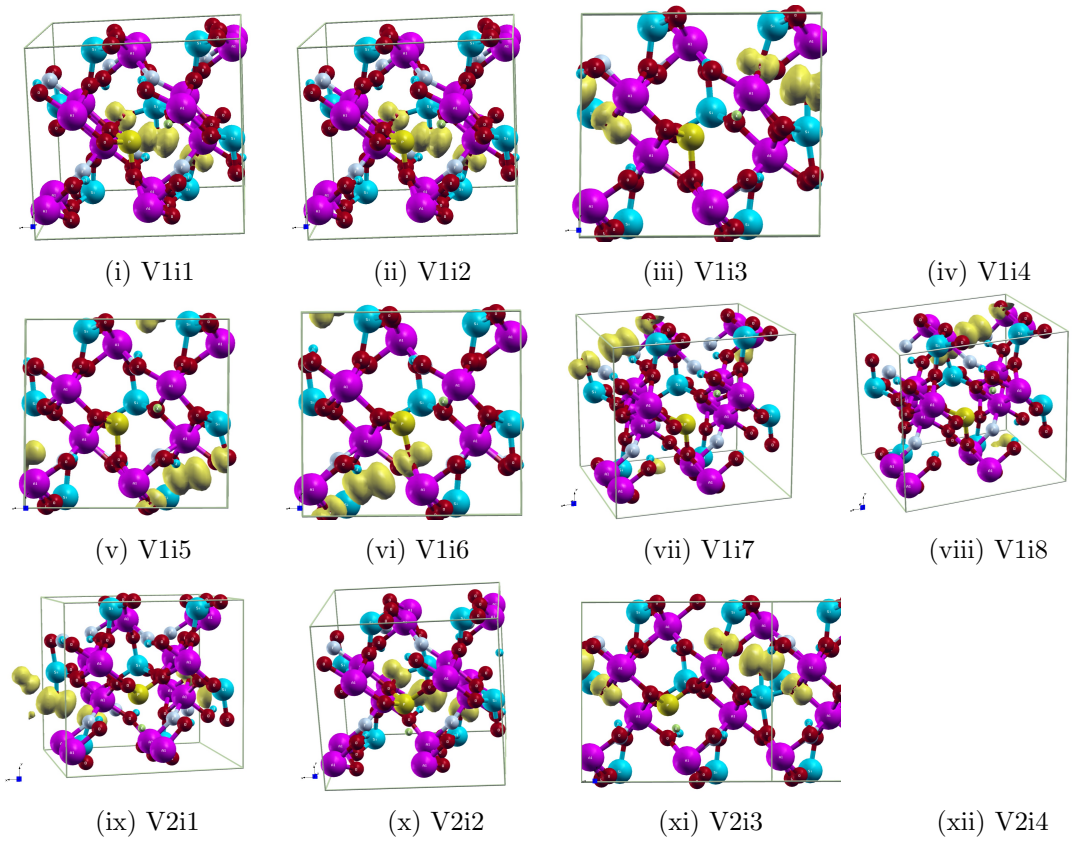

(i) V1i1 (ii) V1i2 (iii) V1i3 (iv) V1i4

(v) V1i5 (vi) V1i6 (vii) V1i7 (viii) V1i8

(ix) V2i1 (x) V2i2 (xi) V2i3 (xii) V2i4

Figure E.3: This figure is continued.

E.4 Density Of States

The density of state for the unique set of defect electronic configurations to arise from the defect formation of $[PO_3]^2 + O_i^{2-}$, for all three F/OH host lattices of topaz,

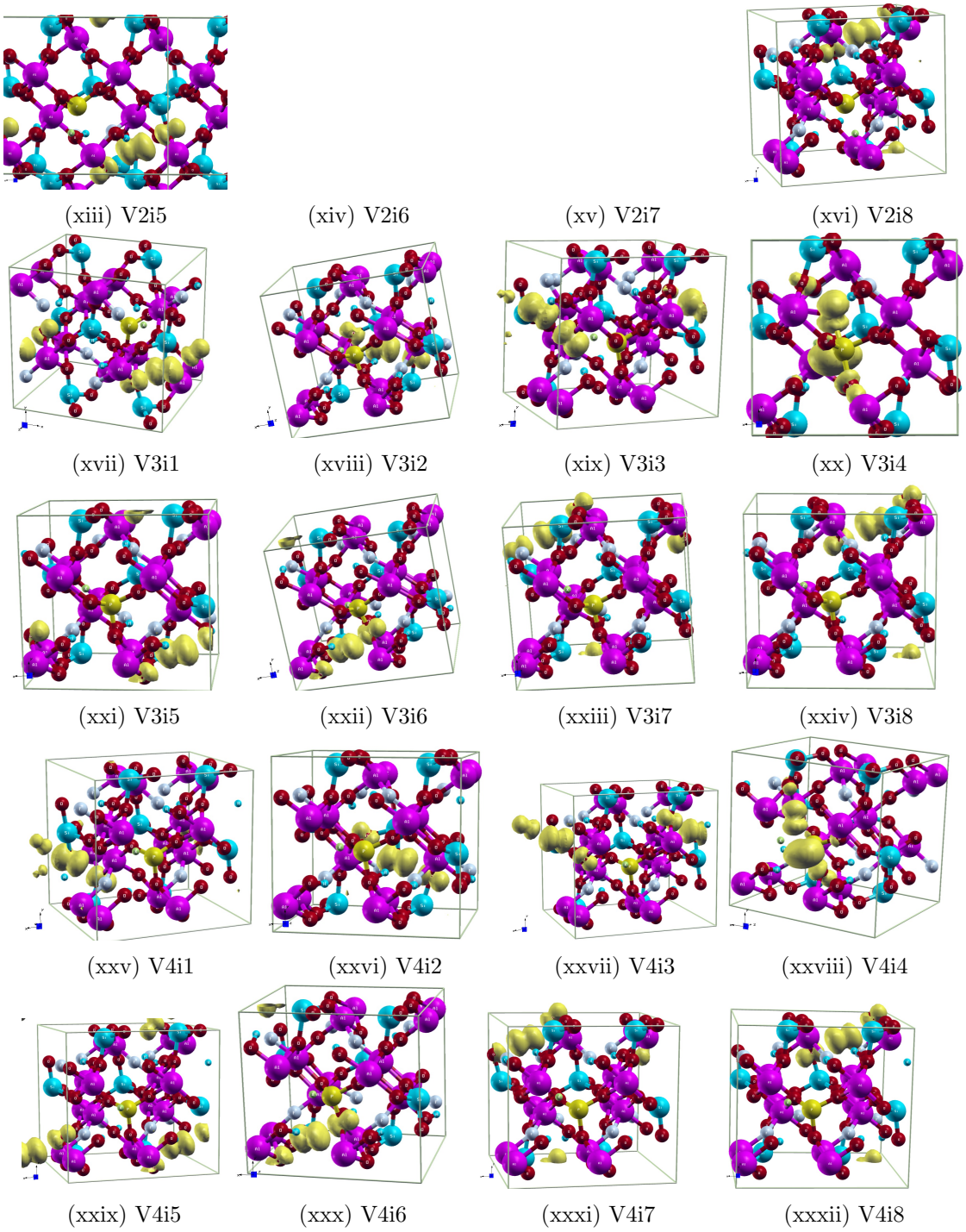

Figure E.3: $(\alpha - \beta)$ spin density projections of the $[PO_3]^{2-} + O_i$ defect in topaz-FOH. Spin density indicated by the yellow shapes and the isovalue used was 0.005.

which include the individual projection of defect species, are given in Figures E.5 and E.6 for CRYSTAL and CP2K calculations respectively.

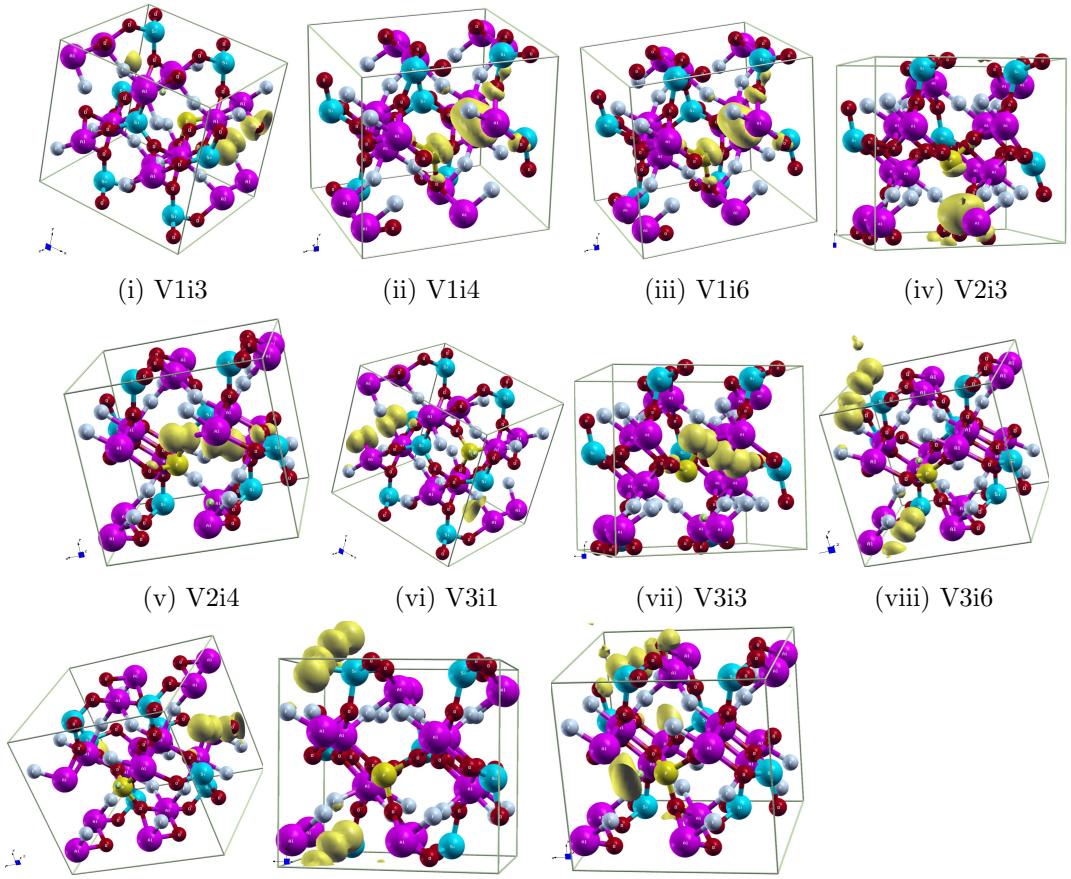

(i) V1i3 (ii) V1i4 (iii) V1i6 (iv) V2i3

(v) V2i4 (vi) V3i1 (vii) V3i3 (viii) V3i6

(ix) V4i1 (x) V4i6 (xi) V4i7

Figure E.4: $(\alpha - \beta)$ spin density projections of the $[PO_3]^{2-} + O_i$ defect in topaz-F. Spin density indicated by the yellow shapes and the isovalue used was 0.005.

E.5 Dynamic Excited State Optical Analysis

The UV-Vis absorption spectra of the $[PO_4]^{4-}$ defect in topaz is given in Figure E.7, and the spectra for $[PO_3]^{2-}$ in topaz-OH, -FOH and -F are given in Figures E.8, E.9 and E.10. The length of simulation is given within each figure. These are supplied here for reference, to state that these calculations had taken place. However, due to the novelty of the method and the lack of electronic information provided by the calculation, we were unable to analyse these further.

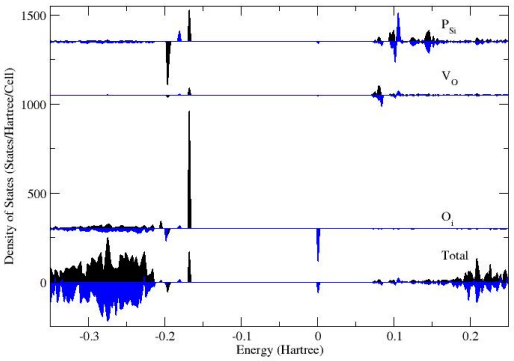

(a) (V2i4) Topaz-OH

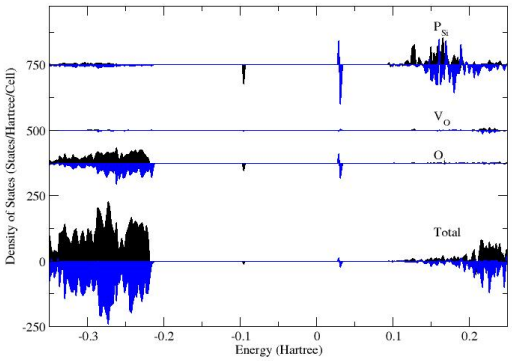

(b) (V2i6) Topaz-OH

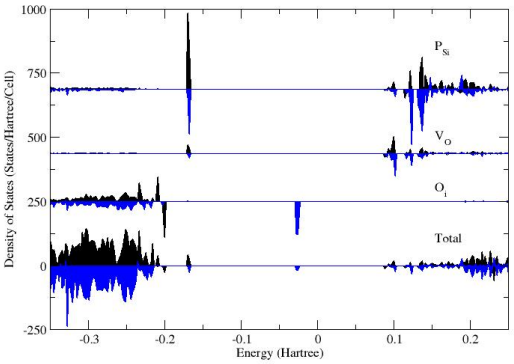

(c) (V3i3) Topaz-FOH

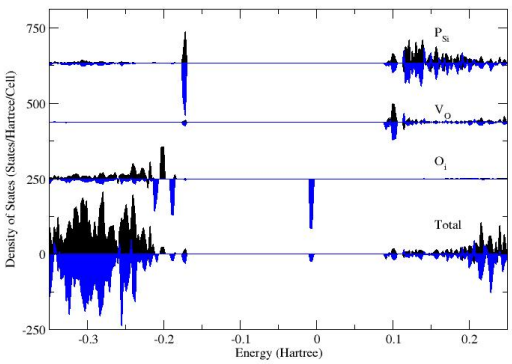

(d) (V4i7) Topaz-FOH

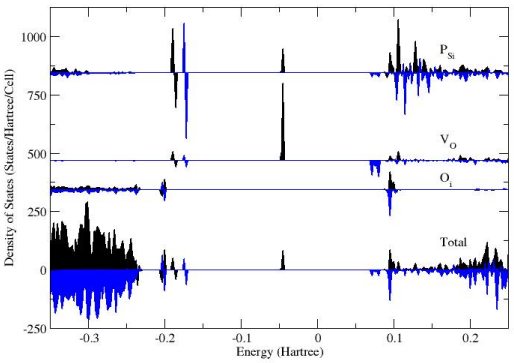

(e) (V1i6) Topaz-F

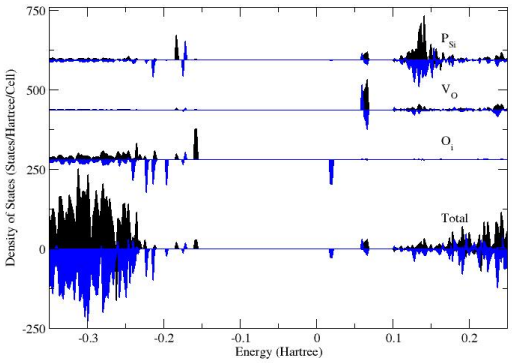

(f) (V2i4) Topaz-F

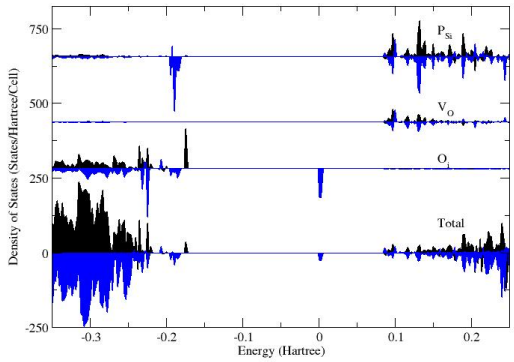

(g) (V4i1) Topaz-F

Figure E.5: The CRYSTAL calculated density of states, with total and defect ion projections (phosphorous, the ghost vacancy site, and the interstitial oxygen), of the $[PO_3]^{2-}$ defect in topaz. The unique electron configurations are labeled.

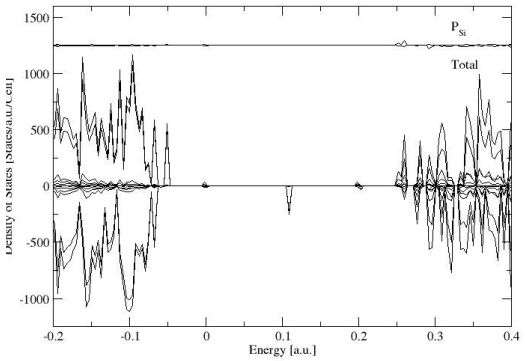

(a) (V2i4) Topaz-OH

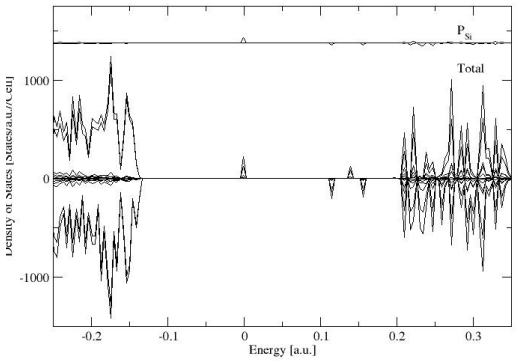

(b) (V2i6) Topaz-OH

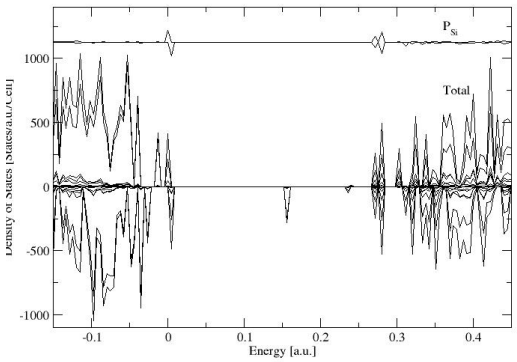

(c) (V3i3) Topaz-FOH

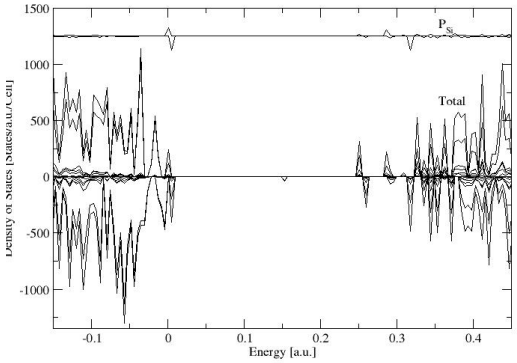

(d) (V4i7) Topaz-FOH

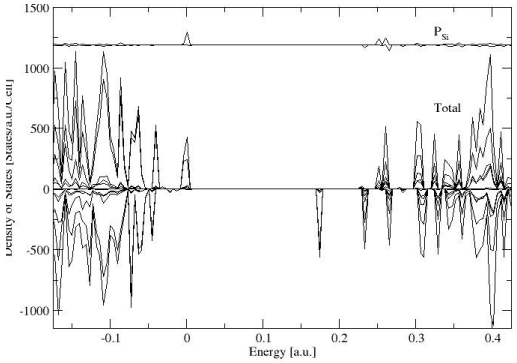

(e) (V1i6) Topaz-F

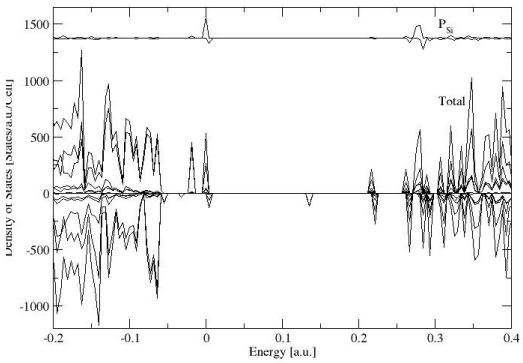

(f) (V2i4) Topaz-F

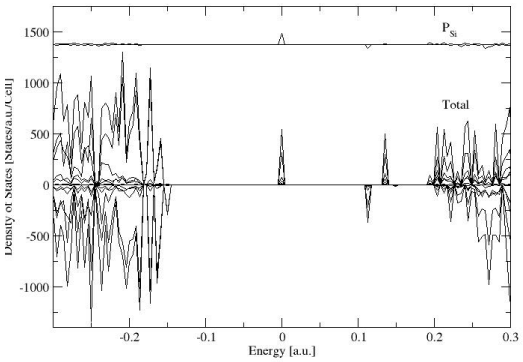

(g) (V4i1) Topaz-F

Figure E.6: The CP2K calculated density of states, with total and defect ion projections (phosphorous, the ghost vacancy site, and the interstitial oxygen), of the $[PO_3]^{2-}$ defect in topaz. The unique electron configurations are labeled.

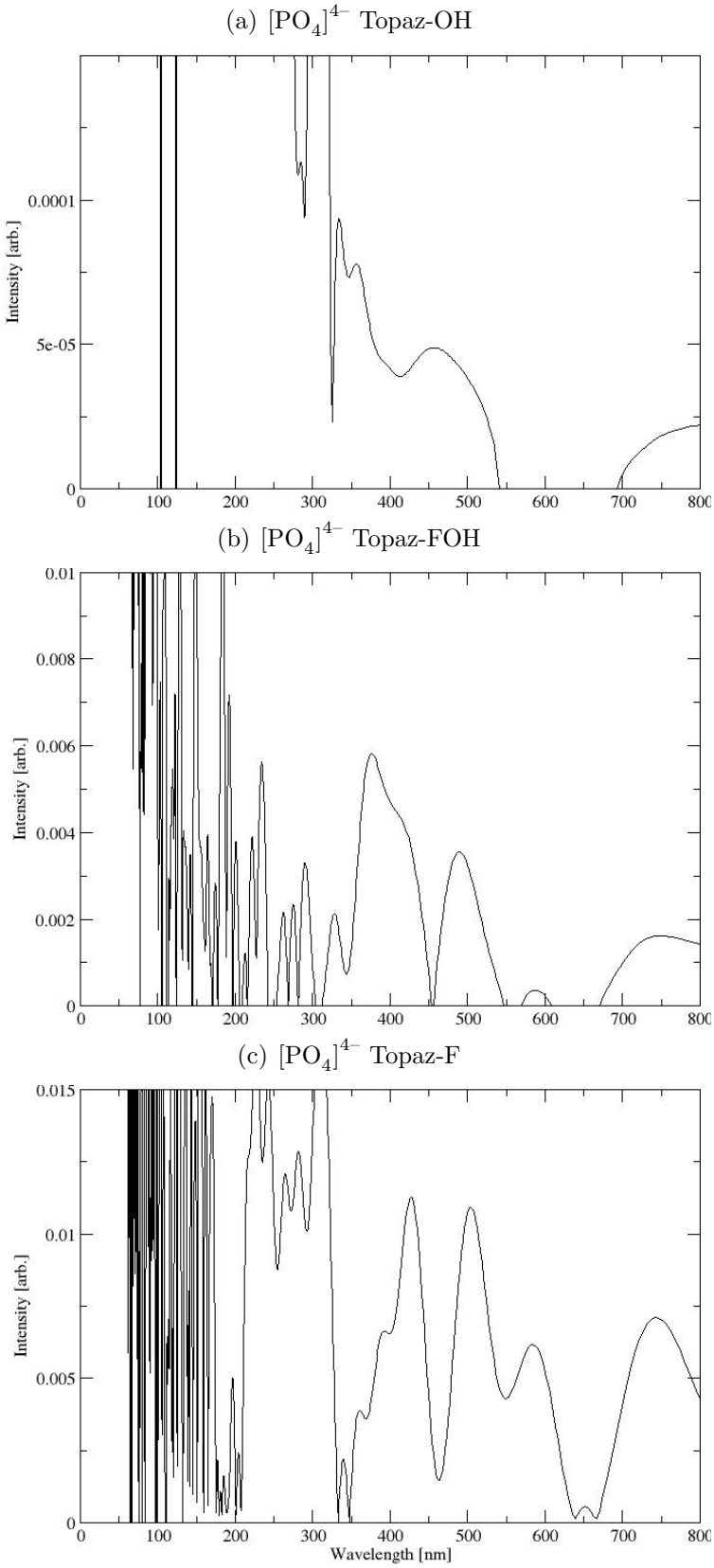

Figure E.7: UV-Vis absorption spectra of the $[PO_4]^{4-}$ defect in ((a)) topaz-OH, ((b)) topaz-=, and ((c)) topaz-F. The total number of MD steps simulated to generate each spectra are 4118, 4334, and 5031 respectively.

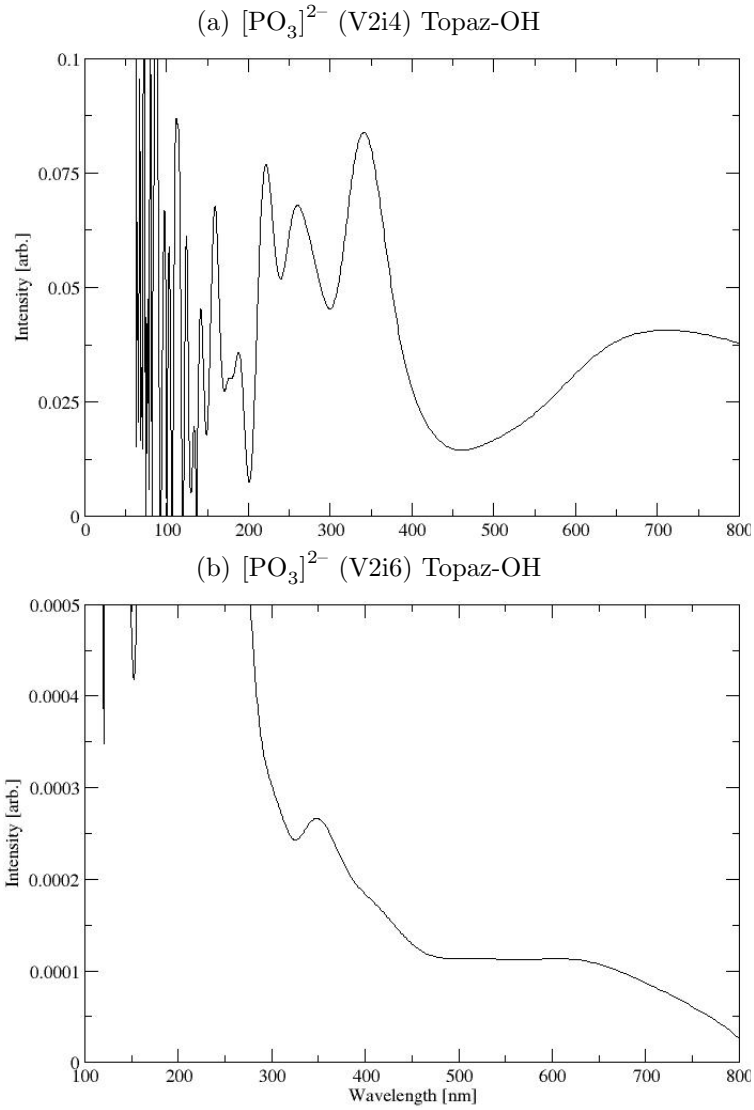

Figure E.8: UV-Vis absorption spectra of the $[PO_3]^{2-}$ defects in topaz-OH: defect configurations ((a)) V2i4 and ((b)) V2i6. The total number of MD steps simulated to generate each spectra are 2309, and 2255 respectively.

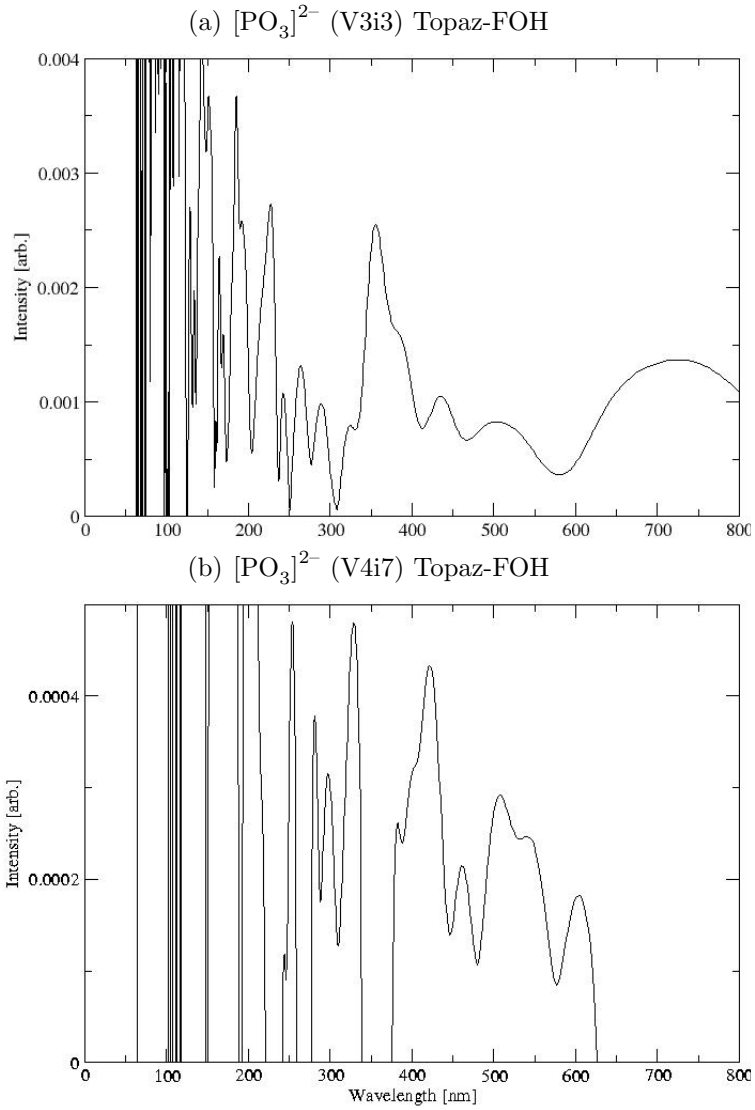

Figure E.9: UV-Vis absorption spectra of the $[PO_3]^{2-}$ defects in topaz-FOH: defect configurations ((a)) V3i3 and ((b)) V4i7. The total number of MD steps simulated to generate each spectra are 4686, and 4832 respectively.

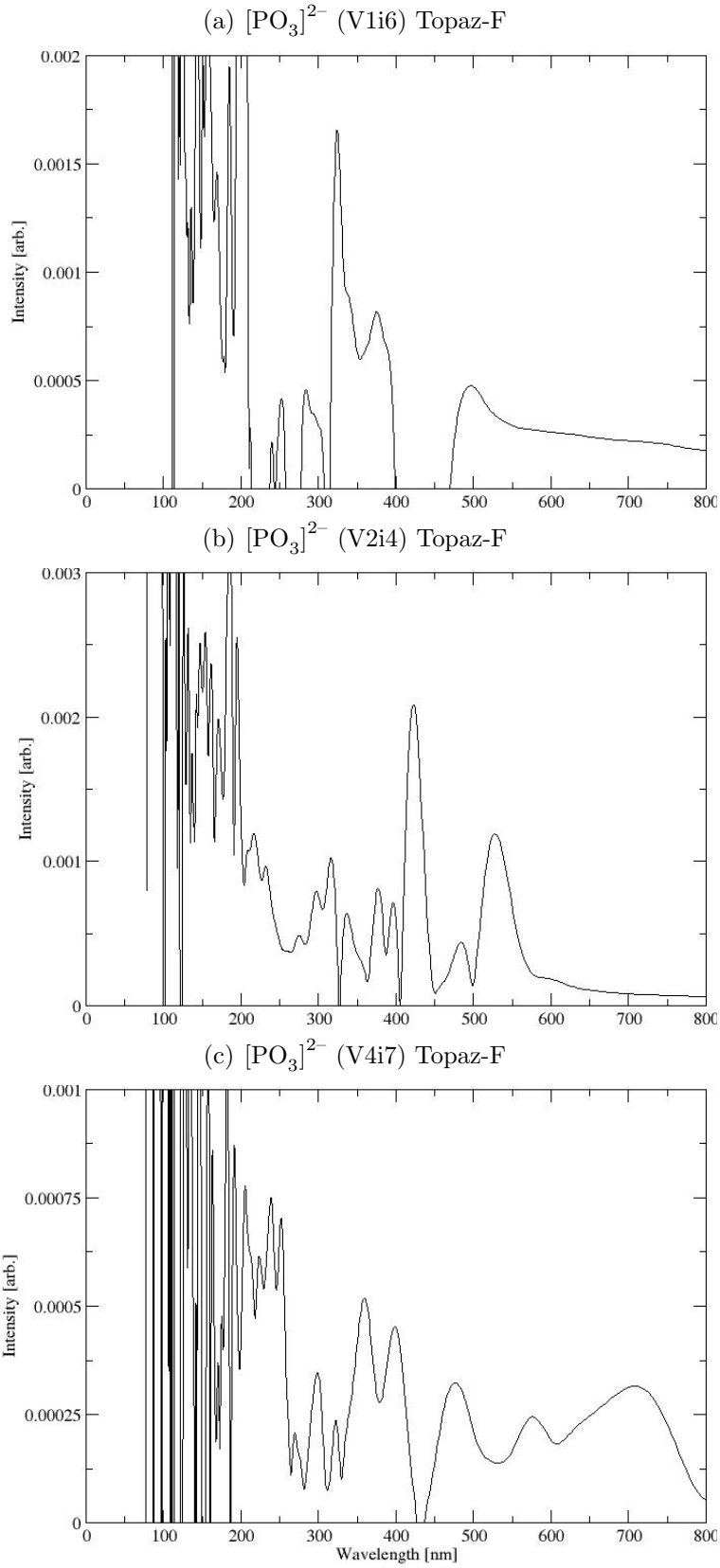

Figure E.10: UV-Vis absorption spectra of the $[PO_3]^{2-}$ defects in topaz-F: defect configurations ((a)) V1i6, ((b)) V2i4, and ((c)) V4i1. The total number of MD steps simulated to generate each spectra are 6146, 5802, and 6175 respectively.

config.	a [Å]	b [Å]	c [Å]	alpha	beta	gamma	Volume [Å^3]	Density [g cm^{-3}]
(a) $[PO_3]^{2-}$ in Topaz-OH								
V1i1	9.6010	8.9005	8.5273	89.88	89.72	91.03	728.57	3.287
V1i3	9.6105	8.9020	8.5164	90.09	89.75	91.05	728.47	3.288
V1i5	9.6054	8.9107	8.5245	89.99	89.80	90.63	729.58	3.283
V1i6	9.5462	8.9384	8.5230	89.72	89.84	90.22	727.23	3.294
V1i7	9.5996	8.9207	8.5118	89.93	89.78	90.65	728.86	3.286
V1i8	9.6051	8.9087	8.5380	89.95	89.78	90.49	730.56	3.279
V2i1	9.5130	8.9498	8.5474	89.77	89.80	90.10	727.70	3.291
V2i2	9.5612	8.9541	8.4852	89.90	89.87	89.99	726.44	3.297
V2i3	9.5289	8.9291	8.5636	89.76	89.72	90.07	728.61	3.287
V2i4	9.6676	8.9747	8.4942	89.82	89.67	90.77	736.90	3.250
V2i5	9.5524	8.9384	8.5309	89.83	89.74	89.44	728.35	3.288
V2i6	9.4470	9.0307	8.4128	90.04	89.98	89.83	717.72	3.337
V3i1	9.5135	8.9492	8.5125	90.25	89.94	89.95	724.72	3.305
V3i2	9.5820	8.8893	8.5357	90.13	89.34	90.16	726.99	3.295
V3i3	9.5676	8.8920	8.5438	90.16	89.45	90.17	726.83	3.295
V3i5	9.5779	8.8928	8.5409	90.11	89.49	89.38	727.39	3.293
V3i6	9.5794	8.9097	8.5302	90.12	89.40	89.23	727.94	3.290
V3i7	9.5989	8.8693	8.5029	90.28	89.53	89.48	723.83	3.309
V3i8	9.5774	8.8951	8.5362	90.02	89.47	89.40	727.14	3.294
V4i2	9.5954	8.8698	8.5577	89.88	90.56	90.30	728.29	3.289
V4i3	9.5716	8.8883	8.5577	90.00	90.53	90.15	728.02	3.290
V4i5	9.5890	8.8800	8.5536	89.83	90.29	89.44	728.30	3.289
V4i6	9.5860	8.8896	8.5567	89.76	90.58	89.44	729.08	3.285
V4i7	9.5981	8.8556	8.5445	89.63	90.43	89.66	726.21	3.298
V4i8	9.5848	8.8792	8.5554	89.89	90.37	89.53	728.07	3.290
(b) $[PO_3]^{2-}$ in Topaz-FOH								
V1i1	9.5562	8.8443	8.4534	89.86	90.06	90.83	714.40	3.390
V1i2	9.5653	8.8619	8.4364	89.81	90.09	91.02	715.01	3.387
V1i3	9.5453	8.8490	8.4412	89.97	89.91	90.86	712.92	3.397
V1i5	9.5510	8.8592	8.4514	90.04	90.11	90.49	715.08	3.387
V1i6	9.5201	8.8586	8.4493	90.04	90.14	90.19	712.57	3.399
V1i7	9.5381	8.8554	8.4486	89.89	89.83	90.33	713.58	3.394
V1i8	9.5639	8.8496	8.4498	89.72	89.91	90.44	715.13	3.386
V2i1	9.4710	8.8997	8.4582	89.94	90.15	90.04	712.93	3.397
V2i2	9.4777	8.9136	8.4459	89.94	90.20	90.00	713.51	3.394
V2i3	9.4739	8.8871	8.4743	90.16	89.97	90.30	713.48	3.394
V2i5	9.4727	8.9021	8.4594	90.01	90.08	89.67	713.34	3.395
V2i8	9.4794	8.8895	8.4819	89.86	89.98	89.58	714.73	3.388
V3i1	9.4988	8.8568	8.4679	89.96	89.81	90.21	712.38	3.399
V3i2	9.5217	8.8323	8.4788	90.05	89.66	90.21	713.03	3.396
V3i3	9.4832	8.8759	8.4778	89.85	88.90	89.96	713.46	3.394
V3i5	9.5209	8.8394	8.4777	90.24	89.72	89.71	713.45	3.394
V3i6	9.5010	8.8626	8.4729	90.29	89.57	89.65	713.41	3.395
V3i7	9.5000	8.8352	8.4787	90.19	89.54	89.79	711.62	3.403
V3i8	9.5052	8.8451	8.4809	89.99	89.59	89.67	713.00	3.396
V4i1	9.4357	8.9022	8.4743	89.63	90.16	89.82	711.81	3.402
V4i2	9.5261	8.8414	8.4713	89.83	90.56	89.95	713.45	3.394
V4i3	9.5074	8.8565	8.4653	90.13	90.31	90.03	712.79	3.397
V4i5	9.5169	8.8536	8.4666	90.14	90.45	89.42	713.33	3.395
V4i7	9.5177	8.8352	8.4484	89.69	90.28	89.49	710.39	3.409
V4i8	9.5103	8.8442	8.4788	89.94	90.32	89.49	713.12	3.396
(c) $[PO_3]^{2-}$ in Topaz-F								
V1i3	9.4157	8.8088	8.5493	90.39	90.18	90.74	709.01	3.453
V1i4	9.5566	8.8430	8.4517	90.05	89.65	90.02	714.23	3.428
V1i6	9.4784	8.8354	8.4998	90.21	89.53	90.27	711.78	3.439
V2i3	9.5071	8.9227	8.4391	90.01	90.17	90.59	715.84	3.420
V2i4	9.4898	8.8370	8.4920	90.11	90.76	90.27	712.07	3.438
V3i1	9.3788	8.7972	8.5775	90.34	90.04	90.11	707.69	3.459
V3i6	9.3802	8.8018	8.5686	89.53	89.95	89.48	707.39	3.461
V4i1	9.3763	8.8035	8.5774	90.30	90.51	90.10	707.97	3.458
V4i6	9.3834	8.8071	8.5658	89.67	90.65	89.54	707.80	3.459

Table E.1: CRYSTAL calculated lattice parameters for the $[PO_3]^{2-}$ defect in (a) topaz-OH, (b) topaz-FOH, and (c) topaz-F.

CP2K Lattice Parameters								
[F] [%]	Config.	a [Å]	b [Å]	c [Å]	alpha	beta	gamma	Volume [Å^3]
(a) Pure Topaz (for reference)								
0		9.451	8.886	8.421	90.000	89.924	90.000	707.187
50		9.384	8.910	8.408	89.856	90.000	90.000	702.998
100		9.282	8.776	8.399	89.935	90.044	89.978	684.079
(b) $[PO_4]^{4-}$								
0		0.000	0.000	0.000	0.000	0.000	0.000	0.000
50		0.000	0.000	0.000	0.000	0.000	0.000	0.000
100		0.000	0.000	0.000	0.000	0.000	0.000	0.000
(c) $[PO_3]^{2-} + O_i^{2-}$								
0	V1i2	0.000	0.000	0.000	0.000	0.000	0.000	0.000
0	V2i4	0.000	0.000	0.000	0.000	0.000	0.000	0.000
0	V2i6	0.000	0.000	0.000	0.000	0.000	0.000	0.000
50	V3i3	9.420	8.829	8.480	89.813	90.800	90.031	705.144
50	V4i7	9.391	8.819	8.498	90.111	89.982	90.454	703.710
100	V1i6	9.336	8.769	8.502	90.383	90.358	89.941	695.978
100	V2i4	9.315	8.797	8.492	90.792	89.662	90.346	695.706
100	V4i1	9.250	8.764	8.460	90.044	90.034	90.485	685.863

Table E.2: CP2K calculated phosphorus defects, $[PO_4]^{4-}$ and $[PO_3]^{2-} + O_i^{2-}$, lattice parameters in topaz-OH, -FOH and -F. Pure lattice parameters of the host lattice provided for reference.

Interstitial Atomic Fractional Coordinates			
no.	x	y	z
1	0.9486	0.3691	0.7500
2	0.4486	0.3691	0.7500
3	0.0514	0.6309	0.2500
4	0.5514	0.6309	0.2500
5	0.1986	0.1309	0.2500
6	0.6986	0.1309	0.2500
7	0.8014	0.8691	0.7500
8	0.3014	0.8691	0.7500

Table E.3: The fractional coordinates of interstitial atomic species in topaz. These were taken from reference [142].

Appendix F

Supporting Information for Silicon Based Defects in Topaz

The additional information provided in Appendix F supports the results and discussion on phosphorous based defect in topaz as presented in Chapter 8.

F.1 Lattice Parameters

The values of the lattice parameters for topaz including the defect $[SiO_3]^{2-}$ as calculated by CRYSTAL are given in Table F.1. These include the cell dimensions (a, b, and c), cell angles (α, β, and γ), volumes and densities defect configurations (see Appendix E for labeling definition) successfully optimised.

F.2 Mulliken Population Analysis

The Mulliken population analysis of all the atoms where the unpaired spin has localised, for all the different structural configurations of the $[SiO_3]^{2-}$ defect in topaz-OH, FOH and F, are given in full in Table F.2. The defect electronic configuration has also been assigned.

config.	a [Å]	b [Å]	c [Å]	alpha	beta	gamma	Volume [$Å^3$]	Density [$g\,cm^{-3}$]
(a) $[SiO_3]^{2-}$ in Topaz-OH								
V1i1	9.5640	8.8950	8.4856	89.89	89.68	90.36	721.86	3.311
V1i2	9.5580	8.9013	8.4898	89.94	89.79	90.38	722.29	3.309
V1i3	9.5599	8.8890	8.4903	89.92	89.59	90.32	721.45	3.313
V1i4	9.5701	8.9958	8.4053	90.07	89.52	91.08	723.46	3.304
V1i5	9.5572	8.9065	8.4915	90.31	89.71	90.04	722.79	3.307
V1i7	9.5665	8.8993	8.4815	90.29	89.78	89.98	722.06	3.310
V1i8	9.5599	8.8947	8.4772	90.33	89.71	89.78	720.81	3.316
V2i1	9.5544	8.8946	8.5009	89.58	89.82	90.22	722.40	3.309
V2i2	9.5519	8.9001	8.4962	89.36	89.67	90.19	722.23	3.309
V2i3	9.5590	8.8881	8.4953	89.52	89.82	90.22	721.75	3.312
V2i4	9.5559	8.9043	8.4981	89.35	89.74	90.21	723.03	3.306
V2i5	9.5513	8.8932	8.5087	90.10	89.86	89.77	722.74	3.307
V2i8	9.5529	8.8953	8.5019	89.87	89.73	89.71	722.44	3.309
V3i1	9.5444	8.8983	8.4816	89.88	89.98	90.18	720.33	3.318
V3i2	9.5642	8.8965	8.4774	89.83	89.99	90.08	721.32	3.314
V3i3	9.5429	8.8898	8.4984	89.99	90.01	90.29	720.95	3.315
V3i5	9.5564	8.8982	8.4792	90.32	90.01	89.66	721.00	3.315
V3i7	9.5570	8.8945	8.4848	90.32	89.95	89.67	721.22	3.314
V3i8	9.5553	8.8959	8.4862	90.31	89.99	89.65	721.33	3.314
V4i1	9.5804	8.8926	8.4724	89.81	89.97	90.14	721.80	3.311
V4i2	9.5720	8.8901	8.5008	89.74	90.10	90.22	723.38	3.304
V4i3	9.5737	8.8946	8.4844	89.78	89.99	90.16	722.48	3.308
V4i5	9.5811	8.8928	8.4851	90.27	90.03	89.58	722.92	3.306
V4i7	9.5694	8.8933	8.4909	90.17	90.01	89.63	722.59	3.308
V4i8	9.5798	8.8958	8.4820	90.29	90.04	89.62	722.81	3.307
(b) $[SiO_3]^{2-}$ in Topaz-FOH								
V1i1	9.5080	8.8611	8.4348	89.99	89.80	90.02	710.64	3.401
V1i2	9.5092	8.8654	8.4275	89.98	89.76	90.11	710.45	3.402
V1i3	9.4913	8.8580	8.4400	90.03	90.14	89.98	709.58	3.406
V1i5	9.4978	8.8729	8.4389	90.08	89.74	90.21	711.16	3.398
V1i6	9.4932	8.8615	8.4380	90.08	89.84	89.92	709.84	3.405
V1i7	9.5023	8.8665	8.4313	89.96	90.12	90.04	710.35	3.402
V1i8	9.5025	8.8642	8.4311	89.97	90.08	90.01	710.17	3.403
V2i1	9.4887	8.8753	8.4525	89.83	89.87	90.00	711.82	3.395
V2i2	9.4838	8.8824	8.4465	89.70	89.79	89.96	711.52	3.397
V2i3	9.4882	8.8568	8.4516	90.03	90.17	90.10	710.22	3.403
V2i4	9.4579	8.9075	8.4694	90.05	90.01	89.94	713.51	3.387
V2i5	9.4858	8.8736	8.4581	90.10	89.91	90.13	711.94	3.395
V2i6	9.3754	9.0582	8.3994	90.03	90.06	89.82	713.31	3.388
V2i7	9.4988	8.8571	8.4476	89.90	90.15	90.05	710.72	3.400
V2i8	9.4925	8.8672	8.4520	89.88	90.14	90.09	711.42	3.397
V3i1	9.5012	8.8642	8.4195	90.00	89.93	89.92	709.10	3.408
V3i2	9.5076	8.8638	8.4327	90.02	89.95	89.83	710.64	3.401
V3i3	9.4833	8.8617	8.4445	90.16	90.27	90.11	709.65	3.405
V3i4	9.4068	8.9684	8.3942	89.79	89.81	89.60	708.14	3.413
V3i6	9.4899	8.8721	8.4442	90.20	89.93	90.06	710.96	3.399
V3i7	9.4575	8.8773	8.4561	90.02	90.24	90.18	709.94	3.404
V3i8	9.4949	8.8607	8.4374	90.09	90.29	89.98	709.84	3.405
V4i1	9.5019	8.8723	8.4234	90.02	89.77	89.78	710.11	3.403
V4i2	9.5011	8.8657	8.4450	89.92	89.87	89.90	711.35	3.397
V4i3	9.4674	8.8753	8.4552	89.94	90.05	89.87	710.46	3.402
V4i5	9.4908	8.8703	8.4387	90.07	89.77	89.86	710.41	3.402
V4i6	9.5052	8.8720	8.4362	90.12	89.95	89.80	711.41	3.397
V4i7	9.5015	8.8613	8.4368	89.86	90.19	89.92	710.33	3.402
V4i8	9.4961	8.8678	8.4373	89.92	90.12	89.90	710.50	3.401
(c) $[SiO_3]^{2-}$ in Topaz-F								
V1i1	9.3702	8.8047	8.4985	90.00	90.00	90.01	701.14	3.485
V1i2	9.3754	8.8056	8.4972	89.99	90.00	89.96	701.50	3.483
V1i5	9.3781	8.8077	8.4999	89.99	90.00	89.86	702.08	3.480
V1i7	9.3713	8.8037	8.4989	90.00	89.99	89.77	701.17	3.484
V1i8	9.3668	8.8038	8.4978	89.98	90.01	89.71	700.75	3.487
V2i1	9.5571	8.9443	8.4314	89.98	90.14	90.61	720.68	3.390
V2i2	9.3773	8.8142	8.4984	90.01	90.01	90.14	702.41	3.478
V2i5	9.3839	8.8031	8.5043	89.97	89.99	90.03	702.52	3.478
V2i7	9.3823	8.8000	8.4993	89.99	90.00	90.02	701.74	3.482
V3i1	9.3840	8.8072	8.4840	89.95	90.16	89.98	701.17	3.484
V3i2	9.3807	8.8097	8.4968	90.07	90.08	90.04	702.19	3.479
V3i3	9.3726	8.8083	8.4976	90.07	90.17	90.05	701.53	3.483
V3i4	9.3747	8.8712	8.4413	89.70	89.73	89.57	701.98	3.480
V3i5	9.3780	8.8104	8.4971	90.02	90.13	89.84	702.06	3.480
V3i7	9.3731	8.8094	8.4965	90.02	90.18	89.83	701.56	3.483
V3i8	9.3726	8.8119	8.4962	90.00	90.14	89.85	701.71	3.482
V4i2	9.3787	8.8099	8.4990	89.92	89.90	90.05	702.23	3.479
V4i3	9.3726	8.8081	8.4977	89.92	89.83	90.05	701.52	3.483
V4i4	9.3739	8.8716	8.4414	90.26	90.25	89.59	701.96	3.481
V4i5	9.3782	8.8101	8.4963	89.99	89.87	89.82	701.98	3.480
V4i7	9.3720	8.8101	8.4966	89.97	89.81	89.83	701.54	3.483
V4i8	9.3746	8.8102	8.4964	89.98	89.86	89.85	701.73	3.482

Table F.1: CRYSTAL calculated lattice parameters for the $[SiO_3]^{2-}$ defect in (a) topaz-OH, (b) topaz-FOH, and (c) topaz-F.

$[SiO_3]^{3-} + O_i^-$										
Config.	Defect Energy [eV]	Elect. Config.	Atom	Spin	Atom	Spin	Atom	Spin	Atom	Spin
(a) Topaz-OH										
V1i1	11.317	$[O_4]^{2-}$	O_i	1.467	O	0.282	O	0.116	O	0.123
V1i2	11.274	$[O_4]^{2-}$	O_i	1.460	O	0.254	O	0.140	O	0.135
V1i3	11.207	$[O_4]^{2-}$	O_i	1.435	O	0.271	O	0.139	O	0.137
V1i4	6.546	$[SiO]^{2-}$	Si	0.613	O_i	0.953				
V1i5	11.288	$[O_4]^{2-}$	O_i	1.474	O	0.252	O	0.145	O	0.119
V1i7	11.380	$[O_4]^{2-}$	O_i	1.481	O	0.257	O	0.122	O	0.130
V1i8	11.423	$[O_4]^{2-}$	O_i	1.466	O	0.273	O	0.119	O	0.130
V2i1	11.290	$[O_4]^{2-}$	O_i	1.459	O	0.274	O	0.121	O	0.132
V2i2	11.216	$[O_4]^{2-}$	O_i	1.446	O	0.291				
V2i3	11.324	$[O_4]^{4-}$	O_i	1.116	O	0.356	O	1.041	O	1.013
V2i4	11.473	$[O_4]^{2-}$	O_i	1.446	O	0.300	O	0.118	O	0.120
V2i5	11.443	$[O_4]^{2-}$	O_i	1.457	O	0.289	O	0.117	O	0.122
V2i8	11.317	$[O_4]^{2-}$	O_i	1.460	O	0.269	O	0.128	O	0.131
V3i1	11.415	$[O_4]^{2-}$	O_i	1.464	O	0.260	O	0.135	O	0.129
V3i2	11.438	$[O_4]^{2-}$	O_i	1.468	O	0.260	O	0.146	O	0.115
V3i3	11.393	$[O_4]^{2-}$	O_i	1.482	O	0.262	O	0.116	O	0.130
V3i5	11.323	$[O_4]^{2-}$	O_i	1.472	O	0.249	O	0.136	O	0.132
V3i7	11.422	$[O_4]^{2-}$	O_i	1.449	O	0.277	O	0.132	O	0.130
V3i8	11.366	$[O_4]^{2-}$	O_i	1.459	O	0.268	O	0.125	O	0.137
V4i1	11.451	$[O_4]^{2-}$	O_i	1.479	O	0.247	O	0.135	O	0.128
V4i2	11.362	$[O_4]^{2-}$	O_i	1.449	O	0.268	O	0.126	O	0.125
V4i3	11.485	$[O_4]^{2-}$	O_i	1.482	O	0.265	O	0.122	O	0.121
V4i5	11.365	$[O_4]^{2-}$	O_i	1.464	O	0.261	O	0.128	O	0.136
V4i7	11.288	$[O_4]^{2-}$	O_i	1.450	O	0.283	O	0.147	O	0.103
V4i8	11.442	$[O_4]^{2-}$	O_i	1.467	O	0.258	O	0.130	O	0.135
(b) Topaz-FOH										
V1i1	11.304	$[O_4]^{2-}$	O_i	1.583	O	0.196	O	0.114	F	0.020
V1i2	11.310	$[O_4]^{2-}$	O_i	1.556	O	0.183	O	0.134	F	0.017
V1i3	11.297	$[O_4]^{2-}$	O_i	1.582	O	0.161	O	0.133	F	0.020
V1i5	11.286	$[O_4]^{2-}$	O_i	1.573	O	0.191	O	0.124	F	0.020
V1i6	11.188	$[O_4]^{2-}$	O_i	1.520	O	0.250	O	0.097	F	0.017
V1i7	11.308	$[O_4]^{2-}$	O_i	1.582	O	0.182	O	0.121	F	0.018
V1i8	11.375	$[O_4]^{2-}$	O_i	1.574	O	0.184	O	0.117	F	0.017
V2i1	11.466	$[O_4]^{2-}$	O_i	1.613	O	0.202	O	0.103	F	0.023
V2i2	11.396	$[O_4]^{2-}$	O_i	1.626	O	0.191	O	0.106	F	0.023
V2i3	11.351	$[O_4]^{2-}$	O_i	1.587	O	0.194	O	0.118	F	0.021
V2i4	11.689	$[O_4]^{2-}$	O_i	1.613	O	0.244	F	0.042	O	0.067
V2i5	11.482	$[O_4]^{2-}$	O_i	1.606	O	0.198	O	0.110	F	0.022
V2i6	6.699	$[SiO]^{2-}$	Si	0.807	O_i	0.901				
V2i7	11.411	$[O_4]^{2-}$	O_i	1.584	O	0.195	O	0.115	F	0.020
V2i8	11.458	$[O_4]^{2-}$	O_i	1.594	O	0.189	O	0.121	F	0.021
V3i1	11.368	$[O_4]^{2-}$	O_i	1.552	O	0.196	O	0.130	F	0.016
V3i2	11.425	$[O_4]^{2-}$	O_i	1.605	O	0.202	O	0.098	F	0.026
V3i3	11.324	$[O_4]^{2-}$	O_i	1.562	O	0.196	O	0.122	F	0.015
V3i4	8.115	$[SiO]^{2-}$	Si	0.782	O_i	0.857				
V3i6	11.398	$[O_4]^{2-}$	O_i	1.588	O	0.262	F	0.028	O	0.087
V3i7	11.311	$[O_4]^{2-}$	O_i	1.630	O	0.217	F	0.034	O	0.073
V3i8	11.377	$[O_4]^{2-}$	O_i	1.566	O	0.181	O	0.127	O	0.127
V4i1	11.419	$[O_4]^{2-}$	O_i	1.574	O	0.189	O	0.119	F	0.021
V4i2	11.434	$[O_4]^{2-}$	O_i	1.594	O	0.188	O	0.114	F	0.020
V4i3	11.424	$[O_4]^{2-}$	O_i	1.611	O	0.211	F	0.026	O	0.092
V4i5	11.400	$[O_4]^{2-}$	O_i	1.578	O	0.182	O	0.130	F	0.018
V4i6	11.422	$[O_4]^{2-}$	O_i	1.538	O	0.271	O	0.090	F	0.021
V4i7	11.316	$[O_4]^{2-}$	O_i	1.539	O	0.188	F	0.011	O	0.139
V4i8	11.433	$[O_4]^{2-}$	O_i	1.570	O	0.187	O	0.124	F	0.018

Table F.2: The CRYSTAL and CP2K calculated band gaps of P-based defects in topaz, for (a) the $[PO_4]$ and (b) $[PO_3] + O_i$, in topaz. (The labeling convention used to distinguish different starting phosphite configurations is outlined in Appendix E.1).

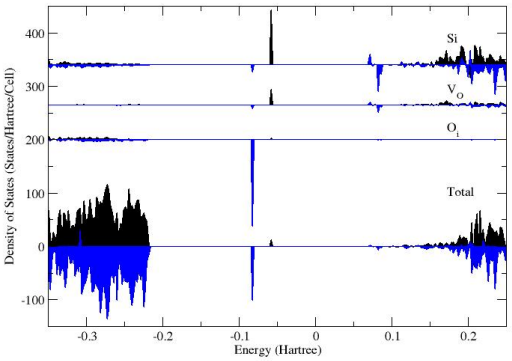

(a) (V1i4) Topaz-OH

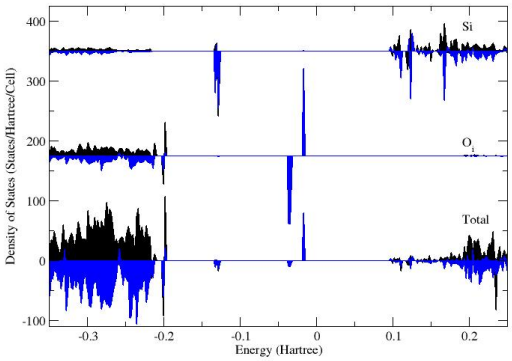

(b) (V1i3) Topaz-OH

Figure F.1: This figure is continued.

$[SiO_3]^{3-} + O_i^-$										
Config.	Defect Energy [eV]	Elect. Config	Atom	Spin	Atom	Spin	Atom	Spin	Atom	Spin
(c) Topaz-F										
V1i1	9.548	$[O_4]^{2-}$	O_i	1.606	O	0.306	F	0.035	F	0.035
V1i2	9.567	$[O_4]^{2-}$	O_i	1.635	O	0.272	F	0.038	F	0.038
V1i5	9.601	$[O_4]^{2-}$	O_i	1.630	SI	-0.022	F	0.037	F	0.037
V1i7	9.571	$[O_4]^{2-}$	O_i	1.622	O	0.284	F	0.038	F	0.037
V1i8	9.563	$[O_4]^{2-}$	O_i	1.612	O	0.294	F	0.037	F	0.037
V2i1	11.331	$[SiV]^{2-}$	Si	0.670	V_O	0.822				
V2i2	9.515	$[O_4]^{2-}$	O_i	1.618	O	0.284	F	0.035	F	0.033
V2i5	9.613	$[O_4]^{2-}$	O_i	1.621	O	0.288	F	0.034	F	0.033
V2i7	9.549	$[O_4]^{2-}$	O_i	1.631	O	0.279	F	0.036	F	0.036
V3i1	9.550	$[O_4]^{2-}$	O_i	1.622	O	0.287	F	0.037	F	0.037
V3i2	9.574	$[O_4]^{2-}$	O_i	1.625	O	0.284	F	0.037	F	0.034
V3i3	9.527	$[O_4]^{2-}$	O_i	1.626	O	0.287	F	0.036	F	0.033
V3i4	6.609	$[O_2]^-$	O_i	0.843	O	0.157	F	0.002	F	0.001
V3i5	9.545	$[O_4]^{2-}$	O_i	1.630	O	0.275	F	0.039	F	0.038
V3i7	9.448	$[O_4]^{2-}$	O_i	1.613	O	0.294	F	0.037	F	0.035
V3i8	9.548	$[O_4]^{2-}$	O_i	1.621	O	0.284	F	0.039	F	0.037
V4i2	9.569	$[O_4]^{2-}$	O_i	1.622	O	0.286	F	0.038	F	0.033
V4i3	9.527	$[O_4]^{2-}$	O_i	1.625	O	0.288	F	0.037	F	0.032
V4i4	6.597	$[SiO]^{2-}$	Si	0.846	O_i	0.846				
V4i5	9.542	$[O_4]^{2-}$	O_i	1.628	O	0.276	F	0.038	F	0.038
V4i7	9.443	$[O_4]^{2-}$	O_i	1.613	O	0.294	F	0.037	F	0.035
V4i8	9.545	$[O_4]^{2-}$	O_i	1.622	O	0.283	F	0.039	F	0.037

Table F.2: This is a continued Table.

F.3 Density Of States

The total and atomic projected densities of states for the $[Sio_3]^{2-}$ defect in topaz-OH and topaz-FOH are given in Figure F.1.

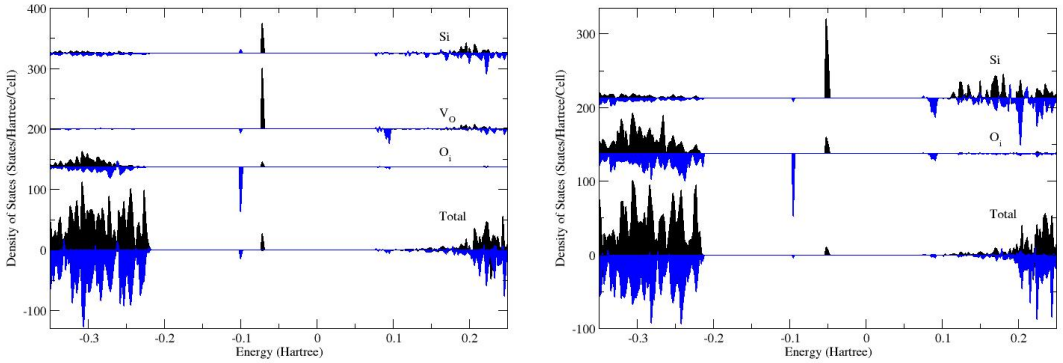

(c) (V2i6) Topaz-FOH

(d) (V3i4) Topaz-FOH

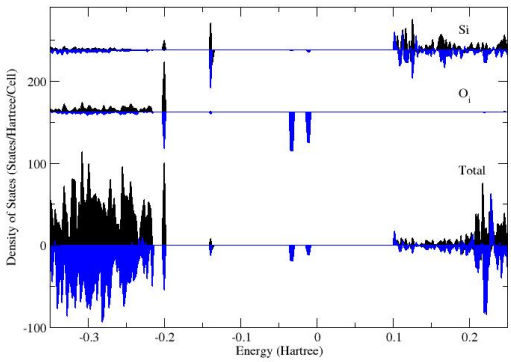

(e) (V1i6) Topaz-FOH

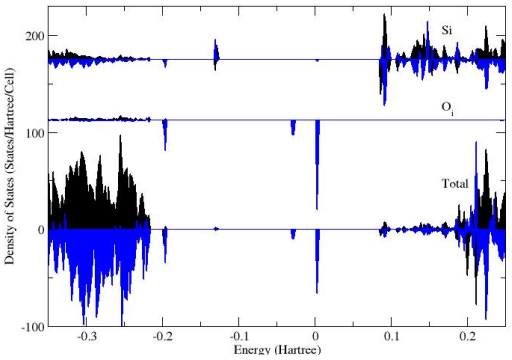

(f) (V2i4) Topaz-FOH

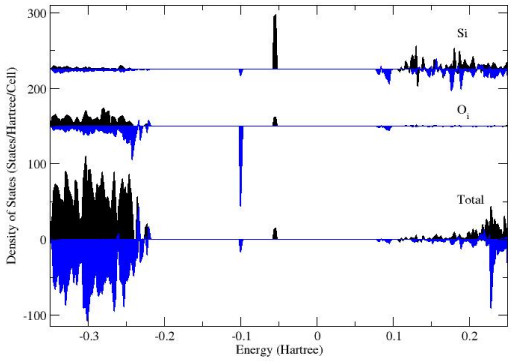

(g) (V4i4) Topaz-F

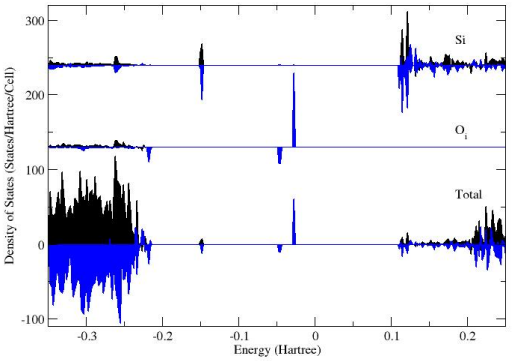

(h) (V4i7) Topaz-F

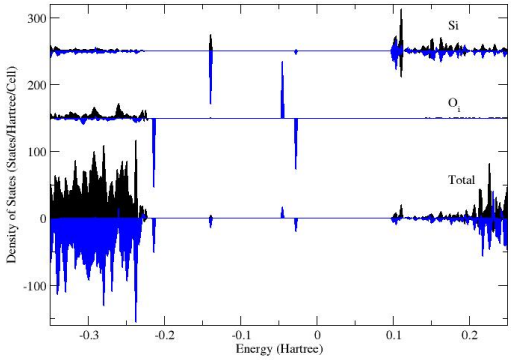

(i) (V2i2) Topaz-F

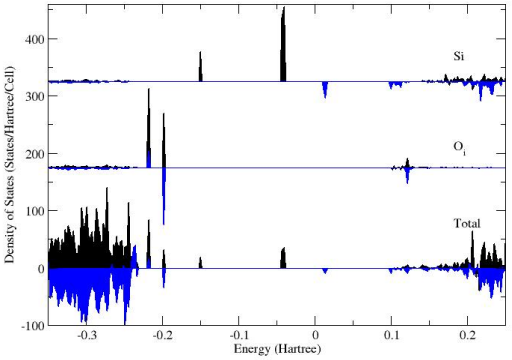

(j) (V2i1) Topaz-F

Figure F.1: The CRYSTAL calculated density of states, with total and defect ion projections (silicon, the ghost vancancy site, and the interstisial oxygen), of the $[SiO_3]^{2-}$ defect in topaz. The unqiue electron configurations are labeled.

Appendix G

Supporting Information for Hydroxy Based Defects in Topaz

The additional information provided in Appendix G supports the results and discussion on phosphorous based defect in topaz as presented in chapter 9.

G.1 Lattice Parameters

The values of the lattice parameters for topaz including the defect $[OV_H]^- + H_i^-$ as calculated by CRYSTAL are given in Table G.1. These include the cell dimensions (a, b, and c), cell angles (α, β, and γ), volumes and densities defect configurations (see Appendix E for labeling definition) successfully optimised.

config.	a [Å]	b [Å]	c [Å]	alpha	beta	gamma	Volume [$Å^3$]	Density [$g\,cm^{-3}$]
(a) $[OV_H]^- + H_i^-$ in Topaz-OH								
OHi1	9.5392	8.9197	8.4085	90.07	89.79	90.08	715.45	3.341
OHi2	9.5348	8.9219	8.4118	90.06	89.77	90.08	715.57	3.340
OHi3	9.5368	8.9211	8.4084	90.06	89.81	90.10	715.37	3.341
OHi4	9.5371	8.9189	8.4106	90.07	89.80	90.09	715.40	3.341
OHi5	9.5322	8.9274	8.4110	90.11	89.82	89.96	715.75	3.339
OHi6	9.5401	8.9179	8.4095	90.08	89.85	89.92	715.46	3.341
OHi7	9.5365	8.9202	8.4120	90.04	89.80	89.90	715.58	3.340
OHi8	9.5382	8.9196	8.4094	90.05	89.81	89.89	715.43	3.341
(b) $[OV_H]^- + H_i^-$ in Topaz-FOH								
OHi1	9.4279	8.8952	8.4365	89.98	89.99	89.87	707.52	3.416
OHi2	9.4253	8.8978	8.4398	89.98	89.98	89.86	707.80	3.414
OHi3	9.4266	8.8953	8.4368	89.98	89.93	89.86	707.44	3.416
OHi4	9.4269	8.8955	8.4401	89.95	89.92	89.86	707.75	3.415
OHi5	9.4304	8.8938	8.4202	90.08	89.96	89.91	706.22	3.422
OHi6	9.4299	8.8928	8.4167	90.04	89.96	89.96	705.81	3.424
OHi7	9.4262	8.8966	8.4379	89.97	89.92	90.06	707.61	3.415
OHi8	9.4262	8.8960	8.4372	89.98	89.93	90.06	707.51	3.416

Table G.1: CRYSTAL calculated lattice parameters for the $[OV_H]^- + H_i^-$ defect in (a) topaz-OH, (b) topaz-FOH, and (c) topaz-F.

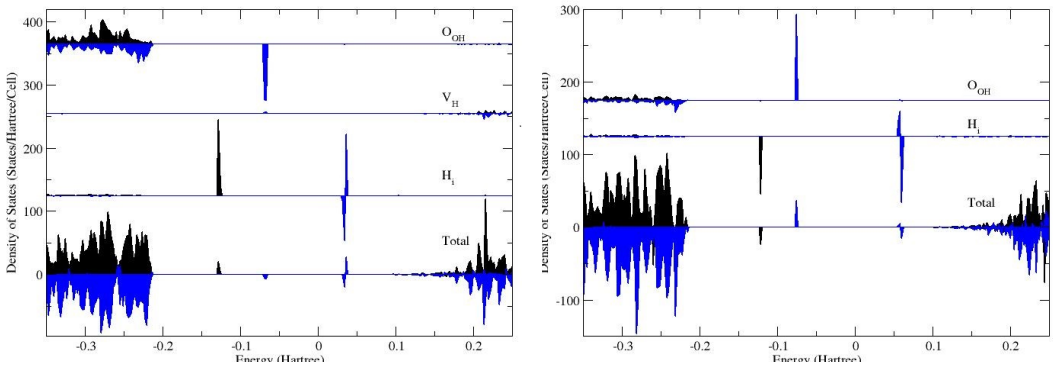

(a) (OHi5) Topaz-OH (b) (OHi6) Topaz-FOH

Figure G.1: The CRYSTAL calculated density of states, with total and defect ion projections (oxygen of the hydroxyl group and the interstisial hydrogen), of the $[OV_H]^- + H_i$ defect in topaz. The unqiue electron configurations are labeled.

G.2 Density Of States

The total and atomic projected densities of states for the $[OH]^- \longrightarrow [O^{\bullet}V_H^{\times}]^- + H_i'$ defect in topaz-OH and topaz-FOH are given in Figure G.1.

Bibliography

[1] Schott, S.; Rager, H.; Schurmann, K.; Taran, M. Spectroscopic study of natural gem quality Imperial-Topazes from Ouro Preto, Brazil *European Journal of Mineralogy* **2003**; 15(4), 701–706; 0935-1221.

[2] Taran, M.; Tarashchan, A.; Rager, H.; Schott, S.; Schurmann, K.; Iwanuch, W. Optical spectroscopy study of variously colored gem-quality topazes from Ouro Preto, Minas Gerais, Brazil *Physics and Chemistry of Minerals* **2003**; 30(9), 546–555; 0342-1791.

[3] Goto, H.; Niwa, A.; Greenidge, D. C.; Kato, a. N.; Ida, T.; Mizuno, M.; Endo, K.; Tada, T. Analysis of UV-Visible Absorption Spectra for Quartz and Topaz in Silicate Minerals by MO Calculations Using the Cluster Model Molecules *Journal of Surface Analysis* **2005**; 12(2), 249–253.

[4] Nelson, J.; Baum, J.; *Health risk assessment of irradiated topaz*; Tech. Rep.; Brookhaven National Laboratory; Upton, NY (United States); 1993.

[5] Ashbaugh III, C. E. Radioactive and Radiation Treated Gemstones *Gemological Institute of America* **1991**; 2(1), 42–57.

[6] da Silva, D.; Guedes, K.; Pinheiro, M.; Spaeth, J.; Krambrock, K. The microscopic structure of the oxygen-aluminium hole center in natural and neutron irradiated blue topaz *Physics and Chemistry of Minerals* **2005**; 32(5-6), 436–441; 0342-1791.

[7] Krambrock, K.; Ribeiro, L. G. M.; Pinheiro, M. V. B.; Leal, A. S.; de Menezes, M. A.; Spaeth, J. M. Color centers in topaz - A comparison between neutron and gamma irradiation *Physics and Chemistry of Minerals* **2007**; 34(7), 437–444; 0342-1791.

[8] Leal, A. S.; Arambrock, K.; Ribeiro, L. G. M.; Menezes, l.; Vermaerckec, M.; Sneyers, P. Study of neutron irradiation-induced colors in Brazilian topaz *Nuclear Instruments and Methods in Physics Research. Section A, Accelerators,*

Spectrometers, Detectors and Associated Equipment **2007**; 580(1), 423–426; 0168-9002.

[9] Wasim, M.; Zafar, W.; Tufail, M.; Arif, M.; Daud, M.; Ahmad, A. Elemental analysis of topaz from northern areas of Pakistan and assessment of induced radioactivity level after neutron irradiation for color induction *Journal of Radioanalytical and Nuclear Chemistry* **2011**; 287(3), 821–826; 0236-5731.

[10] Salama, S.; Helal, A.; Gomaa, M.; Abou-Salem, L.; Nafie, H.; Badawi, E. In *EG1100453 Coloring of Topaz after Irradiation*; Nasr City, Cairo, Egypt; Tenth Radiation Physics and Protection Conference. `http://www.iaea.org/inis/collection/NCLCollectionStore/_Public/42/076/42076629.pdf`.

[11] Dickinson, A.; Moore, W. Paramagnetic resonance of metal ions and defect centres in topaz *The Journal of Physical Chemistry* **1967**; 71, 231–40.

[12] Nassau, K.; Prescott, B. Blue and brown topaz produces by gamma-irradiation *The American Mineralogist* **1975**; 60(7-8), 705–709.

[13] Yukihara, E. G.; Yoshimura, E. M.; Okuno, E. Paramagnetic radiation-induced defects in gamma-irradiated natural topazes *Nuclear Instruments and Methods in Physics Research. Section B: Beam Interactions with Materials and Atoms* **2002**; 191(1-4), 266–270.

[14] Priest, V.; Cowan, D.; Reichel, D.; Ross, F. A dangling-silicon-bond defect in topaz *Journal of Applied Physics* **1990**; 68(6), 3035–3037; 0021-8979.

[15] Churakov, S. V.; Wunder, B. Ab-initio calculations of the proton location in topaz-OH, $Al_2SiO_4(OH)_2$ *Physics and Chemistry of Minerals* **2004**; 31(3), 131–141; 0342-1791.

[16] Abbott, R. Topaz: Energy Calculations Bearing on the Location of Hydrogen *The Canadian Mineralogist* **1990**; 28(4), 827–833; 0008-4476.

[17] Ribbe, P. H.; Rosenberg, P. E. Optical and X-ray determinative methods for fluorine in topaz *The American Minerologist* **1971**; 56.

[18] Northrup, P. A.; Leinenweber, K.; Parise, J. B. The location of H the high-pressure synthetic $Al_2SiO_4(OH)_2$ topaz analog *The American Mineralogist* **1994**; 79(3-4), 401–404; 0003-004X.

[19] Zhang, R. L.; Shu, J. Hydroxyl-rich topaz in high-pressure and ultrahigh-pressure kyanite quartzites, with retrograde woodhouseite, from the Sulu terrane, eastern China *The American Mineralogist* **2002**; 87(4), 445–453; 0003-004X.

[20] Wunder, B.; Rubie, D. C.; II Ross, C. R.; Medenbach, O.; Seifert, F.; Schreyer, W. Synthesis, stability, and properties of $Al_2SiO_4(OH)_2$ - a fully hydrated analog of topaz *The American Mineralogist* **1993**; 78(3-4), 285–297; 0003-004X.

[21] Wyckoff, R. W. G. *Crystal Structures*; Wiley: New York, 1968; Vol. 4.

[22] Priest, V.; Cowan, D. L.; Yasar, H.; Ross, F. ESR, Optical-absorption, and luminescence studies of the peroxy-radical defect in topaz *Physical Review. B, Condensed matter* **1991**; 44(18), 9877–9882; 0163-1829.

[23] NIMSoffice; *Crystal structure of topaz*; 2009; en.wikipedia. `http://en.wikipedia.org/wiki/File:Topaz.GIF`.

[24] Dantas, C. S.; Valerio, M. E. G.; dos Santos, M. A. C.; do N. Souza, D. Photoinduced emission and thermoluminescence in topaz *Nuclear Instruments and Methods in Physics Research. Section B: Beam Interactions with Materials and Atoms* **2006**; 250(1-2), 386–389; 0168-583X.

[25] Souza, D. N.; de Lima, J. F.; Valerio, M. E. G. Thermoluminescence of natural topaz crystals of differing genesis *Materials Science Forum* **1997**; 239-, 765–768; 0255-5476.

[26] Steinhauser, G.; Sterba, J. H.; Hammer, V. M. F. Nuclear forensics of a colored gemstone: evidence of proton bombardment of a blue topaz *Applied Radiation and Isotopes* **2013**; 75(0), 18–21.

[27] Pinheiro, M. V. B.; Fantini, C.; Krambrock, K.; Persiano, A. I. C.; Dantas, M. S. S.; Pimenta, M. A. OH/F substitution in topaz studied by Raman spectroscopy *Physical Review B* **2002**; 65(10), 104301.

[28] Jo, M.; *Genuine topaz gemstones in various colours, mystic and azotic topaz is also seen.*; 2010; Open Source. `http://commons.wikimedia.org/wiki/File:Large_Topaz_Gemstones.jpg`.

[29] Dholakia, A.; *White Topaz Loose Stones from Anil B. Dholakia, Inc.*; 2010; Anil B. Dholakia, Inc., 4961 Highlands Road, Franklin NC 28734. `http://www.gemanil.com/fb-white-topaz.html`.

[30] Gemsquares.com; *Imperial Topaz*; 2015; America. `http://www.gemsquares.com/imperial-topaz/`.

[31] Preziosi, C.; *Topaz*; 2012; Agrigento, Italy. `http://precioustip.blogspot.co.uk/2012/10/topaz.html`.

[32] Schmetzer, K. Irradiation-induced blue color in topaz - evidence for the formation of color-centers by nuclear-reaction *Naturwissenschaften* **1987**; 74(3), 136–137; 0028-1042.

[33] Nassau, K. Altering the Color of Topaz *Gems and Gemology* **1985**; 21, 26–34.

[34] Lind, S. C.; Bardwell, D. C. The coloring and thermophosphorescence produced in transparent minerals and gems by radium radiation *The American Mineralogist* **1923**; 8(10), 171–180.

[35] Bonventi, W.; Isotani, S.; Pereira Albuquerque, A.; Bonventi Jr, W. Color Dependence on Thickness in Topaz Crystal from Brazil *Advances in Condensed Matter Physics* **2012**; 2012, 1–8.

[36] Isotani, S.; Matsuoka, M.; Albuquerque, A. R. P. L. Isothermal annealing of a 620nm optical absorption band in Brazilian topaz crystals *Physical Review B: Condensed Matter* **2013**; 415(0), 38–43.

[37] Schirmer, O. O^- bound small polarons in oxide materials *Journal of Physics: Condensed Matter* **2006**; 18(43), R667–R704; 0953-8984.

[38] da Silva, D.; Guedes, K.; Pinheiro, M.; Schweizer, S.; Spaeth, J.; Krambrock, K.; 400. The $O^--(Al_2)$ center in topaz and its relation to the blue colour *physica status solidi (c)* **2005**; 2(1), 397–400.

[39] Petrov, I.; Ph.D. thesis *Anwendung Physikalischer Methoden zur Lösung Kristallchemischer Problem: Paramagnetische Zentren in Topas - Kristallchemische Klassifikation Natürlicher Topase durch Korrelation ihrer Optischen Absorptions-, EPR- und TL-Spektren*; Naturwissenschaftlich-Mathemtischen Gesamtfakultät; Ruprecht - Karls - Universität Heidelberg; 1983.

[40] Albuquerque, A. R. P. L.; Isotani, S.; Morato, S. Irradiation and heating effects in topaz crystals from minas cerais, Brazil *Radiation Effects* **1988**; 106(1-2), 143–150.

[41] Lehmann, G.; Harder, H. Optical spectra of di- and trivalent iron in corundum *The American Mineralogist* **1970**; 55(1-2), 98–105.

[42] Goldman, D. S.; Rossman, G. R. The identification of Fe^{2+} in the M_4-site of calcic amphiboles - reply *The American Mineralogist* **1982**; 67(3-4), 340–342.

[43] Taran, M.; Koch Mueller, M.; Koch Müller, M. Octahedral cation ordering in Mg, Fe2+-olivine: an optical absorption spectroscopic study *Physics and Chemistry of Minerals* **2006**; 33(8-9), 511–518.

[44] Dotto, C.; Isotani, S. Irradiation and heating effects in amethyst crystals from Brazil *Radiation effects and defects in solids* **1991**; 117(4), 355–361.

[45] Kloprogge, J. T.; Frost, R. L. Raman microscopic study at 300 and 77 K of some pegmatite minerals from the Iveland-Evje area, Aust-Agder, Southern Norway *Spectrochimica Acta Part A: Molecular and Biomolecular Spectroscopy* **2000**; 56(3), 501–513.

[46] Friebele, E. J.; Griscom, D. L.; Stapelbroek, M.; Weeks, R. A. Fundamental Defect Centers in Glass: The Peroxy Radical in Irradiated, High-Purity, Fused Silica *Physical Review Letters* **1979**; 42(20), 1346.

[47] Förster, H. *UV-VIS Spectroscopy*; Karge, H.; Weitkamp, J., Eds.; Molecular Sieves – Science and Technology, Vol. 4; Springer Berlin Heidelberg, 2004; Chapter 4, pp 337–426.

[48] Nystrøm, B. O. G.; Roots, J. E.; Norby, P. A.; *Color in Materials - Emner innen matematikk og naturvitenskap: Semesterside for KJM3100 Vår 2007*; 2007; Universitetet i Oslo. `http://www.uio.no/studier/emner/matnat/kjemi/KJM3100/v07/undervisningsmateriale/kjm3100_2007_09_colour_b.pdf`.

[49] Cotton, F. A. *Chemical Applications of Group Theory*, 3rd ed.; Wiley: New York, 1990; The Crystal Field Theory.

[50] Chakkaparn; *Causes of Color in Minerals*; 2007; Geology Department, Chulalongkorn University, Thailand. `http://geosolutionsauthority.com/download/esfs_educator_resource_compilation/from_kamloops_exploration_group_-_keg/rocks-minerals/coloursinminerals-ppt.pdf`.

[51] Fritsch, E.; Rossman, G. An update on color in gems. Part 1: Introduction and colors caused by dispersed metal ions *Gems and Gemology* **1987**; 23(3), 126–139.

[52] Tarashchan, A.; Taran, M.; Rager, H.; Iwanuch, W. Luminescence spectroscopic study of Cr^{3+} in Brazilian topazes from Ouro Preto *Physics and Chemistry of Minerals* **2006**; 32(10), 679–690; 0342-1791.

[53] Meyer, B.; Lohse, F.; Spaeth, J.; Weil, J. Optically detected magnetic-resonance of the $[AlO_4]_3$ centre in crystalline quartz *Journal of physics. C. Solid state physics* **1984**; 17(1), L31–L36.

[54] Souza, D. N.; de Lima, J. F.; Valerio, M. E. G.; Alves, E.; Sasaki, J. M.; Caldas, L. V. E. Radiation-induced charge trapping and recombination process in natural topaz studied by TL, EPR and XRD *Nuclear Instruments and Methods in Physics Research. Section B: Beam Interactions with Materials and Atoms* **2004**; 218, 123–127; 0168-583X.

[55] Roque-Malherbe, R. *Adsorption and Diffusion in Nanoporous Materials*; Taylor and Francis, 2007.

[56] Burns, R.; Putnis, A.; Liebermann, R. *Mineralogical Applications of Crystal Field Theory*, 2nd ed.; Cambridge University Press: Cambridge, 2005.

[57] Taran, M. N.; Langer, K.; Platonov, A. N.; Indutny, V. V. Optical-absorption investigation of Cr^{3+} ion-bearing minerals in the temperature-range $77-797$K *Physics and Chemistry of Minerals* **1994**; 21(6), 360–372.

[58] Jackson, R. A.; Heide, G.; Valerio, M. E. G. Computer modeling of the structure, lattice and defect properties of F- and OH-topaz *Radiation Effects and Defects in Solids* **2002**; 157(6-12), 845–848; 1042-0150.

[59] Mott, N. F.; Littleton, M. J. Conduction in Polar Crystals. I. Electrolytic Conduction in Solid Salts *Transactions of the Faraday Society* **1938**; 34, 485; 0014-7672.

[60] Gale, D. J. GULP: A computer program for the symmetry-adapted simulation *Journal of the Chemical Society. Faraday Transactions* **1997**; 93(4), 629; 0956-5000.

[61] Jackson, R. A.; Valerio, M. E. G. A computational study of the structure, lattice and defect properties of pure and doped F- and OH–topaz *Journal of Physics: Condensed Matter* **2004**; 16(27), S2771–S2779; 0953-8984.

[62] Jackson, R. A.; Valerio, M. E. G. Computer modeling of doping and ion implantation in F- and OH–topaz *Nuclear Instruments and Methods in Physics Research. Section B: Beam Interactions with Materials and Atoms* **2004**; 218, 42–45; 0168-583X.

[63] Bernal, C. R.; Souza, D. N.; Valerio, M. E. G.; Cruz-Vazquez, C.; Barboza-Flores, M. Optically stimulated luminescence dosimetry performance of natural Brazilian topaz exposed to beta radiation *Radiation Protection Dosimetry* **2006**; 119(1-4), 161–163; 0144-8420.

[64] de Magalhães, C.; Macedo, Z.; Valerio, M.; Hernandes, A.; Souza, D. Preparation of composites of topaz embedded in glass matrix for applications in solid state thermoluminescence dosimetry *Nuclear Instruments and Methods in Physics Research. Section B: Beam Interactions with Materials and Atoms* **2004**; 218, 277–282.

[65] de Magalhães, C.; Souza, D.; Caldas, L. Use of composites of topaz-glass as TSEE and TL dosemeters *Radiation Protection Dosimetry* **2006**; 119(1-4), 323–326; 0144-8420.

[66] Souza, D.; Valerio, M.; de Lima, J. The use of pellets of Brazilian natural topaz as radiation dosimeters *Radiation Effects and Defects in Solids* **2001**; 156(1-4), 325–330; 1042-0150.

[67] Souza, D.; de Lima, J.; Valerio, M.; Fantini, C.; Pimenta, M.; Moreira, R. Influence of thermal treatment on the Raman, infrared and TL responses of natural topaz *Nuclear Instruments and Methods in Physics Research. Section B: Beam Interactions with Materials and Atoms* **2002**; 191, 230–235; 0168-583X.

[68] Souza, D. N.; de Lima, J. F.; Valerio, M. E. G.; Alves, E.; Caldas, L. V. E. Effects of ion implantation on the thermoluminescent properties of natural colourless topaz *Nuclear Instruments and Methods in Physics Research. Section B: Beam Interactions with Materials and Atoms* **2002**; 191, 196–201; 0168-583X.

[69] Souza, D. N.; de Lima, J. F.; Valerio, M. E. G.; Caldas, V. E. Performance of pellets and composites of natural colourless topaz as radiation dosemeters *Radiation Protection Dosimetry* **2002**; 100(1-4), 413–416; 0144-8420.

[70] Souza, D. N.; Meira, R. A.; Lima, J. F.; Valerio, M. E. G.; Caldas, L. V. E. Evaluation of doses in radiotherapy using solid-state composites based on natural colourless topaz *Applied Radiation and Isotopes* **2003**; 58(4), 489–494; 0969-8043.

[71] Souza, D. N.; de Lima, J. F.; Valerio, M. E. G.; Caldas, L. V. E. Thermally stimulated luminescence and EPR studies on topaz *Applied Radiation and isotopes* **2006**; 64(8), 906–909; 0969-8043.

[72] Yukihara, E.; Okuno, E. On the thermoluminescent properties and behaviour of Brazilian topaz *Nuclear Instruments and Methods in Physics Research. Section B: Beam Interactions with Materials and Atoms* **1998**; 141(1-4), 514–517; 0168-583X.

[73] Souza, D. N.; Valerio, M. E. G.; de Lima, J. F.; Caldas, L. V. E. Dosimetric properties of natural brazilian topaz - A thermally stimulated exoeletronic emission and thermoluminescence study *Nuclear Instruments and Methods in Physics Research. Section B. Beam Interactions with Materials and Atoms* **2000**; 166-167, 209–214; 0168-583X.

[74] Moss, A.; McKlveen, J. Thermoluminescent properties of topaz *Health Physics* **1978**; 34(2), 137–140; 0017-9078.

[75] Valentin, J. Relative biological effectiveness (RBE), quality factor (Q), and radiation weighting factor (wR): {ICRP} Publication 92 *Annals of the ICRP* **2003**; 33(4), 1–121.

[76] Keifer, J.; Mayshart, P.; Mejdhal, V. *Radiation Protection Dosimetry*; Attix, F.; Roesch, W.; Tochilin, E., Eds.; Academic Press, Incorporated, 1969; Vol. Vol. III.

[77] Marques, C.; Falcao, A.; Silva, R. C. d.; Alves, E. Annealing behaviour of natural topaz implanted with W and Cr ions *Nuclear Instruments and Methods in Physics Research. Section B: Beam Interactions with Materials and Atoms* **2000**; 166, 204–208; 0168-583X.

[78] Marques, C.; Falcao, A.; da Silva, R. C.; Alves, E. Structural and optical characterization of topaz implanted with Fe and Co *Nuclear Instruments and Methods in Physics Research. Section B. Beam Interactions with Materials and Atoms* **2002**; 191(1-4), 312–316; 0168-583X.

[79] Thomas, L. H. The calculation of atomic fields *Proceedings of the Cambridge Philosophical Society* **1927**; 23, 542.

[80] Fermi, E. Eine statistische Methode zur Bestimmung einiger Eigenschaften des Atoms und ihre Anwendung auf die Theorie des periodischen Systems der Elemente *Zeitschrift für Physik* **1928**; 48(1-2), 73–79.

[81] Cramer, C. J. *Essentials of Computational Chemistry: Theories and Models*, 2nd ed.; Wiley, 2004.

[82] Hohenberg, P.; Kohn, W. Inhomogeneous Electron Gas *Physical Review. B, Condensed Matter* **1964**; 136(3B), B864–B871.

[83] Kohn, W.; Sham, L. J. Self-Consistent Equations Including Exchange and Correlation Effects *Physical Review* **1965**; 140(4A), A1133.

[84] Corà, F.; Alfredsson, M.; Mallia, G.; Middlemiss, D. S.; Mackrodt, W. C.; Dovesi, R.; Orlando, R. The Performance of Hybrid Density Functionals in Solid State Chemistry *Structure and Bonding* **2004**; 113, 171–232; 0081-5993.

[85] Corà, F. The performance of hybrid density functionals in solid state chemistry: the case of $BaTiO_3$ *Molecular Physics* **2005**; 103(18), 2483–2496; 0026-8976.

[86] Gonzalez Rivas, N.; González Rivas, N.; Cedillo, A. Performance of density functional theory methods to describe intramolecular hydrogen shifts *Journal of Chemical Sciences* **2005**; 117(5), 555–560.

[87] Swart, M.; Sola, M.; Bickelhaupt, F. M.; SolÃ , M.; Sol, M. Energy landscapes of nucleophilic substitution reactions: A comparison of density functional theory and coupled cluster methods *Journal of Computational Chemistry* **2007**; 28(9), 1551–1560.

[88] Jacquemin, D.; Perpete, E.; Ciofini, I.; Adamo, C.; Perpète, E. Assessment of Functionals for TD-DFT Calculations of Singlet−Triplet Transitions *Journal of Chemical Theory and Computation* **2010**; 6(5), 1532–1537.

[89] Burns, L.; Vazquez Mayagoitia, A.; Sumpter, B.; Sherrill, C. D. Density-functional approaches to noncovalent interactions: A comparison of dispersion corrections (DFT-D), exchange-hole dipole moment (XDM) theory, and specialized functionals *The Journal of Chemical Physics* **2011**; 134(8), 084107.

[90] Charaf-Eddin, A.; Planchat, A.; Mennucci, B.; Adamo, C.; Jacquemin, D. Choosing a Functional for Computing Absorption and Fluorescence Band Shapes with TD-DFT *Journal of Chemical Theory and Computation* **2013**; 9 (6), 2749–2760.

[91] Ernzerhof, M.; Perdew, J. P.; Burke, K. Density functionals: Where do they come from, why do they work? *Topics in current physics* **1996**; 180, 1–30.

[92] Adamo, C.; Barone, V. Toward reliable density functional methods without adjustable parameters: The PBE0 model *The Journal of Chemical Physics* **1999**; 110(13), 6158–6170; 0021-9606.

[93] Adamo, C.; Barone, V. Inexpensive and accurate predictions of optical excitations in transition-metal complexes: the TDDFT/PBE0 route *Theoretical Chemistry Accounts* **2000**; 105(2), 169–172; 1432-881X.

[94] Runge, E.; Gross, E. Density-functional theory for time-dependent systems *Physical Review Letters* **1984**; 52(12), 997–1000.

[95] van Leeuwen, R. Causality and Symmetry in Time-Dependent Density-Functional Theory *Physical Review Letters* **1998**; 80(6), 1280.

[96] Gross, E.; Ullrich, C.; Gossmann, U. Density functional theory of time-dependent system *NATO advanced study institutes series. Series B, Physics* **1995**; 337, 149–171.

[97] Gross, E.; Dobson, J.; Petersilka, M. Density functional theory of time-dependent phenomena *Topics in Current Physics* **1996**; 181, 81–172.

[98] Marques, M.; Gross, E. Time-dependent density functional theory *Lecture notes in physics* **2003**; 620, 144–184; 0075-8450.

[99] Ullrich, C.; Gossmann, U.; Gross, E. Time-dependent optimized effective potential *Physical Review Letters* **1995**; 74(6), 872–875.

[100] Dobson, J.; Bunner, M.; Gross, E. Time-dependent density functional theory beyond linear response: An exchange-correlation potential with memory *Physical Review Letters* **1997**; 79(10), 1905–1908.

[101] Kohanoff, J. *Electronic structure calculations for solids and molecules: theory and computational methods*; Cambridge University Press, 2006.

[102] Arnold, S. *Chemical Physics Research Trends*; Nova Science Publishers, 2007.

[103] VandeVondele, J.; Krack, M.; Mohamed, F.; Parrinello, M.; Chassaing, T.; Hutter, J. QUICKSTEP: Fast and accurate density functional calculations using a mixed Gaussian and plane waves approach *Computer physics communications* **2005**; 167(2), 103–128; 0010-4655.

[104] Dovesi, R.; Saunders, V.; Roetti, C.; Orlando, R.; Zicovich-Wilson, C. M.; Pascale, F.; Civalleri, B.; Doll, K.; Harrison, N.; Bush, I.; D'Arco, P.; Llunell, M.; *CRYSTAL06 User's Manual*; University of Torino, Torino; 2006. `http://www.crystal.unito.it/Manuals/crystal06.pdf`.

[105] Grau-Crespo, R.; Peralta, A. G.; Ruiz-Salvador, A. R.; Gomez, A.; Lopez-Cordero, R. A computer simulation study of distribution, structure and acid strength of active sites in H-ZSM-5 catalyst *Physical Chemistry Chemical Physics* **2000**; 2(24), 5716–5722; 1463-9076.

[106] Jackson, R. A.; Catlow, C. R. A. Computer Simulation Studies of Zeolite Structure *Molecular Simulation* **1988**; 1, 207–224.

[107] de Leeuw, N. Resisting the onset of hydroxyapatite dissolution through the incorporation of fluoride *The Journal of Physical Chemistry. B* **2004**; 108(6), 1809–1811; 1520-6106.

[108] Allan, N.; Barrera, G.; Lavrentiev, M.; Todorov, I.; Purton, J. Ab initio calculation of phase diagrams of ceramics and minerals. *Journal of Material Chemistry* **2001**; 11(1), 63–68.

[109] Dovesi, R.; Orlando, R.; Civalleri, B.; Roetti, C.; Saunders, V.; Zicovich Wilson, C. CRYSTAL: a computational tool for the ab initio study of the electronic properties of crystals *Zeitschrift für Kristallographie* **2005**; 220(5-6), 571–573.

[110] Dovesi, R.; Saunders, V.; Roetti, C.; Orlando, R.; Zicovich-Wilson, C. M.; Pascale, F.; Civalleri, B.; Doll, K.; Harrison, N.; Bush, I.; D'Arco, P.; Llunell, M.; *CRYSTAL09 User's Manual*; University of Torino, Torino; 2009. `http://www.crystal.unito.it/Manuals/crystal09.pdf`.

[111] Perdew, J. P.; Burke, K.; Ernzerhof, M. Generalized gradient approximation made simple *Physical Review Letters* **1996**; 77(18), 3865–3868.

[112] Monkhorst, H. J.; Pack, J. D. Special points for Brillouin-zone integrations *Physical Review B* **1976**; 13(12), 5188–5192; PRB.

[113] Catti, M.; Valerio, G.; Dovesi, R.; Causa, M. Quantum-mechanical calculation of the solid-state equilibrium $MgO + \alpha{-}Al_2O_3 \rightleftharpoons MgAl_2O_4$ (spinel) versus pressure *Physical Review. B, Condensed Matter* **1994**; 49(20), 14179–14187; 0163-1829.

[114] Pascale, F.; Zicovich-Wilson, C.; Orlando, R.; Roetti, C.; Ugliengo, P.; Dovesi, R. Vibration frequencies of $Mg_3Al_2Si_3O_{12}$ pyrope. An ab initio study with the CRYSTAL code *The Journal of Physical Chemistry. B* **2005**; 109(13), 6146–6152; 1520-6106.

[115] Valenzano, L.; Torres, F.; Klaus, D.; Pascale, F.; Zicovich Wilson, C. Ab initio study of the vibrational spectrum and related properties of crystalline compounds; the case of $CaCO_3$ calcite *Zeitschrift für physikalische Chemie* **2006**; 220(7-2006), 893–912.

[116] Nada, R.; Catlow, C.; Pisani, C.; Orlando, R. An ab-initio Hartree-Fock perturbed-cluster study of neutral defects in LiF *Modeling and simulation in materials science and engineering* **1993**; 1(2), 165–187; 0965-0393.

[117] Gatti, C.; Saunders, V. R.; Roetti, C. Crystal-field effects on the topological properties of the electron-density in molecular-crystals - the case of urea *The Journal of Chemical Physics* **1994**; 101(12), 10686–10696.

[118] Catti, M.; Sandrone, G.; Valerio, G.; Dovesi, R. Electronic, magnetic and crystal structure of Cr_2O_3 by theoretical methods *Journal of Physics and Chemistry of Solids* **1996**; 57(11), 1735–1741.

[119] Ruiz, E.; Llunell, M.; Alemany, P. Calculation of exchange coupling constants in solid state transition metal compounds using localized atomic orbital basis sets *Journal of Solid State Chemistry* **2003**; 176(2), 400–411.

[120] Zicovich Wilson, C.; Bert, A.; Roetti, C.; Dovesi, R.; Saunders, V. Characterization of the electronic structure of crystalline compounds through their localized Wannier functions *The Journal of Chemical Physics* **2002**; 116(3), 1120–1127.

[121] Corno, M.; Busco, C.; Civalleri, B.; Ugliengo, P. Periodic ab initio study of structural and vibrational features of hexagonal hydroxyapatite $Ca_{10}(PO_4)_6(OH)_2$ *Physical Chemistry Chemical Physics* **2006**; 8(21), 2464–72.

[122] The CP2K developers group *Cp2k*, CP2K is a freely available (GPL) program, written in Fortran 95, to perform atomistic and molecular simulations of solid state, liquid, molecular and biological systems. It provides a general framework for different methods: density functional theory (DFT) using a mixed Gaussian and plane waves approach (GPW), classical pair and many-body potentials, semi-empirical (AM1, PM3, MNDO, MNDOd, PM6) Hamiltonians, Quantum Mechanics/Molecular Mechanics (QM/MM) hybrid schemes relying on the Gaussian Expansion of the Electrostatic Potential (GEEP).; version 2.3.43 (Development Version); http://www.cp2k.org/: ETH Zürich, University of Zürich, Switzerland, 2009. `http://www.cp2k.org/`.

[123] Goedecker, S.; Teter, M.; Hutter, J. Separable dual-space Gaussian pseudopotentials *Physical Review B* **1996**; 54(3), 1703–1710; PRB.

[124] Hartwigsen, C.; Goedecker, S.; Hutter, J. Relativistic separable dual-space Gaussian pseudopotentials from H to Rn *Physical Review B* **1998**; 58(7), 3641–3662; PRB.

[125] Krack, M. Pseudopotentials for H to Kr optimized for gradient-corrected exchange-correlation functionals *Theoretical Chemistry Accounts* **2005**; 114 (1-3), 145–152.

[126] VandeVondele, J.; Sulpizi, M.; Sprik, M. Electron transfer properties from atomistic simulations and density functional theory *CHIMIA International Journal for Chemistry* **2007**; 61(4), 155–158.

[127] Guidon, M.; Hutter, J.; VandeVondele, J. Auxiliary Density Matrix Methods for Hartree Fock Exchange Calculations *Journal of Chemical Theory and Computation* **2010**; 6(8), 2348–2364.

[128] Schiffmann, F.; Hutter, J.; VandeVondele, J. Atomistic simulations of a solid/liquid interface: a combined force field and first principles approach to the structure and dynamics of acetonitrile near an anatase surface *Journal of Physics: Condensed Matter* **2008**; 20(6), 064206.

[129] Guidon, M.; Schiffmann, F.; Hutter, J.; VandeVondele, J. Ab initio molecular dynamics using hybrid density functionals *The Journal of Chemical Physics* **2008**; 128(21), 214104; 0021-9606.

[130] Marques, M. A. L.; Castro, A.; Bertsch, G. F.; Rubio, A. octopus: a first-principles tool for excited electron-ion dynamics *Computer Physics Communications* **2003**; 151(1), 60–78.

[131] Pauling, L. *The Nature of the Chemical Bond and the Structure of Molecules and Crystals: An Introduction to Modern Structural Chemistry*; G - Reference, Information and Interdisciplinary Subjects Series; Cornell University Press, 1960.

[132] Shackelford, J.; Doremus, R. *Ceramic and Glass Materials: Structure, Properties and Processing*; Springer UK, 2008.

[133] Shlygin, E.; Ivanov, V.; Pustovarov, V.; Kruzhalov, A.; *Low-Temperature Time-Resolved Spectroscopy of Natural Topaz Crystals*; Ural State Technical University, Ekaterinburg, 620002, Russia. `http://hasyweb.desy.de/science/annual_reports/2005_report/part1/contrib/42/15082.pdf`.

[134] Jackson, R. A.; *CHE-30005 Solids, Surfaces and Catalysis: Solid State Chemistry lecture 5*; 2005; Keele University. `http://slideplayer.com/slide/1711057/`.

[135] Atkins, P. *Shriver and Atkins Inorganic Chemistry*, 5th ed.; Oxford University Press: Oxford, 2010.

[136] Lancashire, R. J.; *Chemistry of Transition Metal Complexes: The Russell Saunders Coupling Scheme*; 2000; University of the West Indies. `http://wwwchem.uwimona.edu.jm/courses/RScoupling.html`.

[137] Reddy, S. L.; Endo, T.; Reddy, G. S. *Electronic (Absorption) Spectra of 3d Transition Metal Complexes*; Farrukh, M. A., Ed.; InTech, 2012; Chapter 1.

[138] Gatta, G. D.; Nestola, F.; Bromiley, G. D.; Loose, A. New insight into crystal chemistry of topaz: A multi-methodological study *The American Mineralogist* **2006**; 91(11-12), 1839–1846.

[139] Krack, M.; Golze, D.; *RESP charges: calculation of CP2K properties*; 2013; CP2K Google Groups. `https://groups.google.com/forum/#!msg/cp2k/G3THGbvvIcU/X1zNNKy4x8cJ`.

[140] Goodenough, J. B. Theory of the Role of Covalence in the Perovskite-Type Manganites $[\mathrm{La}, M(\mathrm{II})]\mathrm{MnO}_3$ *Physical Review* **1955**; 100, 564–573.

[141] Kanamori, J. Superexchange interaction and symmetry properties of electron orbitals *Journal of Physics and Chemistry of Solids* **1959**; 10(2-3), 87–98.

[142] Jinan, N.; Yinghuai, Q.; Zhihui, W.; *Computer modeling of properties of topaz by CLAYFF*; 2010; School of Materals Science and Engineering, China University of Mining and Technology, Jiangsu Xuzhou (221116). `http://www.paper.edu.cn`.

[143] Abragam, A.; Bleaney, B. *Electron Paramagnetic Resonance of Transition Ions*; International series of monographs on physics; Clarendon P.: University of Michigan, 1970.

[144] Atkins, P.; de Paula, J. *Atkins Physical Chemistry*, 7th ed.; Oxford University Press: Oxford, 2002.

[145] Bailey, C. L.; Liborio, L.; Mallia, G.; Tomić, S.; Harrison, N. M. Calculating charged defects using CRYSTAL *Journal of Physics: Conference Series* **2010**; 242(1), 012004.

[146] Castleton, C. W. M.; Hoglund, A.; Mirbt, S.; Höglund, A. Density functional theory calculations of defect energies using supercells *Modelling and Simulation in Materials Science and Engineering* **2009**; 17(8), 084003.

[147] Finnis, M.; Lozovoi, A.; Alavi, A. The oxidation of NiAl: What can we learn from ab initio calculations? *Annual Review of Materials Research* **2005**; 35 (1), 167–207.

[148] Hutter, J.; Iannuzzi, M.; Schiffmann, F.; VandeVondele, J. CP2K: atomistic simulations of condensed matter systems *Wiley Interdisciplinary Reviews: Computational Molecular Science* **2014**; 4(1), 15–25.

[149] Isotani, S.; Regina Blak, A.; Watanabe, S. UV optical absorption spectra analysis of beryl crystals from Brazil *Physical Review B: Condensed Matter* **2010**; 405(6), 1501–1508.

[150] Jensen, F. *Introduction to Computational Chemistry*, 2nd ed.; Wiley, 2002.

[151] Karamertzanis, P.; Raiteri, P.; Parrinello, M.; Leslie, M.; Price, S. The thermal stability of lattice-energy minima of 5-fluorouracil: metadynamics as an aid to polymorph prediction *The Journal of Physical Chemistry. B* **2008**; 112(14), 4298–308.

[152] McCandless, D.; Hancock, M.; *Radiation Dosage Chart*; 2012; London. `http://www.informationisbeautiful.net/visualizations/radiation-dosage-chart/`.

[153] Mitra, S. *Fundamentals Of Optical, Spectroscopic And X-Ray Mineralogy*, 2nd ed.; New Age International Publishers, 1996.

[154] Nassau, K. *Color for Science, Art and Technology*; AZimuth; Elsevier Science, 1997.

[155] Northrup, P.; Reeder, R. Evidence for the importance of growth-surface structure to trace-element incorporation in topaz *The American Mineralogist* **1994**; 79(11-12), 1167–1175; 0003-004X.

[156] Pignataro, B. *New Strategies in Chemical Synthesis and Catalysis*; Wiley, 2012.

[157] Pines, D.; Nozières, P. *The Theory of Quantum Liquids: Normal Fermi liquids*; W.A. Benjamin, 1966.

[158] Zhang, S. B.; Northrup, J. Chemical potential dependence of defect formation energies in GaAs: Application to Ga self-diffusion *Physical Review Letters* **1991**; 67(17), 2339–2342.